Impact of surface chemistry on oxygen exchange in perovskite electrodes

Tripkovic, Dordije

Publication date:
2018

Document Version
Publisher's PDF, also known as Version of record

Ph.D. Thesis

DTU Energy
Department of Energy Conversion and Storage

Impact of surface chemistry on oxygen exchange in perovskite electrodes

Đorđije Tripković

Roskilde 2018

DTU Energy
Department of Energy Conversion and Storage
Technical University of Denmark

Frederiksborgvej 399
Building 775
4000 Roskilde, Denmark
Phone +45 4677 5800
info@energy.dtu.dk
www.energy.dtu.dk

Abstract

Solid oxide cells (SOC) enable direct and highly efficient conversion of chemical into electrical energy and vice versa. SOC have the potential to play a vital role in future energy systems based on renewable and intermittent energy sources such as wind and solar. The insufficient long-term stability hinders the full potential of SOC technology and their widespread use. A way to mitigate the problem is to reduce the operating temperature, thereby slowing down the degradation rates. This would bring an additional benefit by enabling the use of cheaper materials for auxiliary SOC components (e.g. sealings and interconnects). However, lower operating temperatures severely impede the electrode reactions, especially oxygen reduction/evolution reaction (ORR/OER) which usually has high activation energy. Therefore, the electrode materials with better catalytic activity towards ORR/OER are needed.

The focus of this thesis is the improvement of SOC oxygen electrode and the understanding of the factors determining its activity and stability. The study is based mostly on perovskite $(La_{0.6}Sr_{0.4})_{0.99}FeO_{3-\delta}$ (LSF), which is a good electronic and ionic conductor and stable in both oxidizing and reducing atmospheres, and $(La_{0.6}Sr_{0.4})_{0.99}CoO_{3-\delta}$ (LSC), which is a highly active ORR/OER material, but less stable compared to LSF. Many of the insights from the thesis are expected to be relevant for many other electrode materials of similar composition, and in particular for $(La_{1-x}Sr_{1-x})FeO_{3-\delta}$, $(La_{1-x}Sr_{1-x})CoO_{3-\delta}$, and $(La_{1-x}Sr_{1-x})(Fe_{1-y}Co_y)O_{3-\delta}$ (LSCF). All the measurements were carried out on model electrodes which are well-suited for fundamental studies of the critical phenomena on the oxygen electrode. Throughout the thesis, the emphasis was placed on the relations between the surface properties examined by X-ray photoelectron spectroscopy (XPS) and the oxygen exchange activity probed by electrical conductivity relaxation (ECR) and electrochemical impedance spectroscopy (EIS). The results are divided into five independent manuscripts, each forming a chapter in this thesis.

First, LSC and LSF electrodes were modified by introducing perovskite/Ruddlesden-Popper interfaces on the surface. In this way, oxygen exchange kinetics measured at 650°C and the pO_2=0.1 bar was improved up to 2-3 times in the case of LSF and 4-5 times in the case of LSC electrodes. This study has also revealed inconsistencies in the reported literature values, which can be much larger than the improvements obtained after the intentional electrode modifications.

Consequently, the following three manuscripts were devoted primarily to the investigation of non-modified electrodes. The results suggested the existence of two distinct states of perovskite surfaces. The states were labelled as 'activated' and 'passive' state

and found to differ in both surface chemistry and oxygen exchange kinetics (k_{chem} values at 650°C could be up to 60 times different). Furthermore, the transition from one state to another was found to be reversible and to be present in both thin film and bulk electrodes. After reaching the state of low oxygen activity ('passive state'), the electrodes could be reactivated by a high-temperature thermal treatment at 1000°C or by rinsing the electrodes in deionized water. In both cases, the reactivation was correlated with the disappearance 'non-lattice' strontium from the surface.

Finally, thin film LSF electrodes were modified by drop casting the metal-nitrate solutions of the following ions: Sr^{2+}, Fe^{3+}, Ce^{4+}, Gd^{3+}, Ba^{2+}, and Zr^{4+}. This study revealed a beneficial effect of barium on the activity and stability of the LSF electrodes, by removing or preventing the formation of the detrimental 'non-lattice' strontium.

Preface

This thesis is submitted to the evaluation committee and the Ph.D. school of the Technical University of Denmark in candidacy for a Ph.D. degree. The work was carried out from December 2015 to December 2018 at the Department of Energy Conversion and Storage funded by Innovationsfonden 4106-00006B in frame of the SYNFUEL project. Part of the project was carried out at Massachusetts Institute of Technology in Laboratory for Electrochemical Interfaces (group of professor Bilge Yildiz) thanks to the additional funding provided by the Otto Mønsteds Fond.

Roskilde, December 14, 2018

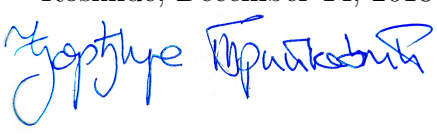

Đorđije Tripković

Acknowledgements

First, I would like to thank my principal supervisor **Peter Vang Hendriksen** for giving me the opportunity to join DTU Energy and meet all the nice people listed below. Thank you for your always constructive and clear advice, for optimism, for professionalism, and always having time to discuss. I will always wonder how you manage to remember even the tiniest details of my work even if I ambush you in the hallway.

- **Mogens Bjerg Mogensen** for always asking interesting questions and being cheerful;
- **Rainer Küngas** for helping me much more than he was supposed to and for giving me useful life advice;
- **Bilge Yildiz** for hosting me in her group at MIT and for proposing interesting experiments;
- **Jiayue Wang** for helping me with the surface the analysis and being a great guide to MIT;
- **Heidi Adler Berggren** for making even the most distracting and dull bureaucracy work fun and easy;
- **Belma and Stefano** for being great office-mates securing the supply of bananas on Monday mornings;
- **Cigdem and William** for being funny and talkative office-mates at MIT;
- **Friday Bar/Risø Empire crew** for making the Risø campus the best place to work;
- **Vladimir Srdić** for showing me the magic of materials science;
- **Jelena, Branimir, Elvira, Jovana, Ivan, Marija** for making the first baby-steps in science and having tons of fun while doing it;

I want to thank my parents **Snjezana** and **Nenad** for always being strong support and a safe harbor and accepting my absence. This whole effort, however, would not be possible without one very special person who has given me so much comfort, understanding, love, and laugh - my beloved wife **Kristina**. Thank you for giving birth to our little bag of joy, **Andrej**, to whom I dedicate this thesis.

Contents

CHAPTER 1

Introduction

1.1 Motivation

Climate change poses an existential threat to humanity. According to a recent report by The World Meteorological Organization, the past four years – 2015, 2016, 2017, and 2018 were the warmest years on record.[1] There is a scientific consensus that the rise of global temperatures in the last 150 years is caused by human activity and release of heat-trapping gases such as carbon-dioxide and methane. Despite the alarming reports, as of 2018, CO_2 content in Earth's atmosphere is steadily increasing. This is accompanied by a rise in global temperatures which has recently reached 1°C above the pre-industrial levels (mid-19$^{\text{th}}$ century), melting of polar ice, and a rise in sea level (Figure 1.1).

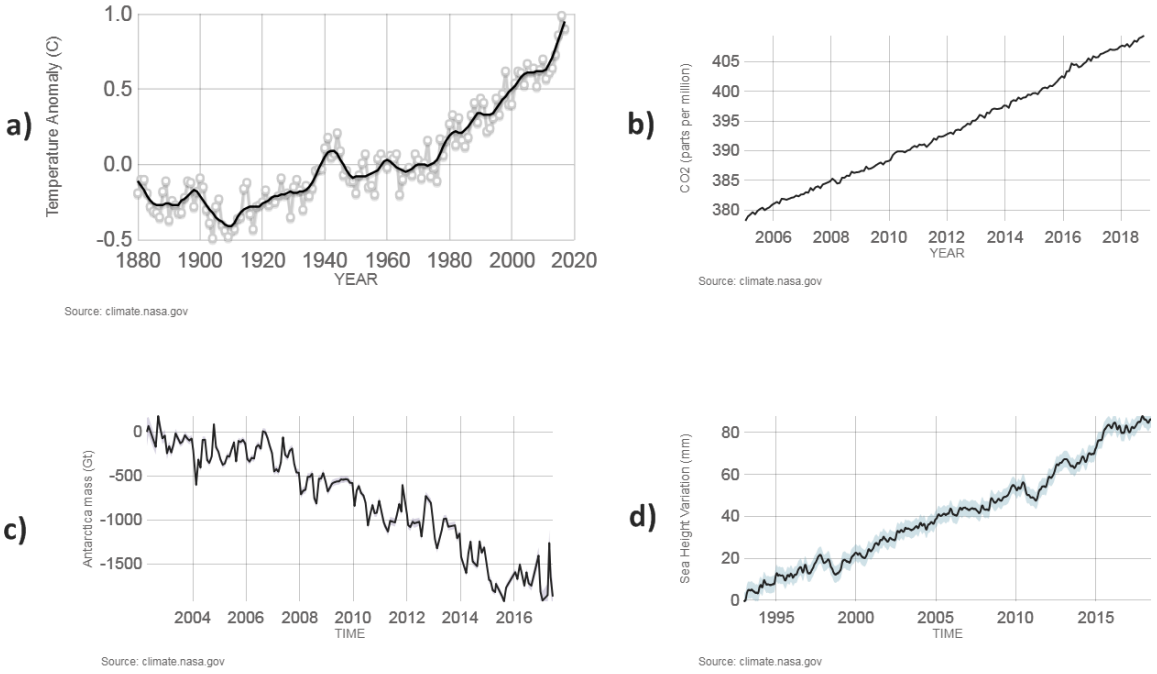

Figure 1.1: Global trends related to the climate change; a) Rise in global temperature in the last 140 years; b) Increase in CO_2 content in the Earth's atmosphere; c) Melting of polar ice; d) Rising sea level. Source: `climate.nasa.gov`.

In order to alleviate climate change, in December 2015, 195 countries have signed The Paris Agreement[2] with the central aim to keep the global temperature rise below 2°C. This ambitious goal requires substantial changes in the existing energy systems which will have to increasingly rely on renewable energy sources such as wind and solar. However, more 'green' electricity in the future grid will require a significant increase in energy storage capacity to compensate for the intermittent nature of renewables. According to the International Energy Agency, in order to meet the goals set by The Paris Agreement, energy storage capacity will have to increase from 140 GW (in year 2014) to 400 GW by 2050.[3] In general, electricity can be stored in one of the following ways:

- Mechanical (pumped hydro, flywheels, compressed air);
- Electrical (supercapacitors, superconducting coils);
- Thermal (molten-salt, hot rocks);
- Electrochemical (secondary batteries, flow batteries);
- Chemical (hydrogen, methane, methanol).

The abovementioned storage technologies differ in cost, discharge rates, capacity, energy density, and other aspects. Storing energy in form of chemical bonds by using electrolysis is particularly attractive as it enables high energy densities and fast discharge rates. It consists in converting low free energy species, such as H_2O and CO_2, into high free energy species, such as H_2, CH_4, hydrocarbons). This approach is also frequently termed as Power-to-Gas (P2G). There are currently several electrolysis technologies at different levels of maturity. Alkaline electrolysis cell (AEC) is a readily-available technology that has been widely used for industrial-scale applications for almost a century, but it operates at relatively low current densities which limits overall efficiency. Proton exchange membrane electrolysis cell (PEMEC) is another well-established technology which offers higher power density, but requires a higher capital cost mainly because of the use of expensive platinum catalyst. Solid oxide electrolysis cell (SOEC) operates at high temperatures (above 700°C). In comparison with alternatives, SOEC has a great potential in terms of efficiency and better economics. Another advantage of SOECs is the possibility of co-electrolytic conversion CO_2 and steam into syngas ($CO+H_2$), which can be used for production of CO_2-neutral fuels for the transportation sector via Fischer-Tropsch synthesis.[4] Furthermore, high operation temperature enables SOEC to work without the use of expensive catalysts and to utilize waste heat generated by other exothermic processes (Figure 1.2).

However, SOEC is a less mature technology than AEC and PEMEC. Despite the listed advantages, at the time of writing there are still no SOEC plants on the megawatt scale. The reason is mainly insufficient long-term stability which limits their commercial significance. The operating principle, reasons for long-term degradation, and possible strategies to mitigate the problem will be outlined briefly in the coming text.

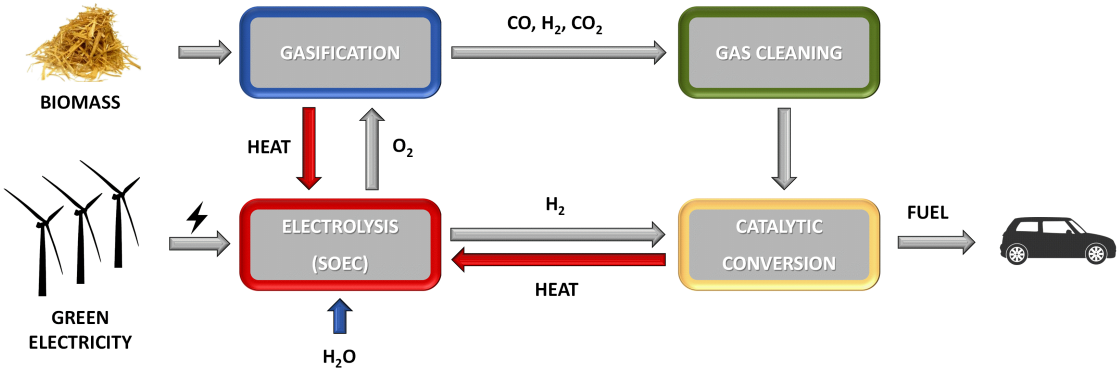

Figure 1.2: A scheme showing production of sustainable fuels for vehicular applications from biomass and green electricity proposed in the frame of SYNFUEL project. SOEC unit utilizes waste heat from exothermic processes, while producing oxygen and hydrogen from steam.

1.2 Solid Oxide Cell

Solid Oxide Electrolysis Cell can operate in a reverse mode, whereby consuming fuel (H_2, CH_4, CO) and oxygen it generates electricity. A cell operated in this way is Solid Oxide Fuel Cell (SOFC). Since selection of materials and general working principle is the same for both modes of operation, it is convenient to use an umbrella term Solid Oxide Cell (SOC).

1.2.1 Working principle

Solid oxide cell is an electrochemical device which enables highly efficient conversion of electrical to chemical energy and vice-versa. General working principle of SOC in both modes of operation is shown in Figure 1.3. In the simplest form, SOC consists of three functional and solid-state parts: porous oxygen- and fuel electrodes, separated by oxygen ion conducting, but electronically insulating electrolyte. In the SOFC mode of operation, electrons produced in oxidation of H_2 at the fuel electrode (anode) travel through an external circuit to the oxygen electrode (cathode), performing useful work. After reaching oxygen electrode, the electrons get consumed in oxygen reduction reaction (ORR). The oxygen ions generated in ORR travel through electrolyte reaching the fuel electrode. There, they are used in oxidation of fuel which closes the cycle. In the SOEC mode of operation, the electrochemical potential of the fuel electrode is changed by applying an external voltage to the cell. Fuel electrode then works as a cathode and reduces steam to H_2, generating oxygen ions. The ions then travel through the electrolyte to the oxygen electrode (anode) where they get oxidized and released as oxygen molecules via the oxygen evolution reaction (OER). It should be noted that besides H_2, O_2, and H_2O, the cell can operate with other compounds such as hydrocarbons and CO. Furthermore, the example shown in Figure 1.3 represents a planar cell design, but other cell designs (tubular, flat-tubular etc.) have been developed.

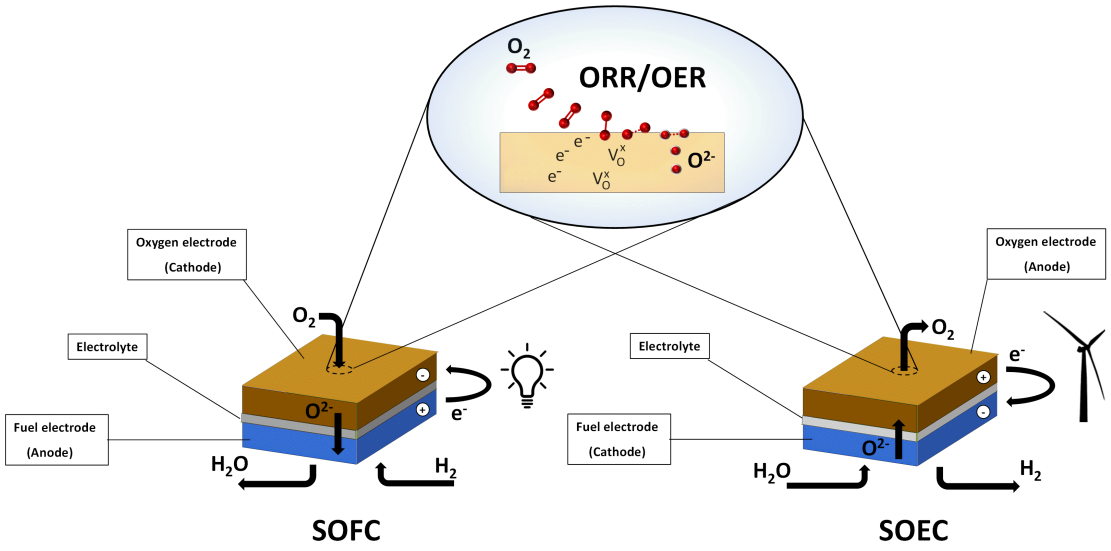

Figure 1.3: General working principle of Solid Oxide Fuel Cells (SOFC) and Solid Oxide Electrolysis Cell (SOEC), collectively termed as Solid Oxide Cells (SOC). Fast oxygen reduction/evolution reaction (ORR/OER) is one of the determining factors for overall efficiency of SOCs, especially at the intermediate (500-750°C) and low temperatures (<500°C).

The reactions occurring at fuel- and oxygen electrode in the two operating modes are following:

	SOFC	SOEC
Fuel electrode:	$H_2 + O^{2-} \rightarrow H_2O + 2e^-$	$H_2O + 2e^- \rightarrow H_2 + O^{2-}$
Oxygen electrode:	$\frac{1}{2}O_2 + 2e^- \rightarrow O^{2-}$	$O^{2-} \rightarrow \frac{1}{2}O_2 + 2e^-$
Overall:	$H_2 + \frac{1}{2}O_2 \rightarrow H_2O$	$H_2O \rightarrow H_2 + \frac{1}{2}O_2$

1.2.2 Materials

Materials used in solid oxide cells must meet several requirements including stability at high temperatures and mutual chemical and mechanical compatibility. Other requirements are dictated by the materials function in the cell.

Electrolyte materials require high ionic conductivity, but also low electronic conductivity, stability in both oxidizing and reducing atmospheres. Most commonly used electrolyte materials are fluorites (Figure 1.4a), including yttria-stabilized zirconia (YSZ) and gadolinium-doped ceria (GDC or CGO). YSZ has been material of choice in many SOC systems due to its good ionic conductivity and mechanical properties at high temperatures. The disadvantages of YSZ as electrolyte include its reactivity with La-based perovskite electrodes and the formation of insulating phases such as $La_2Zr_2O_7$ and $SrZrO_3$.[5] On the other hand, CGO has a higher ionic conductivity than YSZ. However, at temperatures above 500°C and in highly reducing conditions, Ce^{4+} ions get reduced

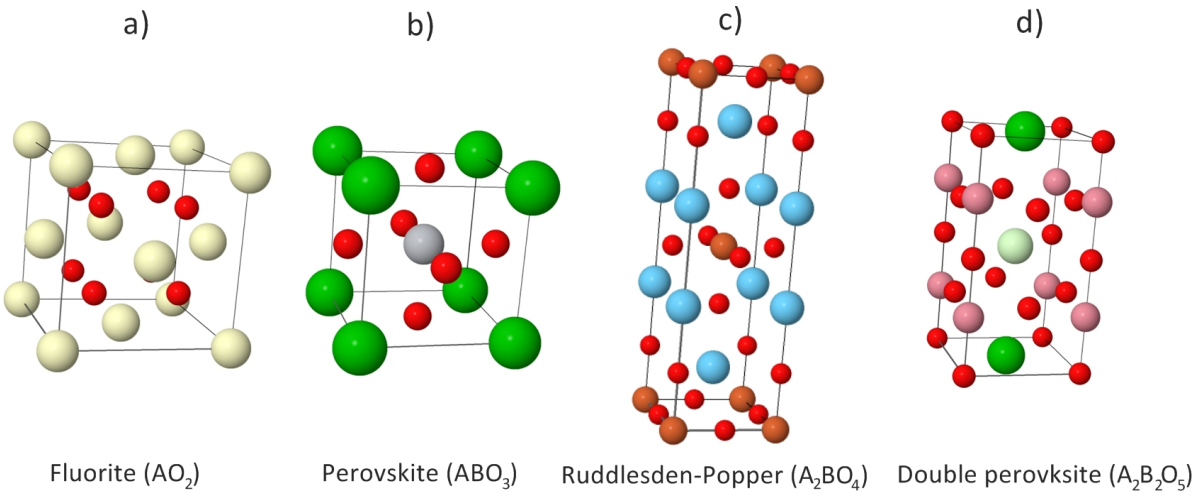

Figure 1.4: Most of materials used in solid oxide cells belong to one of the following structural groups: a) Fluorite; b) Perovskite; c) Ruddlesden-Popper; d) Double perovskite.

to Ce^{3+}, thereby introducing n-type electrical conductivity in the material which can lead to short-circuiting of the electrolyte.[6,7]

Fuel electrode requires good electronic and ionic conductivity, optimized microstructure to allow diffusion of gaseous species, and a high catalytic activity towards hydrogen oxidation/steam reforming. Porous composites of nickel and YSZ (Ni-YSZ cermets) are used almost exclusively for this purpose. This is because nickel is an excellent catalyst for hydrogen oxidation/steam reforming and it does not react with YSZ in a wide range of pO_2 and temperature. Furthermore, nickel and YSZ have similar thermal expansion coefficients and thus good mechanical compatibility.[8] However, Ni-YSZ cermets suffer from long-term degradation due to coarsening of nickel particles, which has been ascribed to differences in free surface energy between the two components.[9]

Oxygen electrode requires good electronic and ionic conductivity and high catalytic activity towards ORR/OER. Historically, the most commonly used oxygen electrodes have been composites Sr-doped lanthanum-manganite ($La_{1-x}Sr_xMnO_3$, LSM) and YSZ. In such electrode, LSM acts as an electronic conductor and ORR/OER catalyst, while YSZ acts as an ionic conductor. However, since ORR/OER reaction requires the presence of both electrons and oxygen vacancies and since LSM is poor ionic conductor, the active sites in LSM/YSZ electrodes will be limited to triple phase boundaries between LSM, YSZ, and the gas phase. In order to extend the reaction zone, the use of materials possessing both oxygen ion- and electronic conductivity has been proposed.[10] These mixed ionic and electronic conductors (MIEC) are typically of perovskite (1.4b), or perovskite-related (1.4c,d) structure with a wide variety of possible compositions and properties. Most commonly used are Sr-substituted lanthanum-cobaltites and ferrites ($La_{1-x}Sr_xCo_{1-y}Fe_yO_{3-\delta}$). New MIEC materials with better catalytic properties are constantly being developed. Some of the notable examples include perovskites such as $(Ba_{0.5}Sr_{0.5})(Co_{0.8}Fe_{0.2})O_{3-\delta}$,[11] double perovskites such as $PrBaCo_2O_{5+\delta}$, and Ruddlesden-Popper materials such as $LaNiO_{4+\delta}$.[12,13]

1.2.3 Strategies for improving electrode performance

The commercialization of solid oxide cells is hindered by degradation during long-term operation and the high capital costs. The latter could be greatly reduced by operation in so-called intermediate temperature range (500-750°C) which would enables the use of cheaper materials for auxiliary components (e.g. interconnects, sealings).[14] However, electrochemical performance of SOCs is also strongly temperature dependent as the electrode reactions and ionic conductivity of the electrolyte follow Arrhenius type dependence. Whereas the reduced ionic conductivity of the electrolyte can be compensated by decreasing its thickness, maintaining high electrochemical activity can be compensated by high overpotentials, which in turn aggravates the degradation. This is particularly true for oxygen electrode because of the higher activation energies of ORR/OER,[10] while cell performance at lower temperatures tends to be more affected by degradation of oxygen electrode than fuel electrode.[15]

Improvement of the electrochemical performance of the oxygen electrode has been studied extensively within the SOC community. Better electrode performance would enable lower overpotentials and thereby lower degradation rates. There are many different strategies to achieve better performance including:

- *Tuning of bulk chemical composition* (Figure 1.5a) - catalytic activity towards ORR/OER is altered by changing cation contents, however this also affects material thermodynamic stability and mechanical properties;
- *Composite electrodes* (Figure 1.5b) - by mixing materials which have superior ionic/electronic conductivity with ones that are good catalysts, one can achieve both properties simultaneously, but also some more profound forms of synergy;[16]
- *Infiltration/surface modification* (Figure 1.5c) - a small amount of an infiltrating agent (typically metal-nitrates) can be deposited on the electrode which, after calcination, results in surface covered with small particles, thereby increasing the catalytic activity;

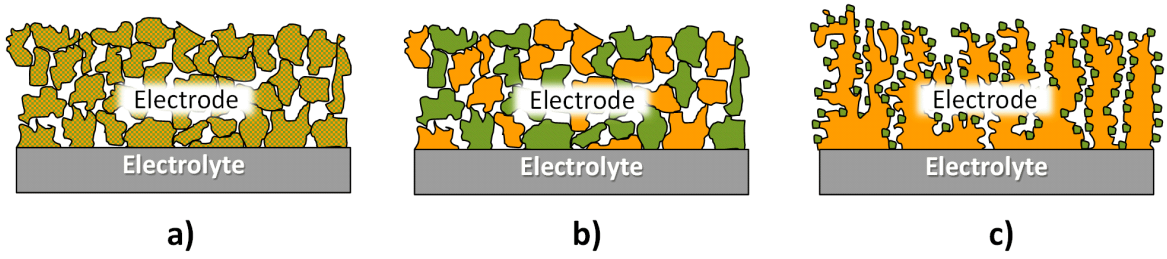

Figure 1.5: Schematic representation of three most frequently used strategies for improvement of oxygen electrodes: a) Tuning of bulk composition; b) Composite electrodes; c) Infiltration/-surface modification.

1.3 Methodology

Throughout the thesis, oxygen exchange activity was probed by Electrical Conductivity Relaxation (ECR) and Electrochemical Impedance Spectroscopy (EIS). Surface chemistry was by Photoelectron X-Ray Spectroscopy (XPS). These three methods form the backbone of this thesis as outlined in Table 1.1.

Table 1.1: Outline of the experimental methods used in the thesis

	ECR	EIS	XPS
Chapter 2	✓		
Chapter 3	✓		
Chapter 4	✓		✓
Chapter 5	✓	✓	✓
Chapter 6		✓	✓

1.3.1 Electrical conductivity relaxation

In electrical conductivity relaxation (ECR), the kinetics of oxygen exchange over the gas/solid interface is studied by observing changes in sample properties upon imposing a chemical potential gradient to the surface of the sample. ECR enables determination of the surface exchange coefficient (k_{chem}) and the bulk chemical diffusion coefficient (D_{chem}) by fitting the measured conductivity (or change in mass, optical properties) trends with the diffusion model by choosing the optimal k_{chem} and D_{chem} values for a geometrically well-defined piece of material. The diffusion model is given by Crank,[17] based on the solution by Carslaw and Jaeger:[18]

$$\begin{aligned}\frac{\sigma_\infty - \sigma_t}{\sigma_\infty - \sigma_0} = &\sum_{p=1}^{\infty} \frac{2L_x^2 \cdot exp(\frac{\beta_{p,x}^2 D_{chem} t}{a})}{\beta_{p,x}^2(\beta_{p,x}^2 + L_x^2 + L_x)} \\ &\times \sum_{q=1}^{\infty} \frac{2L_y^2 \cdot exp(\frac{\beta_{q,y}^2 D_{chem} t}{b})}{\beta_{q,y}^2(\beta_{q,y}^2 + L_y^2 + L_y)} \\ &\times \sum_{r=1}^{\infty} \frac{2L_z^2 \cdot exp(\frac{\beta_{r,z}^2 D_{chem} t}{c})}{\beta_{r,z}^2(\beta_{r,z}^2 + L_z^2 + L_z)}\end{aligned} \tag{1.1}$$

Here βs are the positive roots of the respective equations:

$$\beta_{p,x} \cdot tan\beta_{p,x} = L_x \tag{1.2}$$

$$\beta_{q,y} \cdot tan\beta_{q,y} = L_y \tag{1.3}$$

$$\beta_{r,z} \cdot tan\beta_{r,z} = L_z \tag{1.4}$$

Further, a,b and c stand for halves of width, length and height of a rectangular sample and are used for calculating the respective dimensionless parameters:

$$L_x = \frac{a \cdot k_{chem}}{D_{chem}} \tag{1.5}$$

$$L_y = \frac{b \cdot k_{chem}}{D_{chem}} \tag{1.6}$$

$$L_z = \frac{c \cdot k_{chem}}{D_{chem}} \tag{1.7}$$

If one of the samples dimensions is much larger than the others (e.g. $a \gg b, c$), then the diffusion along that dimension can be neglected which can simplify the equation 1.1 to a 2D or 1D expression. The dimensionless parameter L (Eq. 1.5-1.7) directly determines the sensitivity of estimating k_{chem} and D_{chem}. For instance, if L happens to be large, then the estimation of k_{chem} becomes difficult and the measurement is said to be in diffusion-controlled regime. On the other hand, small L means more difficult estimation of D_{chem} and a surface-controlled regime. For intermediate values, $0.03 \ll L \ll 30$,[19] the measurement is in mixed-control regime and both k_{chem} and D_{chem} can be determined properly. A MATLAB application $ECReX$ is created for the purpose of ECR data fitting in this thesis. More information about $ECReX$ can be found in the Appendix A.

1.3.2 Electrochemical impedance spectroscopy

Electrical impedance spectroscopy is a very powerful tool for *in situ* analysis of electrochemical systems. Impedance is simply the ratio between voltage and current and describes circuit's ability to resist the flow of electrical current. Impedance can be seen as a more general term than simple resistance given by the Ohm's law. Besides resistance, impedance also takes into account the response of other circuit elements such as capacitors (C) and inductors (L). For a circuit composed of resistors, capacitors and inductors, the overall response to alternating current (AC) will be complex resistance as a consequence of capacitor and inductor phase shifts (Equation 1.8).

$$Z = \frac{E(t)}{I(t)} = \frac{E_0 \cdot sin(\omega t)}{I_0 \cdot sin(\omega t + \phi)} \tag{1.8}$$

Impedance spectroscopy applies periodic alternating-current of small amplitude (a few mV or mA depending on if the measurement is voltage-controlled or current-controlled) to perturb an electrochemical system at equilibrium or steady-state non-equilibrium. The impedance response is measured at different frequencies (typically in the range from 1 mHz to 1 MHz) of oscillating current which provides the information about the processes that have different relaxation times.

Two most common ways of presenting the impedance data are Bode plot (Z vs. $frequency$) and Nyquist plot (Z_{ideal} vs. Z_{real}) shown in Figure 1.6. The analysis of impedance spectroscopy results consists in fitting the obtained data with an equivalent circuit comprised of simple elements such as resistor, capacitor, inductor, but also

some circuit elements specific to electrochemical systems such as Warburg and Gerischer element.

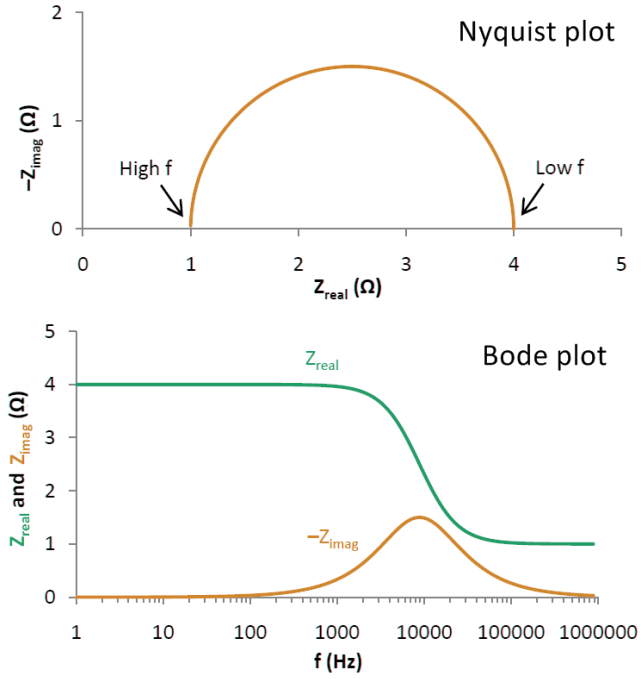

Figure 1.6: Simulated impedance spectrum of an equivalent circuit consisting of a resistor connected in series to a RC element (resistor and capacitor connected in parallel) represented in the two most common ways: (up) Nyquist plot and (down) Bode plot.

1.3.3 X-ray photoelectron spectroscopy

X-ray photoelectron spectroscopy (XPS) is a surface-sensitive characterization technique based on the measurement of kinetic energy of photoelectrons. Photoelectron is emitted when an X-ray photon of sufficient energy knocks out an inner-shell electron (Figure 1.7). The expelled electron has a certain kinetic energy (E_k) which is related to binding energy of the photoelectron (E_B) in the following way (Equation 1.9):

$$E_B = h\nu - E_K - \Phi \tag{1.9}$$

where h is Planck's constant, ν is frequency, and Φ is work function, dependent on both spectrometer and the material. Knowing the binding energy allows chemical analysis, since each element has a characteristic fingerprint. The most important feature of XPS is its surface sensitivity. This is because the emitted photoelectrons can escape only from the outermost surface layers (10 nm or less) due to their relatively low kinetic energies (typically 20-1100 eV). Furthermore, XPS can be used for quantitative analysis. By comparing the peak areas associated with the certain elements, one can obtain rela-

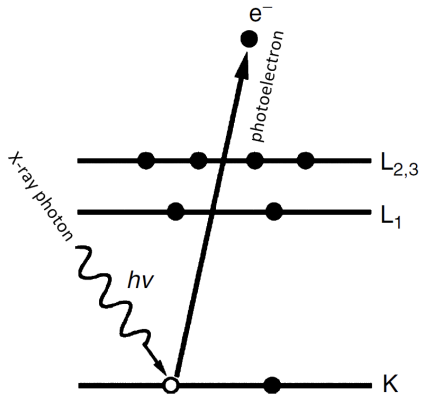

Figure 1.7: An illustration the photoelectron emission process.

tive atomic ratios of the surface layers. More information about the XPS quantification procedure can be found in the Appendix B.

1.4 Objective and scope of the thesis

The main goal of this project to contribute to the understanding of processes occurring at the solid/gas interface in the SOC oxygen electrodes. This insight is necessary for a rational development of highly efficient electrodes, and thus better overall cell performance. Furthermore, fast oxygen exchange (ORR/OER) between oxides and the surrounding atmosphere is important for other fields of application such as oxygen sensors, oxygen separation membranes, and metal-air batteries.

Throughout the thesis, special focus will be placed on the connections between surface chemistry and the electrode performance, both in terms of electrochemical activity and long-term stability. The study is based mainly on $(La_{0.6}Sr_{0.4})_{0.99}FeO_{3-\delta}$, a typical perovskite MIEC with good stability in both oxidizing and reducing atmospheres, often used as oxygen electrode for SOC.

The thesis is divided into 7 chapters. **Chapter 1** (Introduction) provides a general overview of the thesis including motivation, explanation of some basic concepts, and a brief overview of the methodology. **Chapter 7** concludes the thesis and gives an overall summary and outlook. The remaining chapters contain main scientific results of the project. They are written as independent manuscripts; however, many key concepts such as the ”activated” and the ”passive” electrode state, permeate through all 5 chapters. Chapters 2, 3, and 4 deal with bulk electrodes (dense rectangular bars), while Chapters 5 and 6 are based on thin film electrodes (Figure 1.8). The advantage of using model electrodes instead of porous systems is the simplified interpretation of the measured performance which can be influenced by porosity, tortuosity, and surface area.

Chapter 2 examines the effect of hetero-interfaces on the oxygen exchange activity of $(La_{0.6}Sr_{0.4})_{0.99}FeO_{3-\delta}$ (LSF) and $(La_{0.6}Sr_{0.4})_{0.99}CoO_{3-\delta}$ (LSC). The inspiration was found in the literature reports where extremely high oxygen exchange rates were observed

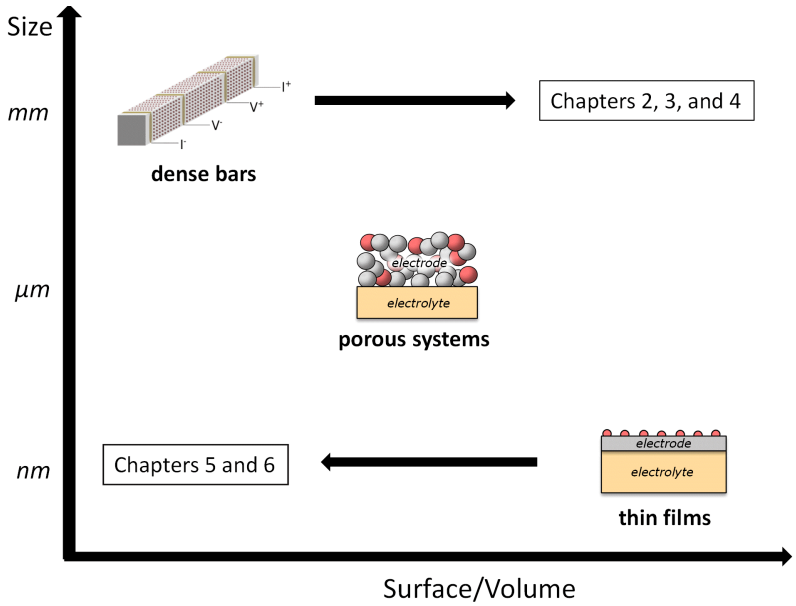

Figure 1.8: Schematic representation of the model electrodes used for measurement of oxygen exchange activity throughout the thesis.

at the interface between perovskite/Ruddlesden-Popper phases (113/214 interface).[20,21] However, the study presented here shows that measurements of this effect by ECR is not trivial as the effect can be masked by an increase in surface area. This initial work also revealed the importance of having a well-defined reference values of oxygen exchange activity for the estimation of enhancement/deterioration by surface modification.

Following up on these insights, **Chapter 3** is dedicated solely to the measurement of oxygen exchange kinetics of the non-modified LSF and LSC electrodes. This study revealed some unexpected phenomena. It was found that the oxygen exchange activity varied greatly below 700°C depending on samples thermal history. Furthermore, the activity of the electrodes could be reversibly switched between the two states, labelled as 'activated' and 'passive'.

Chapter 4 examines the transition from 'activated' to 'passive' state in greater detail with the aim to identify its origin. A clear connection was found between the oxygen exchange activity, surface chemistry, and noticable microstructural changes on the surface, all of which could be reversibly cycled by thermal treatment.

Chapter 5 is a study of non-modified thin film LSF electrodes by EIS and ECR with the aim of establishing reference values of oxygen exchange activity between 400-600°C. The two states of activity ('activated' and 'passive') observed in Chapters 3 and 4 were present also in thin films.

Chapter 6 investigates the effect of surface modification on the electrochemical performance of thin film LSF electrodes. Oxygen exchange activity obtained for electrodes modified by drop casting with nitrate solutions of Sr^{2+}, Fe^{3+}, Ce^{4+}, Gd^{3+}, Ba^{2+}, and Zr^{4+} was compared with the reference values from Chapter 5.

CHAPTER 2

Ruddlesden-Popper/perovskite interfaces and their effect of oxygen exchange activity

Abstract

The surface of dense ferrite- and cobaltite-based perovskite bars was decorated with the corresponding Ruddlesden-Popper phases ($LaSrFeO_4$ and $LaSrCoO_4$) by dip and spray coating. The effects of the thus formed perovskite/Ruddlesden-Popper interfaces on oxygen exchange activity was investigated by electrical conductivity relaxation between 650°C and 900°C at pO_2=0.1 bar. Further, the pO_2-dependence of the exchange rate was examined at 700°C in the pO_2 range between 0.05 and 0.5 bar. An increase in oxygen exchange activity by up to 5 times is observed after decorating the surface with nanoparticulate Ruddlesden-Popper phase. This study also demonstrates the importance of having consistent reference values for meaningful estimation of the enhancement due to the decoration.

2.1 Introduction

Solid oxide cells (SOC) enable highly efficient conversion of chemical to electrical chemistry and vice versa. A key challenge on the way to full commercialization is their long-term stability. Decreasing the operating temperature from 800°C, which is typical today, to the so-called intermediate temperature region (500-750°C) would be advantageous for long-term stability by slowing down the rate of degradation processes. Lower operating temperatures would also enable the use of cheaper materials for auxiliary cell components such as interconnects and sealings. On the other hand, decreasing operating temperature also affects the ionic conductivity of the electrolyte and electrode processes. This effect is particularly severe for oxygen electrodes and the related oxygen reduction/evolution reaction (ORR/OER) which usually has high activation energy. Improvement of the oxygen electrode performance is therefore important to enable the targeted reduction in operation temperature.

Perovskite materials of the general chemical formula ABO_3, where A is rare earth metal (usually lanthanum), B is a transition metal (usually cobalt, iron or nickel) are frequently studied and employed as oxygen electrodes for SOC. Materials belonging to the wide class of Ruddlsden-Popper phases ($nABO_3 \cdot AO$) have also been investigated as oxygen electrode materials with A being, for example, La or Pr and B typically Ni or Fe/Co. Here, we shall in particular study the n=1 end-member of this series (the perovskite phase can be seen as the other end member of this wide series with n=∞).

A remarkable observation of increased oxygen exchange activity at the interface between perovskite and Ruddlesden-Popper phase (often labelled as 113/214) interface was reported in 2008 by Sase *et al.*[22] Based on isotope exchange and secondary ion mass spectroscopy (SIMS) characterization of a sample studied at 500°C, the authors have estimated the oxygen exchange activity at the interface between perovskite $La_{0.6}Sr_{0.4}CoO_3$ and RP precipitates $(La,Sr)_2CoO_4$ (formed during sintering) to be three orders of magnitude higher than on the surface of $La_{0.6}Sr_{0.4}CoO_3$.[22]

The same group of authors then reproduced the effect in 1.5-2 µm thick model electrodes produced by pulsed laser deposition (PLD). Using the same characterization methods and well-defined interfaces between $LaSrCoO_4/La_{0.6}Sr_{0.4}CoO_3$ and $La_{1.5}Sr_{0.5}CoO_4/La_{0.6}Sr_{0.4}CoO_3$ the authors showed preferential incorporation of oxygen at the (a couple of microns wide) junction between the two phases.[20]

Two years later, Crumlin *et al.*[21] investigated the effect by decorating the surface of perovskite, $La_{0.8}Sr_{0.2}CoO_3$ thin film (85 nm) electrode with a small amount of $LaSrCoO_4$ phase, and observed 3-4 orders of magnitude increase in oxygen kinetics at 550°C by impedance spectroscopy at a partial surface coverage corresponding to thickness of 0.1 nm.

The first theoretical explanation of the origin of the enhanced oxygen exchange kinetics was given in 2012 by Han and Yildiz.[23] Using first-principles-based calculations in the framework of density functional theory (DFT), the authors proposed two factors that contribute to oxygen exchange kinetics: i) energetically favorable adsorption of oxygen at the interface region and ii) lattice strain which facilitates incorporation of oxygen. These two factors could, according to the model, account for a 400-fold increase in oxygen exchange kinetics at 500°C.

A year later, Hayd *et al.*[24] suggested that the beneficial interface effects could also be observed in more technologically relevant electrodes. By investigating $La_{0.6}Sr_{0.4}CoO_3$ microelectrodes prepared by metal-organic deposition sintered at 800°C, the authors observed 47x faster oxygen exchange at 600°C in comparison with bulk electrodes of the same composition. The enhancement was partially ascribed to the specific microstructure of the electrode, but partly also to the formation of Ruddlesden-Popper phase which is confirmed by X-ray diffraction. It was also observed that the kinetics was faster when the amount of the secondary phase was higher.

In the following years, the beneficial effect of 113/214 interface was attributed to various factors including electronic activation of Ruddlesden-Popper phase,[25] anomalous segregation of Sr at the interface,[26] and transfer of oxygen vacancies across the interface.[27] However, the exact mechanism and the extent of the effect are still not known.

It should be noted that several recent studies on the topic have shown only a mod-

erate improvement. Using thin film model electrodes consisting of the vertically aligned nanocomposite of $La_{0.8}Sr_{0.2}CoO_3$ and $LaSrCoO_4$ phases, Ma *et al.*[28] obtained 1 order of magnitude faster oxygen exchange than in the $La_{0.8}Sr_{0.2}CoO_3$ between 320 and 400°C. Furthermore, the performance of the electrodes was found to be unstable above 400°C.[28] In a very detailed study of $(La,Sr)CoO_3/(La,Sr)_2CoO_4$ nanocomposite (grain size approximately 50 nm), Stämmler obtained only 2/3 order of magnitude improvement.[29]

Besides in cobaltite systems, introduction of fast interfaces 113/214 has been attempted in other electrode materials with varying degrees of success. Lee *et al.*[30] have shown that decorating the surface of $La_{0.6}Sr_{0.4}Co_{0.2}Fe_{0.8}O_3$ (LSCF) with $LaSrCoO_4$ in an experiment very similar to Crumlin *et al.*[21] had almost no effect on its activity and stability, whereas the same procedure improved the performance of $La_{0.8}Sr_{0.2}CoO_3$ by two orders of magnitude. However, the performance of the electrode with $La_{0.8}Sr_{0.2}CoO_3$/ $LaSrCoO_4$ heterointerfaces (the one which is improved 2 orders of magnitude) had a performance similar to that of the LSCF electrode (that did not improve). In other words, a poorly-performing electrode could be significantly promoted, but a well-performing electrode could not be improved further. In a recent electrical conductivity relaxation study by Hong *et al.*,[31] a perovskite $La_{0.8}Sr_{0.2}FeO_3$ bar-shaped sample was decorated by infiltrating metal nitrate precursors which led to the formation of nano-islands of RP phase ($LaSrFeO_4$) *in situ* during the measurement. The authors reported an increase in oxygen exchange activity between 650 and 800°C of 1 order of magnitude in comparison with the non-modified electrodes. Similar to Lee *et al.*,[30] the activity of non-modified electrode was somewhat lower than the literature values for similar materials. These above examples illustrate a general issue within the field of electrode performance enhancement studies: the observed enhancement (regardless of the method used for the enhancement) is in many studies to a high degree determined by the performance of the unmodified electrodes. Unfortunately, the reported values for oxygen exchange parameters for commonly used solid oxide cell electrode materials vary by several orders of magnitude.

The present study aims to contribute to the understanding of 113/214 interface and its effect on oxygen exchange activity in Co-free systems. It involves the use of bulk and geometrically well-defined bar-shaped samples. The perovskite $(La_{0.6}Sr_{0.4})_{0.99}FeO_3$ and $(La_{0.6}Sr_{0.4})_{0.99}CoO_3$ bars were decorated with the corresponding RP phases ($LaSrFeO_4$ or $LaSrCoO_4$), but also with perovskite phases to obtain a suitable reference, where surface roughness and exchange area is also enhanced, but there are no (or less) hetero-interfaces. This was done in attempt to separate simple area effects from surface chemistry effects. After decoration, oxygen exchange activity was measured by electrical conductivity relaxation between 650 and 900°C at a pO_2 of 0.1 bar. Subsequently, pO_2 was varied between 0.01 and 1 bar at 700°C.

2.2 Experimental

Dense rectangular bars for electrical conductivity measurements were prepared from commercial powders $(La_{0.6}Sr_{0.4})_{0.99}CoO_{3-\delta}$ (CerPoTech AS, >99%) and $(La_{0.6}Sr_{0.4})_{0.99}FeO_{3-\delta}$ (Kusaka Rare Metal Products Co.Ltd., >99%). Powders were pressed uniaxially at 50 MPa for 30 s, followed by isostatic pressing at 300 MPa. The samples were then sintered following a procedure outlined by Søgaard *et al.*[32,33] which consist of two-step thermal treatment, the first at 1200°C for 4h and the second at 1150°C for 16h. Ramp rates during heating and cool-down were 120°C/min and 60°C/min, respectively. After sintering, the samples were gradually ground on each side with SiC sandpapers down to grit size of 1000 which removed at least 0.5 mm of material. Grinding was followed by polishing with diamond paste down to 1 µm of diamond particle size. The samples were rinsed in an ultrasound bath for 5 minutes with acetone, followed by ethanol, and finally, deionized water to remove glue and leftovers from polishing. After drying in ambient air, the surface of the samples was decorated by respective Ruddlesden-Popper phases in two ways:

(a) By dip coating the samples with nitrate solutions (Figure 2.1a);

(b) By spraying the earlier synthesized particles with an air-gun (Figure 2.1b);

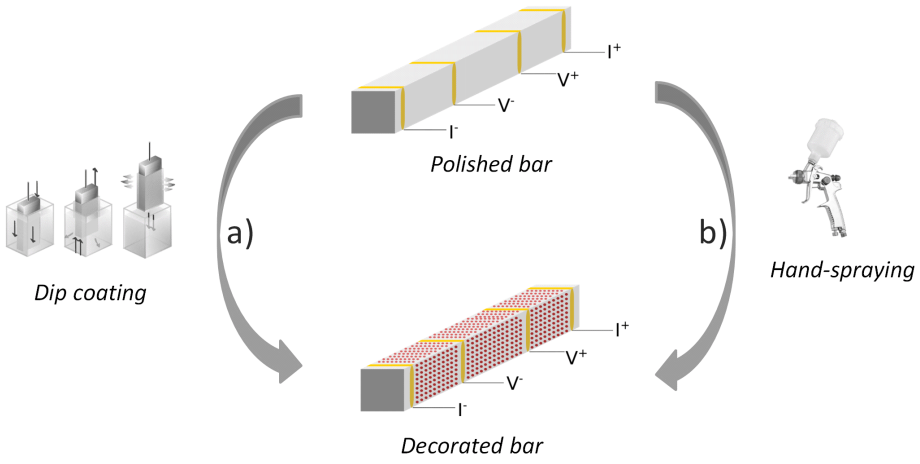

Figure 2.1: Two procedures used for decoration of perovskite surface; a) Dip coating; b) Hand-spraying.

The solutions for dip coating were prepared by mixing the metal nitrate precursors of stoichiometric ratios corresponding to:

- Perovskite phases $La_{0.6}Sr_{0.4}FeO_3$ and $La_{0.6}Sr_{0.4}CoO_3$ ('P');
- Ruddlesden-Popper phases $LaSrFeO_4$ and $LaSrCoO_4$ ('RP');

Following the synthesis procedure outlined by Jennings *et al.*,[34] the solutions were mixed with 3 mol equivalents of citric acid (Sigma-Aldrich, >99%) and 0.75 mol equivalents of ethylene glycol (Sigma-Aldrich, >99.7%). The precursors were mixed with 2 vol.% of surfactant Triton X-100 (Sigma-Aldrich) to facilitate wetting. The samples were dip-coated by immersion in precursors for 1 min. The samples were then left in ambient air 1 cm above a hot plate set to 150°C for 2-3 hours to support gelation.

$LaSrFeO_4$ powder for spray decoration was synthesized by high-energy ball milling and subsequent calcination at 1300°C for 10 hours of the following oxides:

- La_2O_3 (Sigma-Aldrich, >99%, dehydrated before weighting);
- $SrCO_3$ (Sigma-Aldrich, >99.9%);
- Fe_2O_3 (Alfa-Aesar, >99.9%);

Rietveld analysis of the calcined powder has shown 91.5 w.% of $LaSrFeO_4$ (RP phase) and 8.5 w.% of $La_{0.5}Sr_{0.5}FeO_3$. The calcination was also attempted at 1150, 1200, and 1250, which has resulted in lower content in RP phase (87% after calcination at 1150°C). Two slurries, one containing $(La_{0.6}Sr_{0.4})_{0.99}FeO_3$ (Kusaka Rare Metal Products Co.Ltd., >99%) and the other containing the calcined $LaSrFeO_4$ powder, were prepared by mixing the 10 grams of powder 15 grams of ethanol and 1 gram of polyvinylpyrrolidone binder. The slurries were deposited using a handheld spray gun. The decorated samples were left to dry in ambient air. In parallel, the specific surface area of the deposited layers was estimated by BET analysis of the powders obtained by calcination of the slurries at 1000°C for 2 hours.

Table 2.1 lists the samples used in this study along with the explanation of sample notation and loading of decorated material.

Table 2.1: Samples used in this study

Label	**Dimensions (mm)**	**Loading (mg/cm²)**	**Description**
LSF_P spray	2.1 x 2.1 x 19.4	11	$(La_{0.6}Sr_{0.4})_{0.99}FeO_3$ bar decorated with $(La_{0.6}Sr_{0.4})_{0.99}FeO_3$ by spray coating
LSF_{RP} spray	2.2 x 2.2 x 20.0	21	$(La_{0.6}Sr_{0.4})_{0.99}FeO_3$ bar decorated with $LaSrFeO_4$ by spray coating
LSF_P dip	2.1 x 2.1 x 18.4	0.6	$(La_{0.6}Sr_{0.4})_{0.99}FeO_3$ bar decorated with $La_{0.6}Sr_{0.4}FeO_3$ (nitrate precursors) by dip coating
LSF_{RP} dip	2.0 x 2.2 x 18.3	0.3	$(La_{0.6}Sr_{0.4})_{0.99}FeO_3$ bar decorated with $LaSrFeO_4$ by dip coating
LSC_P dip	2.1 x 2.1 x 17.7	0.4	$(La_{0.6}Sr_{0.4})_{0.99}CoO_3$ bar decorated with $La_{0.6}Sr_{0.4}CoO_3$ (nitrate precursors) by dip coating
LSC_{RP} dip	2.0 x 2.0 x 18.5	0.5	$(La_{0.6}Sr_{0.4})_{0.99}CoO_3$ bar decorated with $LaSrCoO_4$ by dip coating

After the decoration by dip and spray coating, samples were inserted in a quartz tube reactor of approximately 10 ml in volume to be analyzed by electrical conductivity

relaxation (ECR). Electrical contacts were established by twisting high-purity (99.99%) platinum wires around the samples at the edges (current terminals) and in the center (voltage sensing) with equidistant separation. Before the measurement, the samples were heated to 1000°C for two hours. The samples were tested from high to low temperatures at making a pO_2 jump from 0.2 to 0.1, followed by a pO_2-dependence test at 700°C. The tests were carried out in an O_2/N_2 mixture, where O_2 gas is known to contain up to 100 ppm of water. The total gas flow was kept constant at 5 ml/s (measured at room temperature), enabling abrupt changes of oxygen partial pressure, monitored by a zirconia sensor placed on the exhaust pipe. The temperature was measured with a thermocouple positioned in the vicinity of the sample (within 2 mm). The gasses were fed through stainless steel pipes and the rig holding the sample was made of alumina. The relevant experimental values were monitored automatically and logged with the sampling rate of 1 Hz. ECR parameter fitting in this study was done using ECReX (Appendix A). After the ECR test, the samples were further examined by grazing incidence XRD (GI-XRD) using Rigaku SmartLab and a glancing angle of 1°. Scanning electron microscopy (SEM) was carried out in a Zeiss Merlin Microscope. The surface roughness was examined by an optical Cyberscan Vantage Profilometer.

2.3 Results and Discussion

2.3.1 Surface characterization

The surface of the decorated bars was characterized by GI-XRD, SEM, and profilometry. The characterization was carried out on the samples after the electrochemical testing, but the results are presented before ECR analysis as the interpretation of k_{chem} values is influenced by the state of the surface. Figure 2.2 shows diffractograms of the tested samples collected at a glancing angle of 1°. All XRD patterns had peaks originating from the perovskite structure. As intended, a certain amount of Ruddlesden-Popper phase was present in LSC_{RP} (dip), LSF_{RP} (dip), and LSF_{RP} (spray) samples. RP phase on dip coated samples is probably formed during the calcination at 1000°C for two hours before the ECR test which was also the highest temperature the samples were exposed to after the decoration. This means that the RP phase was likely present during the whole ECR experiment.

SEM images of dip- and spray-coated samples after the ECR test are shown in Figure 2. Decorating samples by spray coating resulted in porous layers consisting of previously synthesized particles. The thickness of the surface layers was estimated to be 5±1 µm for perovskite and 8±1 µm for RP layer. BET analysis has shown a drastic difference (60x) in the specific surface area of the porous perovskite (1.83 m^2/g) and Ruddlesden-Popper (0.03 m^2/g) layers. More details of BET analysis can be found in the Supplementary Information. These results show that a comparison of oxygen exchange activities between spray coated samples is challenging as the samples vary both with respect to surface area enhancement and surface chemistry. Dip coating the samples with

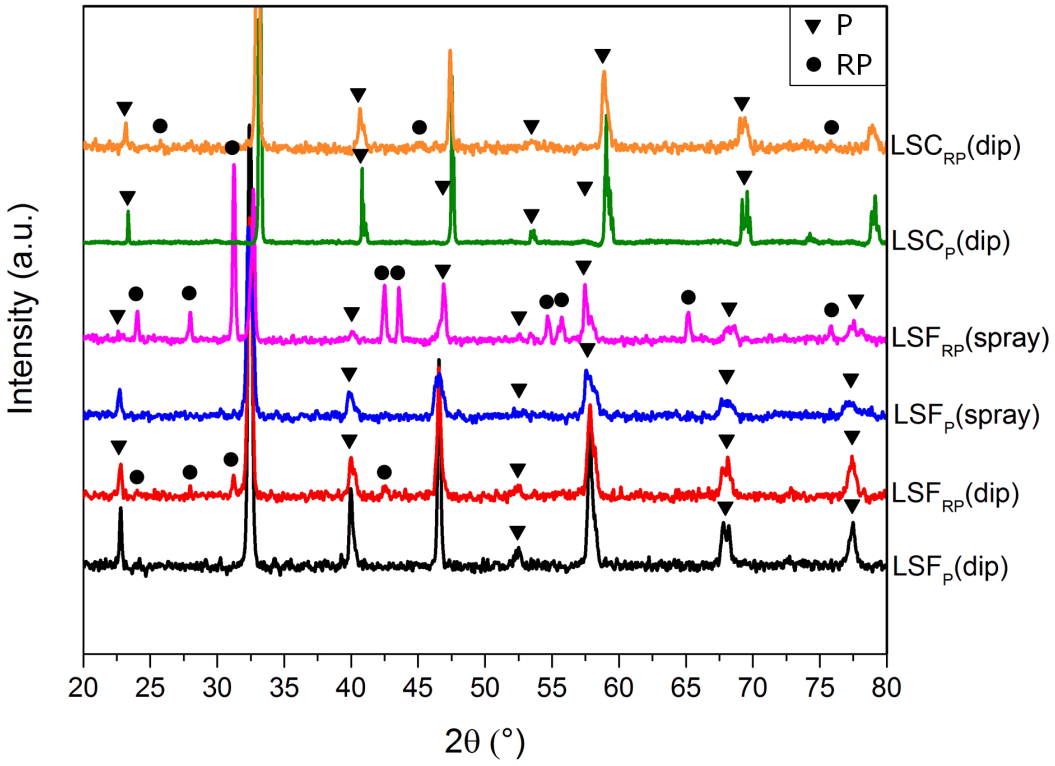

Figure 2.2: Grazing incidence XRD analysis collected at glancing angle of Φ=1° after the ECR test. XRD patterns used for identification of peaks: $La_{0.6}Sr_{0.4}FeO_3$ (ICSD 78065), $La_{0.6}Sr_{0.4}CoO_3$ (ICSD 82817), $LaSrFeO_4$ (ICSD 188895), $LaSrCoO_4$ (ICSD 415838).

nitrate solutions results in the formation of sparsely distributed islands/particles on the surface. The shape and size of the formed surface features varied for different decorating agents. LSF bar dip-coated with perovskite phase was covered with submicron particles sporadically agglomerated into islands of more than 10 µm in size. The surface of the LSF bar dip-coated with the RP phase was covered in micron-sized particles and loosely attached agglomerates of several microns in size. LSC bars dip-coated with perovskite phase was covered in micron-sized, partially delaminated, plate-like structures. The surface of LSC dip-coated with RP phase featured a coating of submicron microstructure which appeared to be preferentially deposited on grain boundaries.

The estimation of the specific surface area of dip-coated bars turned out to be difficult. One possibility was atomic force microscopy (AFM). However, due to relatively slow scanning rates, AFM analysis is usually constrained to a rather small surface (usually 10 µm x 10 µm). Furthermore, a very sensitive AFM tip is not well suited for capturing the wide variety of surface features present at the surfaces (Figure 2.3). Using BET analysis was also impractical due to a small specific surface area. Therefore, we used optical profilometry which has a broader measurement range and is much faster than AFM. An estimate of the increase in specific surface area could be obtained by comparing the average roughness of the bars (S_A, according to ISO 25178) calculated from profilometry data using Equation 2.1.

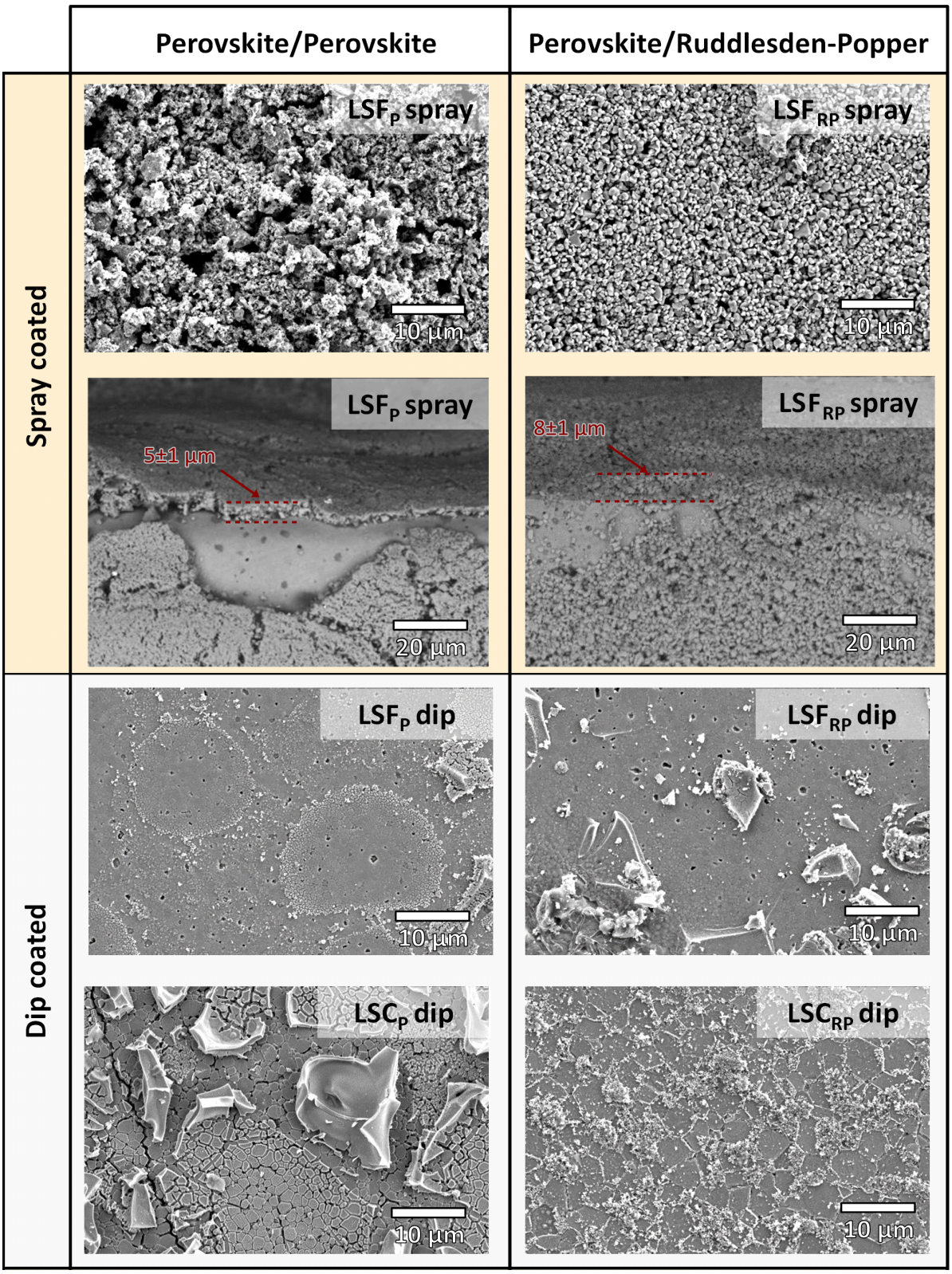

Figure 2.3: SEM images of the tested samples after ECR.

$$S_A = \frac{1}{A} \iint_A |Z(X,Y)|\, dx\, dy \tag{2.1}$$

The average roughness represents an overall measure of bar texture and simply put, should correspond to the specific surface area. However, it should be noted optical profilometry is insensitive to features such as nanoporosity which may further contribute to the active surface area. The average roughness of the dip coated samples, as well as the obtained surface profiles, are shown in Figure 2.4 and compared with the surface before the decoration. Calculation of surface roughness and rendering of the plots was done in MATLAB. Dip-coated bars had approximately 4x higher average surface roughness than the non-modified bars (polished and subsequently treated at 1000°C). An exception is the LSF bar dip-coated with perovskite phase which had only 2x higher S_A.

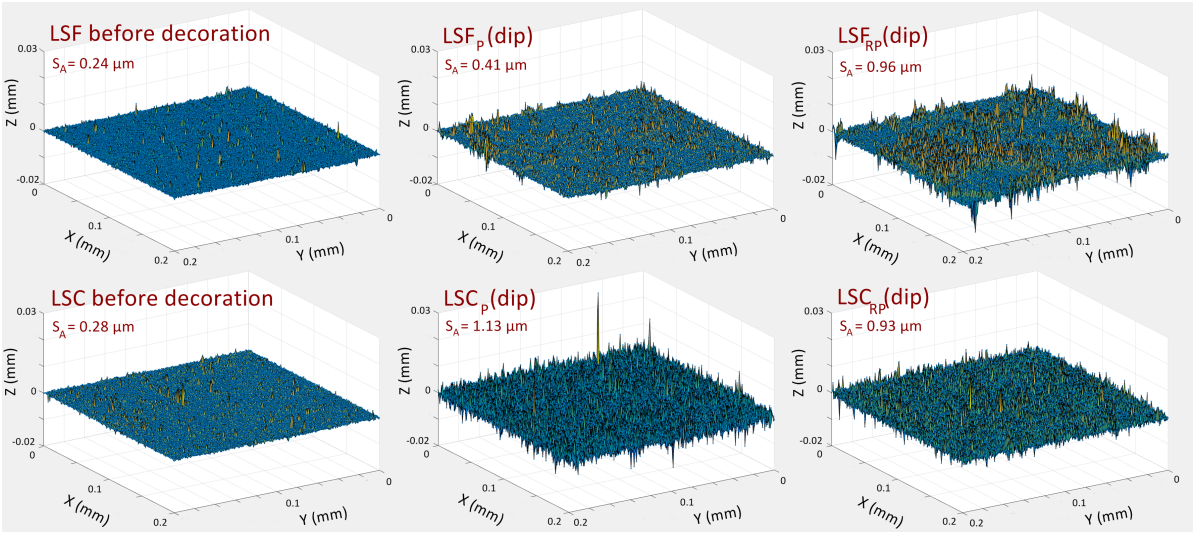

Figure 2.4: Surface profiles and the calculated average surface roughness S_A (Eq. 2.1) of the dip-coated bars compared with the non-modified surface.

2.3.2 Electrical conductivity relaxation

The results of temperature dependence test of the surface exchange rate of the ferrite- and cobaltite-bars are shown in Figure 2.5. At first, we compared the obtained k_{chem} with the other ECR studies from the literature. For ferrites, we used values reported by Søgaard *et al.*[33] on $(La_{0.6}Sr_{0.4})_{0.99}FeO_3$, ten Elshof *et al.*[35] on $La_{0.6}Sr_{0.4}FeO_3$, and the values obtained by Hong *et al.*[31] on $La_{0.8}Sr_{0.2}FeO_3$ before and after the decoration with RP phase ($LaSrFeO_4$). For cobaltites, the values are compared with studies of Søgaard *et al.*[32] on $(La_{0.6}Sr_{0.4})_{0.99}CoO_3$ and Egger *et al.*[36] on $La_{0.6}Sr_{0.4}CoO_3$. There is an obvious scatter among the values reported in the literature. In case of ferrites, the values reported by Søgaard *et al.*[33] at 900°C are almost one order of magnitude higher than the ones reported by ten Elshof *et al.*[35] Situation is the opposite at 700°C, where

k_{chem} reported by ten Elshof *et al.*[35] was ≈ 5 times higher. The apparent activation energy of k_{chem} found by Søgaard *et al.*[33] was 199±23 kJ/mol, which is roughly 1.5 times the value reported by ten Elshof *et al.*[35](131±14 kJ/mol). Furthermore, in the study by Hong *et al.*[31] oxygen exchange kinetics of the non-decorated $La_{0.8}Sr_{0.2}FeO_3$ electrode were much slower than in all other studies, while the RP-decorated electrode was only slightly better than the bare $La_{0.6}Sr_{0.4}FeO_3$ from the study of ten Elshof *et al.*[35] A considerable difference in k_{chem} is observable in cobaltite electrodes as well. Even though LSC in studies by Søgaard *et al.*[32] and by Egger *et al.*[36] had similar temperature dependence, the latter had almost one order of magnitude higher k_{chem} values.

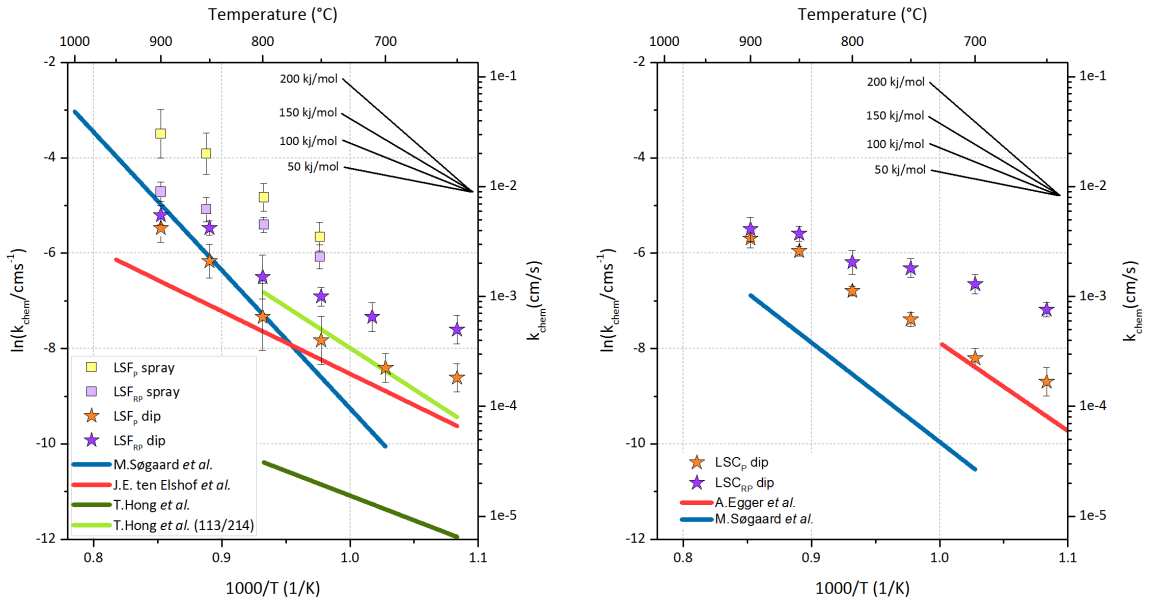

Figure 2.5: Temperature dependence of k_{chem} of Left) ferrite-based bars; Right) cobaltite-based bar. The results are compared with the selected literature values.[32,33,35,36]

Due to the inconsistencies mentioned above, the estimation of the effect of 113/214 interface based on comparison with literature is difficult. Furthermore, decoration causes an increase in specific surface area (Figures 2.3 and 2.4) which results in an increase in overall oxygen exchange rate, but not necessarily in the specific activity (normalized to material surface area). To decouple the effect of the increase in specific surface area from the effects of 113/214 interface, samples decorated with the perovskite phase were tested as well. Samples decorated with the perovskite phase were used as a reference, even though they are expected to have higher k_{chem} values than a non-decorated bar. Departure from the 'perovskite on perovskite' values can then be used for the estimation of any special effects of the 113/214 interfaces. The approach adopted here has its drawbacks as it can be hard to obtain the same specific surface area (as shown in case of spray coated samples). However, it gives a better assessment of effects ascribable to the addition of fast interfaces or changes in surface chemistry than when the improvement is compared to non-decorated bars.

The LSF bars decorated with a perovskite phase by spray-coating had very high k_{chem} values (approximately 4 times higher than the value reported for the non-decorated surface Søgaard *et al.*[33]). The very fast oxygen exchange kinetics is the reason for the large error bars in Figure 2.5. The sample was approaching the diffusion-controlled regime, where the determination of k_{chem} from ECR measurements becomes less precise. LSF bars decorated with RP phase by dip-coating had lower k_{chem} values, but notably, a different temperature dependence. The activation energies were found to be 150 kJ/mol for the perovskite decorated bar and 90 kJ/mol for the RP decorated bar. The fact that the apparent k_{chem} values were higher for perovskite decorated bar is likely a consequence of the difference in surface area of the deposited layer. To account for these differences, we used a simple model proposed by Li *et al.*[37] for the estimation of 'real' k_{chem} values by correcting for area variations (Equation 2.2).

$$k_{chem} = \frac{(1-\epsilon) \cdot k_{chem}^{app}}{l \cdot S} \tag{2.2}$$

In the Equation 2.2, k_{chem} and k_{chem}^{app} stand for actual and the apparent k_{chem} values, respectively, ϵ stands for porosity, l for thickness, and S for the surface area of the layer which is calculated by multiplying specific surface area obtained by BET with the total mass of the deposited layer (difference in sample mass after and before decoration). Using the Equation 2.2, 'real' k_{chem} values of perovskite decorated bar were estimated to be 3 times smaller (and very close to Søgaard *et al.*[33]). In other words, the perovskite-decorated samples showed no true enhancement in oxygen exchange kinetics, when the observed k_{chem} values were corrected for the surface area of the decorated phase. The same approach could not be applied to the RP-decorated bars due to a very small specific surface area (0.03 m^2/g), which suggests the decoration leads to performance enhancement that is not explainable by surface area increase alone.

The LSF bar decorated with perovskite phase by dip-coating seemed to have two distinct regimes of temperature dependence. At high temperatures (800°C and above) this sample followed the trend similar to LSF in the study by Søgaard *et al.*,[33] while at temperatures below 800°C it resembled the behavior of LSF. in ten Elshof[35] study. A similar trend was observed for the bar decorated with RP phase by dip coating. This bar had 2-4 times higher k_{chem} values than the sample decorated in the same way with the perovskite phase. However, this sample also had a higher average surface roughness (0.96 µm in comparison with 0.41 on perovskite decorated bar). This means that if 113/214 interface has a beneficial effect of oxygen exchange activity in ferrite systems, the magnitude of the improvement (often referred to in the literature as "enhancement factor") is not larger than 2-4 times, i.e. much less than 1 order of magnitude improvement reported by Hong *et al.*[31] or the 3-4 orders of magnitude increase found in cobaltite-based model electrodes.[21,22]

Oxygen exchange coefficients of LSC bar decorated with perovskite phase was in a very good agreement with the values obtained by Egger *et al.*,[36] but also significantly higher than the values obtained by Søgaard *et al.*[32] Despite smaller surface roughness (S_A = 0.93 µm as opposed to 1.13 µm in perovskite-decorated bar), RP-decorated bar had higher k_{chem} values than the perovskite-decorated bar, especially at lower temperatures

(4-5x increase). The two bars had markedly different activation energies of k_{chem}, 120 kJ/mol for P-decorated bar and 60 kJ/mol for RP-decorated bar. Different temperature dependence together with very similar values of surface roughness (perovskite-decorated bar had even higher S_A than RP-decorated one, 1.13 µm) suggest that the enhancement in oxygen exchange kinetics at 113/214 interfaces is a real phenomenon and indeed more pronounced in the cobaltite systems. The low activation energy of k_{chem} in the RP-decorated LSC bar indicates that the enhancement may be higher at lower temperatures.

Figure 2.6 summarizes the observed differences between RP- and perovskite-decorated bars. The columns visualize the apparent improvement expressed as k_{chem}(RP-decoration)/ k_{chem}(perovskite-decoration).

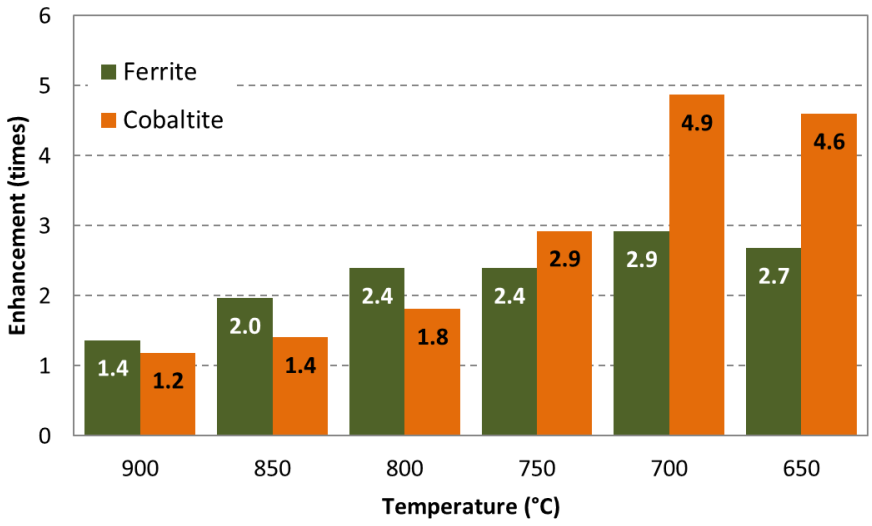

Figure 2.6: Visualization of the observed enhancement expressed as difference between k_{chem} values in RP- and P-decorated bars. Enhancement = k_{chem} (RP-decorated)/ k_{chem} (P-decorated).

In some studies where a very strong 113/214 effect is observed, the effect was found to be more pronounced at lower oxygen partial pressures.[21,30,38] Figure 2.7 shows the pO_2-dependence of the dip-coated bars at 700°C along with earlier discussed literature values.[32,33,35,36] We could not identify any significant change in pO_2-dependence of k_{chem} as the slope in log-log plot was between ½ and 1 in both P- and RP-decorated bars.

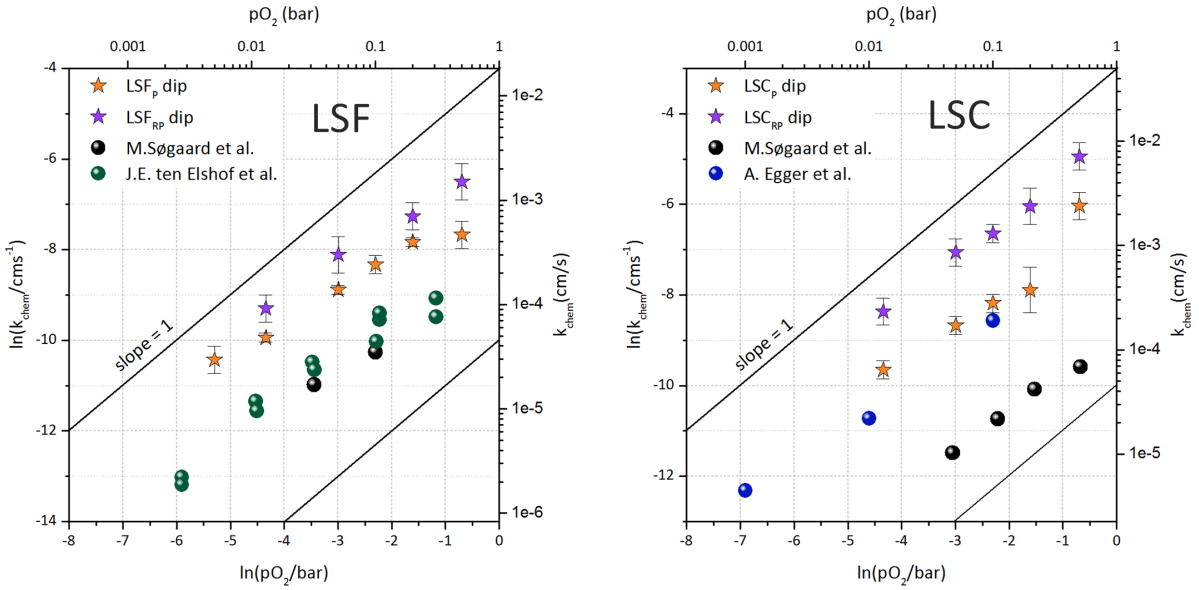

Figure 2.7: pO_2-dependence test of dip-coated bars at 700°C. Left) Ferrites; Right) Cobaltites.

The results of temperature- and pO_2 dependence are summarized in Table 2.

Table 2.2: Summarized results of the bars investigated in this study

Sample	**E_A (kJ/mol)**	**pO_2-dependence**
LSF_P (spray)	115 ± 12	-
LSF_{RP} (spray)	92 ± 6	-
LSF_P (dip)	147 ± 7	0.54
LSF_{RP} (dip)	90 ± 4	0.75
LSC_P (dip)	120 ± 5	0.98
LSC_{RP} (dip)	61 ± 5	0.94

2.4 Conclusion

The effect of perovskite/Ruddlesden-Popper (113/214) interfaces on oxygen exchange activity was investigated on dense ferrite and cobaltite samples by electrical conductivity relaxation between 650 and 900°C at pO_2 between 0.2 and 0.1 and at 700°C in the pO_2 range from 0.05 to 0.5 bar. The results suggest that introducing an RP-phase surface decoration (thereby introducing possibly fast 113/214 interfaces or changing in a beneficial manner the surface chemistry) has a mild effect on oxygen exchange activity of the materials in this study. In ferrites, it leads to an enhancement of up to 2-3x, while in cobaltites it leads to 4-5x higher oxygen activity. The effect is more pronounced at lower temperatures. By testing the samples with different surface areas, we have shown the importance of surface microstructure on the estimation of oxygen exchange

activity. Furthermore, a comparison with literature values was complicated due to a considerable scatter between the values reported by different groups. We, therefore, find that a more thorough investigation of the reference materials is required as differences between nominally identical and non-modified surfaces can be much higher than the effects of deliberate surface modifications.

Supplementary Information

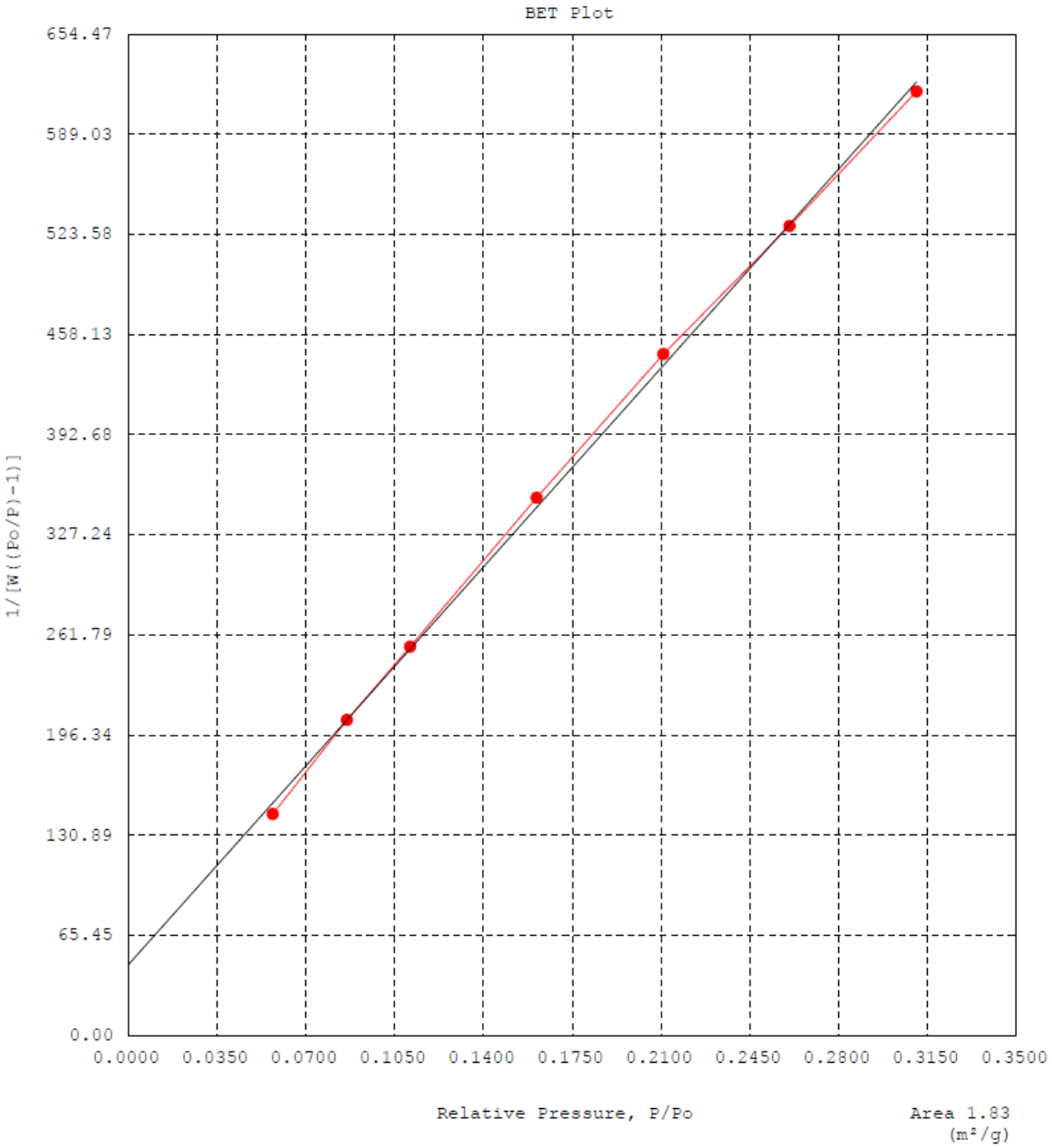

Figure 2.8: BET analysis of the perovskite powder obtained after calcination of slurry used for spray coating at 1000°C for 2 h.

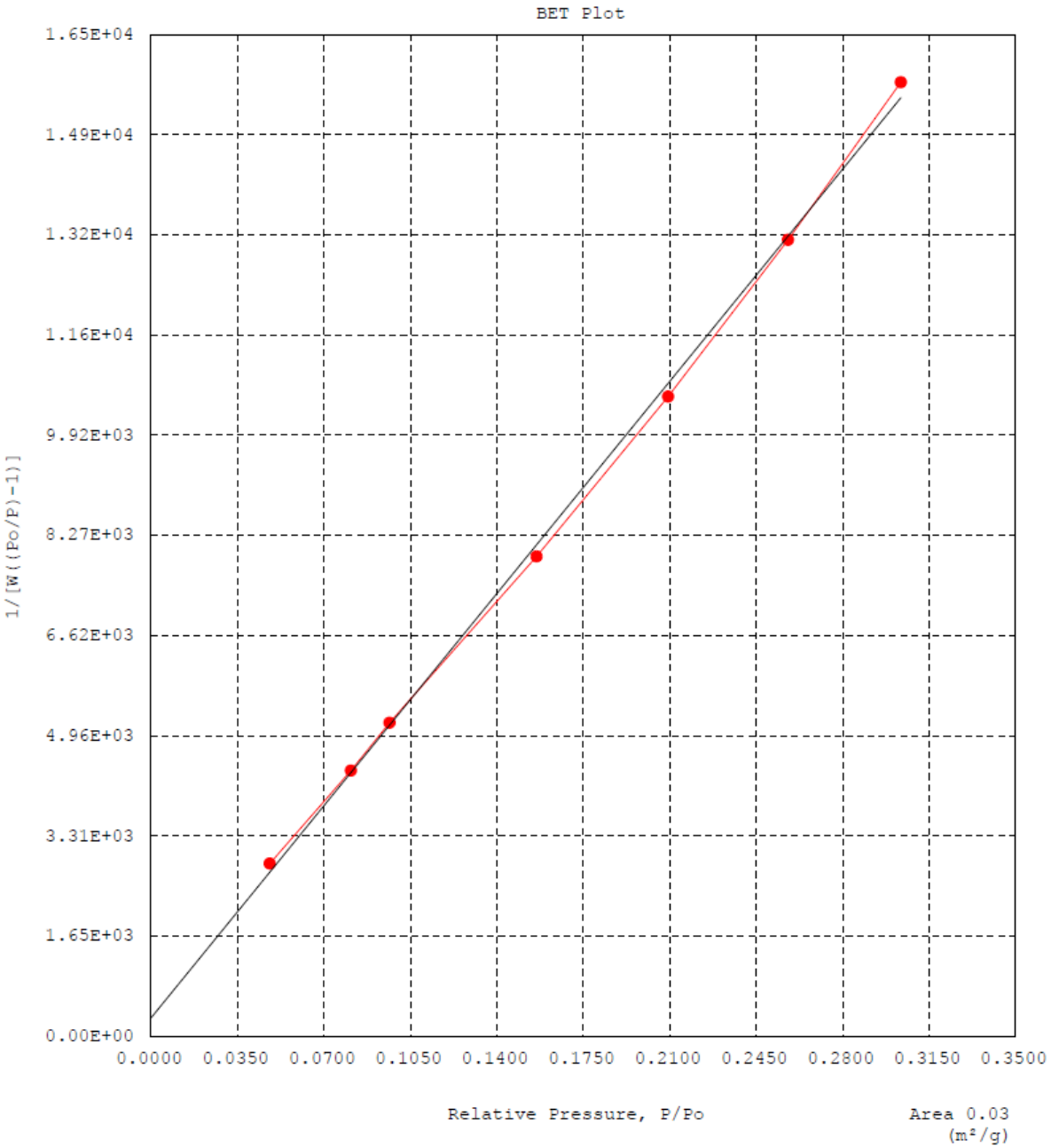

Figure 2.9: BET analysis of the Ruddlesden-Popper powder obtained after calcination of slurry used for spray coating at 1000°C for 2 h.

CHAPTER 3

Surface recrystallization – an underestimated phenomenon affecting oxygen exchange activity

Abstract

The rate of oxygen exchange on $(La_{0.6}Sr_{0.4})_{0.99}CoO_{3-\delta}$ (LSC) and $(La_{0.6}Sr_{0.4})_{0.98}FeO_{3-\delta}$ (LSF) was investigated by means of electrical conductivity relaxation (ECR) in oxidizing atmospheres (0.2-0.1 bar pO_2) from 650°C to 900°C. The reversible and reproducible changes in materials' performance are observed as a consequence of thermal treatment, manifested through drastic change in surface exchange coefficient (k_{chem}) and related activation energy with thermal history. The effect is found to be more pronounced in case of LSF, where k_{chem} at 650°C and 0.1 bar pO_2 can vary from $3 \cdot 10^{-4}$ to $1.1 \cdot 10^{-5}$ cm/s, while bulk properties such as electrical conductivity and the chemical diffusion coefficient of oxygen remain constant. The changes are related to a surface-confined phenomenon and the transition from one state to another is found to follow classical models of nucleation and growth processes. The findings demonstrate the importance of thermal history for studies of oxygen exchange kinetics in perovskite materials and offer an explanation for some of discrepances found in literature.

3.1 Introduction

Perovskite oxides belonging to the family; $(La_{1-x}Sr_x)_s(Co_{1-y}Fe_y)_{3-\delta}$ ($0 \leq x \leq 1$, $0 \leq y \leq 1$, $s \approx 1$) have found use as electrodes for solid oxide cells (SOC) and oxygen sensors and are also being explored as potential materials for oxygen separation membranes. This is due to their good ionic and electronic transport properties, high activity for oxygen reduction/evolution reactions (ORR/OER) and the fact that via tailoring the composition the properties can be 'tuned' with a view to the specific application. Preferred compositions that have been widely studied include $La_{0.6}Sr_{0.4}CoO_{3-\delta}$, $La_{0.6}Sr_{0.4}FeO_{3-\delta}$, and $La_{0.6}Sr_{0.4}Co_{0.8}Fe_{0.2}O_{3-\delta}$ designated here as LSC,LSF, and LSCF,

respectively.[32,33,35,36,39,40] Significant research efforts to improve the catalytic activity of perovskite materials are ongoing, since this could enable faster sensors, and allow SOCs to operate at lower temperatures. This would in turn make SOC technology more cost-competitive through use of cheaper auxiliary materials e.g. the interconnect steel.

Various strategies have been employed to improve the kinetics of the ORR/OER on (La,Sr)(Co,Fe)$O_{3-\delta}$ electrodes. The most straightforward way of achieving this, and one that has also been extensively pursued, is tuning of the bulk chemical composition of the perovskite by doping.[36,40–48] In this approach, one has to compromise between obtaining fast reaction kinetics whilst maintaining sufficient thermodynamic stability and suitable mechanical properties. In general, oxygen exchange rates increase as more of the La in the structure is substituted with Sr (increasing the vacancy concentration) and as more of the Fe is substituted with Co. For instance, by slightly changing the La:Sr ratio in LSC, Egger *et al.*.[36] obtained 5x faster reaction kinetics at 725°C for $La_{0.5}Sr_{0.5}CoO_{3-\delta}$ in comparison with $La_{0.6}Sr_{0.4}CoO_{3-\delta}$. However, increasing Co content in (La,Sr)(Co,Fe)$_{3-\delta}$ leads to a decrease in the thermodynamic stability of the compound and increases the mismatch in coefficient of thermal expansion (CTE) between the perovskite and typical electrolyte materials, e.g. yttria-stabilized zirconia (YSZ) and Gd-doped ceria (CGO). The increase of alkali-earth and Co-content also makes the perovskite more reactive towards zirconia. Unless the physical contact between such perovskites and zirconia is prevented (e.g. by the use of a ceria-based barrier layer), high-resistivity phases, e.g. $La_2Zr_2O_7$ and $SrZrO_3$ are formed at the perovskite-zirconia interface, which leads to a higher area-specific resistance (ASR) of the device.[5] Finally, due to cation size mismatch and charge interactions, alkali-earth dopants have a tendency to segregate to the surface and form more resistive and/or catalytically less active layers.[49–54] The material with the composition $La_{0.6}Sr_{0.4}Co_{0.8}Fe_{0.2}O_{3-\delta}$[44–46,55] offers a good compromise between stability and mechanical properties for SOC. Nevertheless, the two 'end-member' materials of the (La,Sr)(Co,Fe)$_{3-\delta}$ class; a pure cobaltite (LSC) and a pure ferrite (LSF), are still under study for both sensor and SOC applications, the former due to its superior oxygen exchange properties and the latter due to its virtues with respect to cost, ease of handling, and high stability.[32] There are also noteworthy attempts to describe the catalytic activities of the materials in terms of other bulk descriptors such as such as the center of O_{2p} band proposed by Lee *et al.*.[56] and the position of Fermi level relative to the conduction band proposed by Jung and Tuller.[57]

A fruitful approach to fabrication of commercially relevant electrodes with rapid ORR/OER kinetics has been to manufacture composites where perovskites are combined with fast ionic conductors like Gd-doped ceria or even zirconia.[16,40,58–61] In such an approach, one utilizes the best properties of the constituting materials – the fluorite serves as the primary path for oxygen ions, while the perovskite provides catalytic activity for oxygen exchange and a path for electrons. Sometimes, besides providing their separate functions for charge transport more elaborate forms of synergy between the two materials have been reported, where a beneficial effect on one material emerges only when the other one is present. For instance, Druce *et al.*.[16] have shown that oxygen exchange on $La_{0.6}Sr_{0.4}Co_{0.8}Fe_{0.2}O_{3-\delta}$ directly benefits from the presence of $Ce_{0.9}Gd_{0.1}O_{1.95}$, thereby increasing the overall oxygen exchange rate. Similarly, in a recent paper by Ovtar *et*

al.,[59] a five-fold improvement in surface reaction kinetics at 750°C in comparison with pure $(La_{0.6}Sr_{0.4})_{0.98}FeO_{3-\delta}$ has been ascribed to the inreased amount of $Ce_{0.9}Gd_{0.1}O_{0.195}$ in the composite.

Finally, a very promising route for enhancing ORR/OER kinetics of this class of perovskite materials is via surface modification.[20,21,31,62–65] This strategy includes "infiltration": a method where a small amount of an infiltrating agent (typically nitrate precursors with the desired cations) is deposited onto the perovskite surface and after a thermal treatment forms a nano-particulate surface decoration increasing the catalytic activity. Some groups have reported large improvements of almost 3 orders of magnitude when small amount of LSC Ruddlesden-Popper phase (i.e. $(La,Sr)_2CoO_{4\pm\delta}$) is placed in contact with the corresponding perovskite ($(La,Sr)CoO_{3-\delta}$).[20,21] Most studies where such large effects have been observed have been done on model electrodes typically in the form of thin dense films. Albeit smaller, beneficial effects have also been reported on more technologically relevant electrodes.[24]

When assessing the efficacy of a particular improvement route, one usually compares the catalytic activity with a reference – a non-modified sample or a literature value. However, establishing a suitable reference point is not necessarily trivial (see Chapter 2). A good illustration is given by Hayd *et al.*[24] where a literature review reveals that area specific resistance of LSC measured by different groups can differ up to 2 orders of magnitude in absolute values, but also deviate strongly with respect to the apparent activation energies. Interestingly, in the same paper, the authors have observed that "LSC" electrodes prepared by a metal organic decomposition route performed 47x faster than the material with the same nominal composition in bulk form. This was ascribed to the multi-phase character and the formation of fast heterointerfaces due to the specific fabrication procedure. Making meaningful comparisons between results obtained by different groups is further complicated by the fact that the thermal history of the samples prior to measurement is rarely detailed in literature. Furthermore, it is often not clear how stable the reported enhancements are and whether the reference samples have representative and stable performance themselves.

Here, we report the dependence of the oxygen exchange rate on the thermal history of both LSF and LSC. The oxygen exchange was studied via conductivity relaxation on bulk samples. It was found that a high-temperature treatment can lead to a transient enhancement in surface exchange kinetics which diminishes slowly over several days at 650°C. An important implication of these findings is that differences in thermal history of the samples may account for some of the discrepancies found in the literature for oxygen exchange on LSF and LSC, and potentially also other perovskite materials.

3.2 Theory

Transformation kinetics

The measured transport properties are found to be time dependent. The behavior seems to be related to a re-crystallization or surface precipitation phenomenon. Transformation from one phase to another by a crystallization mechanism can be described by the Avrami equation.[66–68]

$$X = 1 - exp(-k \cdot t^n) \tag{3.1}$$

Here, X represents the extent of the transformation (fraction) and t is time. The graphical interpretation of this equation yields a characteristic S-shaped curve. The equation 3.1 is equivalent to the equation 3.2:

$$ln(-ln(1 - X)) = ln(k) + n \cdot ln(t) \tag{3.2}$$

The form of Avrami equation, where double logarithm of the extent of transformation is plotted versus time, is useful for determination of k and n from slope and intercept. These coefficients bear information about the rate of transformation and its dimensionality. In the case where the amount of nucleation sites is not changing over time, $n \approx 1$ corresponds to 1D, needle-like growth; $n \approx 2$ to a 2D, plate-like growth and $n \approx 3$ to a 3D, globular growth.

3.3 Experimental

All tested samples were in form of dense, rectangular bars prepared from commercial powders (Table 3.1) by uniaxial pressing at 50 MPa followed by isostatic pressing at 300 MPa. Samples were first sintered at 1200°C for 4 h, followed by sintering at 1150°C for 16 h with the ramp rate of 120°C/h during heating and 60°C/h during cool down. Samples were ground gradually on each side with SiC sandpaper down to grit size of 1000 (removing at least 0.5 mm of material), followed by fine polishing with diamond paste down to 1 μm diamond particle size. In order to remove glue and leftovers after polishing the samples were rinsed in an ultrasound bath for 5 minutes with acetone, followed by ethanol and finally deionized water. No further thermal treatments were carried after this point and before the first ECR experiment. An illustration of experimental procedure and thermal treatments can be found in the Supplementary Information (Figure 3.7). Conductivity was measured by the four-probe technique in a quartz tube reactor of approximately 10 ml volume. Contacts were established by twisting high-purity (99.99%) platinum wires around the samples at the edges (current terminals) and in the center (voltage sensing) with equidistant separation. The testing atmosphere was a dry N_2/O_2 mixture with possible impurity being water in amounts less than 100 ppm originating from the oxygen gas. All the experiments were done by changing pO_2 from 0.2 to

0.1 bar (reduction runs) and from 0.1 to 0.2 bar (oxidation runs). The total gas flow was kept constant at 5 ml/s (measured at room temperature) enabling abrupt changes of oxygen partial pressure which is monitored by a zirconia sensor. The temperature was measured with a thermocouple positioned in the vicinity of the sample (within 2 mm). The gasses were fed through stainless steel pipes and the rig holding the sample was made of alumina. The relevant experimental values were monitored automatically and logged with the sampling rate of 1 Hz. ECR parameter fitting was carried out in *ECReX* (Appendix A). The reported values in the results section are average values of two samples for both LSF and LSC, where error bars indicate the maximum and the minimum values. The surface chemistry of the LSF sample after the ECR measurements was analyzed using time-of-flight secondary ion mass spectrometry (TOF-SIMS IV from ION-TOF GmbH, Münster, Germany).

Table 3.1: Samples used in this study

Samples	LSC	LSF
Composition	$(La_{0.6}Sr_{0.4})_{0.99}CoO_{3-\delta}$	$(La_{0.6}Sr_{0.4})_{0.98}FeO_{3-\delta}$
Powder Supplier	CerPoTech AS	Kusaka Rare Metal Products Co. Ltd.
Purity	>99%	>99%
Density	>99%	>98%
Dimensions	2.04 x 2.01 x 18.50	3.70 x 0.75 x 17.60
	2.16 x 2.13 x 17.70	3.40 x 3.45 x 18.60

3.4 Results

3.4.1 Electrical conductivity

The measured electrical conductivity of the LSC and LSF samples are reproduced in Figure 3.1. Error bars are less than 5%. The values are found to be in good agreement with values previously reported in the literature (also included in the plots).[32,33,36] The electrical conductivity of both LSC and LSF decreased with increasing temperature and decreasing pO_2 in the experimental range of this work. The electrical conductivity of LSF was roughly 10 times lower than for LSC and showed a maximum value of 250 S/cm at 500°C.

3.4.2 Temperature dependence of k_{chem} and D_{chem}

As noted in the Experimental section, LSC and LSF samples have not been exposed to high temperatures after grinding and polishing prior to the first ECR measurements. We have measured the temperature dependence of the oxygen transport properties by changing the temperature stepwise from 650 to 900°C and then from 900 to 650°C. Remarkably, as seen in Figure 2, the samples tested in this work showed different behavior

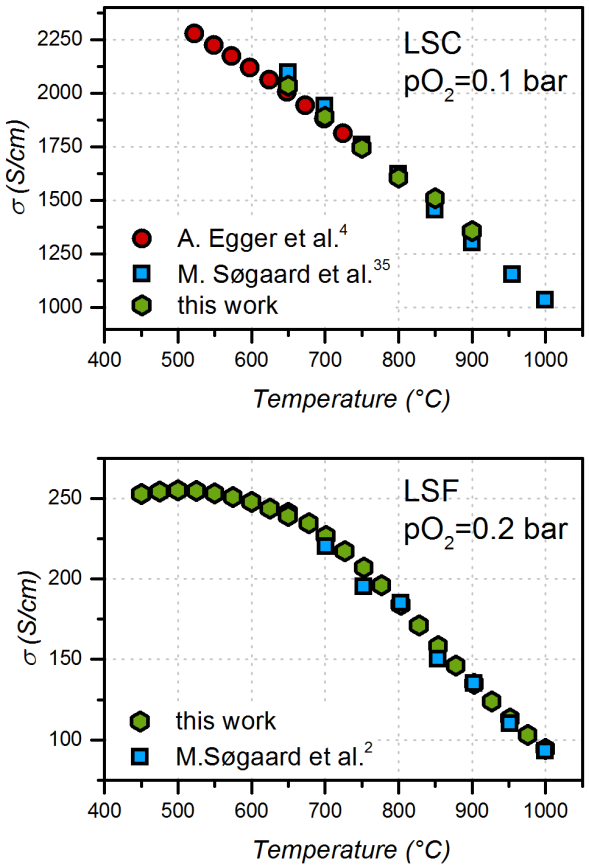

Figure 3.1: Electrical conductivity of LSC (top) and LSF (bottom) at constant pO_2.[32,33,36]

in terms of k_{chem} when measured from low to high (upwards) or from high to low temperatures (downwards). Note that error bars indicating minimum and maximum measured and fitted values are significantly smaller than the observed differences.

Electrical conductivity relaxation results of LSC and LSF have been reported by several groups and are reproduced in the same plot for comparison.[32,33,35,36] While fairly good consensus exists in reported chemical diffusion coefficient (D_{chem}) values, there is a large scatter in reported surface oxygen exchange (k_{chem}) values for both for LSC and LSF. The apparent activation energies for both heating and cooling runs are listed in Table 3.2. Again, the values associated with k_{chem} vary much more than D_{chem} counterparts.

3.4.3 Long-term stability of k_{chem} and D_{chem}

Evidently from the results presented in Figure 3.2 the measured surface exchange coefficient depends on the thermal history of the sample. The strongest differences are observed at the lower temperatures (650°C). To investigate the effect further a new set

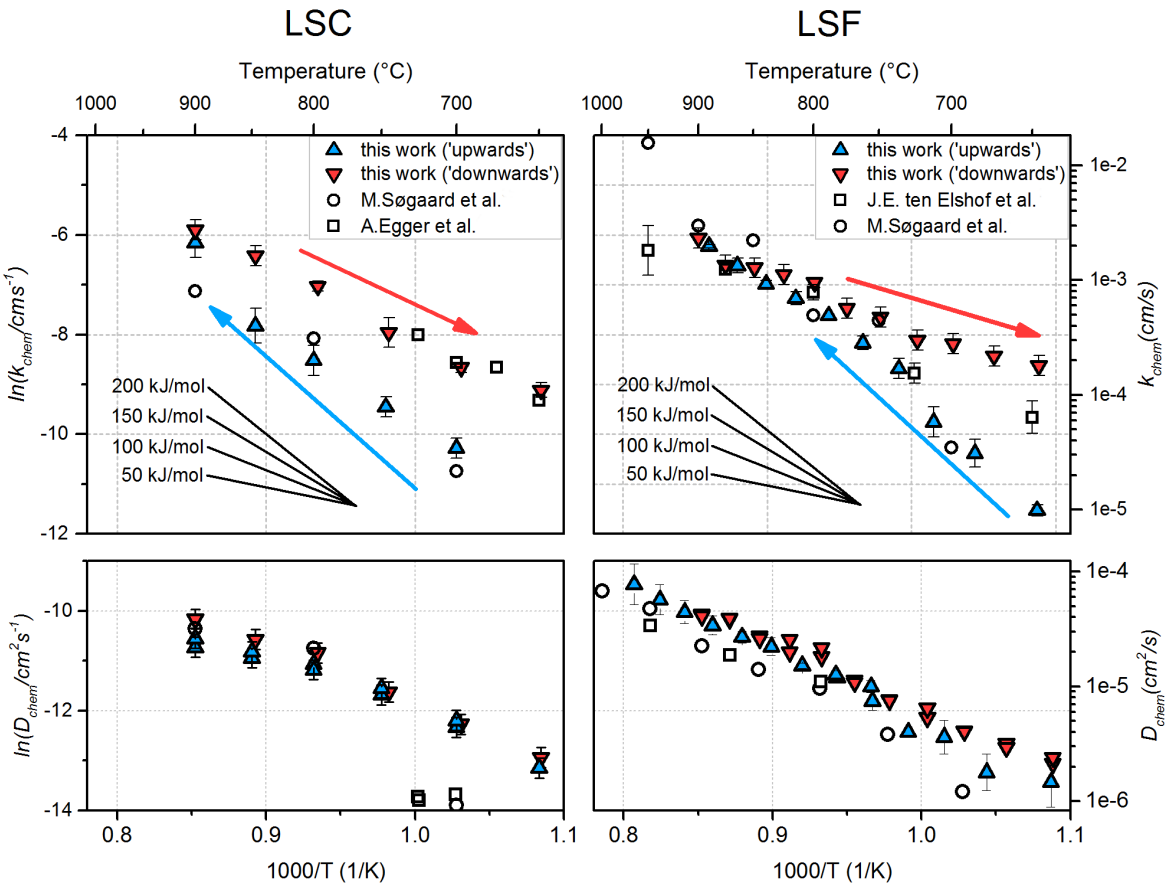

Figure 3.2: Arrhenius plots surface oxygen exchange (k_{chem}) and chemical diffusion coefficient (D_{chem}) of LSC (left) and LSF (right) at pO_2=0.21 bar.[32,33,35,36]'Upwards' and 'downwards' refer to measurements from low to high temperatures and vice-versa, respectively.

of conductivity relaxation measurements was carried out over 10 days for both materials. Before the experiment, the samples were treated at 1000°C for 10 hours and then the samples were cooled down to 650°C in less than an hour. Electrical conductivity stabilizes in less than two hours after the cool-down, but the samples were allowed to equilibrate for a couple of hours more before the first ECR measurement. Hence, the samples are equilibrated with respect to oxygen (the value of δ in $(La,Sr)(Fe,Co)O_{3-\delta}$) at the new temperature, before pO_2 changes related to the ECR measurements were imposed.

The obtained k_{chem} and D_{chem} values are shown as a function of time at 650°C in Figure 3.3a-b. The timescale shown on x-axis represents the time that has passed since the end of thermal treatment at 1000°C. The values of k_{chem} immediately after treatment at 1000°C were surprisingly high, reaching $3 \cdot 10^{-4}$ cm/s for LSF and $4.5 \cdot 10^{-4}$ cm/s for LSC for reduction runs from 0.2 to 0.1 bar pO_2. Over the course of ten days, these values gradually decreased over 30x in case of LSF and about 3-4x in case of LSC (approaching the values measured initially). At the same time, the diffusion coefficient remained

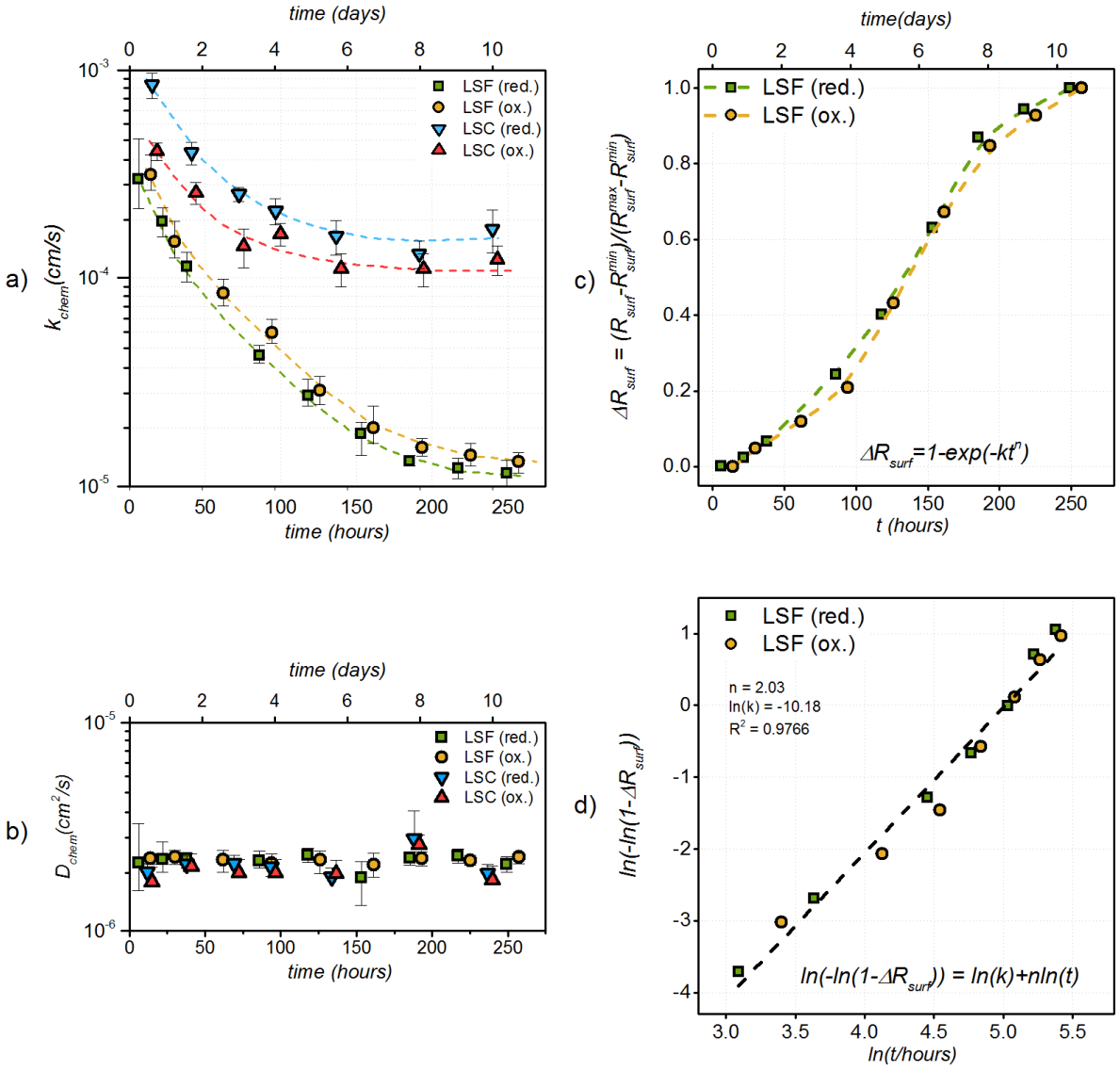

Figure 3.3: Long-term stability of (a) k_{chem} and (b) D_{chem}; (c) Normalized change of surface resistance R_{surf} over time follows the characteristic S-shaped curve; (d) Linearized S-curve with fitting parameters n and k related to dimensionality and speed of phase transformation.

Table 3.2: Activation energies of k_{chem} and D_{chem} for LSC and LSF. 'Upwards'and 'downwards' refer to measurements from low to high temperatures and vice-versa, respectively. (note: literature values are estimated by linear fit through the reproduced data points)

Results and References	E_A [kJ/mol]	
	k_{chem}	D_{chem}
LSC "upwards"	183±18	86±6
LSC "downwards"	124±7	102±5
LSC (M.Søgaard et al.)[32]	-	79±5
LSC (A.Egger et al.)[36]	165	129
LSF "upwards"	185±7	114±6
LSF "downwards"	92±6	110±3
LSF (M.Søgaard et al.)[33]	199±23	137
LSF (J.E. ten Elshof et al.)[35]	131±14	81±12

constant and almost equal for both materials at $2 \cdot 10^{-6} cm^2/s$. Note that conductivities reproduce well and also that the time at temperature is so long that in terms of oxygen the sample is fully equilibrated before the step changes of pO_2. The surface exchange coefficient is inversely proportional to the surface resistance (R_{surf}). If the decrease in surface exchange coefficient shown in Figure 3.3a is instead presented in terms of surface resistance and normalized in a way that $R_{surf}^{min} = 0$ corresponds to $k_{chem}^{max} = 3 \cdot 10^{-4}$ cm/s and $R_{surf}^{max} = 1$ corresponds to $k_{chem}^{min} = 1 \cdot 10^{-5}$ cm/s , we obtain a distinct S-shaped curve shown in Figure 3.3c. A similar approach could not be applied for LSC since the k_{chem} change over 10 days was too small to yield clearly shaped trend when normalized. The obtained S-curve can be well described using the Avrami equation (section 3.2) for which we could extract the parameters after the linearization. The fitting parameters are found to be $n \approx 2$ and $\kappa \approx 3.8 \cdot 10^{-5} h^{-2}$ (3.3d).

After the aging period at 650°C a third line of experiments was initiated, where the samples were thermally treated stepwise to gradually higher temperatures and the kinetics was measured at 650°C between each treatment. The results are illustrated in Figure 3.4. The first changes to k_{chem} (at 650°C) occurred upon thermal treatment at 800°C for 10 hours. Further increase in treatment temperature led to an even higher increase in k_{chem} measured at 650°C. This indicates that the process influencing the change in surface exchange is triggered between 700 to 800°C.

Surface analysis by ToF-SIMS of the LSF sample after the full sequence of ECR measurement and a cool-down to room temperature in N_2/O_2 atmosphere (cooling rate 120°C/h) is shown in Figure 3.5. The data provide only a semi-quantitative estimate of the relative differences between bulk and surface contents of a single ionic species and cannot be used to determine the absolute amounts of different elements. While the amount of La, Sr, and Fe in the bulk (deeper than 20 nm from the surface) is constant, the surface is clearly depleted in lanthanum and enriched in strontium and iron. This region extends to a depth of approximately 20 nm. Further screening for possible contaminants such as silicon, chromium, alkali-, and alkali-earth ions did not show any significant build-up of these ions (Figures 3.14-3.16).

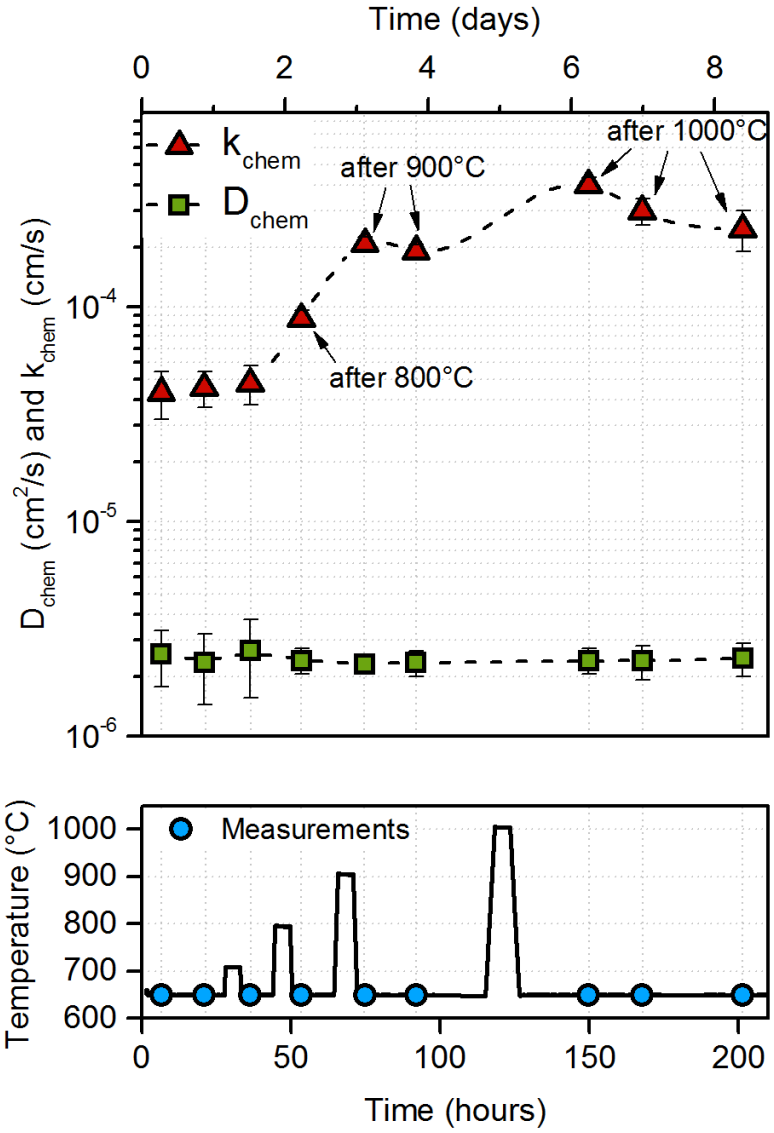

Figure 3.4: The effect of thermal treatment at different temperatures on surface oxygen exchange of LSF.

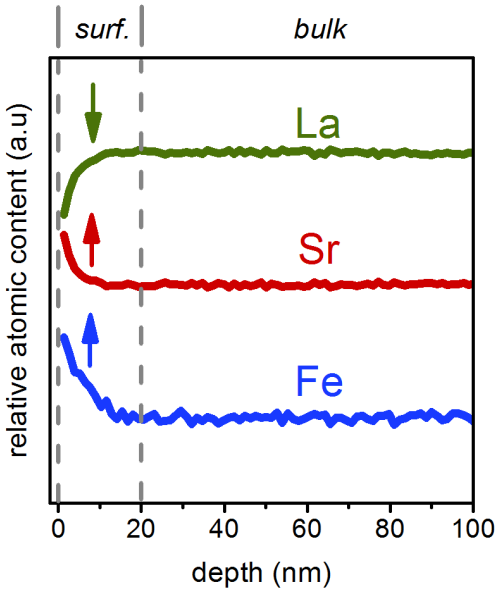

Figure 3.5: ToF-SIMS profiles of the surface of LSF sample after ECR experiments.

3.5 Discussion

The ECR results of LSF and LSC show that surface exchange kinetics can vary substantially over time within the single experimental run and that the measured values can be correlated with thermal history of the sample. As can be seen from Table 3.2, activation energies of D_{chem} measured in 'upward' and 'downward' measurements do not differ significantly when absolute uncertainties related to measurement accuracy are taken into account. In contrast, the differences in k_{chem} values are drastic, especially in case of LSF, where the apparent activation energy upon cooling is halved compared to the activation energy upon heating. Initially surprising, these results become more comprehensible after examining the trends in Figure 3.3. Since the whole 'downward' set of measurements in Figure 3.2 takes a day, the last measurement in this set at 650°C should roughly correspond to the values in Figure 3.3a after the same amount of time after the high temperature treatment. Indeed, k_{chem} values of LSF at 650°C in Figure 3.2 is around $2 \cdot 10^{-4}$ cm/s, while an identical value can be found in Figure 3.2a, 20 h after the high-temperature treatment. Similarly, the k_{chem} value of $1 \cdot 10^{-5}$ cm/s found after the sample has spent 10 days at 650°C (Figure 3.3a) lies close to the first measurement point in Figure 3.2. Hence, whereas the determined values depend on the thermal history complicating the analysis and comparison to the literature, the values are in fact very reproducible. The first measurement point was obtained after a polishing and rinsing. After the heating run and some time at 1000°C a thermal etching takes place, where the surface develops some roughness and grains protrude from the surface (compare Figures 3.9 and 3.10 in the Supplementary Information). After the cooling run and long term aging (10 days) at 650°C the k_{chem} returns to a value close to the

original one. This emphasizes that the enhanced exchange rate is *not* due to the change in morphology at 1000°C (creation of surface roughness).

It is also clear that the surface (at temperatures below 700°C) can be in an activated state (fast oxygen exchange right after the high temperature treatment) and in a passivated state (after several days at 650°C). Further, the sample can reversibly be toggled between these two states; activated by high temperature treatment and passivated by aging at low temperature. This demonstrates difficulties in comparing the results with literature, where thermal history is not always easy to infer. Most likely, some reported k_{chem} and D_{chem} values have been measured on samples that are in the activated state and the others in the passivated state. Also, the results presented here illustrate the challenge in using untreated surfaces as reference points in assessing the effects of a certain surface treatment as the baseline materials it-self changes characteristics over time.[31,63]

The fact that the observed effect is confined to temperatures below 700°C can explain why in many earlier high-temperature studies it was not observed. However, the trend towards finding better catalysts in so-called 'intermediate temperature region' (500-750°C) renders this effect important for future studies. In the following text, we discuss some of the possible reasons for the observed trends.

3.5.1 ECR fitting procedure

First of all, it is important to ascertain that the observed variations in k_{chem} with time are so large that they cannot be due to uncertainties arising from the fitting procedure. Some studies have shown that simultaneous fitting of surface oxygen exchange (k_{chem}) and bulk diffusion coefficient (D_{chem}) complicates accurate assessment of both values from ECR measurements.[69] Further, k_{chem} values will be underestimated if the change in oxygen partial pressure is not instantaneous as assumed in deriving the expression used in the curve-fitting. If the response time approaches the gas switching time ($\tau_{ORR}/\tau_{flushing} < 20$), a correction for reactor flushing time must be applied.[19] This is particularly important in cases where the time constants associated with the oxygen exchange and diffusion are small and approaching the time needed for the surrounding atmosphere to be switched. Our small reactor volume ensures that the complete exchange of atmosphere (flush time) takes place in less than 5 seconds. From the Figure 3.13 it can be seen that the time constants measured in ECR are in range of thousands of seconds at 650°C. At higher temperatures, where complete relaxation can take a couple of minutes (depending on sample dimensions) sluggish flushing can lead to lower apparent k_{chem} values.

Apart from this, depending on the actual k_{chem}, D_{chem} and sample geometry, the measured sample can be in surface-, diffusion- or mixed control regime (see section 1.3.1). The surface-controlled regime, where the estimation of D_{chem} is unreliable, is usually found at low temperatures, while diffusion control can be seen at higher temperatures. This means that high-temperature k_{chem} values are encompassed with a larger uncertainty. By selecting particular geometries (Table 3.1) we ensured that the samples were

mostly in the mixed-control regime where both k_{chem} and D_{chem} could be determined with satisfactory precision. In fact, the values measured at 650°C (where the effect of high-temperature thermal treatment was largest) were the most reliable ones in terms of k_{chem}, thus the clearly observable trend found in Figure 3.3a is not influenced by the fitting procedure. Yet, the same reasoning can possibly explain the discrepancy in high-temperature k_{chem} values observed between Søgaard[32] and the early work of ten Elshof,[35] where the uncertainty on k_{chem} values above 850°C in air is rather large.

3.5.2 Variations in composition

The powders used in this study were fairly pure (Table 3.1). However, small unintended difference in composition could be a reason for discrepancies between values reported here and previous works. Here, it is worth noting that the LSF and LSC results by Søgaard *et al.*[32,33] are obtained in the same lab, but in a different rig more than 10 years ago, using different powders, and yet, values at high temperature are in a very good agreement with the present study. Both LSF and LSC samples used in this study are substoichiometric, being 2% and 1% A-site deficient, respectively. Therefore, it could be speculated that this small difference in composition is causing the observed trends due to the effect of composition on defect chemistry and/or formation of secondary phases.[70] We have chosen to work with A-site deficient compositions in order to avoid the formation of hydroxides and carbonates of Sr and La upon exposure to water vapour and CO_2 present in air, which can lead to mechanical disintegration of the sample. Even though the actual A-site deficiency in the samples can be a little less or more than the desired 1% and 2%, it is enough to prevent the formation of Sr- and La-rich secondary phases to an extent detectable by X-ray diffraciton. A/B stoichiometry will influence electrical conductivity; Søgaard *et al.*[71] have shown that 2% A-site substoichiometric LSC can have a significantly higher electrical conductivity at low temperatures and better transport properties (k_{chem} and D_{chem}) in comparison with nominal stoichiometric composition. A perfect alignment with the electrical conductivity reported by Egger *et al.*[36] on stoichiometric LSC is, therefore, somewhat surprising, but nevertheless indicates that slight substoichiometry in this study did not influence material significantly. Chemical diffusion coefficient does depend on oxygen vacancy concentration, but changes induced in this way are small and expected to be within the error bar which can be up to 40% when the measurement is closer to surface controlled regime. By comparison relative changes in k_{chem} found in this study for LSF are up to 30x (3000%), which is around 100x more than the typical uncertainties. No secondary phases could be observed using CuKα XRD (Figure 3.12), however, a small amount of Fe- or Co-rich particles can be seen by SEM (Figure 3.11). This phase is likely to be strontium hexaferrite/hexacobaltite ($SrFe_{12}O_{19}$ or $SrCo_{12}O_{19}$) as has been earlier found by a synchrotron study of A-site deficient LSF by Striker *et al.*[70] It is known that a small amount of secondary phase can have a strong effect on oxygen reduction reaction.[20,24] However, the amount and the distribution of this phase does not appear to change significantly over time, so this is not likely to be the reason for the observed changes in k_{chem}.

3.5.3 Effect of microstructure

Apparent D_{chem} values will also be affected by sample porosity. All samples in this study had a relative density of at least 98% as presented in Table 3.1. Relative densities of samples from other studies shown in Figure 3.2 were 99%, 94%, 92% and 93.5% in cases of Søgaard LSC,[33] Egger LSC,[36] Søgaard LSF[32] and ten Elshof LSF,[35] respectively, which likely explains the slight differences in D_{chem} values in the mentioned studies. Sample preparation and sintering in this study was done by following the same procedure as described in Søgaard *et al.*[32,33] This has resulted in mean grain size of approximately 430 nm in case of LSF and 4.3 μm in case of LSC (S8-9). It has been shown that the grain size can affect oxygen transport properties.[72,73] Grain growth is an irreversible process favorable at high temperatures; therefore simple grain growth cannot be the mechanism responsible for the enhancement in surface exchange kinetics we observed after the high-temperature treatment, which we have shown to be reversible in nature: enhancements reported in Figure 3.4 are for the samples exposed to high-temperatures for the second time, following the slow deactivation at 650°C. On the other hand, grain size determines the amount of grain boundaries which can act as a sink or source of impurities or nucleation sites for secondary phases.[74] Therefore, grain size can affect the rate at which the samples deactivate at 650°C following the high-temperature treatment. We estimate that the density of grain boundaries is approximately 40x greater in LSF than in LSC, which could explain why k_{chem} values are only affected by a factor of 2-3 in case of LSC, while a 30x difference between the activated and passivated states was observed in case of LSF. Further insights by comparison with literature cannot be made since grain size was not specified in the related studies.

3.5.4 Surface chemistry

As outlined above we can exclude that the changes are due to morphological changes on the sample surface, and also that they are due to inaccuracies in fitting stemming from simultaneous fitting with two correlated parameters. The fact that bulk-related properties (diffusion, electrical conductivity) remain constant strongly suggests that the observed effect is due to changes occurring on the surface of the samples. We hypothesize that the observed reversible activation/deactivation phenomenon is the result of compositional modifications of the perovskite surface which are triggered by exposure to elevated temperatures (above 800°C, see section 3.4.3).

Several ECR studies have reported a similar decrease in performance over time. Bucher *et al.* have observed a decrease in k_{chem} from $2 \cdot 10^{-4}$ cm/s to $1 \cdot 10^{-4}$ at 600°C for $La_{0.6}Sr_{0.4}CoO_{3-\delta}$ in dry O_2-Ar atmosphere after 1000 hours, while D_{chem} remained constant at $1 \cdot 10^{-6} cm^2/s$.[75] The authors associated the observed changes with the 2 nm thick surface layer enriched in Sr and O. Further treatment in humid atmospheres led to a more pronounced degradation and k_{chem} values down to $1 \cdot 10^{-5}$ cm/s accompanied with a similar decrease in D_{chem} as well. The same authors reported a similar behavior in case of $La_{0.58}Sr_{0.4}Fe_{0.8}Co_{0.2}O_{3-\delta}$ in dry O_2-Ar at 600°C where k_{chem} dropped from initial $2 \cdot 10^{-6}$ cm/s to $6 \cdot 10^{-7}$ cm/s after 800 hours.[76] These trends are similar to the transition

from 'activated' to 'passivated' state in this study. Unfortunately, the thermal history of the samples was not detailed and the authors do not report on attempts to reactivate the samples by a high temperature treatment. Furthermore, the authors have found that humidity is contributing to degradation via formation of volatile $Si(OH)_4$. In this study, the samples were exposed only to dry oxygen/nitrogen mixtures with a maximum water content of 100 ppm, and a sealed reactor ensures that the effects of ambient humidity can be excluded. To the best of our knowledge, no sources of chromium or other possible detrimental materials were in contact with the samples during preparation or testing as also indicated by ToF-SIMS data reproduced in Figures 3.14-3.16..

In a LEIS study by Druce *et al.* it was found that perovskite-related materials have almost exclusive A-site termination after a thermal treatment at 1000°C in oxidizing atmosphere.[51] Also, it is known that significant strontium segregation can occur even below 600°C,[53] which is in good agreement with the ToF-SIMS profiles presented in Figure 3.5. The near-surface region, which we estimate to be less than 20 nm, can be either a layer of Sr-rich secondary phases, or Sr-rich perovskite/perovskite-related phase such as $LaSrFeO_4$. In the first case, a layer of Sr-rich phase (e.g. SrO) would readily react with traces of steam or CO_2 forming $Sr(OH)_2{\cdot}xH_2O$ or $Sr(CO)_3$,[50,77] respectively (below the decomposition temperature of these phases). In this light, one could conceive a reversible process where SrO converts to hydroxides and/or carbonate at lower temperatures and passivates the surface, while high-temperature treatment removes hydroxides/carbonates and recovers the activity. However, this explanation is inconsistent with phase diagrams for Sr-hydroxides (Figure 3.17) and carbonates (Figure 3.18) which, for the conditions in this study (H_2O<100 ppm, $CO_2 \ll 100$ *ppm*), are expected to decompose below 300 and 600°C, respectively.

Finally, an alternative and, in our opinion, the most plausible explanation is that a layer of SrO or related detrimental secondary phases is already covering the samples at relatively low temperatures, and gets transformed into perovskite or perovskite-related phase with an increased amount of Sr (e.g. Ruddlesden-Popper phase) at elevated temperatures. Such surface termination would correspond to the activated state with a very low activation energy and high ORR/OER activity (low surface resistance). Upon cooling, the surface then gradually transforms into passivated layer containing less active phases with high activation energy (high surface resistance). An illustration of the process is given in Figure 3.6. The transformation from one state to the other follows the Avrami type behavior depicted by the S-shaped curve in Figure 3.3c. This is a characteristic of crystallization processes and the exponent $n = 2$ indicates that the growth is two-dimensional, probably occurring in the outermost layer of approximately 20 nm as observed by SIMS profiling. The formation of Ruddlesden-Popper phases at the perovskite surface has been reported in literature in case of $La_{0.65}Sr_{0.35}MnO_{3-\delta}$ by Dulli *et al.*[78] and in $SrTiO_3$ by Szot and Speier[79] after thermal treatment 800°C in both oxidizing and reducing atmospheres. On the other hand, Feng *et al.* have found Ruddlesden-Popper phase already at 350°C in air at the surface of epitaxial $La_{0.8}Sr_{0.2}CoO_{3-\delta}$ thin films.[26] The same group, using the same material has also shown that the changes in surface chemistry are reversible and can be altered by electrochemical reduction/oxidation.[80] Similar and reversible activation/deactivation cycles under cathodic/anodic

polarization have been reported for the case of (La,Sr)$MnO_{3-\delta}$ and has been interpreted by dissolution of a passive SrO layer into the underlying perovskite lattice.[81–83] Thus, hypothesizing that a reversible reconstruction of the surface is taking place on thermal cycling seems reasonable assuming that the perovskite materials used in this study are analogous to the materials discussed above. A way to test this hypothesis would be to thoroughly analyze the surface of the material at different points in time during the deactivation process. This, however, is beyond the scope of this study and will be the subject of the following chapter.

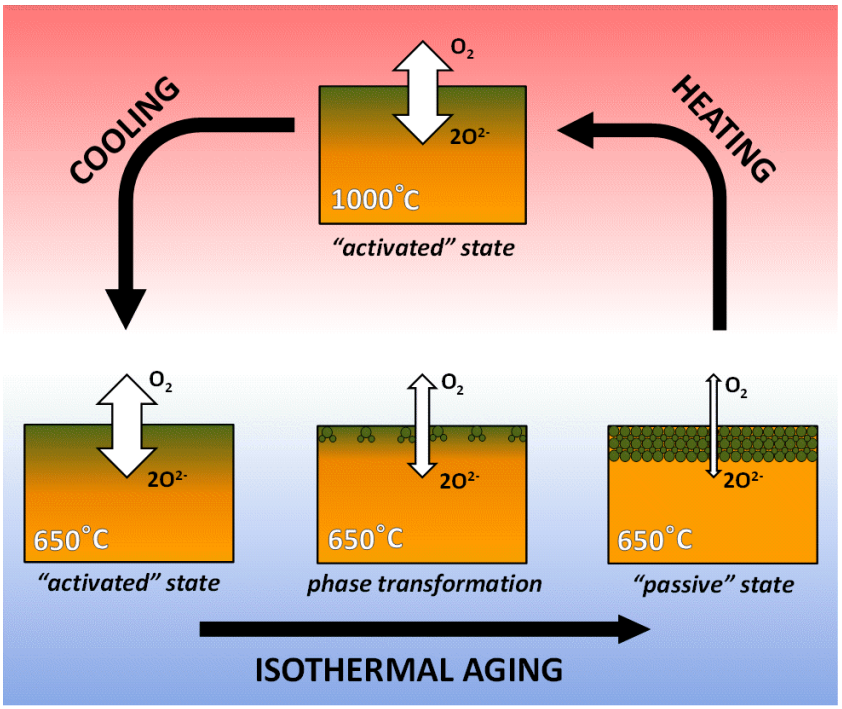

Figure 3.6: An illustration of the activation mechanism and possible connection with surface reconstruction. Green shades stand for increased amounts of strontium related to bulk (yellow shades). This region is estimated to be approximately 20 nm thick (see Figure 3.5). The hypothesis is that strontium enriched surface layers of perovskite or perovskite-like structure (e.g. Ruddlesden-Popper) are being transformed to less active (passive) secondary phases (green circles) after aging at 650°C. High-temperature thermal treatment leads to dissolution of secondary phases in perovskite lattice and the whole process is reversible.

3.6 Conclusion

The electrical conductivity of LSC and LSF was found to decrease with the increasing temperature and decreasing pO_2, which is consistent with the literature and as expected for p-type conductors. Electrical conductivity at 650°C and at pO_2 of 0.1 was found to be 2050 S/cm and 250 S/cm for LSC and LSF, respectively. Electrical conductivity relaxation measurements revealed large differences in the temperature-dependence of the oxygen exchange kinetics between heating and cooling runs, which were found to be a consequence of thermal treatment at high temperatures. Treating samples in O_2/N_2 mixture at 1000°C for 10 hours led to a transient enhancement in surface exchange coefficient with values almost 2 orders of magnitude higher than reported in literature. On prolonged thermal treatment at 650°C (several days) this enhancement gradually diminishes, especially in case of LSF where k_{chem} dropped almost 30x (from $3 \cdot 10^{-4}$ to $1.1 \cdot 10^{-5}$ cm/s) after 10 days. The transient reduction in performance was found to be well described by Avrami-equation. The beneficial effect of thermal treatment at high temperatures was found to be reversible and effective at 800°C and above. The phenomenon is most likely related to a reversible surface transformation via two-dimensional crystallization mechanism. The surface of LSC and LSF can be toggled between an "activated" and "passivated" state with significantly different ORR/OER activation energies. The results illustrate the importance of thermal history for the oxygen exchange kinetics, differences in which may explain some of the discrepancies in k_{chem} values reported in literature for one and the same material.

Supplementary Information

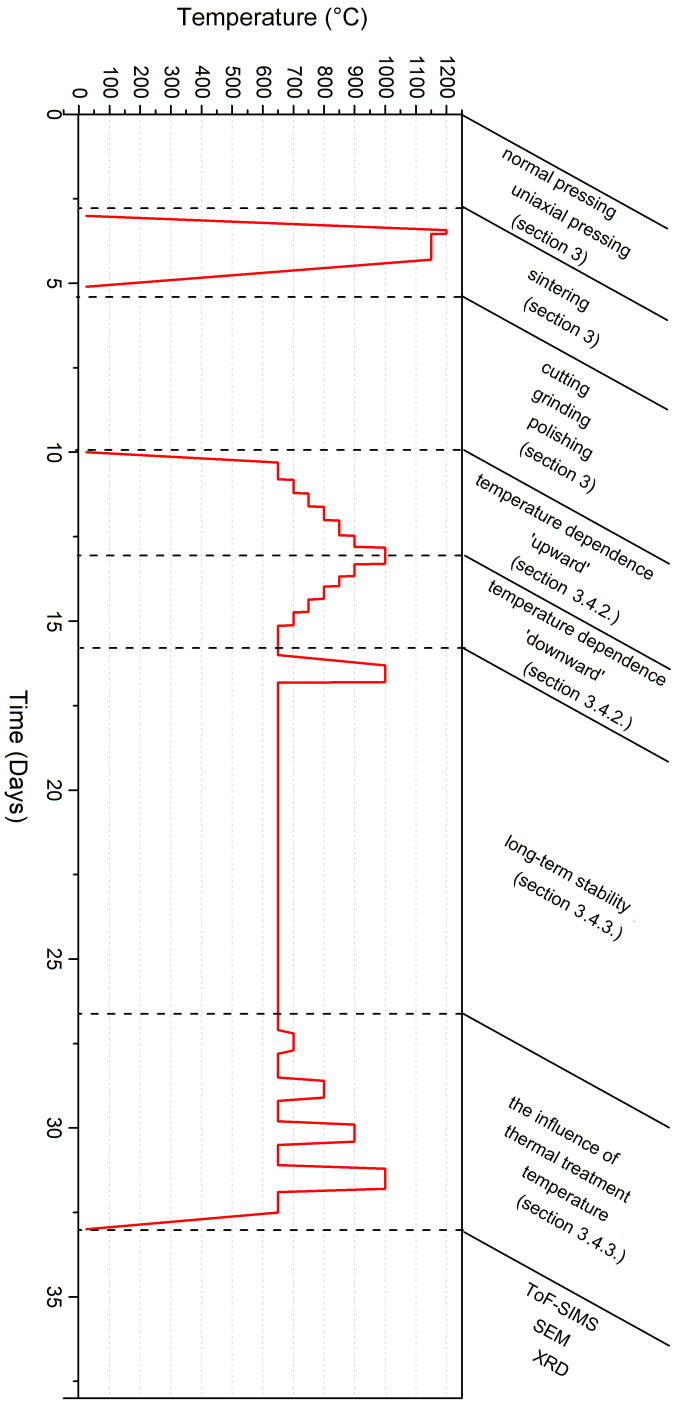

Figure 3.7: A sketch depicting thermal history of the samples investigated in this study and the experimental sequence.

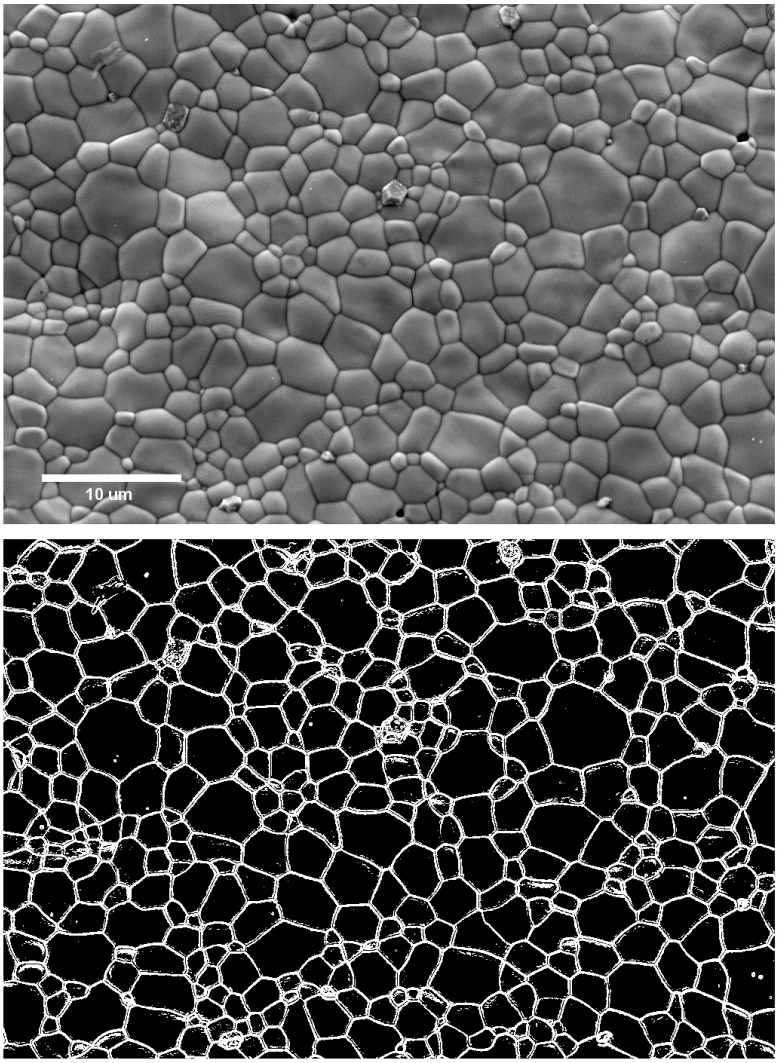

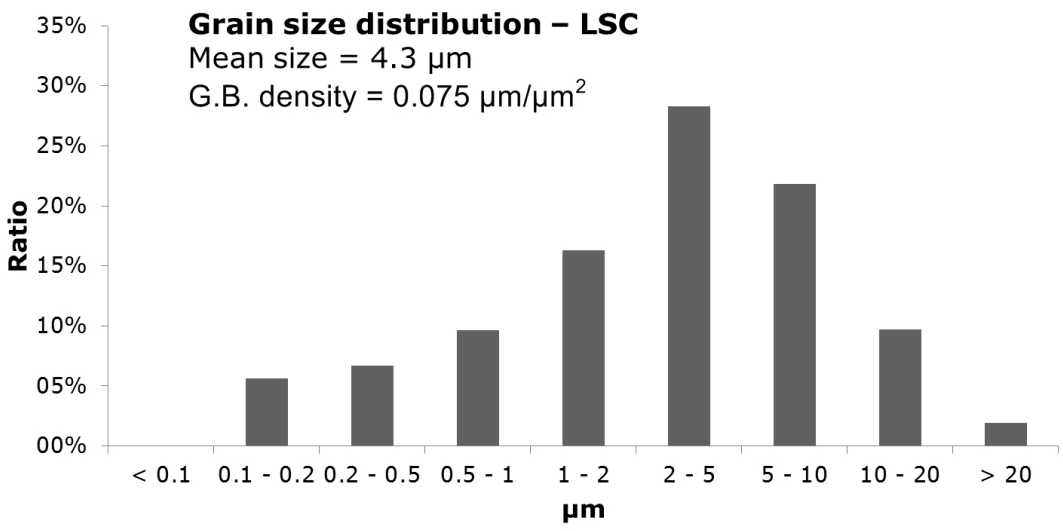

Figure 3.8: SEM of LSC surface after the ECR measurement (HE-SE2 detector, 10kV, 200 pA).

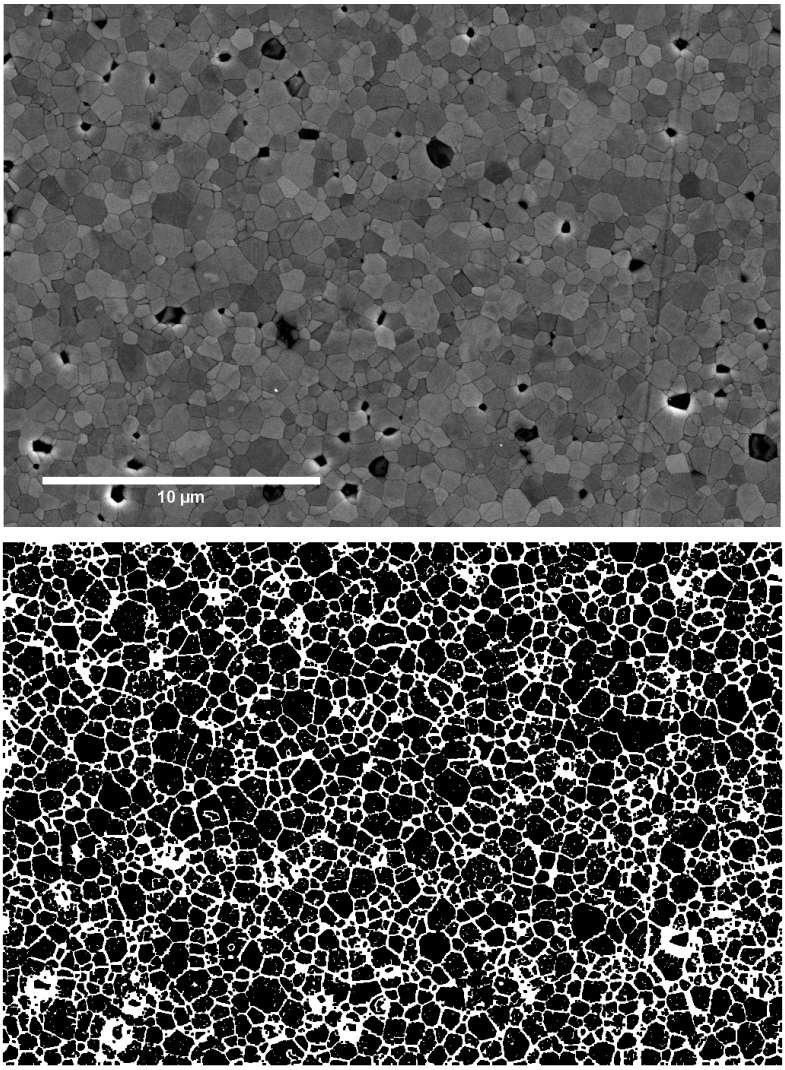

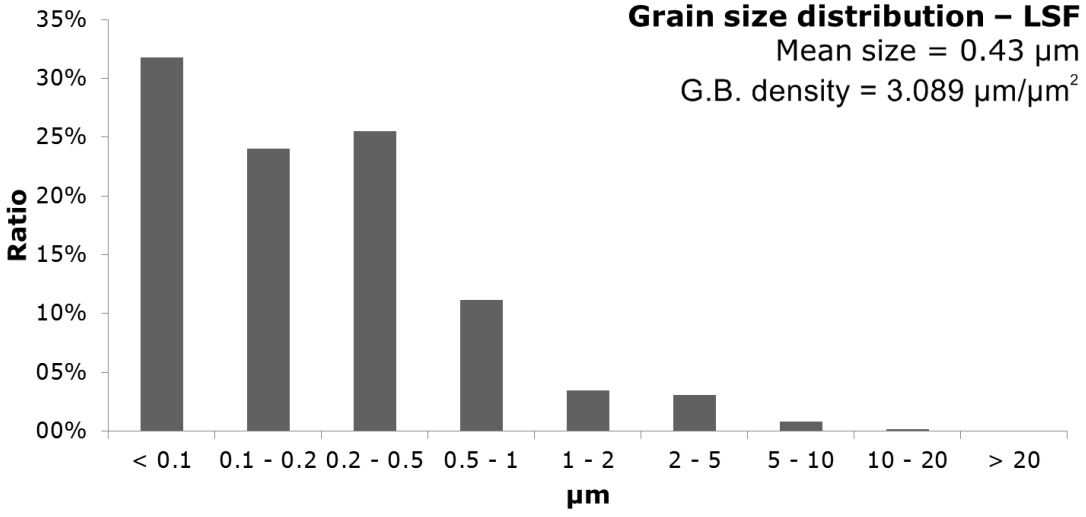

Figure 3.9: SEM of LSF surface after the ECR measurement (HE-SE2 detector, 10kV, 200 pA).

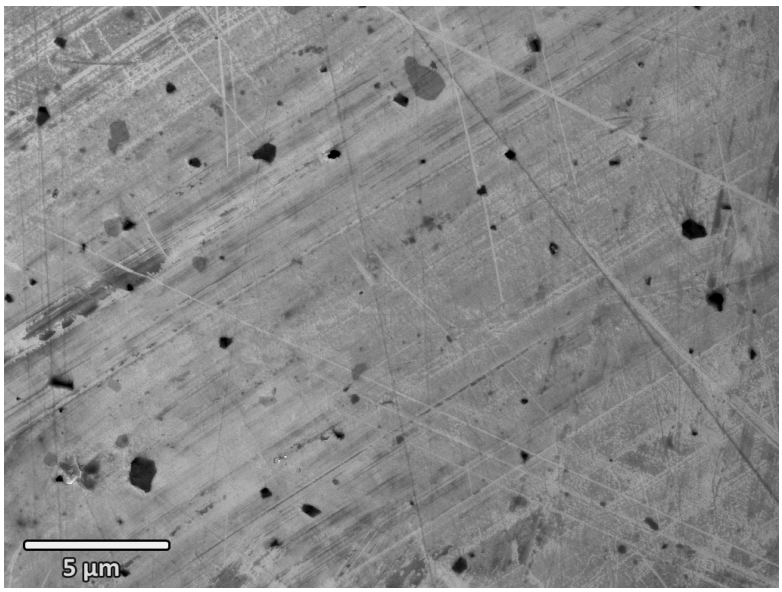

Figure 3.10: SEM of LSF surface after polishing and before the ECR measurement (HE-SE2 detector, 10kV, 200 pA).

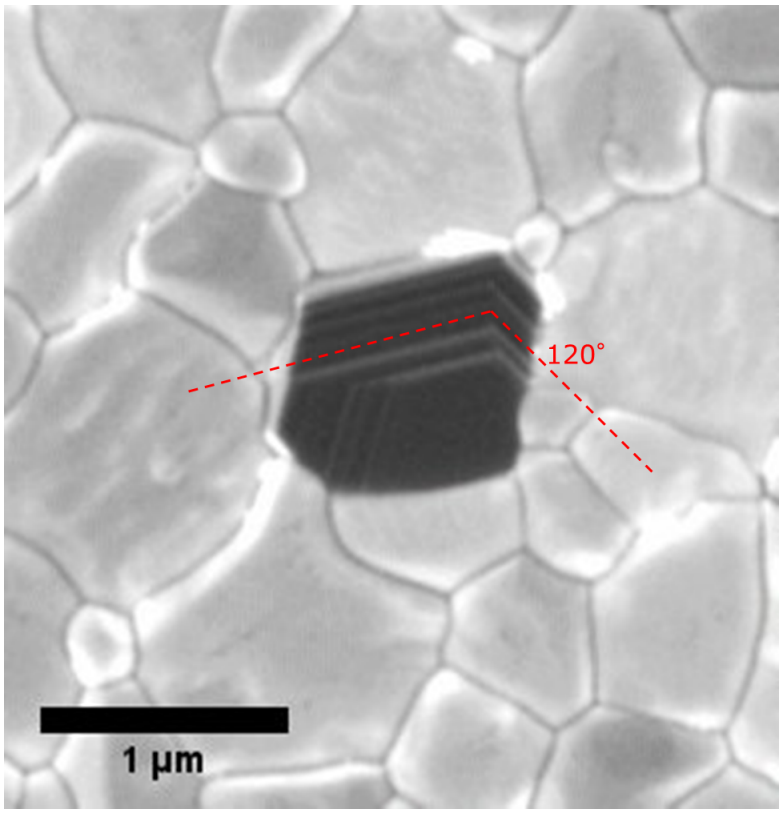

Figure 3.11: Secondary phases present in LSF (HE-SE2 detector, 10kV, 200 pA).

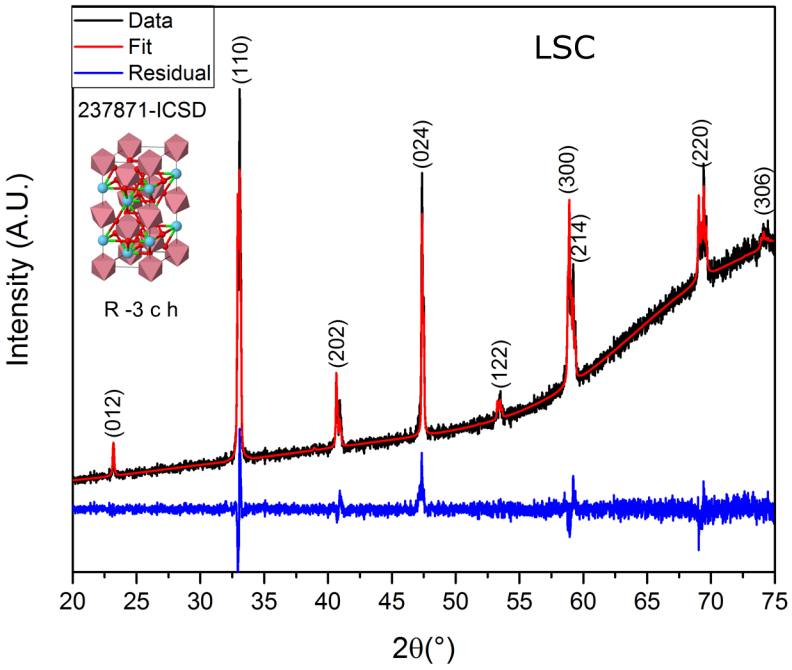

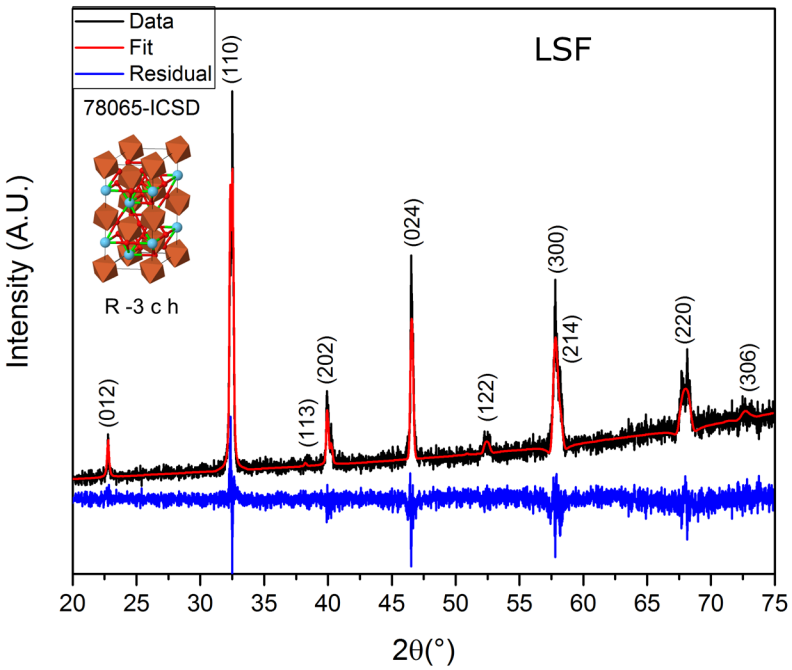

Parameter	LSC	LSF
a	5.4361 Å	5.5307 Å
b	5.4361 Å	5.5306 Å
c	13.2205 Å	13.4355 Å
α	90°	90°
β	90°	90°
γ	120°	120°

Figure 3.12: Rietveld-refinement of LSC and LSF and the obtained unit cell parameters.

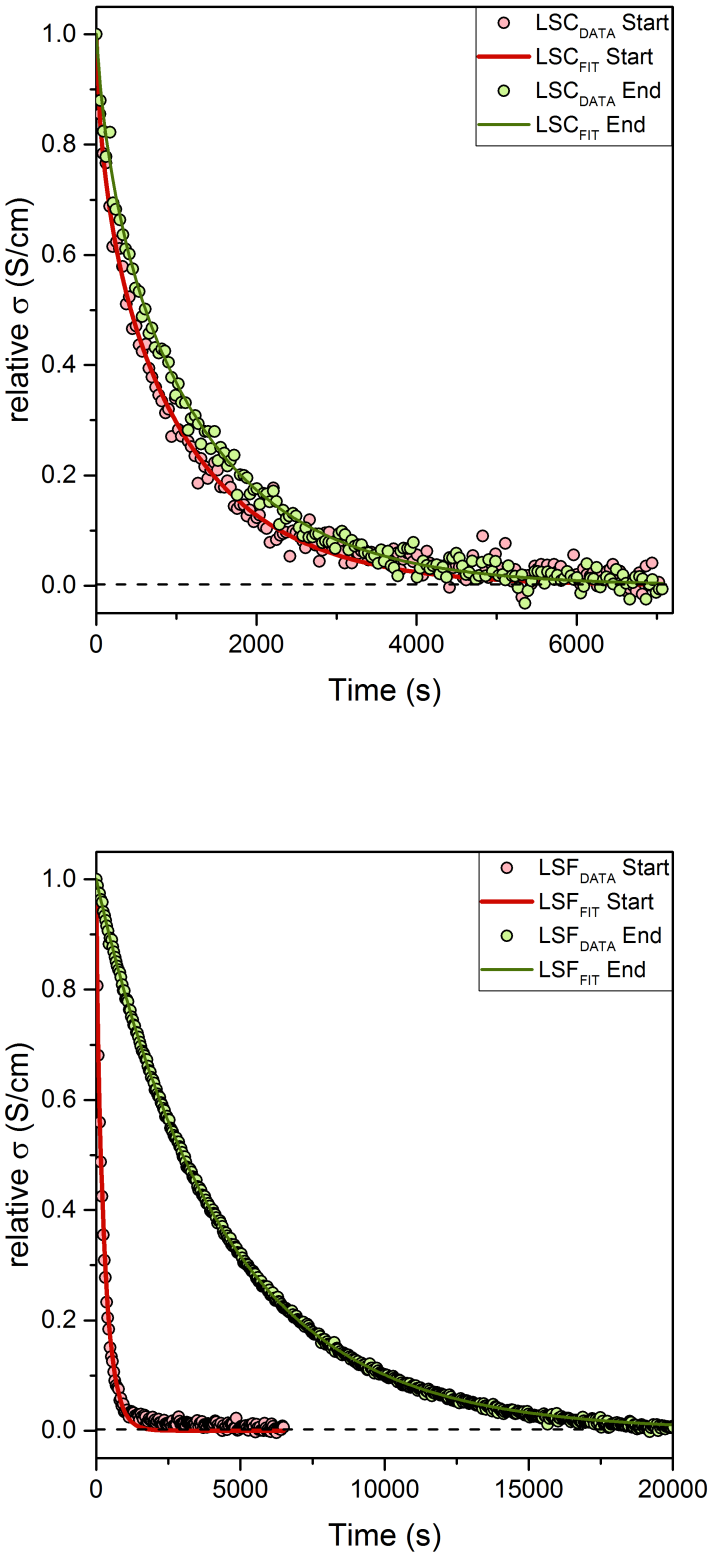

Figure 3.13: Conductivity relaxation curves for LSC (left) and LSF (right) 5 hours after the thermal treatment at 1000°C and after 10 days at 650°C. Note: only 2% of all measured points are plotted for better readability.

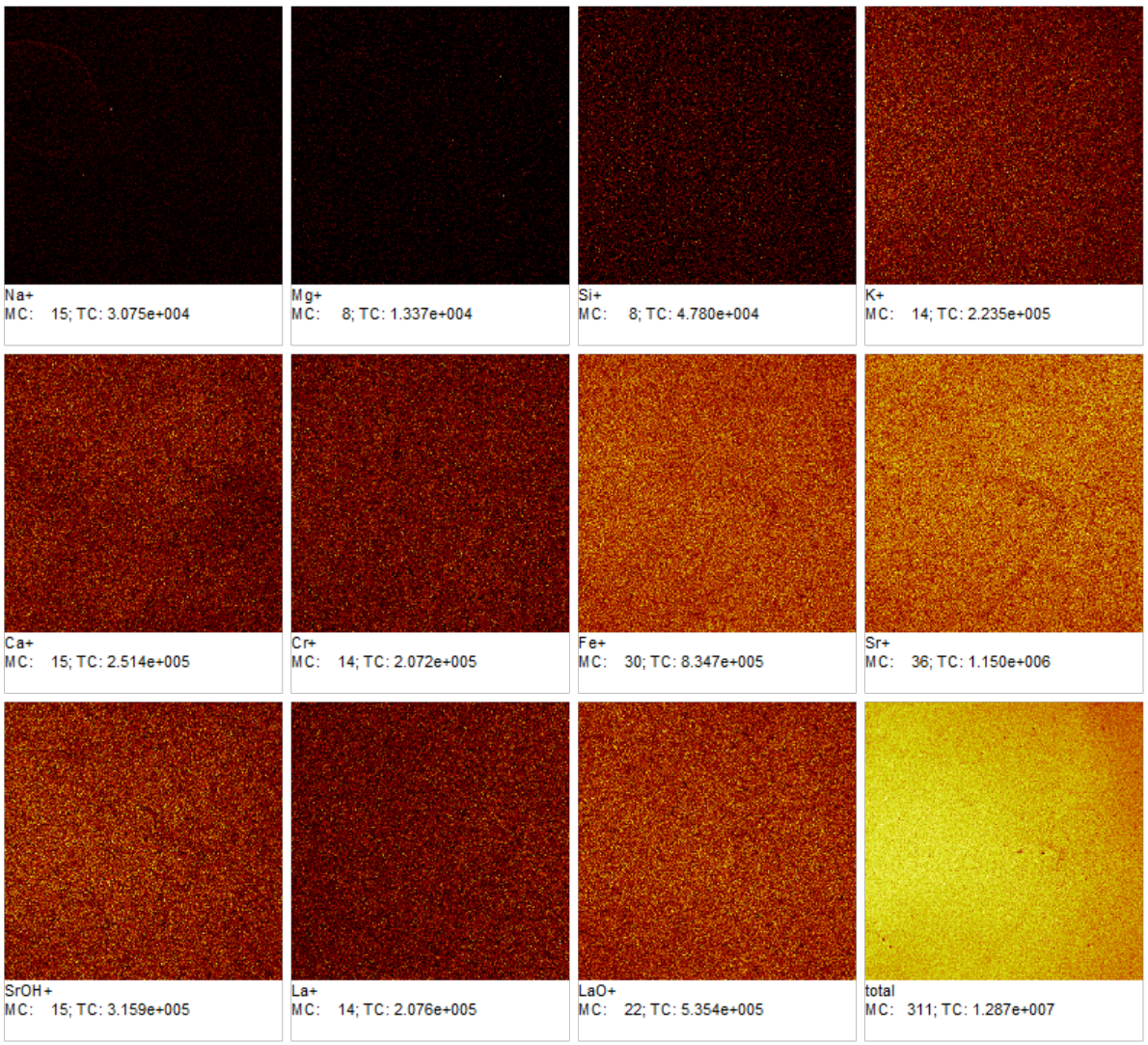

Figure 3.14: ToF-SIMS imaging of LSF after the ECR measurement – square size 500 μm x 500 μm

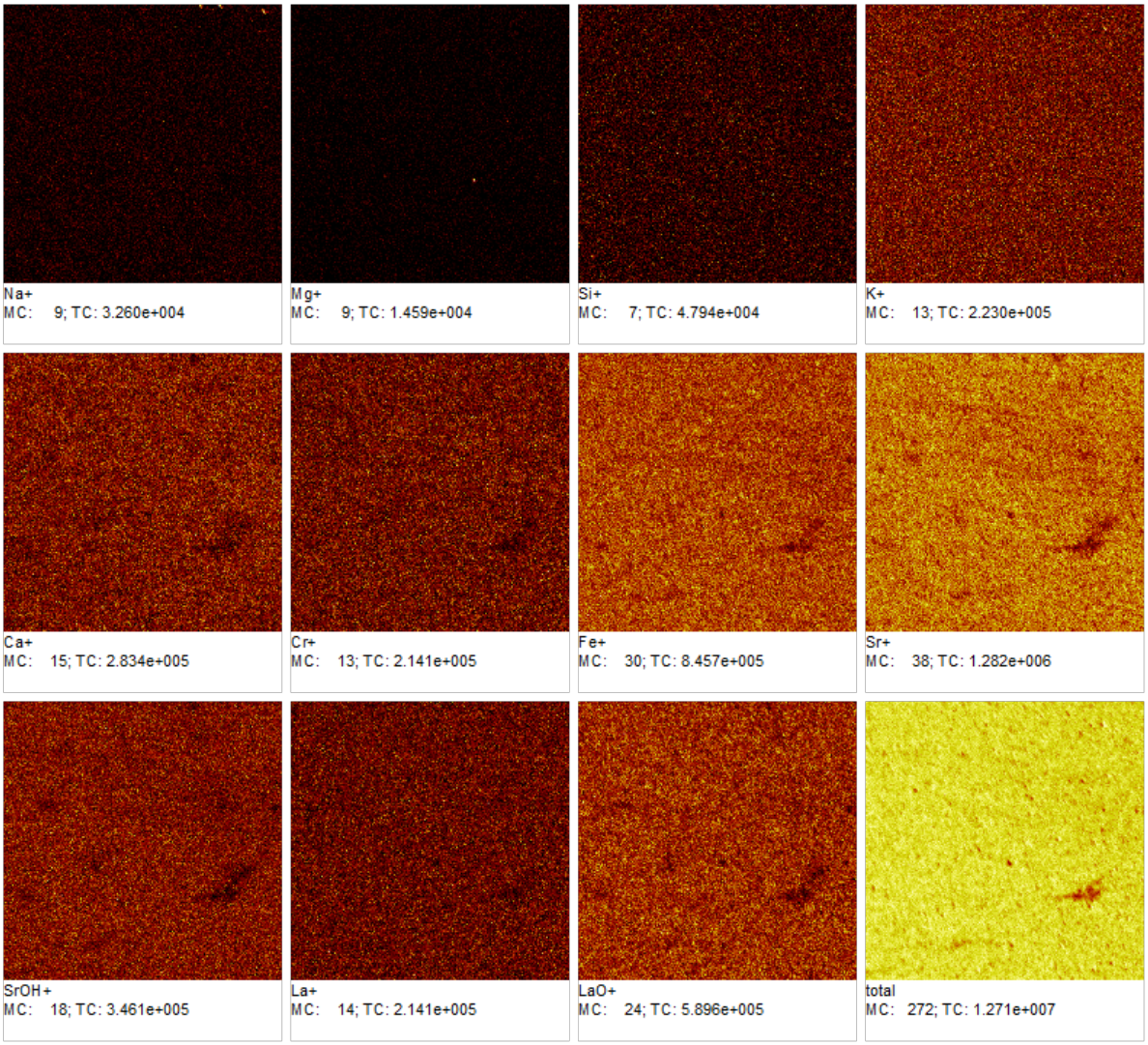

Figure 3.15: ToF-SIMS imaging of LSF after the ECR measurement – square size 100 μm x 100 μm.

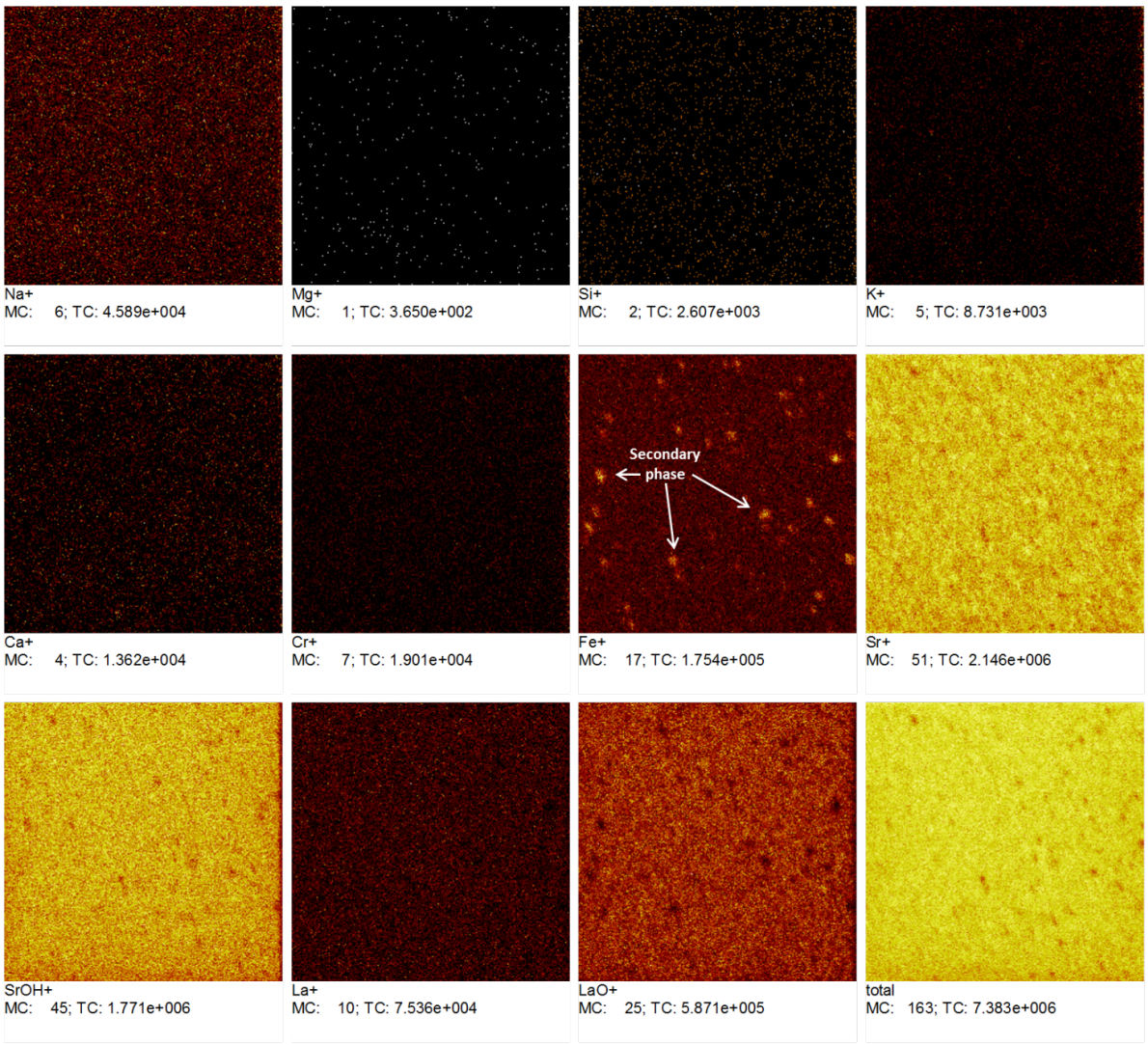

Figure 3.16: ToF-SIMS imaging of LSF after the ECR measurement – square size 50 μm x 50 μm.

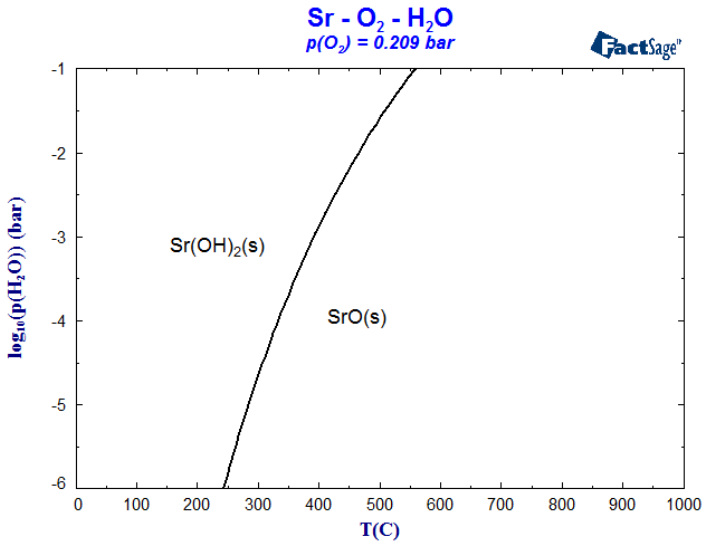

Figure 3.17: Phase diagrams showing the stability of strontium hydroxide at different temperatures rendered by FactSage^{TM}.

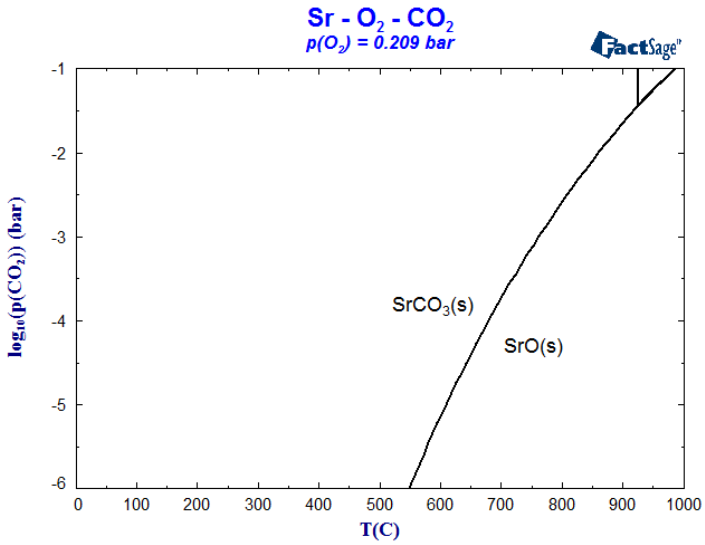

Figure 3.18: Phase diagrams showing the stability of strontium carbonate at different temperatures rendered by FactSage^{TM}.

CHAPTER 4

The role of surface chemistry and reconstruction in oxygen exchange kinetics of perovskites

Abstract

In this work we study the effects of thermal history on the surface composition on bar-shaped samples of $(La_{0.6}Sr_{0.4})_{0.99}FeO_{3-\delta}$. We have previously reported on how the themal history affects the oxygen exchange kinetics on this material – and here we shall investigate this connection in more details. The surface chemistry and oxygen exchange kinetics of $(La_{0.6}Sr_{0.4})_{0.99}FeO_{3-\delta}$ was studied concurrently by X-ray photoelectron spectroscopy and electrical conductivity relaxation. The measured reversible changes in oxygen exchange kinetics due to thermal cycling are associated with the formation of secondary phases on the surface. XPS quantification show that surface composition of all thermally treated samples is far from nominal bulk values and strongly enriched in Sr. The results further indicate that chemical state of Sr, rather than its total amount determine the oxygen exchange rate. More specifically, the surface exchange coefficient k_{chem} can range from $4{\cdot}10^{-4}$ to $6{\cdot}10^{-6}$ cm/s at 635°C and 0.1 bar pO_2, depending on in which phases surplus Sr on the surface is contained. A reconstruction mechanism of the surface layers is suggested as a possible explanation for the observed changes in oxygen exchange activity and the underlying changes in surface chemistry. A tentative time-temperature-transformation diagram is constructed based on kinetics of surface reconstruction at different temperatures.

4.1 Introduction

Understanding surface related phenomena in perovskite materials is crucial for harnessing their immense potential in applications such as electrodes for solid oxide fuel and electrolysis cells,[84–87] oxygen sensors,[88,89] oxygen separation membranes,[90,91] and metal-air batteries.[92,93] For all these applications, fast exchange of oxygen with the surrounding atmosphere on the material's surface via oxygen reduction/evolution reaction (ORR/OER) is a necessary requirement. Catalytic activity towards ORR/OER can be found in many perovskite materials of the general chemical formula ABO_3, where

A is typically a rare-earth element partially substituted with a certain amount of alkaline earth element and B a transition metal. Typical and widely studied compositions include $La_{0.75}Sr_{0.25}MnO_{3-\delta}$ (LSM),[94–96] $La_{0.6}Sr_{0.4}CoO_{3-\delta}$ (LSC),[40,97] $La_{0.6}Sr_{0.4}FeO_{3-\delta}$ (LSF),[32,35,98,99] $La_{0.6}Sr_{0.4}Co_{0.2}Fe_{0.8}O_{3-\delta}$ (LSCF).[100–102]

The performance of this class of materials depends critically on the composition and the chemical state of the outermost surface layers both in terms of catalytic activity and long-term stability. A good illustration is the observation by Crumlin *et al.*[21] who, inspired by the work of Sase *et al.*,[20] investigated the effect of depositing small amounts of Ruddlesden-Popper ($LaSrCoO_4$) phase on the surface of $La_{0.8}Sr_{0.2}CoO_{3-\delta}$ thin film electrodes and reported almost 3 orders of magnitude improvement in oxygen exchange kinetics at 550°C. Furthermore, a recent in situ impedance spectroscopy study by Rupp *et al.*,[103] showed that the deposition of tiny amounts of Sr or Co severely affects the performance of the $La_{0.6}Sr_{0.4}CoO_{3-\delta}$. Intriguingly, in the study by Rupp *et al.*, the changes in kinetics were observed for the amounts corresponding to only a fraction of atomic monolayer.[103] In another study Tsvetkov *et al.* improved the stability of LSC thin film electrodes and achieved 30x faster ORR kinetics after 54 hours at 530°C by modifying the surface with small amount of hafnium.[104] Similar examples have been reported for other perovskites materials. Interestingly, modifications of perovskite surfaces by e.g. atomic layer deposition have been shown to lead to poorer electrode performance.[105] Furthermore, it is known that significant loss in electrode performance can occur over time due to poisoning of the perovskite surface in the presence of elements such as sulfur,[106] silicon[75,107] and chromium.[108–111] Another cause for performance degradation, observed for many perovskite electrodes, is the segregation of alkaline earth ions to the surface at elevated temperatures.[40,53,54,81,112–118] This phenomenon appears to be caused by *elastic* and/or *electrostatic* driving forces.[112] The first is a consequence of size mismatch between A-site cations in the perovskite lattice. The system minimizes the overall elastic energy by expelling the mismatching alkaline earth cation to the surface. The electrostatic driving force emerges as a consequence of increased amount of vacancies at the surface which then attracts the effectively negative alkaline earth ions (e.g. Sr_{La}').

In the most reported cases of Sr segregation, the degradation is often interpreted to be due to the formation of blocking secondary phases[50,54,117,119] (e.g. SrO). Once on the surface, SrO can readily react with water and CO_2 to form $SrCO_3$ and $Sr(OH)_2$ which are believed to have negative effect of ORR kinetics.[118,120] Furthermore, Sr-rich regions are more likely to react with poisonous elements such as Cr, forming inactive $SrCrO_4$.[121]

The exact relation between the increased content of Sr on the surface and the rate of oxygen exchange, however, remains elusive. Some studies have shown that extrinsic Sr decoration on perovskite surface can be beneficial for ORR kinetics, which has been attributed to the creation of more oxygen vacancies, prevention of intrinsic Sr segregation, and creation of fast Ruddlesden-Popper/perovskite interfaces.[24,31,122–124] It should be noted that Ruddlesden-Popper (RP) phases can form on perovskite surfaces at elevated temperatures even without extrinsic Sr decoration. This has been reported in case of $SrTiO_3$[79,125,126] and speculated in case of $La_{0.65}Sr_{0.35}MnO_3$,[78] $La_{0.6}Sr_{0.4}Co_{0.2}Fe_{0.8}O_3$[51] and $NaNbO_3$.[127]

It is noteworthy that surfaces passivated by Sr segregation may recover their oxygen exchange activity is often neglected in the literature. Reactivation can be achieved by simple chemical dissolution of segregated layers with diluted acid[54] or water.[128,129] Other studies have shown that surface composition of perovskites can be reversibly changed by electrochemical reduction.[80] It was also shown that segregated passive SrO layer can be dissolved into perovskite lattice under cathodic polarization leading to increased oxygen exchange activity.[81,130] A reversible activation/passivation behavior has also been observed in case of thermal cycling. In a study by Abernathy *et al.*, $(La_{0.8}Sr_{0.2})_{0.95}MnO_3$ was cycled between 700°C and 800°C for 50 hours and a steady increase in performance at higher temperature and the opposite trend at lower temperature was observed.[131] Our previous study in Chapter 3 on $(La_{0.6}Sr_{0.4})_{0.99}FeO_{3-\delta}$ and $(La_{0.6}Sr_{0.4})_{0.99}CoO_{3-\delta}$ demonstrated that thermal treatment at 1000°C for 10 hours results in markedly increased oxygen exchange kinetics. The effect was ascribed to a reversible surface reconstruction process occurring above 800°C. Thermal passivation/activation phenomena thus offer an additional way to improve overall lifetime and performance of perovskite electrodes. Furthermore, the results presented here and in the previous chapter offer a potential explanation to the large scatter in k_{chem} values in the literature (Chapter 3, Figure 3.2).

In all abovementioned examples, the observed changes can, to various extent, be correlated with the concentration and chemical state of Sr on the surface of the perovskite. In an attempt to further contribute to the understanding of this relationship, the aim of this study is to give answers to the following questions:

(i) What is the connection between increased amounts of Sr on the surface and oxygen exchange kinetics?

(ii) How perovskites passivate during prolonged operation at elevated temperatures?

(iii) How thermal cycling improves the performance?

(iv) What is the role of surface reconstruction?

The study is based on the investigation of dense ceramic samples of a typical perovskite material $(La_{0.6}Sr_{0.4})_{0.99}FeO_{3-\delta}$ (LSF) by two parallel approaches: kinetic measurements by electrical conductivity relaxation and surface characterization by XPS and SEM. The changes are monitored upon systematic thermal cycling between high temperature (1000°C) and intermediate temperatures (630-670°C).

4.2 Experimental

4.2.1 Sample preparation

All samples were prepared from a commercial$(La_{0.6}Sr_{0.4})_{0.99}FeO_{3-\delta}$ powder (Kusaka Rare Metal Products Co.Ltd., >99%) by uniaxial pressing at 50 MPa for 30 seconds and isostatic pressing at 325 MPa for 30 seconds. Sintering was performed at 1200°C for

4h with heating rate of 2°C/min and an additional treatment at 1150°C for 16h, after which the samples were cooled to room temperature with a cooling rate of 1°C/min. Thus prepared sample had a geometrical density of 99% of the theoretical on base on the Rietveld analysis. A diamond saw was used to cut the sample into a rectangular bar of 2 x 2 x 20 mm^3 for oxygen exchange measurements by electrical conductivity relaxation (ECR), and 14 pellets of approximately 4 x 4 x 1 mm^3 for surface analysis by X-ray photoelectron spectroscopy (XPS). The surface of each sample was ground gradually with SiC sandpaper with grit size from 180 to 1000, removing at least 1 mm of material. Subsequently, the samples were polished with diamond pastes with gradually decreasing particle size (9, 3 and 1 μm), followed by cleaning in an ultrasound bath for 5 min in acetone, ethanol, and deionized water, respectively and dried in ambient air. This resulted in a mirror-like, shiny surface. An overview of the sequence of measurements and thermal history of the samples is presented below in Figure 4.1.

4.2.2 Surface analysis

The samples for XPS surface analysis were subjected to a treatment similar to the one during the ECR tests – they were heated to 1000°C for 10 hours in ambient air in a chamber furnace, cooled down to 650°C in an hour and annealed at that temperature for 15 days. After 15 days, the samples underwent another high-temperature treatment followed by 21 days at 650°C and a final high-temperature treatment. In total, 13 samples (4 x 4 x 1 mm^3) were initially in the furnace. Over the course of 40 days (the total thermal treatment time), the samples were collected consecutively from the furnace by quenching. In this way samples were cooled down to room temperature in less than 30 s and should therefore represent a 'frozen image' of the actual state of the surface at the elevated temperatures. One sample was left untreated after polishing and cleaning in order to be used as a reference point for the surface chemical analysis. This sample will be referred as 'as polished' throughout the text. The same sample was afterwards broken in order to examine the cleaved surface.

The XPS analysis was done by using Physical Electronics Versaprobe II X-ray Photoelectron Spectrometer with monochromated Al Kα (1486.65 eV) X-ray radiation source equipped with charge neutralization system under a base pressure of 10^{-9} Torr. The analysis and quantification of the results was done by CasaXPS software. Imaging was done by Zeiss Merlin field-emission scanning electron microscope equipped with EDS and a surface sensitive In-lens detector. The micrographs are taken with accelerating voltage of 3 kV, column current of 200 pA, and working distance of 3.5 mm.

4.2.3 Electrical conductivity relaxation

Electrical conductivity relaxation (ECR) is a characterization technique which enables determination of oxygen transport parameters: surface exchange coefficient (k_{chem}) and chemical diffusion coefficient (D_{chem}), by observing changes in electrical conductivity upon imposing an abrupt change in chemical potential of oxygen in the surrounding

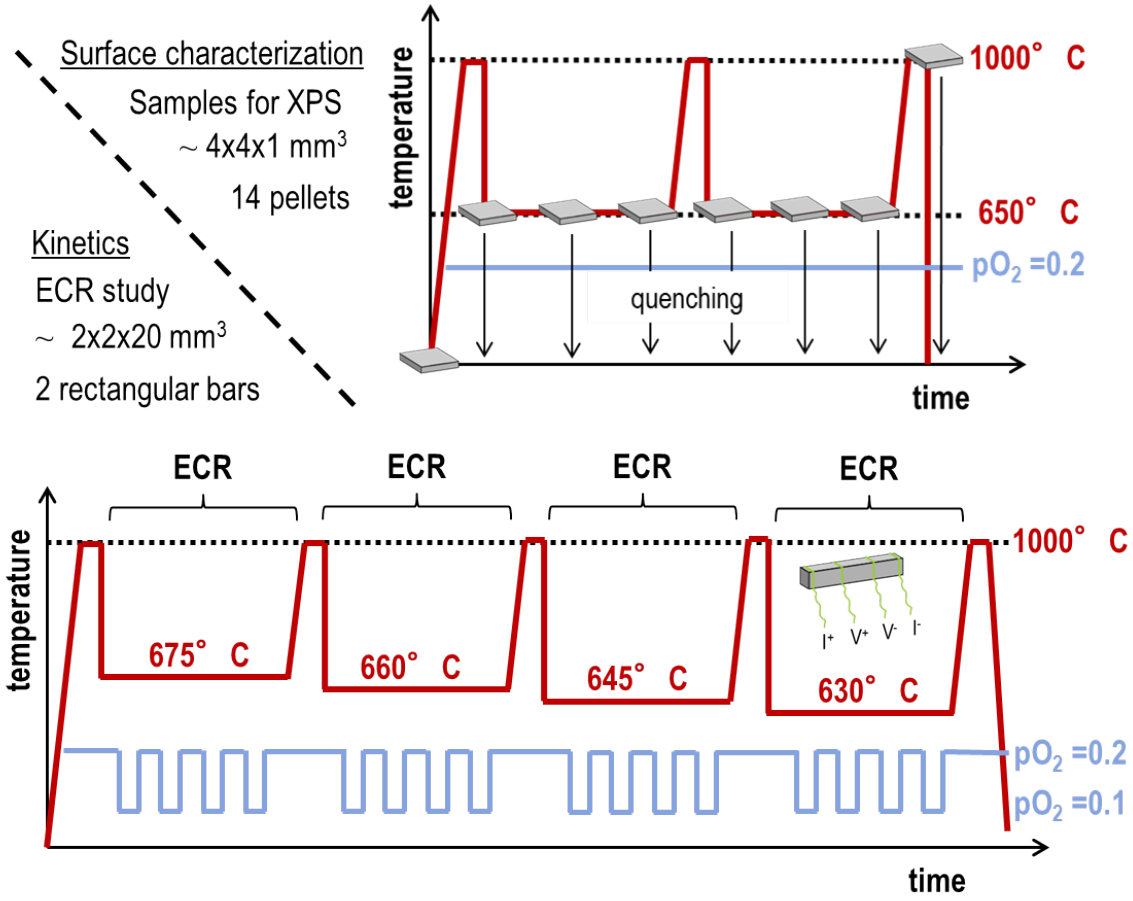

Figure 4.1: A sketch illustrating the experimental procedure: top) thermal treatment of pellets for surface characterization by XPS, bottom) ECR experimental sequence for measuring surface exchange coefficient over time.

atmosphere. The surface exchange coefficient is related to the rate of oxygen reduction/evolution reaction (ORR/OER) on the surface; a high value of k_{chem} corresponds to fast kinetics and high catalytic activity. D_{chem} is the proportionality constant between the flux of oxygen ions and the chemical potential gradient (driving force) in the bulk.

Electrical conductivity was measured by connecting the samples with high-purity (99.99%) platinum wires to a four-probe experimental setup. The contacts were established at equidistant separation with current terminals at the edges and voltage terminals in the center and fixed by twisting the wires around the bar. The ECR experiment was conducted in a sealed quartz-tube reactor of approximately 10 ml in volume. The testing environment was dry N_2/O_2 mixture with possible impurity being water in an amount less than 100 ppm, originating from the oxygen gas. The total gas flow was kept constant at 5 ml/s, enabling abrupt changes in oxygen partial pressure which is monitored by a zirconia sensor. The temperature was measured with a thermocouple positioned in close

vicinity of the sample (within 2 mm). The gasses were fed through stainless steel pipes (only cold part of the system) and the rig holding the sample was made of alumina. The relevant experimental values were monitored automatically and logged with the sampling rate of 1 Hz. After inserting the sample, the quartz tube reactor was heated to 1000°C for 10 hours in 0.2 bar pO_2 with heating rate of 2°C/min (Figure 4.1). In the rest of the text, this step will be referred to as the high-temperature thermal treatment (h.t.t.t.). Following the h.t.t.t. the sample was cooled to a certain intermediate temperature (between 630 and 675°C) in about an hour. The first ECR measurement took place 5 hours after the sample had reached the designated temperature ($\approx$ 6 hours after the h.t.t.t.). This ensured that the sample was (in terms of oxygen stoichiometry) equilibrated with the surrounding atmosphere before the first ECR measurement (indicated by a constant value of electrical conductivity). The ECR measurements were performed by a swift change ($<$ 5 s) of the surrounding atmosphere corresponding to the pO_2 change from 0.2 to 0.1 and from 0.1 to 0.2 bar (in the rest of the text these processes are designated as the reduction and oxidation runs, respectively). The set of ECR experiments were conducted over a period of 15 days, followed by another high-temperature treatment and the whole process repeated once more, but at a lower temperature (Figure 4.1). Finally, after the sample had been cycled for four times, it was heated up to 1000°C for 10 hours, cooled down to room temperature in 3 hours and removed from the reactor for further analysis. The fitting of the measured conductivity relaxation curves with corresponding diffusion equations was done in *ECReX* (Appendix A).

4.3 Results

4.3.1 Measurement of oxygen exchange kinetics

The results of electrical conductivity relaxation are shown in Figure 4.2(a). The x-axis represents the time that had passed since the last thermal treatment at 1000°C. Much alike in our earlier study (Chapter 3), the values of surface exchange coefficient are found to vary almost two orders of magnitude depending on the previous thermal treatment, while the chemical diffusion coefficient remains constant throughout the experiment with a value around $2 \cdot 10^{-6}$ cm^2/s (Figure 4.11). In analogy to that study, we will refer to the state of fast kinetics as 'activated', while the state distinguished by low k_{chem} (slow kinetics) after aging at 650°C we label as 'passive'. Here, as also previously reported in Chapter 3, we find that the sample can be re-activated by a heat treatment; thermal treatment at 1000°C for 10 hours resulted in greatly increased surface exchange kinetics. For instance, after 15 days at 645°C, k_{chem} is $1 \cdot 10^{-5}$ cm/s, while when characterized at 630°C shortly after a high temperature treatment it increases to $4 \cdot 10^{-4}$ cm/s (a 40x enhancement). During annealing at intermediate temperatures, the 'activated' state gradually transforms to the 'passive' state. The transition is initially rapid, but the rate of transformation decreases with time and levels off as the 'passive' state is reached. Evidently, the overall rate of transformation depends on the aging temper-

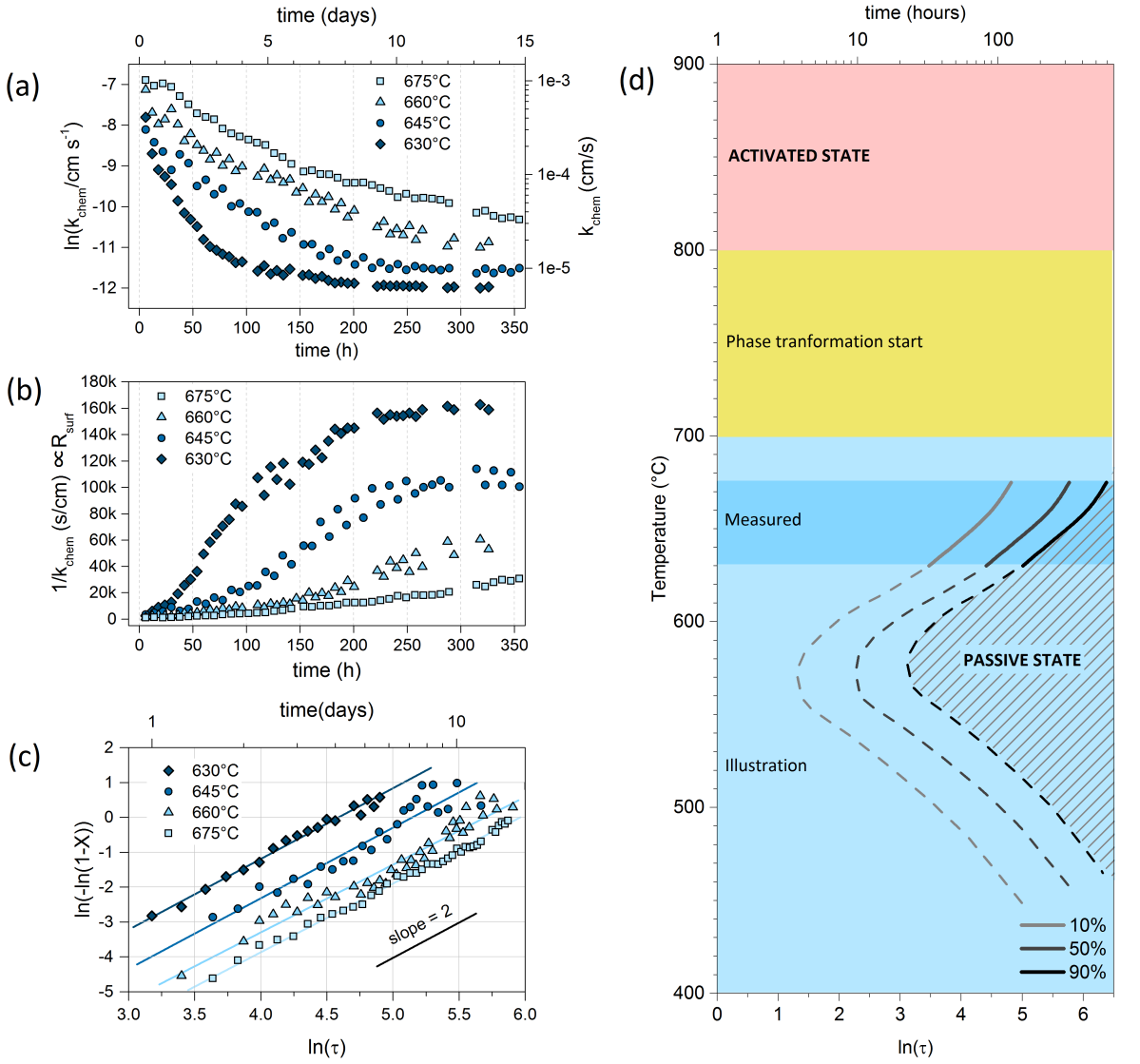

Figure 4.2: Figure 2. The results of a long series of isothermal ECR tests carried out between 0.2 and 0.1 bars at temperatures from 635 to 670°C; k_{chem} values are deduced from ∼50 relaxation runs carried out over a period of 350 hours after each high temperature treatment. (a) The variation of k_{chem} over time time; (b) The equivalent change in surface resistance ($R_{surf.} \sim 1/k_{chem}$); (c) A log-log plot of the extent of the transformation (see Eq. 4.4) versus $\ln(t)$. The Avrami coefficients are extracted from the best fit straight lines to the data points; (d) Time-temperature-transformation (TTT) diagram based on the extracted Avrami coefficients in the measured temperature range (blue). Light-blue region and dashed lines serve as an illustration and are based on typical shapes of TTT diagrams. C-shaped lines show the extent of transformation from 'activated' to 'passive' state. The temperature under which a phase transformation will take place is in Chapter 3 estimated to lie between 700-800°C. The 'activated' state is stable at high temperatures (red) and the 'passive' state is more stable at lower temperatures (hatched). Note: the constructed TTT diagram is intended to serve merely as an illustration.

ature. For instance, the time needed to reach 50% transformation (half-time) is ≈80 hours when aging at 630°C and ≈320 hours when aging at 675°C. The kinetics of the exchange process can also be characterized by a surface resistance (R_{surf}) which is inversely proportional to k_{chem}. The reciprocal values of k_{chem} are plotted in Figure 4.2(b). The observed S-shaped curves are characteristic of crystallization phenomena which are usually described by Avrami kinetics[66–68] and the Johnson-Melvin-Avrami-Kolmogorov (JMAK) equation:

$$X = 1 - exp(-\kappa\tau^n) \tag{4.1}$$

where X stands for the extent of transformation over time (t), κ is transformation rate constant, and n is the Avrami coefficient, which is related to the dimensionality of the transformation in the following way:

$$n = a + b \tag{4.2}$$

Parameter b is 1 in case of 1D needle-like growth, 2 in case of 2D lamellar, and 3 in case of 3D spherical growth. Parameter a is related to nucleation kinetics and takes the value of zero when no new nucleation occurs, the value of unity when there is a constant nucleation rate, and values in between for a nucleation rate decreasing with time.[132,133] Linearization of the JMAK equation yields:

$$ln(-ln(1 - X)) = ln(\kappa) + n \cdot ln(\tau) \tag{4.3}$$

This form of the equation enables the determination of κ and n from intercept and slope in the type of plot illustrated above in Figure 4.2(c). Assuming that the increase in surface resistance over time is a direct consequence of the surface transformation, we can utilize the JMAK equation for interpretation of the obtained S-shaped curves (Figure 4.2(b)).

$$X(t) = \frac{R_{surf}(t) - R_{surf}^{min}}{R_{surf}^{max} - R_{surf}^{min}} \tag{4.4}$$

Combining equations 4.3 and 4.4 results in a plot shown in Figure 4.2(c). The points corresponding to the initial 10-15% and the last 10-15% of the transformation were omitted from the analysis. Therefore, the parameters listed in the Table 4.1 are applicable to the region where the overall rate of transformation is high ($0.1 < X < 0.9$) and the S-shaped curves are clearly defined. The slope (Avrami coefficient) was found to be close to 2 at all temperatures. Equation 4.2 offers two possible interpretations for this case: the transformation is either two-dimensional with a fixed amount of preexisting nucleation sites ($a = 0$; $b = 2$), or one-dimensional with constantly emerging new nucleation sites ($a = 1$; $b = 1$).

It is noteworthy that at all investigated temperatures the extent of the transformation is well described by Eq.4.3 and 4.4 as seen from the R^2 values close to 1 and consistent observation of n values close to 2 (see Table 4.1). In general, the rate of

Table 4.1: Estimation of crystallization rate (κ) at different aging temperatures in the designated intervals and fitting parameters.

Aging temperature [°C]	$\kappa \cdot 10^6[h^{-1}]$	n	R^2	Time interval [days]
630	99.3±25	2.01±0.06	0.986	1–5.61
645	30.3±20.6	2.02±0.13	0.908	1.5–12.5
660	14.3±5.6	1.96±0.08	0.947	2.1–15.2
675	8.0±1.7	1.97±0.04	0.983	1.5–16.8

(re-)crystallization depends on both nucleation and growth processes. Growth is determined by diffusion which is thermally activated and obeys Arrhenius dependence. On the other hand, in a simplified picture, the nucleation rate depends on the critical radius of the nuclei determined by the difference in Gibbs energy between the two states at a given temperature. At lower temperatures, this difference (and therefore the driving force) becomes larger, rendering nucleation faster. Therefore, the fact that the overall rate of transformation is found to be higher at lower temperatures is a clear indication of nucleation-controlled regime of transformation.

In studies of recrystallization in alloys it is customary to interpret phase transformations in terms of temperature-time-transformation diagrams (TTT diagrams). Due to abovementioned opposite trends of the rate of nucleation and growth with temperature, TTT diagrams feature a characteristic "nose" (or C-shape). Based on estimated κ and n values we can construct a part of a such TTT diagram in the investigated temperature range (Figure 4.2(d)). In Chapter 3, we determined that the equilibrium transformation temperature lies between 700 and 800°C (yellow region). At higher temperatures the surface is in an 'activated' state (red region), while at lower temperatures the passive state is more stable and the phase transformation from 'activated' to 'passive' state is taking place (blue region). The three gray lines connect points of the same extent of the transformation (X=10%, 50%, and 90%). Continuous lines are in the region in which κ and n parameters are determined (dark blue region), while dashed parts serve as an illustration of the expected trends at lower temperatures. Measurements at these temperatures have not been attempted due to practical reasons (extremely long time needed for electrical conductivity relaxation experiments). It should be stressed that the purpose of the here constructed TTT diagram is to give a sense of the time scale and the width of the nucleation-controlled regime and not to serve as a tool for precise determination of transformation at the different times and temperatures.

4.3.2 Surface chemistry

As has been outlined in Figure 4.1, parallel to the set of kinetics measurements, a separate line of experiments was conducted with the aim to understand the connection between the observed changes in oxygen exchange kinetics and the detailed surface chemistry. The analysis of the surface chemistry can be divided into three parts: (i) characterization

of a freshly cleaved surface intended to serve as a reference for the quantification of the composition of the quenched samples, (ii) characterization of samples quenched at different points in time after the high-temperature thermal treatment (see Figure 4.1), and (iii) characterization of a sample after the ECR. In all cases, wide-range survey spectra (0-1100 eV) and detailed scans of specific peaks (La 3d, Sr 3d, Fe 2p, and O 1s) were collected. Survey spectra were used for identification of components on the surface and for assessment of escape depth correction (see Appendix B for details). Detailed scans of specific edges are used for peak fitting and quantification. In all analyses, peak fitting was done with the least number of distinguishable peaks possible. This implies that certain peak components can be composed of two or more peaks with such a small energy separation that they cannot be individually resolved. On the other hand, constraints were put on peaks that originate from the same element but are separated due to orbital splitting. Such case is Sr 3d peak, where the constraints are put on energy difference between Sr $3d_{5/2}$ and Sr $3d_{3/2}$ components at 1.7 eV,[54,134] the area ratio of Sr $3d_{5/2}$: Sr $3d_{3/2}$ which is fixed at 3:2, and the peak shape parameters. The detailed information about the fitting parameters can be found in the supplementary information.

4.3.3 Cleaved surface

A freshly cleaved surface obtained after breaking the 'as polished' sample in two pieces was used for examination of the pristine state of a LSF surface without any treatment, neither thermal nor mechanical (polishing). The results of narrow scans of La 3d, Fe 2p, Sr 3d, O 1s, and C 1s peaks are shown in Figure 4.3.

It can be seen that carbon is present on the cleaved surface despite the fact that the whole procedure of breaking the sample and inserting it in the chamber took less than 10 min. Practically, this means that a perovskite surface exposed to atmospheric air at room temperature is always covered with carbon-containing compounds. The oxygen O 1s peak is found to be composed of three different components while Sr 3d consisted of two clearly distinguishable chemical states: a low-energy component at binding energy of 131.9±0.2 eV, and a high-energy component at 133.3±0.3 eV.

In order to remove the carbon layer, the sample was treated inside the chamber at 400°C for 2 hours in a flow of pure oxygen at $1{\cdot}10^{-6}$ mbar. The temperature of 400°C is chosen since it was expected to be sufficient for the removal of carbon and still low enough to avoid strontium segregation.[53] During the thermal treatment the temperature was controlled by a resistive heater and measured with a thermocouple placed below the steel stage of 0.5 mm meaning that the local temperature on the surface was likely several degrees lower. After two hours of treatment all carbon disappeared from the surface. This was accompanied with the disappearance of one component of the O 1s peak which suggests that this originated from the oxygen in carbonates (blue color). The high energy state of strontium was slightly diminished after the treatment. The ratios between low and high energy components of Sr and O were in close match and equal to 2.2. The relative ionic ratios of La:Sr:Fe are similar before and after the treatment and close to the expected nominal values of 0.6:0.4:1. No significant changes could be seen

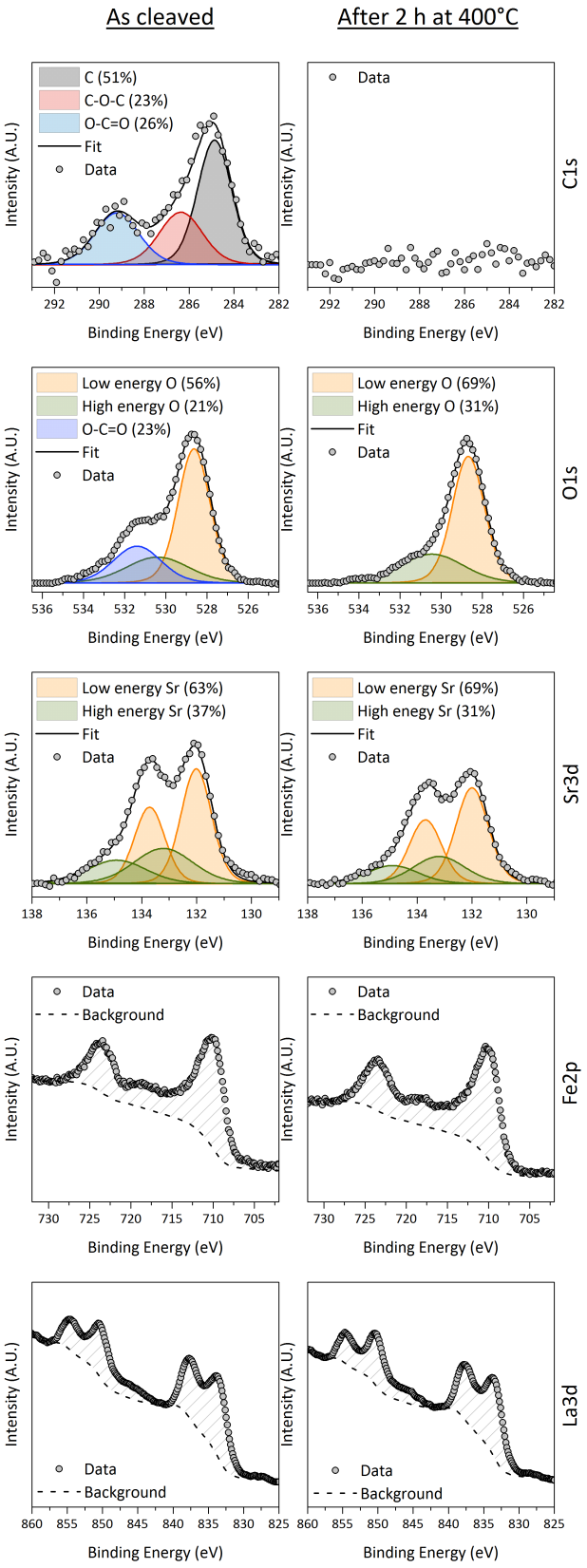

Figure 4.3: XPS spectra of the as cleaved surface immediately after insertion in the chamber (left column) and after 2 hours in O_2 flow at 10^{-6} mbar and 400°C (right column).

for La 3d and Fe 2p peaks.

In brief, the surface analysis of the cleaved sample showed that LSF surface (i) is very prone to carbon "contamination" when exposed to ambient conditions even for short time;(ii) the cation ratio is close to nominal bulk composition, and (iii) there are two distinguishable chemical states of both Sr and O, and the intensity ratios between high and low energy states is the same for both elements (ca. 2.2) suggesting presence of two both Sr- and O-containing phases/environments.

4.3.4 Quenched samples

The thermally treated and quenched samples (see Figure 4.1) were used for investigation of the effect of thermal history on the surface chemistry. The results of XPS survey spectra of quenched samples are shown in Figure 4.4. The spectra are stacked in temporal order, and the sequence from bottom to top roughly represents the time scale (the points in time at which the samples are quenched). The spectrum colors indicate thermal history, where the light shades represent the spectra immediately after the high-temperature thermal treatment (h.t.t.t.) and darker shades samples that after a prolonged treatment at 650°C. Green spectrum is of the 'as polished' sample and blue spectrum is the sample quenched directly from 1000°C after it had spent 39 days in the furnace.

The major elements; La, Sr, Fe, O, and C are observed on the surface of all samples. Most carbon was observed on the 'as polished' sample which reduces the relative intensities of all other peaks making them less intense in comparison with the quenched samples. Despite the use of clean alumina crucibles and a fairly clean chamber furnace for thermal treatment, a small amount of sulfur seems to accumulate on the surface over time, which can be observed through a steady increase of peaks associated with S 2s (229 eV) and S 2p (164 eV) shells.

The summarized results of a quantification of the composition based on narrow scans of selected peaks are shown in Figure 4.5. The corresponding thermal treatment is shown at the bottom for easier reference. The first plot (Figure 4.5(a)) shows relative ratios of La, Sr, and Fe.

It is evident that the 'as polished' sample, which was not thermally treated, has a composition of approximately La:Sr:Fe = 0.60 : 0.40 : 1, which is as expected from nominal composition ($(La_{0.6}Sr_{0.4})_{0.99}FeO_3$) which was also found for the as cleaved surface. Remarkably, the most pronounced change in surface composition occurs after the first high-temperature thermal treatment. There is a sharp increase in Sr content accompanied with a decrease in La and Fe. After this point, all samples quenched from 650°C have similar cation ratios of approximately La:Sr:Fe = 1:1.33:1. The associated error bars originate mainly from uncertainties related to background assignments to particular peaks. Despite this uncertainty it can be safely concluded that the change during the prolonged thermal treatment at is much smaller than after the first h.t.t.t. (compare first two points in Figure 4.5(a)).

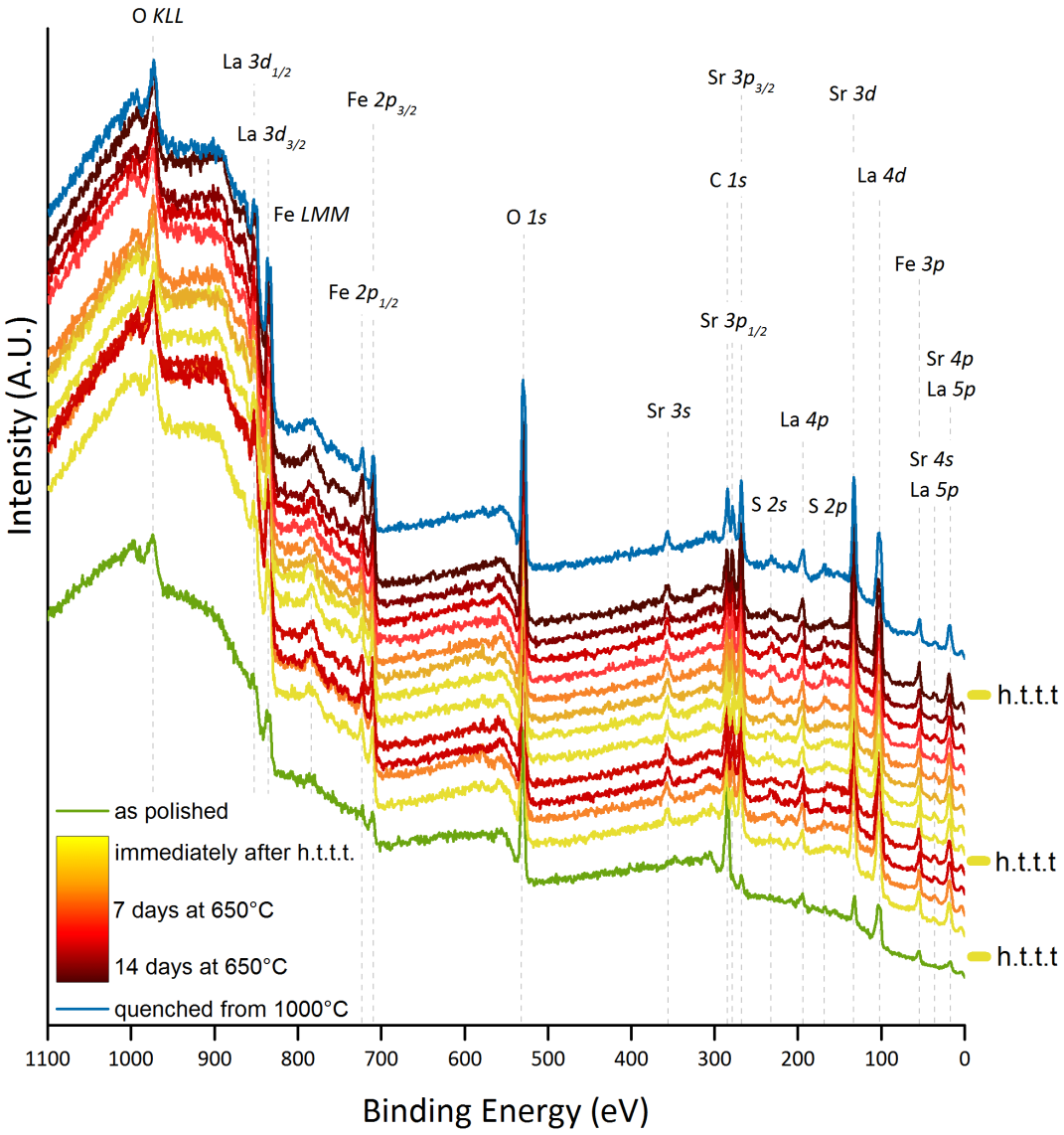

Figure 4.4: Survey spectra of all quenched samples. The green line is the spectrum of the freshly polished sample that has not been thermally treated afterwards. The blue line is the spectrum of the sample quenched from 1000°C after 39 days of thermal treatment. The lines in between are for the samples that were quenched from 650°C at different points in time. Light shades are used for samples immediately after the high-temperature thermal treatment (h.t.t.t.), while darker shades indicate prolonged time at 650°C.

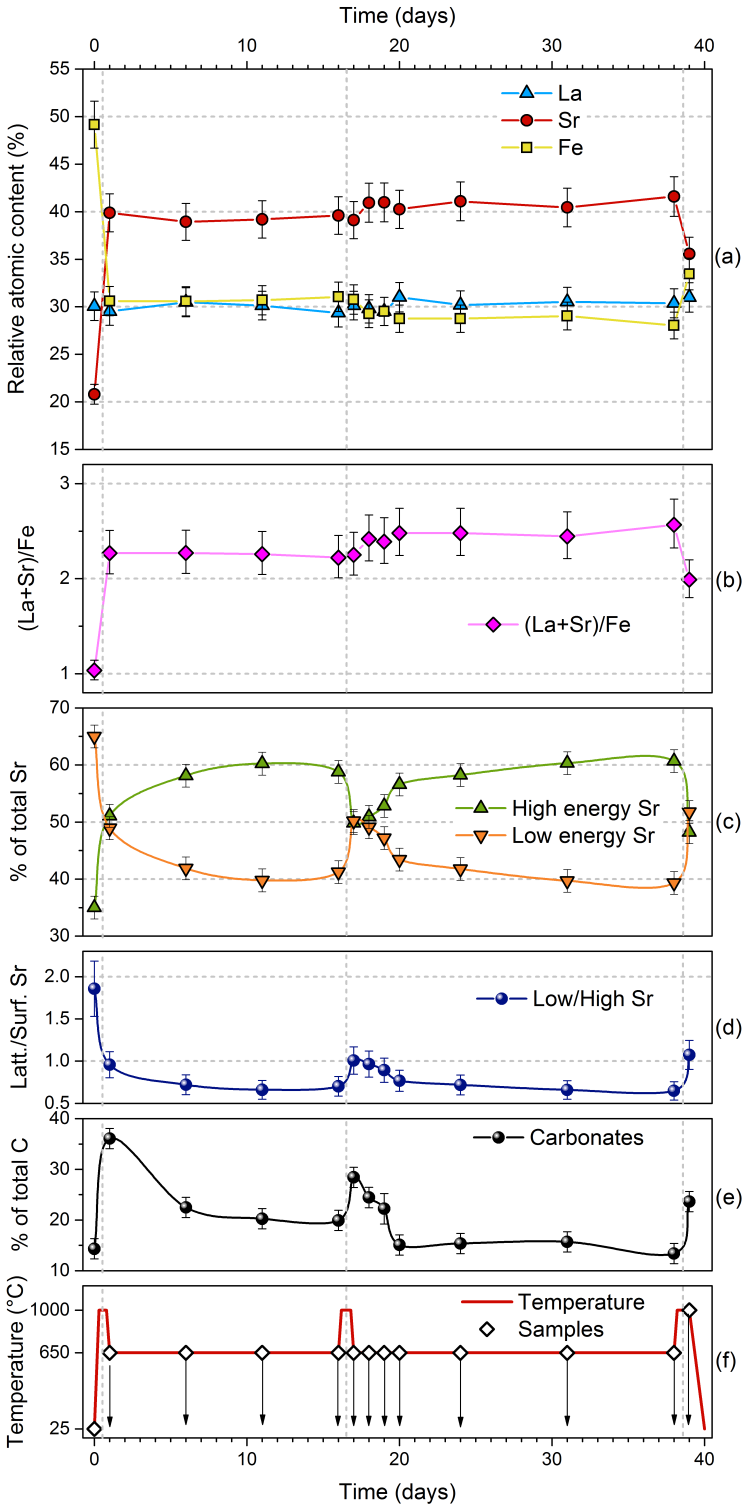

Figure 4.5: Results of surface characterization of quenched LSF samples by XPS plotted in comparison with thermal treatment shown at the bottom. (a) Relative content of La, Sr, and Fe; (b) The ratio of A-site (La and Sr) to B site (Fe) cations (c) Chemical state of Sr, where 'low' stands for the component at 131.9±0.2 eV and 'high' for the component at 133.3±0.3 eV; (e) Relative amount of carbonates on the surface characterized by C 1*s* peak at 288±0.2 eV.

In addition, it is a clear observation that the sample which was quenched directly from 1000° had noticeably different cation ratio close to La:Sr:Fe = 1:1:1 (last point in Figure 4.5(a)) which is far from nominal bulk composition close to the Ruddlesden-Popper compounds of K_2NiO_4 type. The same data are presented in Figure 4.5(b) expressed as ratio of A site (La and Sr) versus B site (Fe). It can be seen that A/B ratio varies from 1 in 'as polished' sample, to values higher than 2 in samples quenched from 650°C, and ≈2 in sample quenched from 1000°C.

Focusing on strontium, we could again observe two distinct chemical states of Sr as in case of the cleaved surface. It is noteworthy that relative amounts of these two components depend on thermal history (Figure 4.5(c,d)) and Figure 4.6. In the 'as polished' sample approximately 2/3 of the Sr signal is in the low energy peak and 1/3 is in the high energy component, which is close to values found on the cleaved surface (Figure 4.3). Immediately after h.t.t.t., the amounts of low and high-energy Sr become equal, while prolonged thermal treatment at 650°C leads to a gradual increase in the high-energy component. In other words, the ratio between the amount of low and high-energy components starts at ≈2 in 'as polished' sample, after h.t.t.t. it is ≈1, and after prolonged thermal treatment at 650°C it reaches value of ≈0.7 (Figure 5(d)).

Furthermore, an analysis of the carbon C 1*s* peak showed that the relative amount of the peak associated with C in form of carbonates at 288±0.2 eV tends to be higher after the h.t.t.t. (Figure 4.5(e)) and Figure 4.6.

Overall, the surface analysis of the thermally treated and quenched samples reveals that: (i) surfaces of all thermally treated samples have higher Sr content than the perovskite bulk; (ii) the samples quenched from 650°C have more carbonates and low-energy Sr component immediately after high temperature thermal treatment, and (iii) the sample quenched from 1000°C has ionic ratio of approximately 1:1:1 and A/B element ratio ≈2.

4.3.5 Bar after ECR

As pointed out in Experimental section and Figure 4.1 after the completion of electrical conductivity relaxation measurements, the sample was thermally treated in O_2/N_2 mixture at $pO_2 = 0.2$ and 1000°C for 10 hours and then cooled down to room temperature in 3 hours. The results of XPS analysis of the sample after this heat treatment are shown in Figure 4.7. Survey spectra confirmed the presence of only La, Sr, Fe, O and C on the surface. No sulfur could be detected on this sample, which suggests that sulfur on the quenched samples probably originates from ambient air or the chamber furnace, and not from material itself. Narrow scans of Sr 3*d* and O 1*s* peaks have shown distinct chemical states of these elements, 2 in case of strontium and 3 in case of oxygen. The amounts of high and low energy components of Sr; low/high energy component ratio ≈1, is as observed right after the h.t.t.t for the surface analysis samples (Figures 4.5 and 4.6). The most prominent component of O 1*s* peak was found to be 531 eV (56% of total oxygen) which can be associated with carbonates as shown in section 4.3.3 The rest of the peak is due to a low energy component at 528 eV (22%) and high energy

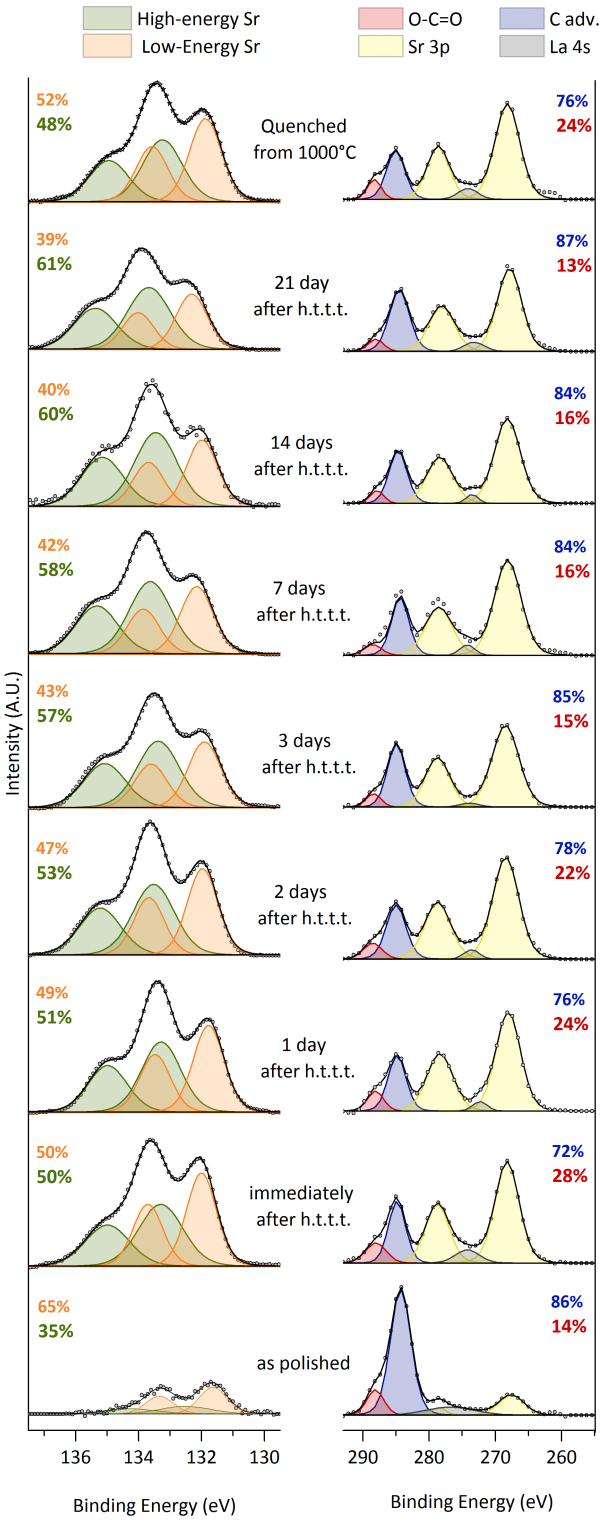

Figure 4.6: Quantification of individual peak components in case of Sr 3*d* (left column) and C 1*s* (right column). Sr 3*d* consists of high energy component at 133.3±0.3 eV and low energy component at 131.9±0.2 eV. Carbon C 1*s* peak can be fitted with two components – adventitious carbon at 284.8 eV and C in carbonates at 288.5 eV. Since C 1*s* overlaps with Sr 3*p* and La 4*s* peaks they also were included in the peak fitting but not in the quantification. Amounts of particular components are shown in percentages in the same color as corresponding peaks.

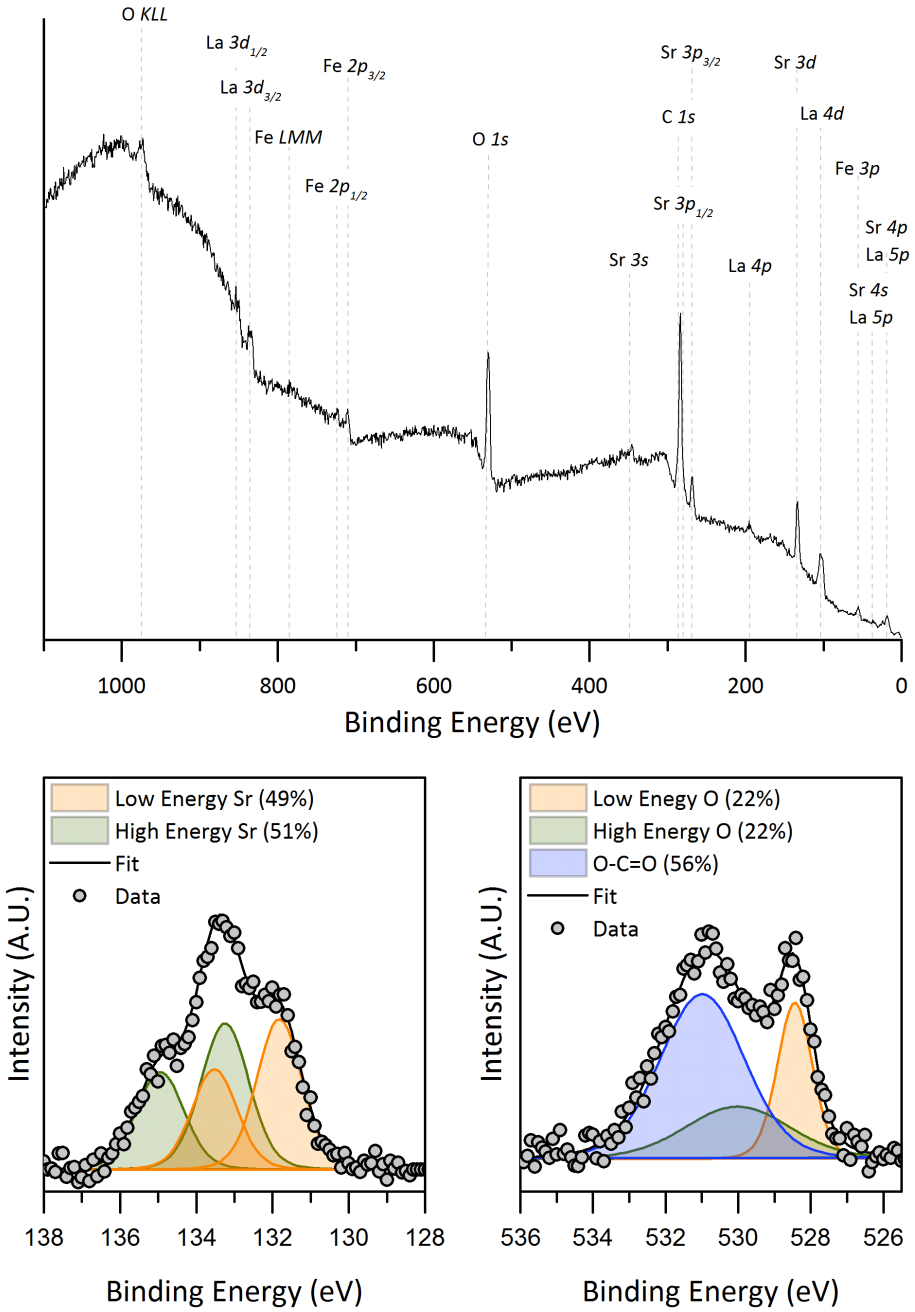

Figure 4.7: XPS analysis of the LSF bar after the ECR measurement. Before removal from the reactor, the bar was treated at 1000°C and pO_2=0.2 for 10 hours and then cooled down to room temperature in 3 hours. Survey spectra showed the presence of La, Sr, Fe, O and C (top). Narrow scans of Sr 3*d* and O 1*s* are shown at the bottom.

component at 529.6 eV (22%). The elemental ratio was found to be La:Sr:Fe = 1:1.33:1. These results show that surface composition of the ECR sample is similar to the samples quenched immediately after the high temperature thermal treatment both in terms of elemental ratios and amounts of low/high energy Sr-phase. This means that even though the sample has not been quenched due to practical reasons, it still corresponds to the quenched samples with similar thermal history. In other words, cooling from 1000°C in 3 hours is equivalent to quenching since the transformation takes several days.

There are two important implications of this finding: (i) the surface composition of the LSF bar during ECR measurements is also far from the nominal composition of La:Sr:Fe = 0.6:0.4:1 and (ii) the use of quenched samples for the surface analysis is justified since the same changes occur in the chamber furnace as in the reactor used in the relaxation experiments.

4.3.6 Surface microstructure

After the XPS analysis, samples were examined by scanning electron microscopy. The results are sorted in temporal order shown in Figure 4.8 and the thermal history is indicated by the color coding in the same way as in Figure 4.4. Namely, green stands for 'as polished' sample, blue for sample quenched from 1000°C (day 39), and transition from yellow to dark-red represents different periods of thermal treatment at 650°C in air.

The surface of the 'as polished' sample is smooth and the individual grains are practically indistinguishable. The grains become clearly visible on the surface of thermally treated samples with a mean size of approximately half a micron. Immediately after the first high temperature thermal treatment (day 1) the surface is clear and homogenous. After 5 days at 650°C (day 6) nanoparticulate precipitates of approximately 10 nm in size can be observed all over the samples surface. Similar particles have been observed in several studies[50,74,114,135,136] and and have been speculated to be SrO_x, usually considered to be detrimental to oxygen exchange reaction. The sample treated for another 5 days at 650°C (day 11) was likewise covered with nanoparticulate precipitates, but also with distinct sharp-angled particles of several hundred nanometers in size. A rough estimate from lower magnification SEM shows that the fraction of the surface that is covered by these sharp angled precipitates is less than 2%. EDS analysis (Figure 4.12) had shown sulfur signal and increased strontium signal in the spots where the particles are formed suggesting these particles are $SrSO_4$. Particles of similar shape and composition have been observed earlier on the surface of (La,Sr)CoO_3[114] and (La,Sr)(Co,Fe)O_3.[137] Five days later (day 16), the situation is similar and both kinds of particles are visible all across the surface. Interestingly, after another high temperature thermal treatment (day 17) both the small precipitates and the $SrSO_4$ platelets vanish and the sample surface resembled the one after the first h.t.t.t (day 1). Prolonged thermal treatment at 650°C led to a similar trend as after the first h.t.t.t. The precipitates first appear on the surface after 3 days (day 19 of the experiment) and the sulfates after 7 days (day 24). Both can be seen also after 14 and 21 days at 650°C (day 31 and 38), but not on the surface

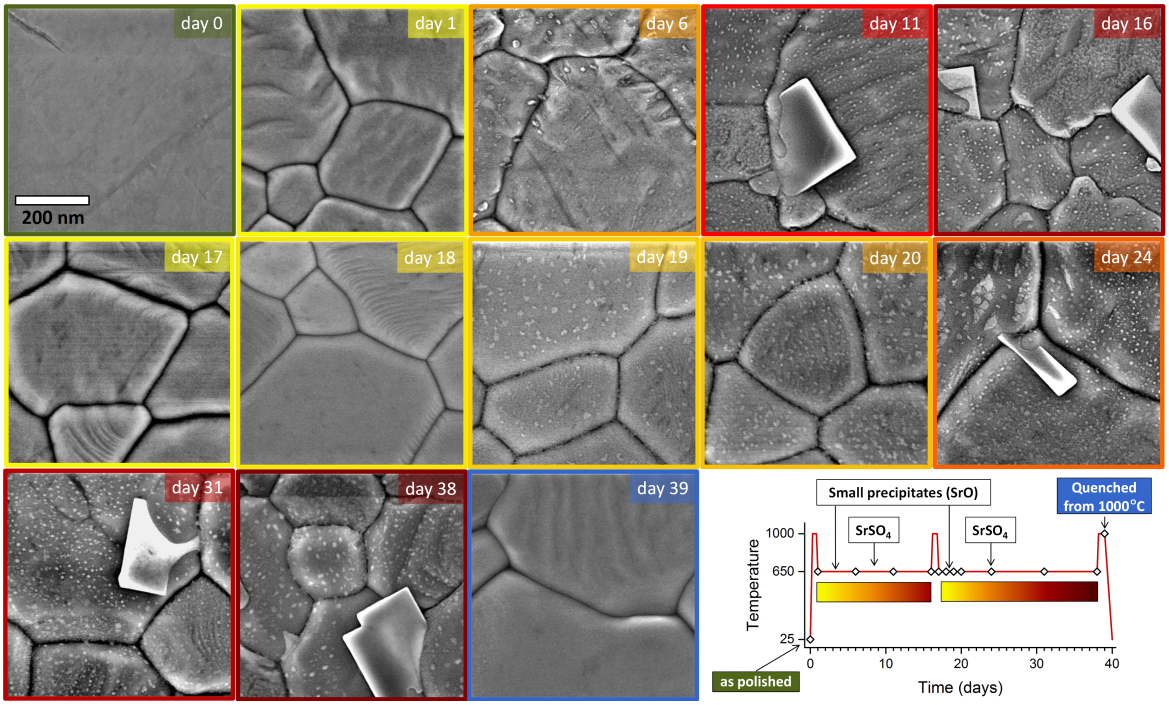

Figure 4.8: SEM micrographs of the surface of the quenched samples examined by XPS in section 4.3.4 The images are collected by surface sensitive In-lens detector at 3 kV, column current of 200 pA, magnification of 200k X and working distance of 3.5 mm. The color of the edges has the same meaning as in Figure 4.4 and indicates thermal history. Green stands for 'as polished' sample, blue for the sample quenched from 1000°C, yellow for the samples quenched from 650°C immediately after high-temperature thermal treatment and transition towards dark-red indicates the treatment at 650°C. Time in upper right corners stands for total time spent in the chamber furnace.

of the sample that was quenched from 1000°C (day 39). Also, the surface of the ECR sample is free of precipitates and sulfates (4.13).

To further test the reversibility of microstructural changes at the surface, the sample which was completely covered in precipitates (day 38) was subjected to a high-temperature thermal treatment after which no secondary phases could be observed (Figure 4.9).

Summarizing the SEM analysis we can conclude that thermal treatment at 650°C in atmospheric air leads to formation of observable nanoparticulate precipitates in 2-3 days and subsequently formation of $SrSO_4$ in 5-7 days. This finding is in line with many earlier studies on similar perovskite surfaces.[50,114,120] However, the most important discovery in this analysis was that these particles can be reversibly incorporated into the sample bulk by a thermal treatment at 1000°C in 10 hours in atmospheric air or get decomposed and evaporated.

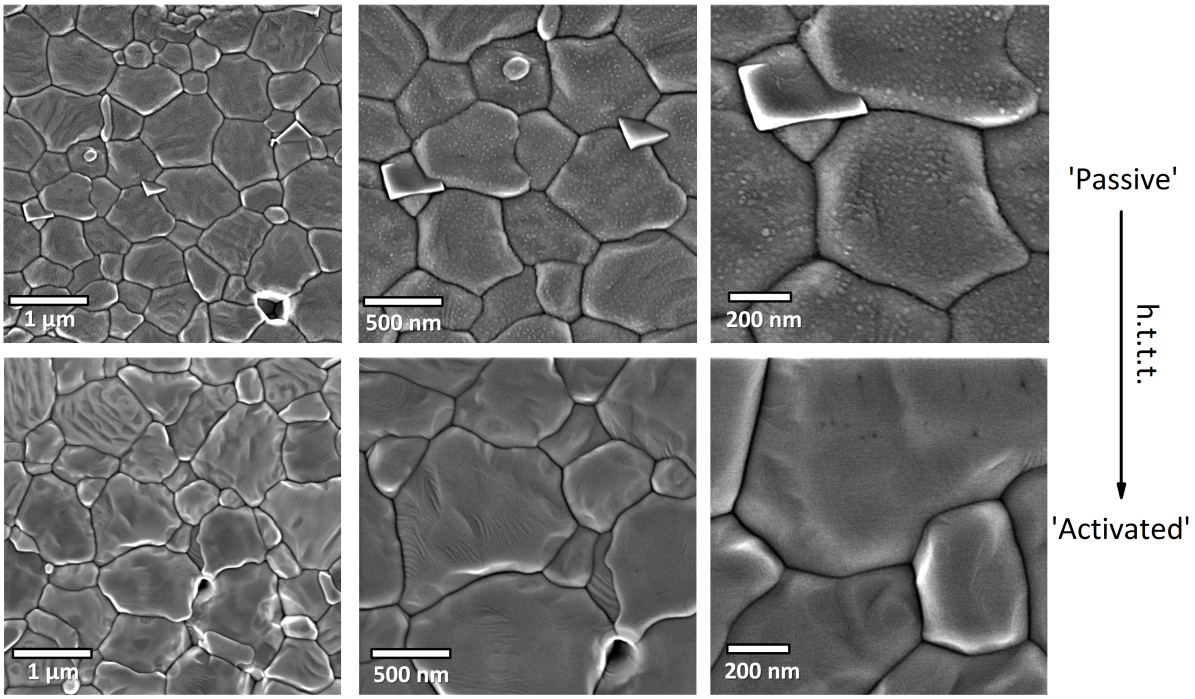

Figure 4.9: Comparison of the sample's surface after it had been treated at 650°C in ambient air for 21 day (top) and the surface of the same sample after a subsequent treatment for 10 hours at 1000°C in ambient air (bottom). SEM images are taken at accelerating voltage of 3 kV, column current 200 pA, working distance of 3.5 mm and with In-lens detector.

4.4 Discussion

In the following text we shall correlate the results collected by different techniques and examine the connection between the surface chemistry and the catalytic activity of perovskite surface towards oxygen reduction reaction expressed via k_{chem}. We will also discuss the reversible nature of the observed changes.

Summarizing the results of ECR, XPS and SEM analysis we can make a clear distinction between the state of fast and slow kinetics ('activated' and 'passive'), which can be reversibly switched between by different thermal treatment as shown in section 4.3.1. Further analysis has shown that the two states differ also in terms of relative elemental rations on the surface, changes in chemical state of strontium (relative abundance of two different Sr-containing phases or crystallographic sites), as well as formation of secondary phases. The observations are summarized in Table 4.2.

Table 4.2: Summary of the results and the observed differences between the two states of LSF.

Method	Property	State	
		'activated'	*'passive'*
ECR	Oxygen exchange kinetics	k_{chem} (at 635°C) = $4 \cdot 10^{-4}$ cm/s	k_{chem} (at 635°C) = $6 \cdot 10^{-6}$ cm/s
XPS	Relative ionic ratio (La:Sr:Fe)	≈ 31:36:33	≈ 30:40:30
		More Fe and La, Less Sr	Less Fe and La, More Sr
	A:B site ratio	≈ 2	> 2
	Chemical state of Sr	More low-energy component Less high-energy component	More high-energy component Less low-energy component
		Low/High Energy Sr = 1	Low/High Energy Sr < 1 and decreasing
	Chemical state of C	More C in form of carbonates	Less C in form of carbonates
SEM	Secondary phases	None, homogenous surface	Nanoparticulate precipitates (≈ 10 nm) and $SrSO_4$ sharp-angled particles (≈ 100 nm)

4.4.1 Surface chemistry and oxygen exchange activity

In our previous study, we suggested that changes in surface chemistry are important for the gradual decrease in k_{chem} at intermediate temperature. It can be seen from Figure 4.5(a) that the surface composition of all thermally treated samples is strongly enriched in strontium. This finding is to some extent expected due to the phenomenon of cation segregation in perovskite oxides at elevated temperatures. As opposed to the assumption that strontium segregation is always detrimental to oxygen exchange, our results show that samples, all with a high surface concentration of Sr, can reversibly switch between 'activated' and 'passive' states. In fact, k_{chem} values ranging from $6 \cdot 10^{-6}$ cm/s to $4 \cdot 10^{-4}$ cm/s could be measured for the same sample at 635°C, depending on the heat treatment (Table 4.2) all with a surface that is Sr-rich. This result suggests that strontium on the surface does not have adverse effect on kinetics *per se*, but rather via formation of blocking secondary phases. Performance degradation due to formation of strontium related secondary phases has already been proposed in case of (La,Sr)CoO_3,[40,54,75] (La,Sr)(Co,Fe)O_3[50,117,118,120] and (Ba,Sr)(Co,Fe)O_3[72] perovskite electrodes.

The materials oxygen exchange performance in this study was measured by ECR and expressed through a surface exchange coefficient (k_{chem}). The decreasing trend of k_{chem} shown in Figure 4.2(a) can be correlated with the change in chemical state of Sr in the surface (Figure 4.5(c)) and microstructural changes on the surface (Figure 4.8). The distinction between the two states of Sr through separation of Sr 3*d* has been pointed out by several groups[54,118,123,124,134,138–140] and the low-energy component is usually ascribed to Sr in the perovskite structure (so called 'lattice' component), while high-energy component is associated with strontium in the outermost layers ('surface' component) or secondary phases such as Brown-Millerites, SrO, or hydroxides. We have observed that approximately 30% of the strontium is in the high-energy ('surface') component even in the case of cleaved surface when no secondary phases are present (Figure 4.3). The tight match between Sr and O in high and low-energy components may further indicate that 'surface' component in case of cleaved surface originates from

Sr in the terminating layer of the perovskite structure. The amount of high-energy Sr component on the 'as polished' surface is 35%. On the other hand, in the thermally treated samples the amount of high-energy component is around 50% immediately after the thermal treatment ('activated' state) at 1000°C and increases to around 60% after prolonged thermal treatment at 650°C ('passive' state). The increase in high-energy Sr component from 30% to 50% in the 'activated' state when no secondary phases could be observed by SEM might be a consequence of surface reconstruction at high temperatures, while further increase in high-energy component from 50 to 60% can be assigned to the clearly visible formation of secondary phases. This means that the high-energy component is likely composed of one ever present peak corresponding to Sr in terminating layers and another one associated with Sr in secondary phases. In other words, the high-energy Sr is either partially or fully outside of the perovskite lattice. This could be the case if the energy separation between the peaks is so small that they cannot be resolved under the experimental conditions used in this study.

Another trend that was closely correlated with the decrease in k_{chem} is, interestingly, the amount of carbon in form of carbonates (Figure 4.5(e) and Figure 4.6). The samples after high-temperature thermal treatment (corresponding to 'active' state) tended to have more carbonates than the samples after prolonged thermal treatment at 650°C ('passive' state). This finding seems counterintuitive since $SrCO_3$ is argued to be one of the detrimental secondary phases,[120] and therefore requires further explanation. Thermodynamically $SrCO_3$ in ambient atmosphere is stable below 850°C (4.14) which means that certain amount of carbonates is expected to form on the surface of the samples during thermal treatment at 650°C. On the contrary, we detected most carbonates on the samples that had spent least time at 650°C. As pointed out in section 4.3.3, the kinetics of carbonate formation seems to be very fast at room temperature. Therefore we believe that most of the detected carbonates are formed during and after quenching. Thus, higher amount of carbonates on the surface of samples corresponding to 'active' state can be understood in terms of increased surface reactivity. After spending several days at 650°C, LSF surface is passivated by formation of nanoparticulate precipitates and $SrSO_4$ which then impede not only oxygen exchange, but also the formation of carbonates upon quenching.

The formation of $SrSO_4$ is another result that requires further explanation. Even though the sulfur signal appears to increase with the total amount of time spent in the furnace (Figure 4.4), $SrSO_4$ could be observed only after 5-7 days at 650°C (Figure 4.8). For instance, sulfur is detectable on the surface of sample quenched from 1000°C by XPS (39 days in the furnace), but no sharp-angled $SrSO_4$ particles could be observed on the surface. Phase diagram of SrO-O_2-SO_2 (Figure 4.14) suggests that $SrSO_4$ is thermodynamically stable in ambient atmosphere at 650°C at $p(SO_2)=10^{-16}$ bar or higher. Therefore, it seems that the formation of $SrSO_4$ is preconditioned by some other phenomenon. Since the nanoparticles that precipitate after 2-3 days at 650°C precede the formation of sulfates, we assume that they serve as nucleation sites for crystallization of $SrSO_4$. This in turn means that sulfur detected on the surface of samples without secondary phases is probably uniformly spread across the surface or accumulated in grain boundaries.

4.4.2 Surface reconstruction and the reversibility of the process

One of the major findings presented in this study is the reversibility of the observed changes both in terms of oxygen exchange kinetics and surface microstructure and chemistry. Our earlier study has shown that bulk related properties such as the chemical diffusion coefficient do not change over time, a finding which is also confirmed in this study (Figure 4.11). Furthermore, XRD analysis (Figures 4.15 and 4.16) has shown that the samples have rhombohedral perovskite structure (space group $Fm-3m$) regardless of the thermal treatment. On the other hand, the elemental ratio found by XPS on the surface of the sample quenched from 1000°C is close to La:Sr:Fe = 1:1:1, with A/B-site ratio of approximately 2. This composition resembles the one in Ruddlesden-Popper, "K_2NiO_4" end-member phase ($LaSrFeO_4$), which has been reported to form at the surface of perovskite materials at high temperatures.[78,125,127] This composition has in comparison to the perovskite ($La_{0.6}Sr_{0.4}FeO_3$) higher content of A-site ions, while it is depleted in iron and oxygen. High strontium content (higher than dictated by the overall sample composition) is evident on all thermally treated samples. It is also well known that the oxygen content in transition metal perovskites decreases with the increasing temperature. Furthermore, crystalline materials have a tendency to transform to space groups of higher symmetry at elevated temperatures. $LaSrFeO_4$ belongs to the tetragonal $I4/mmm$ space group which is more symmetrical than the rhombohedral $Fm-3m$ found in the bulk.

However, as can be seen from Figure 4.5(a,b), all samples quenched from 650°C have slightly higher Sr content then what corresponds to $LaSrFeO_4$. Several studies have shown that after annealing perovskite and perovskite-like structures such as RP have a tendency to terminate with an AO layer,[51,135,141] which in our case is rock-salt SrO layer. A simple estimation indicates that the ionic ratio La:Sr:Fe = 30:40:30 (1:1.33:1) would be valid in case of a 'mixture' of 9 units of $LaSrFeO_4$ and one unit of SrO. In fact, the ratio of SrO to $LaSrFeO_4$ can be even smaller when we consider that most of the photoelectrons that reach the detector originate from the outermost layer of the surface. We speculate that a SrO layer forms quickly during the one hour long step of cooling from 1000°C to 650°C which in terms of thermal history is the only difference between the day 39 sample (elemental ratio; 1:1:1) and the samples retrieved on day 1 and day 17 (elemental ratios; 1:1.33:1). The SrO layer is then stable for approximately 2-3 days, but is subsequently transformed into nanoparticles. Upon re-heating to 1000°C, these nanoparticles engage in a solid state reaction with Sr-depleted $LaFeO_3$ perovskite layer, re-forming Ruddlesden-Popper phase on the surface (giving the 1:1:1 ratio observed on the fast quenched day 39 sample). An illustration of this cyclic process is given in Figure 4.10. As discussed in section 4.3.1. the value of the Avrami coefficient $n \approx 2$ indicates that the transformation is taking place laterally from a fixed amount of nucleation sites. This could be the case of transformation in very thin surface layer where grain boundaries or other defects can act as nucleation sites.

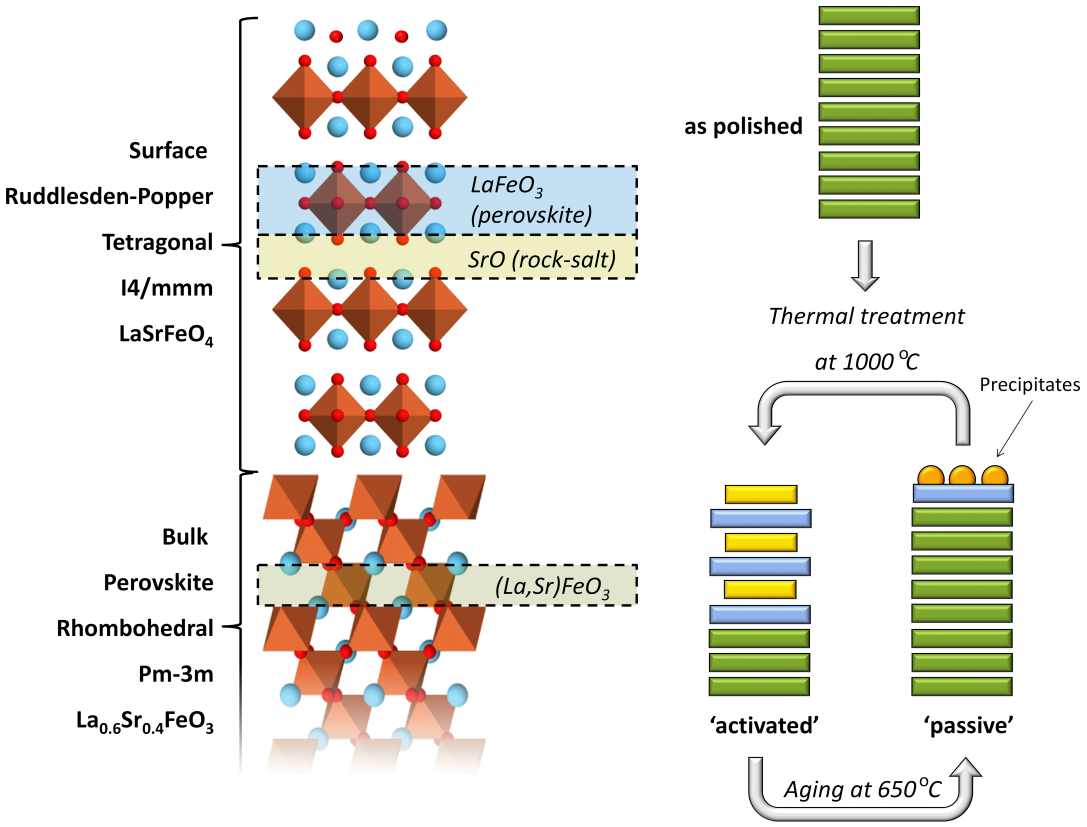

Figure 4.10: A sketch illustrating possible mechanism of surface reconstruction after high temperature thermal treatment. The 'as polished' sample that has not been subjected to thermal treatment is expected to have perovskite structure both in bulk and on the surface (green blocks). After thermal treatment the surface is enriched in Sr and in form of Ruddlesden-Popper phase – alternating layers of perovskite $LaFeO_3$ (blue blocks) and rock-salt SrO layers (yellow blocks).

4.5 Conclusions

The results presented in this work stress the importance of thermal history on the measurement of oxygen exchange kinetics at intermediate temperatures (<800°C) in case of $La_{0.6}Sr_{0.4}FeO_{3-\delta}$. By conducting series of systematic experiments, especially with regard to thermal history, we were able to correlate the catalytic activity of the surface with its surface chemical composition.

A polished surface or an "as-cleaved" surface was found to have a composition as expected from the composition of the studied material. Careful analysis of XPS-spectra and the observation of nominal "correct" composition of the as-cleaved surface enabled a trustworthy determination of the absolute surface composition of the surfaces also after thermal treatment. Higher than nominal bulk concentration of Sr is found on all thermally treated samples. Thermal treatment at high temperatures (1000°C) causes ob-

servable changes in surface microstructure, resulting in the disappearance of secondary phases found after prolonged treatment at low temperature (630 – 675°C). Furthermore, it causes the chemical state of strontium to change towards more of 'low energy' component, often associated with Sr in the lattice structure. These changes are correlated with drastic increase in oxygen exchange kinetics measured by electrical conductivity relaxation. Prolonged thermal treatment at 650°C over several weeks leads to a gradual decrease in oxygen exchange rates, while the surface analysis show changes in the chemical state of Sr towards higher binding energies and the formation of nanoparticulate precipitates (detailed composition not known) and secondary phases ($SrSO_4$). Changes in both oxygen exchange kinetics and surface chemistry, as well as microstructure are found to be reversible i.e. upon a second high temperature treatment secondary phases formed during low temperature aging disappear and elemental ratios return to the ones observed immediately after the first high temperature treatment. Returning to the questions put forward in the Introduction, it was found that:

(i) The total amount of Sr on the surface is not crucial for oxygen exchange kinetics, but rather its chemical state (in which phase it is found). For approximately the same amount of Sr, oxygen exchange kinetics can be very different depending on whether Sr is in low energy ('lattice') state or high energy ('surface') state. The two states are tentatively associated with Sr in the perovskite lattice and Sr in secondary phases, respectively.

(ii) The surface of the perovskite passivates via the formation of nanoparticulate precipitates;

(iii) The secondary phases can be removed by a high-temperature thermal treatment which leads to improvement in oxygen exchange kinetics (re-activation).

(iv) The reversibility of this process is likely connected to a surface reconstruction mechanism where the perovskite structure in the outermost layers gets transformed into a related Ruddlesden-Popper structure at elevated temperatures. Thus formed thin layers of a RP-phase can be reversibly changed to Sr-depleted perovskite and Sr-rich precipitates at intermediate temperatures (below 800°C) and reconstructed at high temperatures (above 800°C).

Supplementary Information

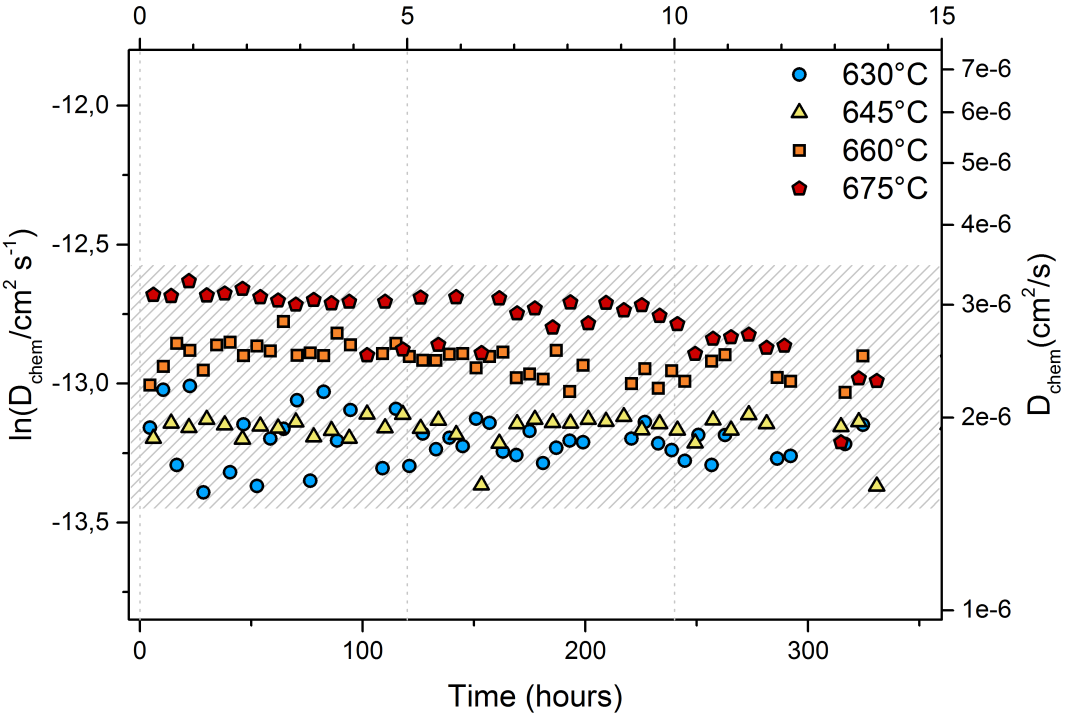

Figure 4.11: The values of chemical diffusion coefficient D_{chem} during aging at different intermediate temperatures over course of 15 days.

Table 4.3: Detailed XPS peak positions and fitting parameters.

Sample	Name	Position (eV)	FWHM	Raw Area	%At Conc
As polished	Sr3d	131.7	1.31	2403	20.79
	Fe2p	709.8	3.33	7953.07	49.16
	La3d	833.2	2.73	11485.5	30.05
Day 1	Sr 3d	133.7	2.99	9744.45	39.89
	Fe 2p	709.8	3.49	10481.4	30.6
	La3d	832.6	2.51	23924.3	29.52
Day 6	Sr 3d	133.5	2.89	9673.39	38.94
	Fe 2p	710.1	3.49	10640.8	30.58
	La3d	832.9	2.06	25096.3	30.48
Day 11	Sr 3d	132.9	2.97	10385.3	39.19
	Fe 2p	709.8	3.76	11392.9	30.69
	La3d	832.2	2.02	26487.6	30.12
Day 16	Sr 3d	133.52	3.08	11189.1	39.6
	Fe 2p	710.02	3.53	12291.4	31.04
	La3d	832.8	2.77	27495.2	29.35
Day 17	Sr 3d	133.64	2.99	11814.6	39.12
	Fe 2p	709.84	3.48	13022.8	30.76
	La3d	832.8	2.52	30159.6	30.12
Day 18	Sr 3d	133.29	2.88	11544.1	40.94
	Fe 2p	709.89	3.45	11562.8	29.27
	La3d	832.8	2.51	27841.1	29.79
Day 19	Sr 3d	133.64	2.92	11775.7	40.98
	Fe 2p	709.74	3.4	11892.3	29.51
	La3d	832.5	2.26	28134.6	29.51
Day 20	Sr 3d	133.48	3.05	10710.5	40.25
	Fe 2p	709.38	3.49	10729.7	28.74
	La3d	832.5	2.08	27374.3	31.01
Day 24	Sr 3d	133.77	2.98	11235.4	41.09
	Fe 2p	709.57	3.51	11024.2	28.74
	La3d	832.5	2.46	27387.8	30.18
Day 31	Sr 3d	133.55	2.82	11343.6	40.45
	Fe 2p	709.55	3.38	11417.8	29.03
	La3d	832.7	2.55	28381.5	30.52
Day 38	Sr 3d	133.87	3.25	9433.61	41.6
	Fe 2p	709.97	3.39	8910.72	28.03
	La3d	832.4	1.89	22869.6	30.37
Day 39 Quenched from 1000°C	Sr 3d	133.41	2.93	10975.1	35.55
	Fe 2p	709.91	3.54	14473.3	33.45
	La3d	832.6	2.52	31734	30.99

Table 4.4: Detailed positions and fitting parameters of Sr 3*d* XPS peak. RSF - relative sensitivity factor; MFP - mean free path.

	Species	Name	Position	FWHM	Raw Area	Area/(RSF*T*MFP)	%At Conc	Goodness of Fit
As polished	High Energy Component 'surface Sr'	Sr3d5/2	132.51	1.94	508.589	6.08399	35.01	178.017
		Sr3d3/2	134.21	1.94	339.059	5.89716		178.017
	Low Energy Component 'lattice Sr'	Sr3d5/2	131.64	1.04	944.797	11.2923	64.99	178.017
		Sr3d3/2	133.34	1.04	629.865	10.9455		178.017
Day 1	High Energy Component 'surface Sr'	Sr3d5/2	133.46	1.5	2972.56	35.5948	51.08	133.408
		Sr3d3/2	135.16	1.5	1981.71	34.5018		133.408
	Low Energy Component 'lattice Sr'	Sr3d5/2	132.11	1.21	2850.97	34.0921	48.92	133.408
		Sr3d3/2	133.81	1.21	1900.65	33.0452		133.408
Day 6	High Energy Component 'surface Sr'	Sr3d5/2	133.38	1.55	3362.54	40.2615	58.13	131.447
		Sr3d3/2	135.08	1.55	2241.7	39.0252		131.447
	Low Energy Component 'lattice Sr'	Sr3d5/2	131.84	1.15	2425.92	29.0016	41.87	131.447
		Sr3d3/2	133.54	1.15	1617.28	28.1109		131.447
Day 11	High Energy Component 'surface Sr'	Sr3d5/2	132.8	1.66	3750.85	44.8833	60.22	167.858
		Sr3d3/2	134.5	1.66	2500.57	43.505		167.858
	Low Energy Component 'lattice Sr'	Sr3d5/2	131.3	1.22	2481.03	29.6435	39.78	167.858
		Sr3d3/2	133	1.22	1654.02	28.7332		167.858
Day 16	High Energy Component 'surface Sr'	Sr3d5/2	133.06	1.86	3937.23	47.1272	58.77	178.563
		Sr3d3/2	134.76	1.86	2624.82	45.68		178.563
	Low Energy Component 'lattice Sr'	Sr3d5/2	131.88	1.06	2765.12	33.0583	41.23	178.563
		Sr3d3/2	133.58	1.06	1843.41	32.0431		178.563
Day 17	High Energy Component 'surface Sr'	Sr3d5/2	133.29	1.67	3537.54	42.3531	49.81	114.602
		Sr3d3/2	134.99	1.67	2358.36	41.0526		114.602
	Low Energy Component 'lattice Sr'	Sr3d5/2	132	1.12	3569.33	42.6785	50.19	114.602
		Sr3d3/2	133.7	1.12	2379.56	41.3679		114.602
Day 18	High Energy Component 'surface Sr'	Sr3d5/2	133.23	1.48	3547.82	42.4732	50.9	138.929
		Sr3d3/2	134.93	1.48	2365.21	41.169		138.929
	Low Energy Component 'lattice Sr'	Sr3d5/2	131.73	1.16	3427.83	40.9746	49.1	138.929
		Sr3d3/2	133.43	1.16	2285.22	39.7165		138.929
Day 19	High Energy Component 'surface Sr'	Sr3d5/2	133.52	1.57	3783.04	45.3031	52.82	168.511
		Sr3d3/2	135.22	1.57	2522.02	43.9119		168.511
	Low Energy Component 'lattice Sr'	Sr3d5/2	131.97	1.15	3384.76	40.47	47.18	168.511
		Sr3d3/2	133.67	1.15	2256.5	39.2272		168.511
Day 20	High Energy Component 'surface Sr'	Sr3d5/2	133.38	1.6	3647.71	43.6756	56.58	199.399
		Sr3d3/2	135.08	1.6	2431.81	42.3344		199.399
	Low Energy Component 'lattice Sr'	Sr3d5/2	131.91	1.24	2804.08	33.5245	43.42	199.399
		Sr3d3/2	133.61	1.24	1869.39	32.495		199.399
Day 24	High Energy Component 'surface Sr'	Sr3d5/2	133.63	1.6	3946.07	47.2637	58.22	148.106
		Sr3d3/2	135.33	1.6	2630.71	45.8124		148.106
	Low Energy Component 'lattice Sr'	Sr3d5/2	132.15	1.23	2836	33.9179	41.78	148.106
		Sr3d3/2	133.85	1.23	1890.67	32.8763		148.106
Day 31	High Energy Component 'surface Sr'	Sr3d5/2	133.45	1.6	4033.9	48.3051	60.3	362.195
		Sr3d3/2	135.15	1.6	2689.27	46.8218		362.195
	Low Energy Component 'lattice Sr'	Sr3d5/2	131.98	1.17	2660.69	31.8143	39.7	362.195
		Sr3d3/2	133.68	1.17	1773.8	30.8375		362.195
Day 38	High Energy Component 'surface Sr'	Sr3d5/2	133.68	1.63	3439.26	41.1967	60.67	120.517
		Sr3d3/2	135.38	1.63	2292.84	39.9316		120.517
	Low Energy Component 'lattice Sr'	Sr3d5/2	132.31	1.18	2232.27	26.7025	39.33	120.517
		Sr3d3/2	134.01	1.18	1488.18	25.8825		120.517
Day 39 Quenched from 1000°C	High Energy Component 'surface Sr'	Sr3d5/2	133.24	1.5	3182.68	38.1024	48.23	94.5065
		Sr3d3/2	134.94	1.5	2121.79	36.9324		94.5065
	Low Energy Component 'lattice Sr'	Sr3d5/2	131.88	1.2	3419.89	40.8863	51.76	94.5065
		Sr3d3/2	133.58	1.2	2279.93	39.6307		94.5065

Table 4.5: Detailed positions and fitting parameters of C 1s peak. C adv. refers to adventitious carbon, O-C=O refers carbon in form of carbonates.

Sample	Name	Position	Raw area	Area/(RSF*T*MFP)	%At Conc
As polished	C 1s adv.	284.3	67631	360.557	75.12
	C1s (O-C=O)	288.14	11244.8	60.2562	12.55
Day 1	C 1s adv.	285.01	27598.1	147.272	39.54
	C1s (O-C=O)	287.98	15509.6	83.0914	22.31
Day 6	C 1s adv.	284.73	32899.5	175.497	45.63
	C1s (O-C=O)	288.22	9505.15	50.9394	13.24
Day 11	C 1s adv.	284.45	28008.2	149.35	42.73
	C1s (O-C=O)	287.56	7073.23	37.8731	10.84
Day 16	C 1s adv.	285.2	29908.6	159.642	43.71
	C1s (O-C=O)	288.72	7405.29	39.7124	10.87
Day 17	C 1s adv.	284.69	34894.9	186.131	45.83
	C1s (O-C=O)	288.17	10189.3	54.6023	13.44
Day 17	C 1s adv.	284.86	27697.1	147.772	37.41
	C1s (O-C=O)	288.05	10956.8	58.7058	14.86
Day 18	C 1s adv.	284.87	26127.9	139.4	39.93
	C1s (O-C=O)	288.1	8420.65	45.1202	12.92
Day 19	C 1s adv.	285	27851	148.618	41.02
	C1s (O-C=O)	288.51	7919.27	42.4569	11.72
Day 20	C 1s adv.	284.97	29861.1	159.339	46.49
	C1s (O-C=O)	288.38	5283.67	28.322	8.26
Day 24	C 1s adv.	284.4	21202.5	113.051	30.25
	C1s (O-C=O)	286.83	15208.3	81.3527	21.77
Day 31	C 1s adv.	284.71	24764.7	132.099	40.14
	C1s (O-C=O)	287.9	4588.97	24.5823	7.47
Day 38	C 1s adv.	284.51	32105.5	171.21	49.08
	C1s (O-C=O)	288.07	4941.19	26.4751	7.59
Day 39	C 1s adv.	285.07	23362.2	124.677	36.31
	C1s (O-C=O)	288.28	7200.07	38.5891	11.24

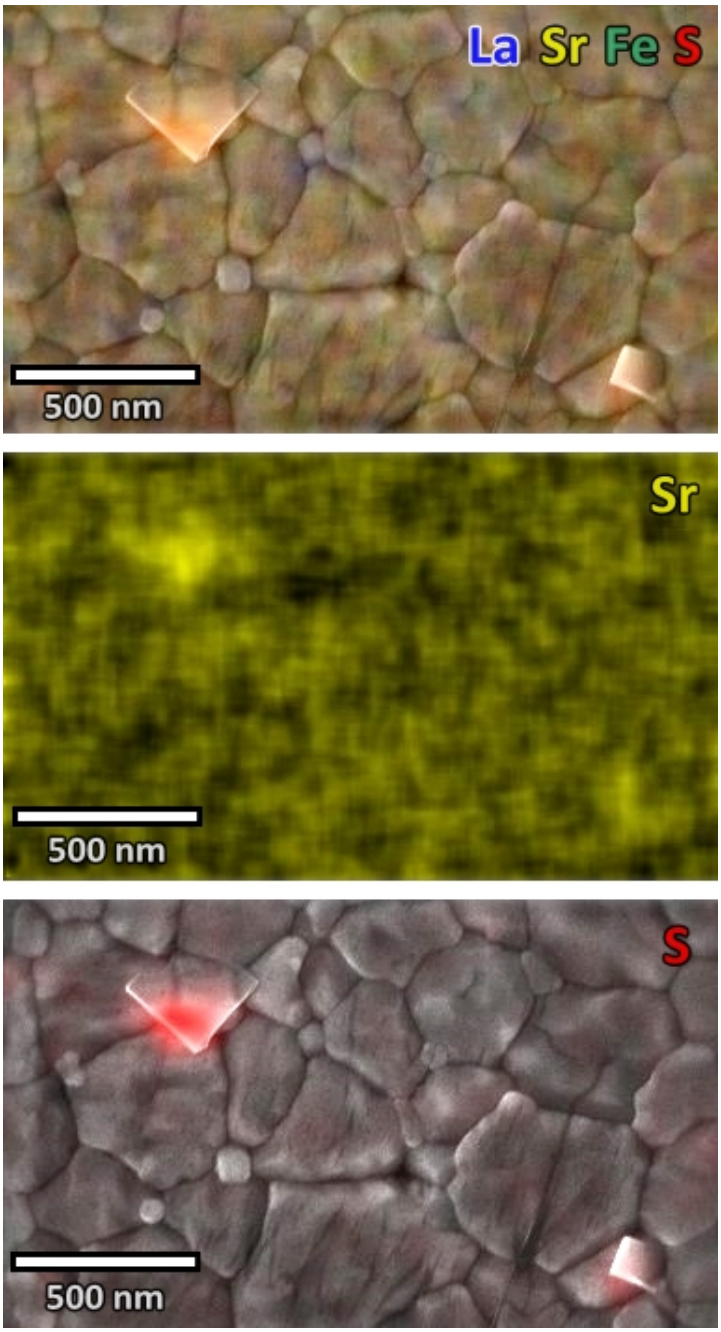

Figure 4.12: EDS mapping of a passivated surface. Sharp-angled particles are enriched in Sr and S and are likely in form of strontium sulfate ($SrSO_4$). SEM imaging parameters were: accelerating voltage 10 kV, column current 260 pA, HE-SE2 detector, working distance 8 mm.

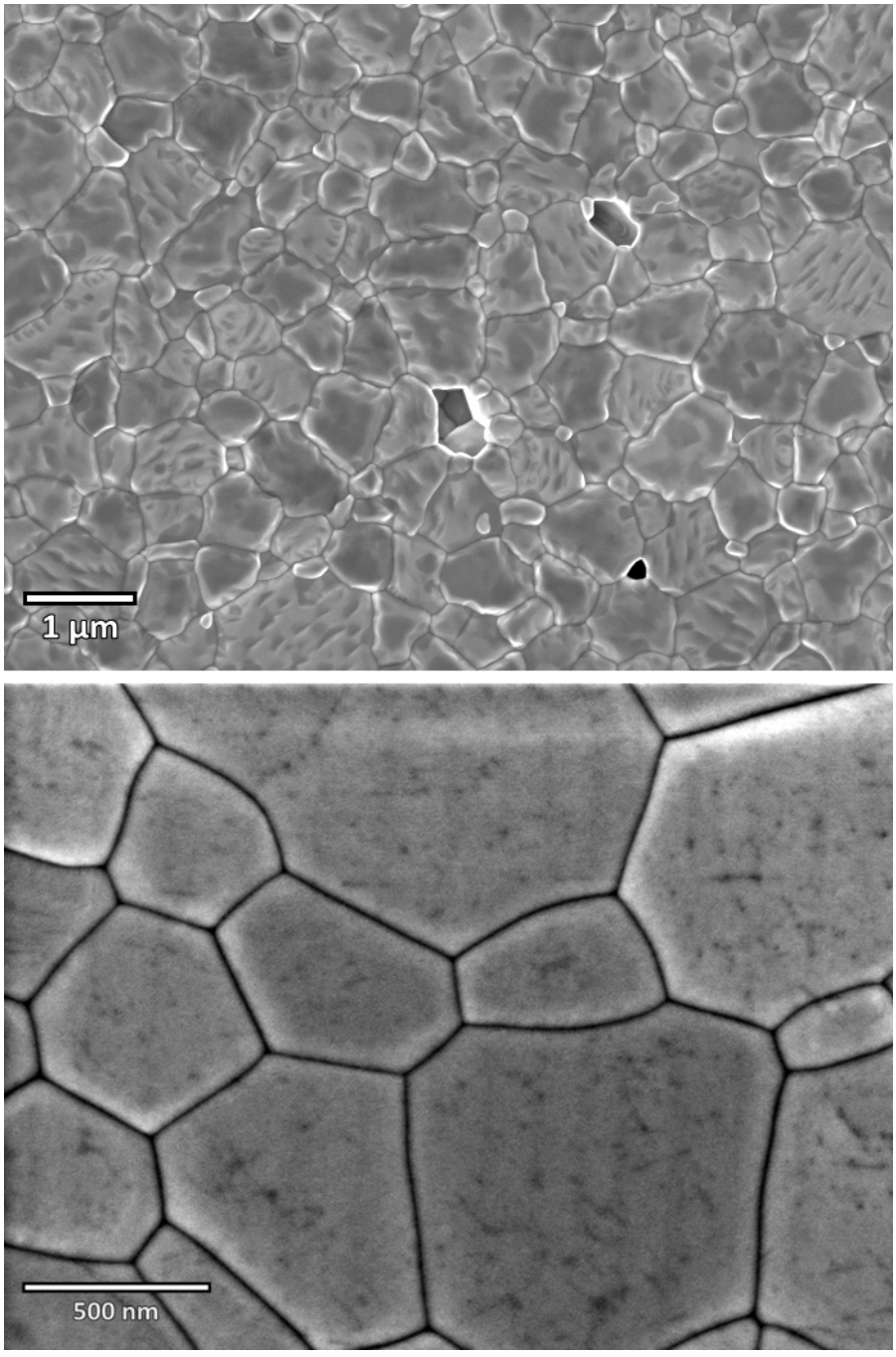

Figure 4.13: SEM image of LSF bar after ECR taken at 3 kV, 200 pA, working distance 3.5 mm with in-lens detector.

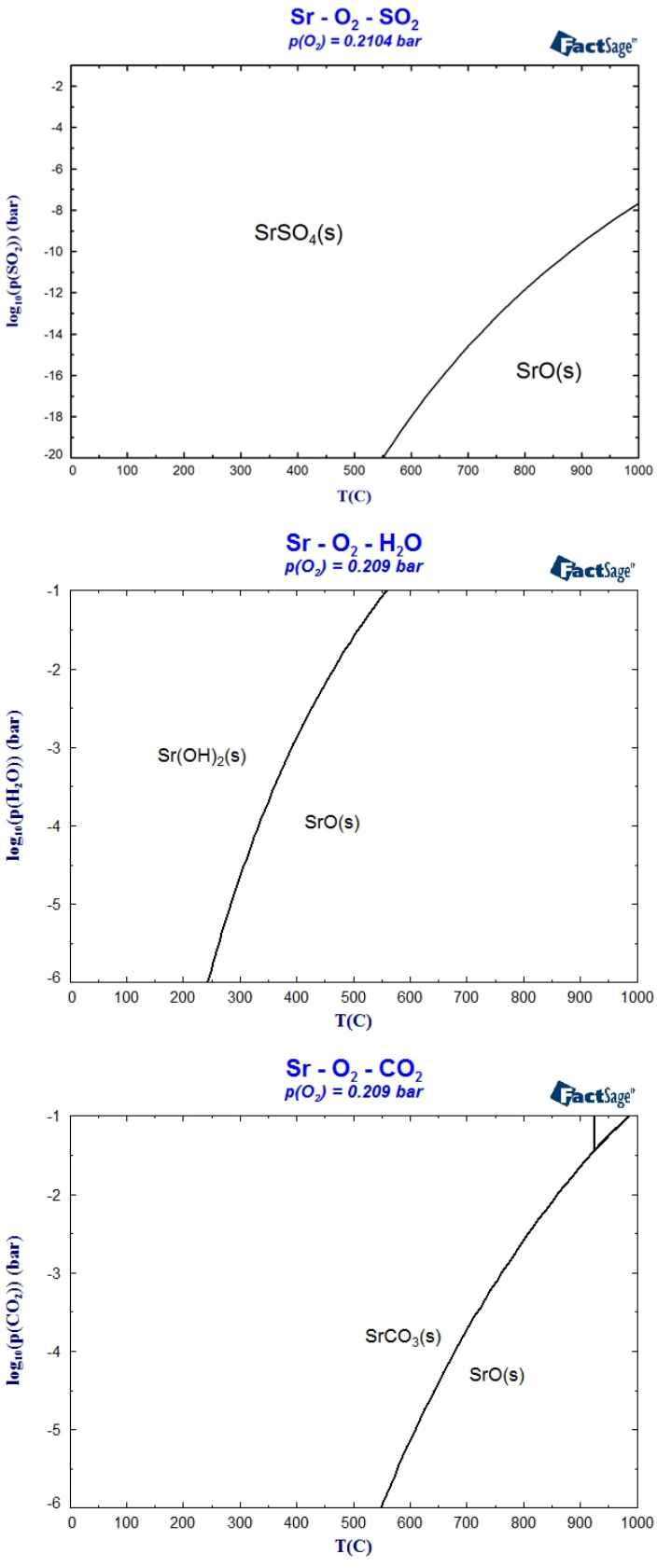

Figure 4.14: Phase diagrams of Sr-sulfate, -hydroxide, and -carbonate rendered using FactSage^{TM}.

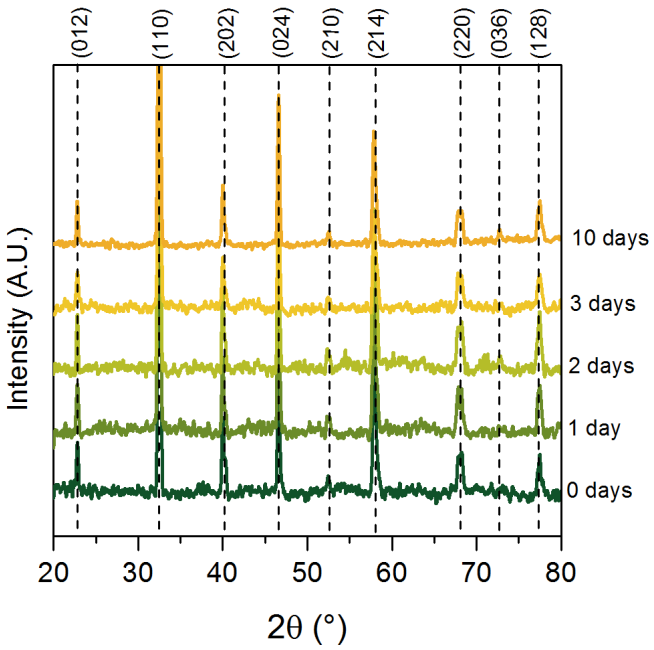

Figure 4.15: Grazing incidence XRD diffractograms of quenched samples aged for different times at 650°C.

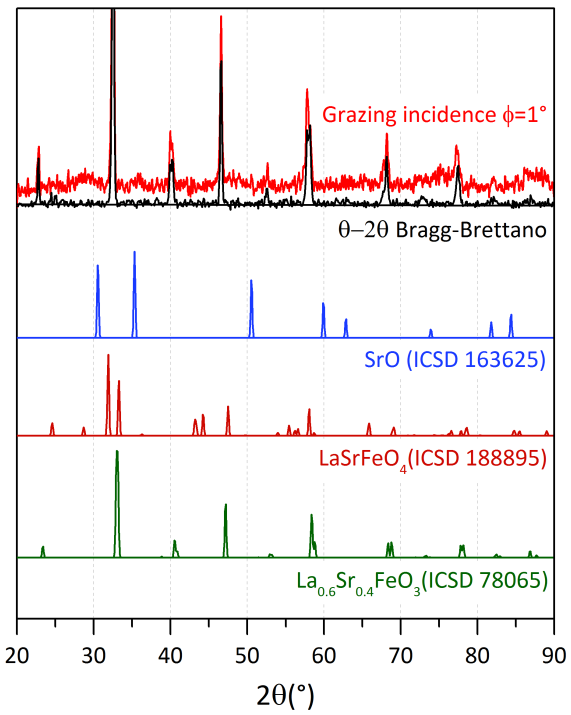

Figure 4.16: Grazing incidence and $\theta - 2\theta$ scan of sample quenched from 1000°C. Below are shown XRD patterns of rock-salt (SrO), Ruddlesden-Popper phase ($LaSrFeO_4$), and perovskite ($La_{0.6}Sr_{0.4}FeO_3$).

CHAPTER 5

Oxygen exchange on $La_{0.6}Sr_{0.4}FeO_3$ thin film electrodes below 600°C

Abstract

Thin dense $La_{0.6}Sr_{0.4}FeO_3$ electrodes prepared by PLD were investigated by electrochemical impedance spectroscopy between 387°C and 594°C in the pO_2 range from 0.05 – 1 bar and the short term was stability tracked over 60 hours. The oxygen exchange coefficient extracted from the impedance characterization was compared with the one obtained by electrical conductivity relaxation on samples prepared in the same way. The electrodes were further characterized by SEM, XPS, and profilometry. An increase in the surface concentration of "non-lattice strontium" is identified as the main cause for the rapid decrease in oxygen exchange rate observed over 60 hours. It was further found that the electrode performance could be recovered by rinsing the passivated electrode in deionized water. Repeated treatments eventually also led to improved electrode stability.

5.1 Introduction

Currently preferred oxygen electrode materials for solid oxide fuel and electrolysis cells are typically mixed ionic and electronic conductors (MIEC). Apart from chemical stability and good mechanical compatibility with other SOC components, the most important additional requirement to the material in such electrodes is high catalytic activity towards the oxygen reduction/evolution reaction (ORR/OER):

$$\frac{1}{2}O_2 + 2e^- + V_O^{\cdot\cdot} \longleftrightarrow O_O^X \tag{5.1}$$

Eq. 5.1 illustrates the incorporation of molecular oxygen (O_2) into the oxide lattice (O_O^X), which requires presence of electrons and oxygen vacancies ($V_O^{\cdot\cdot}$). The equation is written in a simplified overall way, including only initial and final state, neglecting the many possible intermediate steps. In reality the ORR proceeds over several steps including adsorption, molecular dissociation, charge transfer etc.[142,143] The exact mech-

anism of the reaction is still not fully understood and the rates of individual steps are usually not know. One can measure the overall oxygen exchange rate (expressed through an appropriate rate constant k) using techniques such as isotope exchange (IE), electrical conductivity relaxation (ECR), and electrochemical impedance spectroscopy (EIS). The electrochemical performance of technological electrodes utilizing MIEC materials depends directly on the rate of the oxygen exchange[85,144] on the surface of the material, which is why obtaining high oxygen exchange rates is important for SOFC/SOEC applications.

Apart from the rate of oxygen exchange on the constituent materials, the achievable electrode performance depends also on microstructure and porosity.[85,144,145] One way to simplify interpretation of electrode characterizations is to "eliminate" effects of microstructure using dense model electrodes where the area over which the exchange takes place is well-defined. Such model electrodes can be millimeter-sized dense rectangular bars used in electrical conductivity relaxation (ECR) measurements or thin dense films, typically less than 1 µm in thickness deposited on an electrolyte support. By changing the dimensions of the model electrodes, one can vary the sensitivity to different oxygen transport parameters. Sensitivity to oxygen exchange over the surface (k_{chem}) and the chemical diffusion of oxide ions through the bulk (D_{chem}) of the material can be evaluated from a dimensionless parameter L_α:

$$L_\alpha = \frac{L}{L_c} = \frac{L \cdot k_{chem}}{D_{chem}} \tag{5.2}$$

where L is the sample thickness and L_c is characteristic length defined as the ratio between the chemical diffusion coefficient and the surface exchange rate constant ($L_c = D_{chem}/k_{chem}$). L_c is usually in the range from several microns to few millimeters for well conducting MIEC materials.[146] A general rule is that for $L_\alpha > 30$, the measurement is sensitive only to diffusion, for $0.03 < L_\alpha < 30$ both k_{chem} and D_{chem} can be determined simultaneously, while for $L_\alpha < 0.03$ the measurement is in a surface-controlled regime and depends practically only on k_{chem}.[19] The latter is the case for dense MIEC films of submicron thickness which are thus well-suited for characterization of oxygen exchange kinetics.

Up to date, most studied thin film SOC electrodes fall into one of the following categories: (i) micro-patterned electrodes of up to a few hundreds of microns in diameter manufactured using e.g. photolithography,[96,147] or (ii) macroscopic electrodes with surface areas of several tens of mm^2.[143,148] The advantage of micro-patterned electrodes is the possibility of placing hundreds of electrodes on a single sample and that effects of counter-electrode response are negligible, but the small size can be a problem for positioning and contacting, as well determination of local temperature. On the other hand, macroscopic thin film electrodes are easier to fabricate, however problems with current collection can emerge when lateral losses due to in–plane transport of electrons (sheet resistance) become significant.[149–152] This is usually the case if the film thickness is very small, spacing between contact points is large, and the ORR reaction is fast. A general guide of the geometrical requirements under which sheet resistance is negligible for var-

ious values of exchange resistance and material conductivity can be found in Appendix C.

Even for model electrodes, where electrode geometry and the area over which oxygen exchange takes place is well defined, large discrepancies between results obtained by different groups are observed. In a previous study we have discussed the importance of the thermal history of the sample for the measured oxygen exchange kinetics (Chapter 3): treatments at high temperature (T>800°C) activate perovskite samples (LSF and LSC), while at lower temperatures (T<700°C), the electrodes gradually passivate. We have shown that this activation/passivation phenomenon is reversible and correlates with changes in perovskite surface chemistry (Chapter 4).

Due to small size (and thus small overall surface area), thin film electrodes are particularly vulnerable to contamination which may also affect performance.[137] Also, the stability of the measured performance over time is not always addressed in papers on the topic. Another complicating factor in inferring materials properties form thin films and relating these to performance of technological electrodes is the observation that thin film electrodes sometimes behave very differently from bulk electrodes, even if the two are of the same composition. For instance, in studies by Mosleh *et al.* on $La_{0.6}Sr_{0.4}FeO_3$[143] and Plonzcak *et al.* on $La_{0.6}Sr_{0.4}Co_{0.2}Fe_{0.8}O_3$,[148] the performance of thin film electrodes was observed to be more than two orders of magnitude worse than what could be expected from bulk studies. On the other side, la O' *et al.*[153] reported up to 2 orders of magnitude faster oxygen exchange kinetics for $La_{0.8}Sr_{0.2}CoO_3$ relative to bulk .

This study focuses on the investigation of a specific MIEC material; $La_{0.6}Sr_{0.4}FeO_3$ (LSF) in the form of a "macroscopic" thin film electrode by electrochemical impedance spectroscopy. Albeit being a poorer electrocatalyst than Co-containing perovskites, LSF has relatively high catalytic activity towards ORR. It is stable in both oxidizing and reducing atmospheres,[33,154] it has a thermal expansion coefficient close to that of Ni/YSZ, and with respect to cost and ease of handling it is more preferable to its Co-containing analogues. Furthermore, the material has been the subject of thorough analyses of oxygen exchange kinetics on "bulk"-type samples by electrical conductivity relaxation (Chapters 3 and 4). Here, we will combine ECR and EIS studies on LSF thin films, and compare them to the ECR studies of bulk LSF samples prepared from the same starting powder.

5.2 Experimental

5.2.1 Preparation of PLD targets

PLD targets were prepared from commercial powders: $(La_{0.6}Sr_{0.4})_{0.99}FeO_{3-\delta}$ (Kusaka Rare Metal Products Co.Ltd., >99%) for LSF target and $Ce_{0.9}Gd_{0.1}O_{1.95}$ (Solvay S.A., >99%) for CGO target. The powders were pressed into pellets at 50 MPa in an uniaxial press and subsequently consolidated at 325 MPa in isostatic press. The LSF pellet was

then sintered at 1200°C for 4 hours, followed by 16 hours at 1150°C, while the CGO pellet was sintered at 1400°C for 4 hours, followed by additional 16 hours at 1150°C. The heating rate in both cases was 2°C/min and cooling rate was 1°C/min. After sintering, the targets were ground gradually with SiC sandpaper down to grit size 1000 and polished with diamond paste with particle size down to 1 µm which resulted in mirror-like smooth surfaces. The geometrical densities of the targets were above 95% of the theoretical density. Before the insertion in chamber, the targets are cleaned for 5 min in an ultrasound bath in acetone, ethanol, and deionized water, and dried in atmospheric air.

5.2.2 Preparation of counter electrode

The electrolytes were one-side polished, (100)-oriented, monocrystalline substrates of yttrium-stabilized zirconia (YSZ, 9.5 mol% Y_2O_3, CrysTec GmbH, Germany) with the size of 10 mm x 10 mm x 0.5 mm. Before the PLD deposition, a porous and 10 µm thick layer of platinum infiltrated with $Ce_{0.8}Pr_{0.2}O_{1.9}$ (CPO) was prepared on the "backside" of the single crystal to serve as counter electrode for the electrochemical measurement. First, a paste consisting of small platinum flakes (Alfa Aesar, >99.9%) was brush-painted on the non-polished side of the substrate and calcined at 900°C for 2 hours with ramp rate of 2°C/min during heating and cooling. The formed porous layer of platinum was then infiltrated twice with a drop of 3M solution of CPO (mixture of Ce- and Pr-nitrates in 80:20 ratio) mixed with 3 wt% of surfactant Triton X100. After each infiltration, samples were calcined for 1 hour at 300°C. CPO was infiltrated in order to increase the performance of the counter electrode to a level where its contribution to the total impedance of the cell is negligible.

5.2.3 Preparation of working electrode

The films were deposited on the polished surface using the KrF excimer laser (SURFACE Germany) of 248 nm wavelength and fluence of 2.4 J/cm^2 measured at the target. Substrate temperature during all depositions was kept constant at 600°C. A physical mask was used during the deposition which reduced the total electrode area to 66±2 mm^2 (Figure 5.1 (left)). First, a buffer layer of CGO was deposited with 9000 laser pulses in oxygen flow at a pressure of 0.001 mbar and pulse frequency of 5 Hz. On top of that, a layer of LSF was deposited with 100000 pulses in a flow of oxygen at 0.03 mbar and pulse frequency of 10 Hz. In total, 4 cells were prepared using the described procedure. The samples were cooled in the chamber under the same gas activity as applied during film deposition. After deposition, samples were kept in closed containers protecting the surface mechanically and from contamination, but containers were not gas-tight.

5.2.4 Electrochemical characterization

5.2.4.1 Impedance spectroscopy

Electrochemical impedance spectroscopy (EIS) was carried out in a rig made of alumina (Figure 5.1 (middle)). The electrodes were contacted by sandwiching the cells between two current collectors made of woven gold meshes (wire thickness 80 µm, aperture of 250 µm, purity >99.9%) wrapped around CGO pellets. A small mechanical force (≈10 kPa) was applied to ensure the contact. Before the test, all rig elements were acid-cleaned in concentrated HCl and deionized water. The cells were tested in dry O_2/N_2 gas mixtures with total flows of 5 l/h and pO_2 was varied in the range from 1 to 0.05 mbar. The realized oxygen activity was measured by a zirconia-based oxygen sensor placed on the exhaust pipe. Temperature was measured by a thermocouple placed close to the cell (within 2 mm). The impedance was measured at 48 different frequencies in the frequency range from 10^5 to 10^{-1} Hz with no DC current applied. A Solartron 1260 frequency response analyzer was used and the applied signal amplitude was 10 mV. Logging and parameter fitting was done by an in-house developed software Elchemea. The performance was first tested at 11 different temperatures from 387°C to 594°C. The reported values (k_{chem}, k_O, C_{chem} and R_{ORR}) are averages of three measurements at each temperature. After the temperature increase series the electrode performance was tested at different pO_2 from 1 to 0.05 bar at 491°C. Finally, the stability of the film performance at 491°C was tested over 60 hours in pure oxygen (pO_2=1 bar). After this step, the electrode was cooled down to room temperature in oxygen with a ramp rate of 3°C/min. The sample was hereafter removed from the rig and rinsed in deionized water for 5 min at 50°C. Subsequently the sample was reinserted in the rig, heated up to 491°C with a ramp rate of 2°C/min and the stability test continued for 20 days. The electrode was then subjected to another treatment in water and the stability test continued for another 14 days. The sketch of the experimental sequence can be found in the supplementary information (Figure 5.16).

5.2.4.2 Electrical conductivity relaxation

Another thin film LSF electrode prepared in the same way as described in section 5.2.3. was characterized by electrical conductivity relaxation (ECR). The electrode was connected to a four probe measurement setup with high-purity platinum wires (99.99%). The contacting was ensured by applying a small amount of platinum paste (Ferro, 99.2%). The ECR experiment was conducted in a sealed quartz-tube reactor of approximately 10 ml in volume. The total gas flow was kept constant at 5 ml/s and the change in conductivity was measured after imposing an abrupt change in pO_2 from 0.2 to 0.1 bar. Temperature was measured by a thermocouple placed 1 mm above the electrode surface, and pO_2 was measured by a tube zirconia sensor connected to the exhaust pipe. The relevant parameters were logged with sampling rate of 1 Hz. Fitting and parameter extraction was done in ECReX (Appendix A). The experimental setup for ECR of thin films is shown in Figure 5.1 (right).

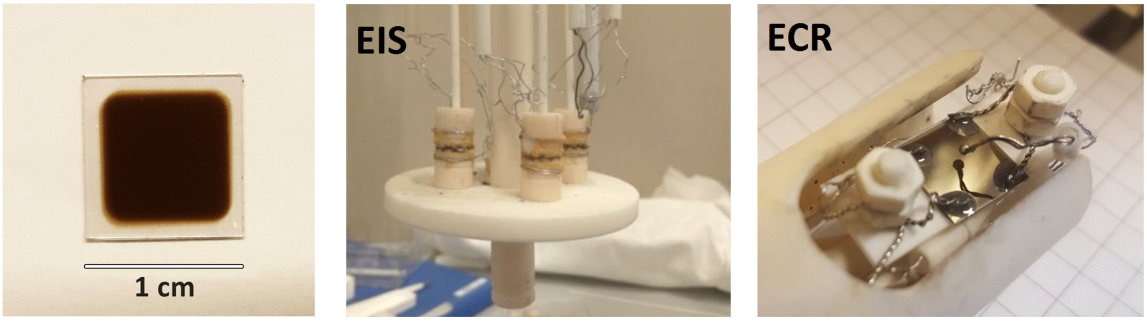

Figure 5.1: Left) Thin film electrode after PLD (only around 2/3 of the electrolyte area is covered due to a physical mask used during PLD); Middle) Experimental setup for electrochemical impedance spectroscopy (EIS). Most parts are alumina. The gold meshes (wrapped around CGO pellets) can be seen on all three sample holders; Right) Four probe setup for electrical conductivity relaxation (ECR) of thin films.

5.2.5 Additional electrode characterization

Crystallinity of the deposited thin films was analyzed by XRD using a Rigaku Smartlab. The electrode surfaces were also characterized by XPS using Physical Electronics Versaprobe II X-ray Photoelectron Spectrometer with monochromated Al Kα (1486.65 eV) X-ray radiation source equipped with charge neutralization system under a base pressure of 10^{-9} Torr. Survey scans and detailed scans focusing on the Sr 3d peak were taken immediately after the PLD ('as deposited electrode'), before the first rinsing ('aged electrode'), and after the long-term test which involved two treatments in water ('rinsed electrode'). The surface and cross section of the electrodes was also examined by scanning electron microscopy (SEM), Zeiss Merlin microscope. Film thickness was measured from cross section by SEM and with Dektak stylus profiler.

5.3 Results

5.3.1 Characterization of as deposited electrode

5.3.2 SEM and film thickness

After the deposition and before electrochemical testing thin film electrodes are examined by SEM and XRD. Figure 5.2 shows schematically the produced cells and SEM images of the surface and cross-sections of the working electrode (LSF + CGO buffer layer) and counter electrode (Pt infiltrated with CPO) before the test. The cross section is obtained by cracking the sample (Figure 5.2b). The two deposited layers are clearly distinguishable. The thickness of the CGO and the LSF layers determined from cross-sections of three cracked samples are 35±5 and 215±5 nm, respectively. Similar results

are obtained by thickness measurement with a Dektak stylus profiler (≈260 nm, Figure 5.2d). The obtained surface profile indicates that CGO buffer layer is buried in LSF (Figure 5.2e). The microstructure of the electrodes could not be clearly resolved, but the films appeared fully dense and flat. The surface of the deposited LSF film is uniform with no observable cracks or extended facets (Figure 5.2c). The image on the bottom shows the microstructure of the counter electrode. The thickness of the counter electrode is approximately 15 µm. A CPO layer is visible around the Pt backbone.

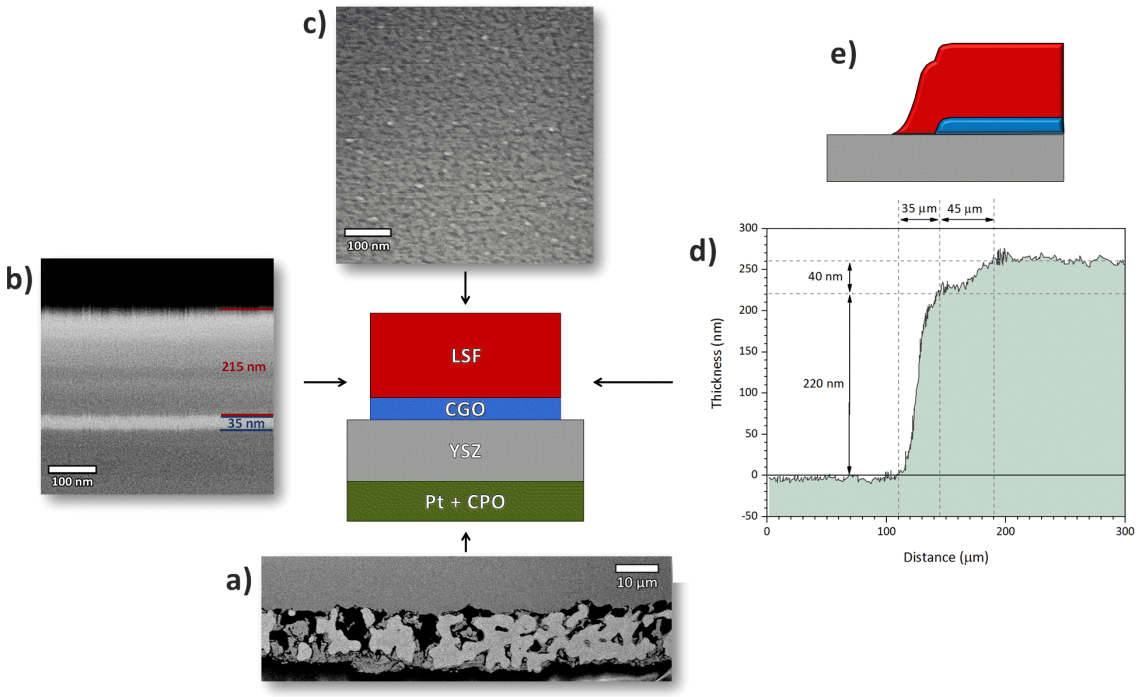

Figure 5.2: A sketch illustrating the half-cell consisting of thin LSF film with CGO buffer layer as working electrode, YSZ electrolyte, and CPO-infiltrated platinum serving as counter electrode. Adjacent are SEM images of the cross section of counter (a) and working electrodes (b) and LSF surface before the electrochemical testing (c). Plot on the right shows thickness measurement by a Dektak stylus profiler (d), as well as a sketch to help interpret Dektak measurements (e).

5.3.3 XRD of the as deposited LSF electrode

XRD diffractogram of the as deposited thin film electrode is shown in Figure 5.3. The observed peaks originate from (100)-oriented YSZ substrate and only specific crystallographic planes of the CGO buffer layer and LSF thin film. This is a strong indication of thin film texture due to preferential growth along (100) direction. The lattice parameters of YSZ and CGO are 5.12 and 5.42 Å, respectively, which gives a lattice mismatch of approximately 6%. Earlier, a and b unit cell parameters of bulk LSF were found to be 5.53 Å (See Figure 3.12), which is 2% larger than CGO. The deposited thin films are

thus expected to be under the compressive strain. Since both YSZ and CGO belong to the cubic $Fm-3m$ space group (Figure 5.3c,d) and due to a small lattice mismatch, the 'cube on cube' epitaxial growth can be expected in case of CGO film.[155] On the other hand, LSF ($La_{0.6}Sr_{0.4}FeO_3$) in bulk belongs to the rhombohedral $R-3ch$ space group (Figure 5.3b) at the experimental conditions used in this study. This space group is characterized by angle of 120°C between x and y axis. Therefore, instead on direct 'cube on cube', LSF is expected to grow with an offset of ½ of the unit cell.

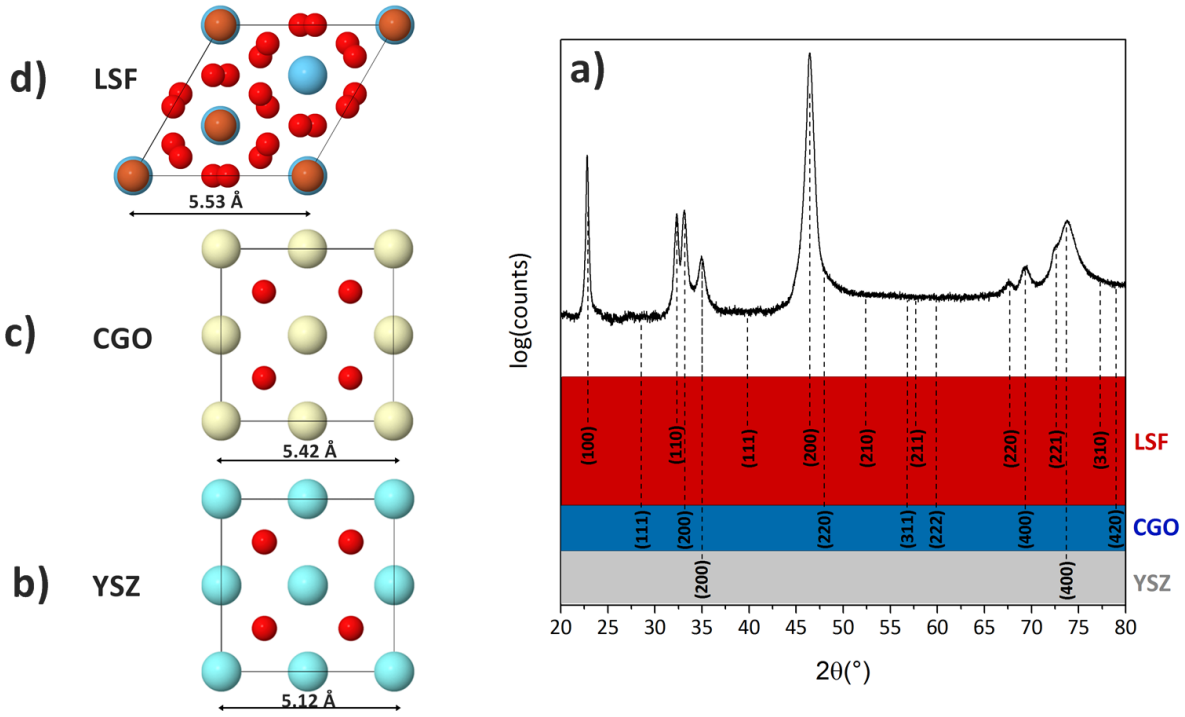

Figure 5.3: XRD diffractogram of the as deposited LSF thin film (a). Unit cells of LSF(b), CGO (c) and YSZ (d), projected along the z-axis.

5.3.4 Electrochemical characterization

5.3.4.1 Interpretation of impedance spectra

Electrochemical impedance spectroscopy enables the determination of many parameters relevant to the electrochemical performance of materials. A typical impedance spectrum obtained in this study is shown in Figure 5.4.

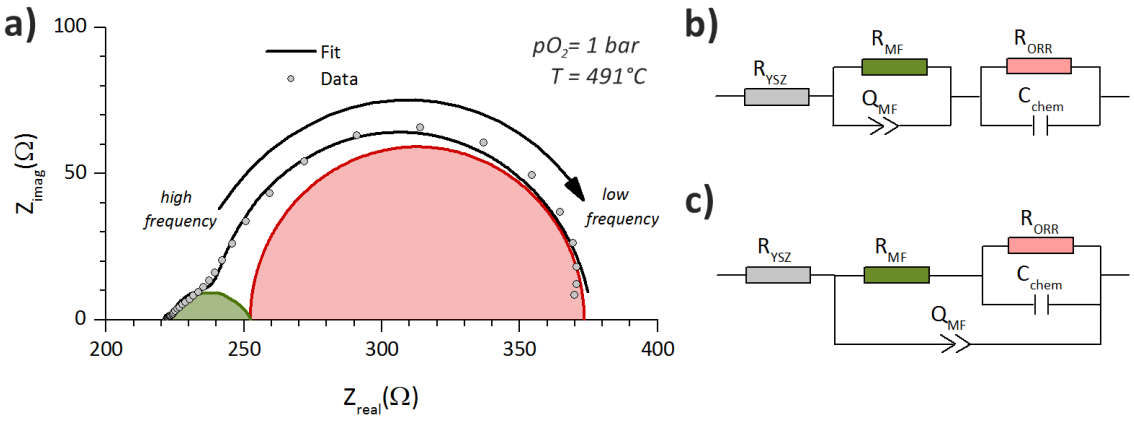

Figure 5.4: Nyquist plot of a typical impedance spectrum obtained in this study

As pointed out in the Experimental section, the impedance response is measured from high to low frequency in the range from 100 kHz to 0.1 Hz. There are three distinguishable features in the illustrated spectrum: a semicircle at low-frequencies (red), a depressed semicircle at mid-frequencies (green) and series resistance at high frequencies (spectrum intercept with Z_{real}-axis). The simplest equivalent circuit that is able to fit the experimental data is an R(RQ)(RC) circuit consisting of a resistor connected in series with a RQ and RC circuits. Here R stands for a resistor, Q for a constant phase element (CPE), and C for a capacitor. The equivalent circuit is mathematically equivalent to the R(Q(R(RC))) circuit used by Baumann *et al.*,[147] and therefore the spectra could equally well be fitted with the latter. The only difference between the two circuits is the physical interpretation of the CPE. Parametrization and the physical interpretation of the observed spectrum features are discussed below.

Low frequency process

At low frequencies, the spectrum can be simulated with a semicircle on a Nyquist plot (RC circuit). This is part of spectrum is commonly associated with surface resistance due to oxygen exchange reaction (R_{ORR}) connected in parallel with a capacitor. The capacitive part is usually associated with chemical capacitance (C_{chem}) related to oxygen stoichiometry changes in the bulk of the electrode.[147,156] Boukamp *et al.* have derived a general impedance model for dense MIEC electrodes under the assumptions of good electronic conductivity and small perturbations of electrical potential and obtained the following relations between R_{ORR} and C_{chem} and oxygen transport parameters; surface exchange coefficient (k_{chem}) and chemical diffusion coefficient (D_{chem}):[151]

$$R_{ORR} = Z_0 \left(\frac{1}{k_{chem}} + \frac{1}{D_{chem}} \right) \tag{5.3}$$

$$C_{chem} = \frac{1}{Z_0\left(\frac{1}{L} + \frac{K_{chem}}{D_{chem}}\right)} \tag{5.4}$$

where

$$Z_0 = \frac{RT}{n^2F^2AC_0} \cdot \gamma = \frac{RT}{8F^2AC_0} \cdot \frac{\partial \ln pO_2}{\partial C_o} \approx -\frac{RTV_M}{8F^2A}\frac{\partial \ln pO_2}{\partial \delta} \tag{5.5}$$

Here, R is universal gas constant, T is temperature, n is the charge of diffusing ion (-2 for oxygen), F is Faraday constant, A is surface area of the electrode, C_O is the concentration of oxygen ions in the lattice, a_O and pO_2 stand for activity and partial pressure of oxygen, V_M is the molar volume of the oxide, and γ is thermodynamic enhancement factor defined as:

$$\gamma = \frac{1}{2}\frac{\partial \ln(pO_2)}{\partial ln(C_0)} \tag{5.6}$$

Due to specific geometry of thin films and good ionic conductivity of LSF we can assume that after being incorporated at the electrodes surface, oxygen ions diffuse through the volume of the electrode instantaneously. When $D_{chem} \to \infty$ the Equations 5.3 and 5.4 simplify to:

$$R_{ORR} = \frac{RT}{n^2F^2AC_0} \cdot \gamma \cdot \frac{1}{k_{chem}} = \frac{RT}{n^2F^2AC_0} \cdot \frac{1}{k_0} \tag{5.7}$$

$$C_{chem} = \frac{n^2F^2ALC_0}{RT} \cdot \frac{1}{\gamma} \approx -\frac{8F^2}{RTV_M}\frac{\partial \delta}{\partial \ln pO_2} \tag{5.8}$$

The Equation 5.7 is usually used in the literature for calculation of k_0 from area specific resistance ($ASR = R_{ORR} \cdot A$). The impedance spectrum of thin MIEC electrode provides even more information. It is well known that time constant of a RC circuit (reciprocal value of summit frequency) can be expressed through:

$$\tau_{RC} = \frac{1}{2\pi f_{summit}} = R \cdot C \tag{5.9}$$

Therefore, time constant of oxygen exchange can be expressed in terms of R_{ORR} and C_{chem}:

$$\tau_{ORR} = R_{ORR} \cdot C_{chem} = \frac{L}{k_{chem}} \tag{5.10}$$

This equation enables the determination of k_{chem} when thickness is known. Furthermore, based on the known relation between k_O and k_{chem}:

$$\gamma = \frac{k_{chem}}{k_0} \tag{5.11}$$

We can use calculated k_0 and k_{chem} values for estimation of thermodynamic enhancement factor.

Medium frequency part

The depressed semicircle found in the mid-frequency range is simulated by a RQ circuit consisting of a resistor and a constant phase element (CPE) connected in parallel. The exponent of the constant phase element had values in range 0.7-0.85. Similar observations have been reported in many MIEC thin film electrodes. Baumann *et al.*[147] attributed this feature to the interfacial resistance and capacitance between electrode and the electrolyte. The resistive element is associated with the transfer of oxide ions between electrode and electrolyte.[147] A pseudocapacitance of the CPE element (CMF) is calculated using the following formula:

$$C_{MF} = (R_{MF}^{1-n} \cdot Q_{MF})^{1/n} \tag{5.12}$$

The calculated values were typically 4-8 times smaller than the capacitance associated with LSF layer (C_{chem}). Since chemical capacitance is an extensive quantity, this might be an indication that the C_{MF} is associated with the CGO buffer layer which is approximately 6 times thinner than LSF electrode.

High frequency part

At high frequencies, the imaginary part of impedance response approaches zero and the spectrum consists of series resistance only. This characteristic is also found to be independent of pO_2 and is therefore attributed to the resistance of the electrolyte (R_{YSZ}). In a study by Baumann *et al.*,[157] based on ∼300 measurements the authors have obtained an empirical relation for the ionic conductivity of 9.5 mol% Y_2O_3-doped ZrO_2 (the same material and the supplier as in this study):

$$\sigma_{YSZ} = 1000 \pm 100 exp\Big(\frac{-0.93 \pm 0.02eV}{kT}\Big)\Big[\frac{S}{cm}\Big] \tag{5.13}$$

Based on this equation we have estimated the resistance of a 0.5 cm thick (L_{YSZ}=0.5 cm) YSZ electrolyte with an area of A_{YSZ}= 1 cm^2 using the following relation:

$$R_{YSZ} = \frac{A_{YSZ}}{\sigma_{YSZ} \cdot L_{YSZ}} \tag{5.14}$$

In order to check whether the YSZ substrates we received had the same resistance, we measured the series resistance values obtained from a symmetrical cell made of 10 µm thick and screen-printed LSCF/CGO electrodes. The symmetrical cells with thick and well-conductive layers are used in order to ensure that the whole electrolyte volume is active and avoid possible problems with sheet resistance. It can be seen that resistance values obtained in this way match very well with the values calculated using the empirical equation by Baumann *et al.*[157](Figure 5.5).

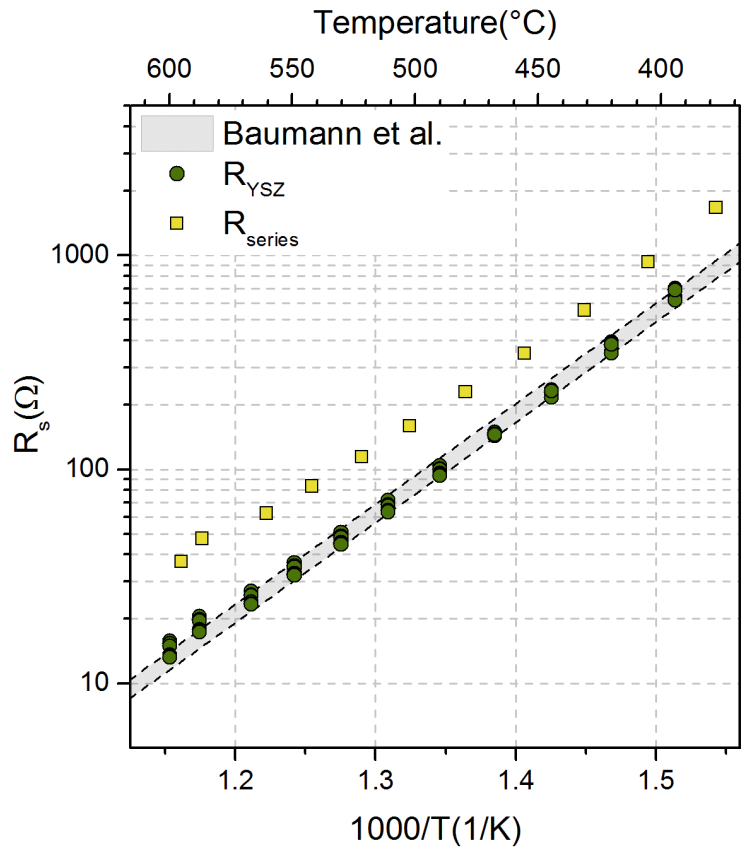

Figure 5.5: A comparison of the resistance values obtained from YSZ conductivity test in a symmetrical cell setup (R_{YSZ}) with two well performing composite electrodes and serial resistance associated with YSZ electrolyte obtained from thin film electrode test (R_{series}). The values calculated from the empirical equation given by Baumann *et al.*[157] are shown as well.

However, the values of the series resistance obtained from the half-cells with the thin film working electrode and Pt+CPO counter electrodes were always higher, while the apparent activation energy was similar and close to 0.9 eV. The observed high values can be a consequence of a reduced active area (volume) of the electrolyte. This may be a consequence of (a) partial contact at the working electrode due to misalignment, (b) lack of mechanical contact between the auxiliary gold mesh and the working electrode , (c) "long" distance between contact points at the working electrode (on the length-scale of the working electrode thickness) which may result in a significant contribution of sheet resistance (Figure 5.6).

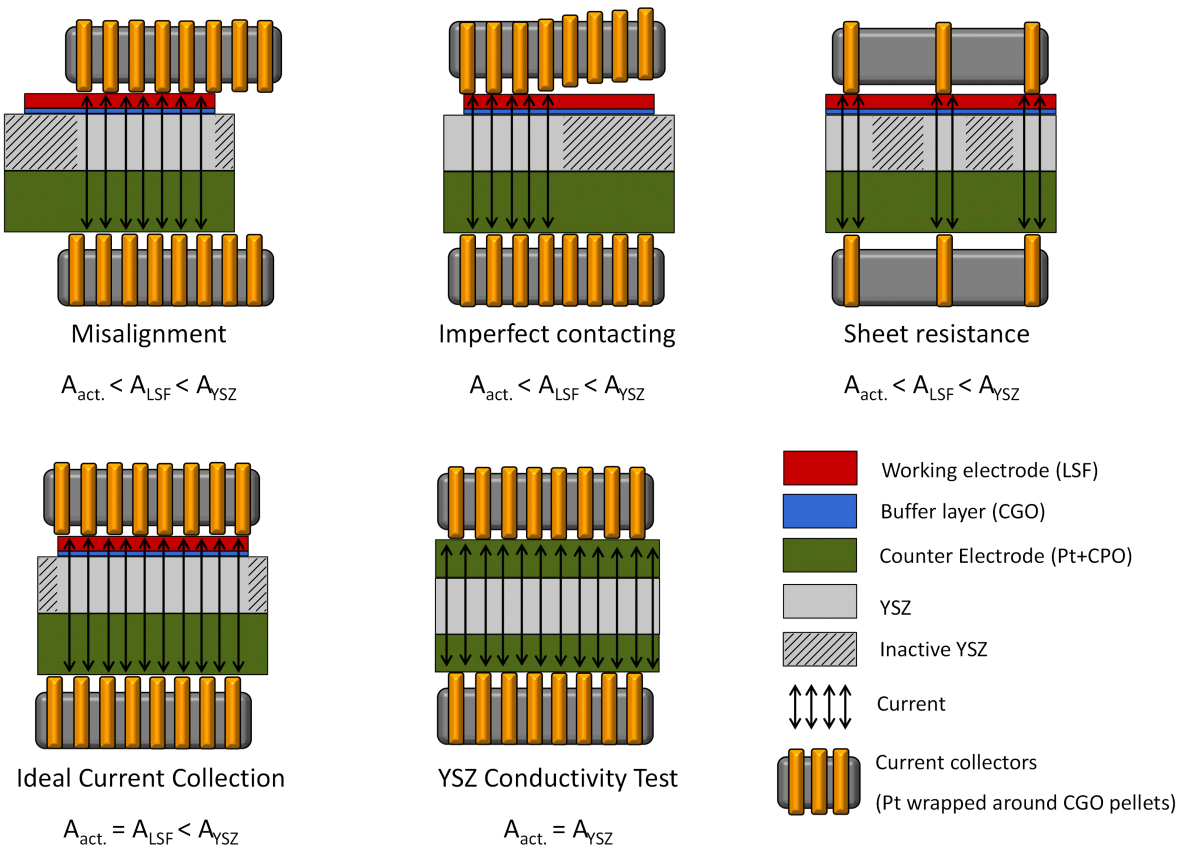

Figure 5.6: Possible reasons for reduced active area of the electrolyte and the schematic description of YSZ conductivity measurement by a LSCF/CGO||YSZ||LSCF/CGO symmetrical cell.

The first two types of imperfections are the result of the particular experimental setup with sandwiched cells. The cell can be misaligned with regards to the current collectors. This renders parts of the electrode and electrolyte inactive. The second problem arises when such setup is used for testing of thin film electrodes. Current collectors consisting of woven gold (prone to deformation by creep) might not establish the perfect contact with the flat thin film surface. Further, some parts of electrode and the underlying electrolyte can be inactive due to sheet resistance.[149,152] This effect is aggravated in case of thinner electrodes, faster surface reaction and low electrical conductance of the working electrode (either due to cracks/porosities or low material conductivity). Even in the case of perfect contacting with LSF electrode ($A_{act} = A_{LSF}$), the active volume of electrolyte will be reduced since the films are deposited only on approximately 2/3 of the electrolyte cross section ($A_{YSZ} = 1$ cm^2).[158] In the case of the symmetrical cell, thick and well conducting layers ensure that current is spread all across the electrolyte surface even if the contacting of mesh to electrode is not perfect. Following this line of argumentation, we can use the difference in measured series resistance for estimation of

the active area for the case of the working electrode and subsequent normalization of the impedance response:

$$A_{act} \cdot R_{series} = A_{YSZ} \cdot R_{YSZ} \rightarrow A_{act} = \frac{R_{YSZ}}{R_{series}}(cm^2) \tag{5.15}$$

Figure 5.7 illustrates the differences between electrolyte area (A_{YSZ}), electrode area (A_{LSF}), and active area (A_{act}) calculated using the equation 5.15. Estimation of the active area of non-modified LSF electrode shows that approximately ½ of the total electrode area is active. Interestingly, active area appears to pass through a maximum at ≈425°C and seems to decrease with the increasing temperature which resembles temperature dependence of LSF conductivity (see Figure 3.1). This may indicate that higher electrical conductivity at lower temperatures can partially compensate for some of the flaws presented in Figure 5.7.

It should be noted that this "effective area correction" is not an accurate account of the effects of imperfect contact at the working electrode on the deduced polarization resistance (or k values) but the "corrected" values are likely closer to the real ones than if neglecting these effects. In other words; corrected values may be considered a lower bound whereas the uncorrected values for sure represent an upper bound.

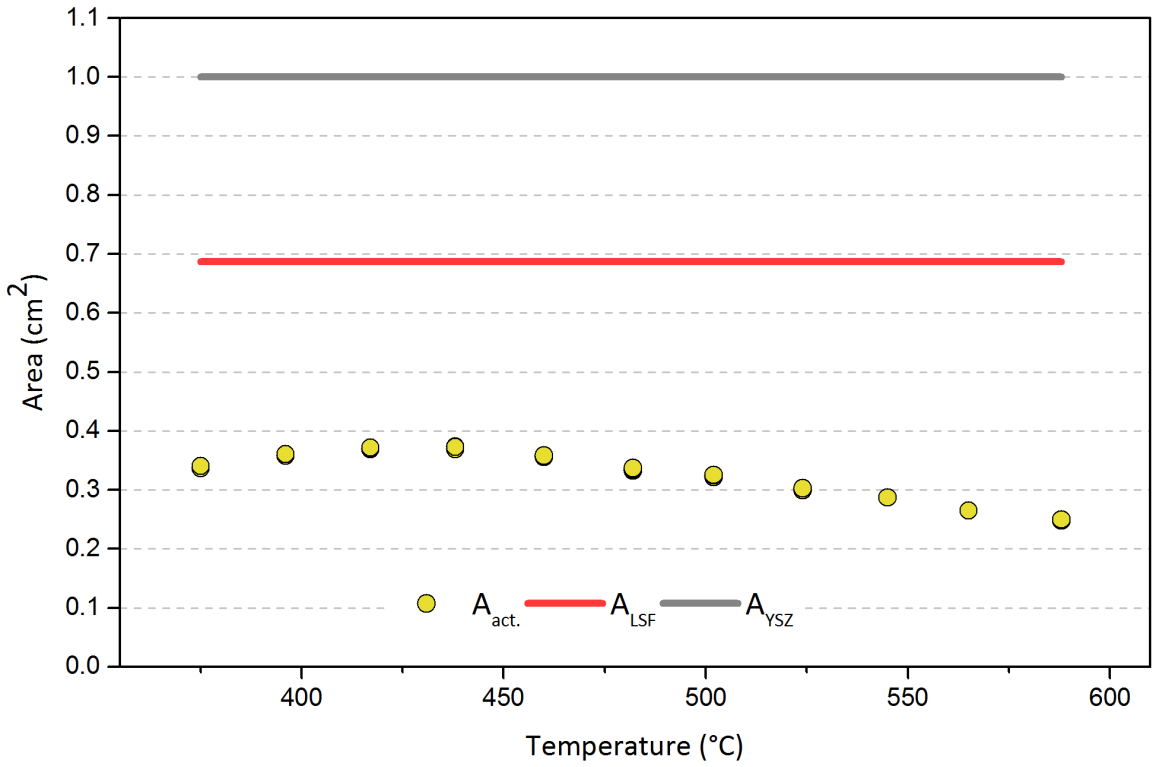

Figure 5.7: Estimation of the active electrode area (A_{act}) calculated as R_{series}/R_{YSZ} and comparison with electrolyte area (A_{YSZ}) and electrode area (A_{LSF}).

5.3.4.2 Parameters investigation

Low-frequency polarization resistance

The area specific resistances measured during the first heating run are shown in Figure 5.8 along with results for several other model electrodes from the literature. The area specific resistance is calculated with ($ASR_{norm} = R_{ORR} \cdot A_{act}$) and without area normalization ($ASR = R_{ORR} \cdot A_{LSF}$). Since $A_{LSF}/A_{act} \approx 2$, the difference between the calculated ASR values is $ASR/ASR_{norm} \approx 2$. The apparent activation energy was found to be 1.45±0.03 eV (≈140 kJ/mol). After 60 hours at 491°C, ASR increases 37x (indicated by an arrow). Inspection of the literature values from several thin film studies reveals that results fall in three groups which do not seem to depend on the composition of the thin film electrode. The ASR obtained in this study follows a similar trend as $Ba_{0.5}Sr_{0.5}Co_{0.2}Fe_{0.8}O_3$ (Baumann *et al.*[157]), $La_{0.6}Sr_{0.4}CoO_3$ (Adler *et al.*[159] and Januschewsky *et al.*[160]), $La_{0.6}Sr_{0.4}Co_{0.2}Fe_{0.8}O_3$ (Darbandi *et al.*[161]), and the behavior of vertically aligned nanocomposite of Ruddlesden-Popper/perovskite $LaSrCoO_4/La_{0.8}Sr_{0.2}CoO_3$ reported by Ma *et al.*[28] The best performance of any thin film electrode was measured by Crumlin *et al.*[21] for $La_{0.8}Sr_{0.2}CoO_3$ electrode modified with small amount of $LaSrCoO_4$. The observed fast kinetics in that study was attributed to the presence of fast Ruddlesden-Popper/perovskite interfaces. The same phenomenon is credited for fast kinetics in case of $La_{0.6}Sr_{0.4}CoO_3$ reported by Hayd *et al.*,[24] though here the electrode is not fully dense (meaning that $A_{act} > A_{geom.}$). On the other hand, ASR values reported by Plonczak *et al.*[148] for $La_{0.6}Sr_{0.4}Co_{0.2}Fe_{0.8}O_3$ and by Baumann *et al.*[157] for $La_{0.6}Sr_{0.4}FeO_3$ were 2-3 order of magnitude higher than in the present study. In case of Plonczak *et al.*[148] the high values of ASR are likely a consequence of the use of a platinum paste for current collection. The paste has later been shown to be detrimental for oxygen exchange kinetics,[137] likely due to the presence of impurities in the paste, which when applied on top a high surface area porous electrode ($A_{act} \gg A_{geom.}$) can be tolerated,[162] but is detrimental when $A_{act} \sim A_{geom.}$). Furthermore, the ASR values reported by Plonzcak *et al.*[148] refer to the electrode performance after aging at 750°C for 42h which this was done to ensure reproducibility (the performance, albeit reduced is more stable after aging).

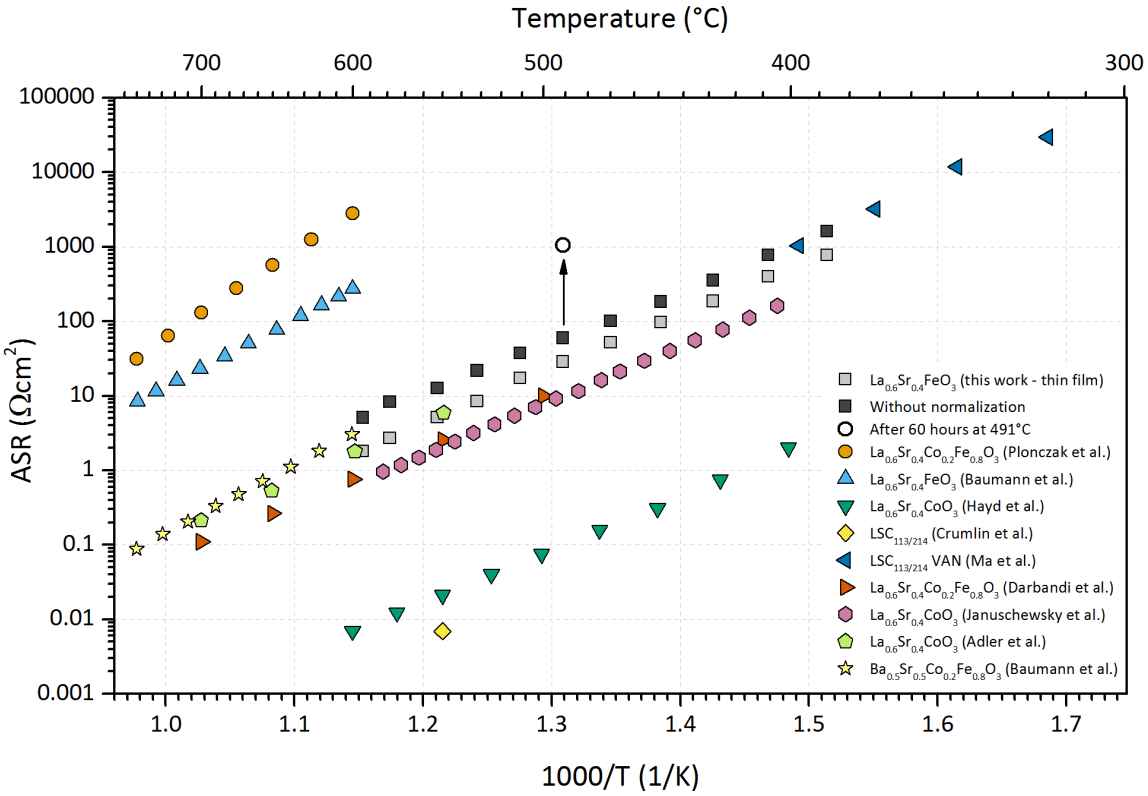

Figure 5.8: Temperature dependence of area specific resistances calculated with ($ASR_{norm} = R_{ORR} \cdot A_{act}$) and without normalization ($ASR = R_{ORR} \cdot A_{LSF}$) and the selected literature values.[21,24,28,148,157,159–161] Arrow indicates the change in ASR observed after 60 hours at 491°C.

Chemical capacitance

The results of temperature-dependence and pO_2-dependence of chemical capacitance are shown in Figure 5.9. The apparent chemical capacitance are normalized to the active volume ($A_{act} \cdot L$). The obtained values were between 1000 and 1150 F/cm^3 and similar to values reported previously in the literature for perovskite thin films.[147,148] It can be seen that chemical capacitance is only mildly dependent on temperature in the experimental range of this study. Since chemical capacitance is related to changes in electrode stoichiometry (formation of oxygen vacancies),[147,156,163] relative insensitivity to temperature of C_{chem} can be explained in terms of very small defect concentration changes in $La_{0.6}Sr_{0.4}FeO_3$ below 600°C and in pure oxygen.[99] Pseudocapacitances of the CPE calculated using Equation 5.12 are shown for comparison. The chemical capacitance measured at 491°C shows an increase with decreasing pO_2 (see Figure 5.9). The slope of linear fit through the measurement points was found to be $7.85 \cdot 10^{-3}$. The increase in C_{chem} with the decreasing pO_2 can also be interpreted via the formation of small amount of oxygen vacancies at low pO_2.

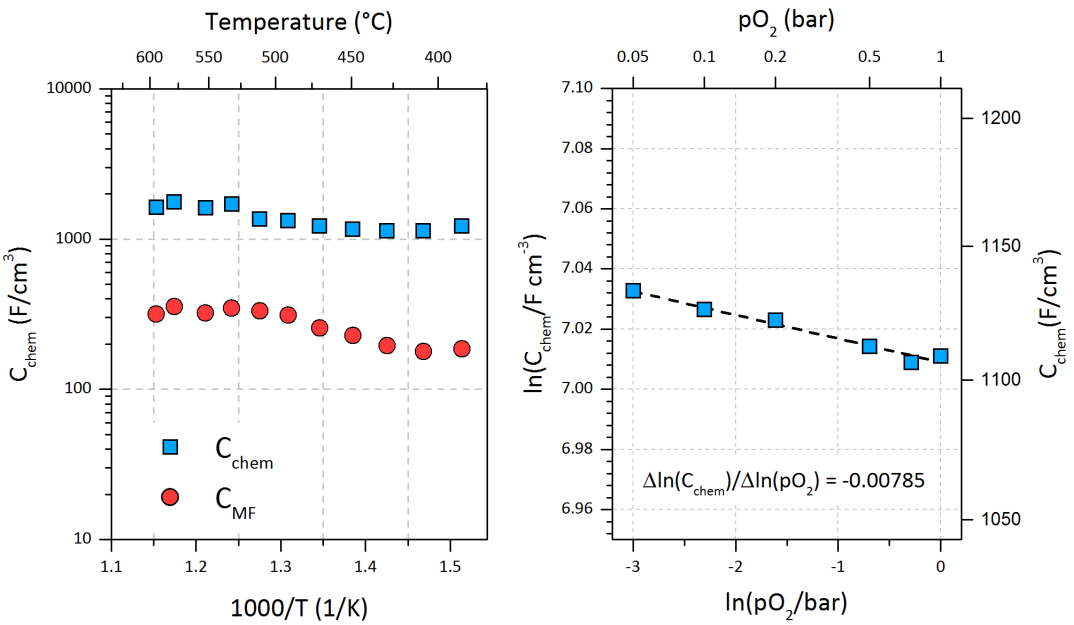

Figure 5.9: Left) chemical capacitance of the low frequency semicircle (C_{chem}) and pseudocapacitance of the constant phase element (Q_{MF}) at different temperatures in oxygen; Right) pO_2-dependence of C_{chem} at 491°C.

Oxygen exchange coefficients

Oxygen exchange coefficients are calculated using the Eq. 5.10 for k_{chem} and equation 5.7 for k_O. Oxygen exchange values at different temperature and pO_2 are shown in Figure 5.10. Both k_{chem} and k_O are found to be strongly temperature-dependent with activation energy of 146.6 kJ/mol in case of k_O and 129.4 kJ/mol in case of k_{chem}. The partial pressure of oxygen also affects the oxygen exchange coefficients. The observed pO_2 dependence can be well described by a power law relation ($k \sim pO_2^n$), which in log-log plot shown in Figure 5.10 gives a straight line. The exponent n is in both cases found to be close to ½, which may indicate that the rate determining step involves dissociation of oxygen molecules.[143] Based on the calculated k_{chem} and k_O values, the thermodynamic enhancement factor (γ) is calculated using Eq. 5.11. The values varied from 45-95 over the tested temperature range, while at different pO_2 at 491°C γ remained constant and close to ≈80.

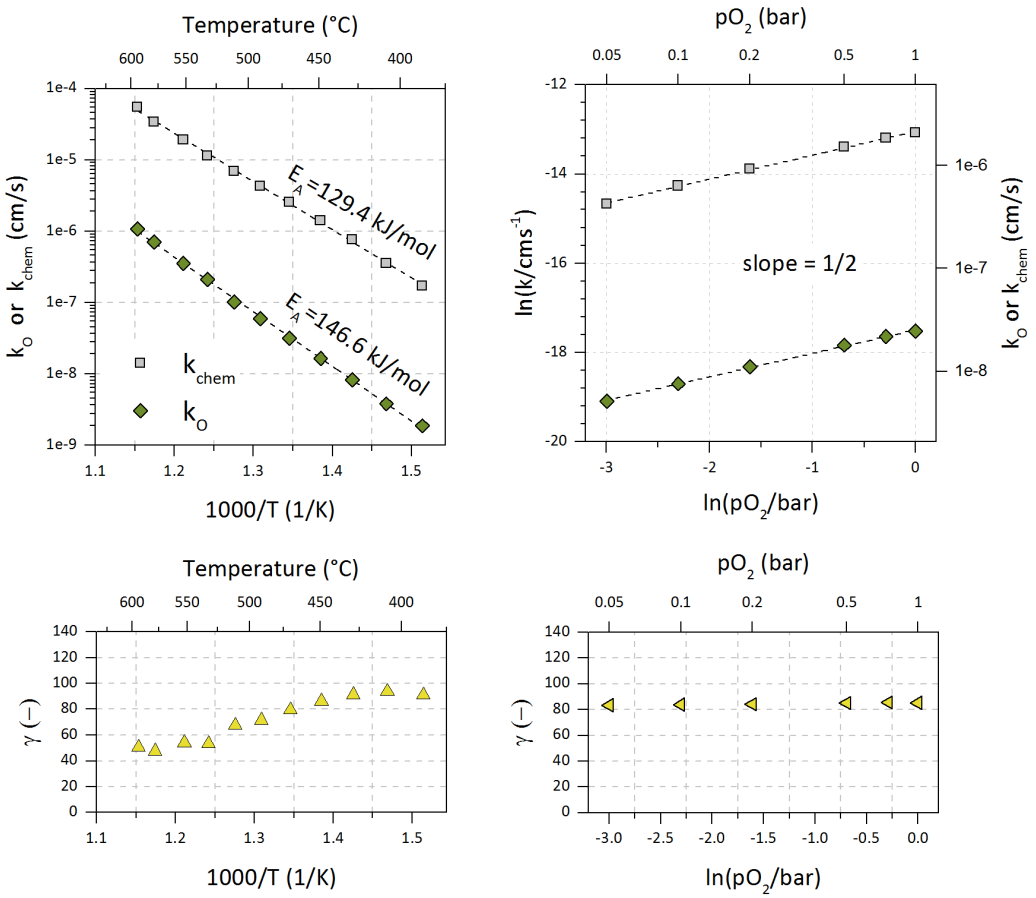

Figure 5.10: Top) Values of oxygen exchange coefficients (k_{chem} and k_O) at different temperatures and (left) and pO_2 (right). Values of thermodynamic enhancement factor calculated by dividing k_{chem} with k_O are shown at the bottom.

The oxygen exchange kinetics of the prepared thin film electrodes was also measured by electrical conductivity relaxation (ECR). Due to thin film geometry and surface-controlled kinetics we can use the following equation for calculating k_{chem}:

$$\frac{\sigma(t) - \sigma_\infty}{\sigma_0 - \sigma_\infty} = exp\left(\frac{-k_{chem} \cdot t}{L}\right) \tag{5.16}$$

where σ, σ_0, and σ_{inf} stand for electrical conductivity at the time t and L is film thickness. A comparison between ECR-measured k_{chem} values and the ones calculated using the equation 5.10 can be found in Figure 5.11. ECR analysis in the ideal case requires instantaneous pO_2 change. This requirement can be fulfilled when the time needed for flushing the reactor is more than 20 times smaller than the time constant of the measured process.[19] Due to small volume, thin film electrodes equilibrate very fast, which needs to be compensated either by short flushing time (high gas flow rates, small reactor volume) or by performing measurements in an experimental region where the reaction kinetics are slower (low temperature and pO_2). Since there were practical limitations to the former, the ECR analysis could be performed only below 430°C and

in lower pO_2. Therefore, in contrast to the EIS study, ECR-derived k_{chem} values were obtained at pO_2=0.1 bar (end pO_2). Therefore, it can be concluded that the k_{chem} values obtained by two different techniques match reasonably well, when difference in pO_2 is taken into account.

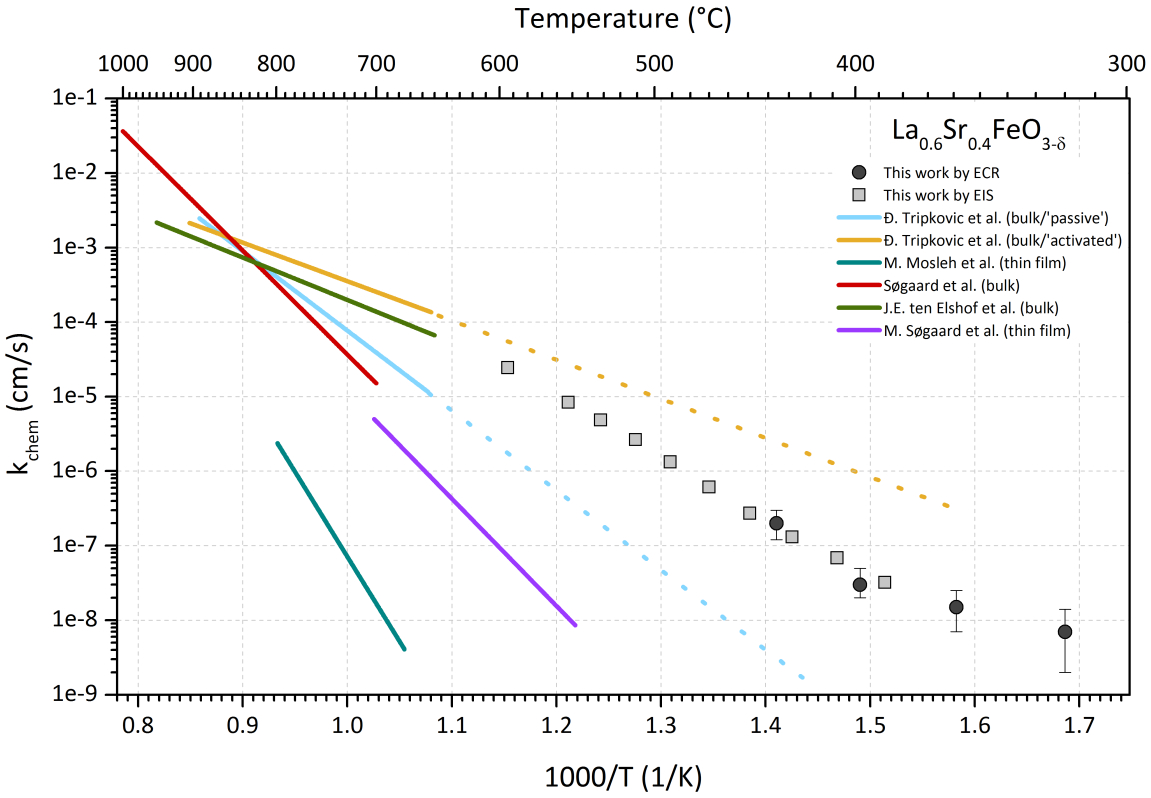

Figure 5.11: Comparison of oxygen exchange coefficient (k_{chem}) values obtained in this study by impedance spectroscopy (using Eq. 5.10) and by electrical conductivity relaxation (Eq. 5.16) with the literature.[32,33,35,143] 'Active' and 'passive' state refers to findings from the earlier study on bulk LSF by ECR (Chapters 3 and 4). Dotted parts are extrapolations to lower temperatures.

Literature values obtained on thin film and bulk electrodes of the same composition are shown as well. A large part of the scatter between the literature values can be ascribed to different thermal history, which has been discussed in a previous study carried out on bulk-type samples (Chapter 3). In that study, it was shown that k_{chem} values can vary greatly (more than a factor of 60 at 650 C) and in a reproducible manner depending on the thermal history of the sample. The strong effect seemed correlated to the formation of inactive Sr-phases on the sample surface (Chapter 4). Figure 5.11 shows the k_{chem} trends (and extrapolations to lower temperatures) associated with the 'activated' and 'passive' state of LSF found in Chapters 3 and 4. The k_{chem} values obtained in this study (in the initial heating run) for thin film electrodes lie close to the extrapolated values of the 'activated' state found in bulk LSF. After aging at 491°C for 15 days the thin film electrode deteriorates and the k_{chem} value drops more than two orders

of magnitude. Remarkably, the new k_{chem} value lies close to the values extrapolated from 'passive' state. Hence, a similar type of passivation, likely ascribable to the same phenomenon, also takes place in the thin film electrodes.

In the discussed bulk studies (Chapters 3 and 4) it was also shown that the samples could be reversibly cycled between the two states by a high temperature thermal treatment, which was observed also to lead to a dissolution (or disapearence) of the Sr-rich phase that impedes surface exchange and reconstruction of an active perovskite or perovskite-like surface.

Assuming that a similar degradation mechanism is taking place in the thin film electrodes, and inspired by work of Rupp *et al.*,[128,164] we attempted to recover the initial performance by dissolving the anticipated passivating Sr-rich layer in deionized water (Figure 5.12). After aging for 3 days in oxygen at 491°C, k_{chem} decreased to $1.7{\cdot}10^{-7}$ cm/s. The sample was cooled down to room temperature and immersed in deionized water for 5 min at 50°C. Upon heating up, the measured k_{chem} was $1.2{\cdot}10^{-6}$ cm/s (≈7x higher than before the treatment). The sample was then aged for 7 days, during which k_{chem} decreased again, reaching $\approx 1.2{\cdot}10^{-8}$ cm/s (100x lower than originally). Further aging for 10 days did not lead to any further deterioration indicating that the electrode is fully passivated, but retains a certain oxygen exchange activity. A second rinsing cycle led to k_{chem} values identical to the values after the first rinsing. In addition, after the second rinsing the deterioration was much slower, and after aging for 10 days, k_{chem} had decreased from $1.2{\cdot}10^{-6}$ cm/s to $0.8{\cdot}10^{-6}$ cm/s (only ≈30%).

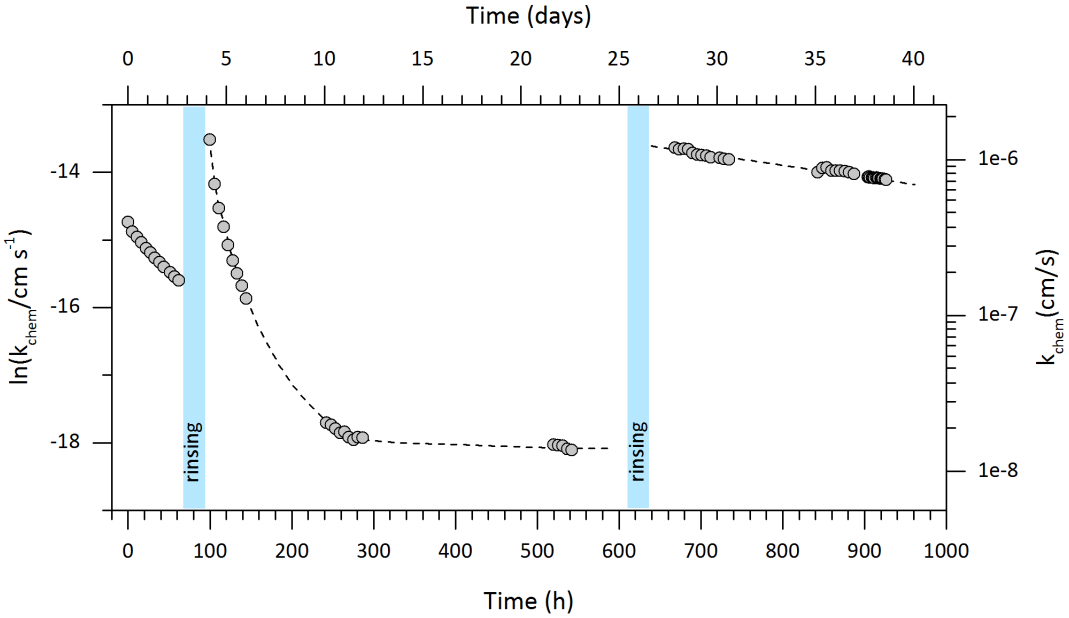

Figure 5.12: Long-term stability at 491°C of non-modified LSF thin film electrode expressed through change in k_{chem} over time. The blue regions indicate the time when the rinsing in deionized water for 5 min at 50°C is performed but also account for time needed for cool-down/heat-up of the rig.

5.3.5 Surface chemistry

The chemical composition of the sample surface was investigated by XPS. Results are shown in Figures 5.13 and 5.14. The spectra are taken at different points in time during the experiment (Figure 5.16). The electrode was analyzed immediately after the PLD deposition ('as deposited electrode'), just before the first rinsing ('aged electrode'), and finally after the whole long-term test and two treatments in water ('rinsed electrode'). Survey spectra (Figure 5.13) show presence of the expected elements; La, Sr, Fe, and O from the electrode and C which inevitably forms when samples are exposed to atmospheric air (Section 4.3.3). No significant differences could be observed based on the survey spectra. This indicates that the degradation is not a consequence of poisoning with some detrimental elements such as chromium, sulfur, or silicon.

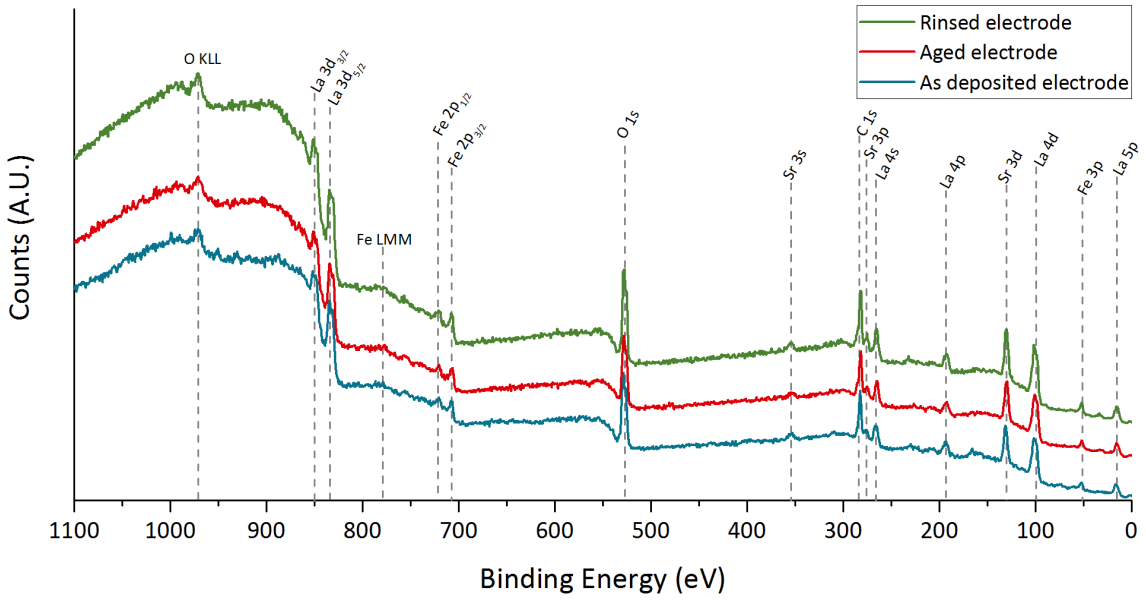

Figure 5.13: XPS survey spectra of LSF thin film electrode taken at different points during the experiment. 'As deposited electrode' refer to the scan immediately after PLD, 'Aged electrode' is the scan taken before the first rinsing, and 'Rinsed electrode' is the scan taken after the long-term test which involved two treatments in water.

In addition to the survey spectra, detailed scans of the Sr 3*d* peak were taken in order to further investigate the origin of electrode degradation (Figure 5.14). Due to orbital splitting, Sr 3*d* peak comes in pairs of Sr $3d_{5/2}$ and Sr $3d_{3/2}$ peaks with the area ratio between them of 3:2 and a fixed energy separation of 1.7 eV. The observed Sr 3*d* peaks could be fitted with two such doublets, labeled here as 'high energy Sr' and 'low energy Sr'. Such a distinction between two states of Sr has also been observed in many other studies[123,134,138,139] of Sr-containing perovskite films. The high energy component is usually suggested to be associated with Sr in form of secondary phases or in the outermost layers of the perovskite surface, while low energy component is

related to strontium in the perovskite lattice. For these reasons, the two components are sometimes designated as 'surface Sr' and 'lattice Sr'.

Immediately after the PLD deposition there are identical amounts of high and low energy Sr (Figure 5.14 (left)). The relative content of high energy component increases to 54% after aging (Figure 5.14 (middle)). In contrast, there is much less high energy component (only 22%) in the rinsed electrode (Figure 5.14 (right)).

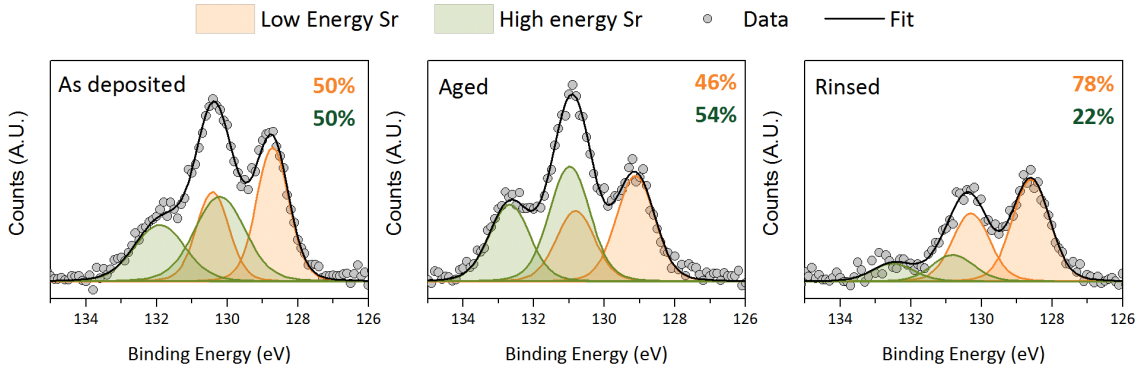

Figure 5.14: Detailed XPS scans of Sr 3*d* peak of LSF thin film electrode taken at different points in the experiment (See Figure 5.16). (Left) The as deposited thin film electrode had identical amounts of high and low energy Sr, similar to 'activated' state found in Chapters 3 and 4. (Middle) A slightly higher amount of high-energy Sr was found on the surface after aging, which was accompanied with loss in performance. (Right) Rinsed electrodes which had high oxygen exchange activity and stability had also much less high energy Sr (22%).

5.4 Discussion

Loss of oxygen exchange activity of perovskite electrodes is widely reported and has in many studies been ascribed Sr segregation.[40,54,128,165] In our previous study on bulk LSF electrodes, we have observed the correlation between the oxygen exchange performance and the two states of Sr on the surface (Chapter 4). There, the samples with fast oxygen exchange kinetics ('activated' state) had almost the same amounts of high and low energy Sr components. After prolonged aging, k_{chem} values decreased to some finite and lower values which was accompanied with an increase in high energy Sr component to ≈60% ('passive' state). A similar correlation between the increase in high energy Sr component and loss of oxygen exchange activity was also found in $La_{0.6}Sr_{0.4}CoO_3$ electrodes.[54]

The same degradation mechanism seems to be responsible for performance loss of thin film electrode in the present study. There is a clear analogy to the transition from 'activated' to 'passive' state found in bulk electrodes. Here, as deposited electrode starts with identical amounts of high and low energy Sr and high oxygen exchange coefficients. Performance then gradually diminishes during the thermal treatment which is accompanied with an increase in relative content of high energy Sr to 54%.

Another similarity with bulk electrodes is the ability to recover the performance after the electrode reaches the passive state. In the bulk electrodes (Chapters 3 and 4), this was accomplished by a thermal treatment at 1000°C which causes the secondary phases to re-dissolve in the perovskite (or first to decompose and remaining Sr to re-disolve). Here, instead of dissolution in perovskite lattice, the recovery of the oxygen exchange activity is accomplished by dissolving the Sr-rich phases in water as was previously shown in the studies by Rupp *et al.*[128,129] This reasoning is supported by XPS results where a very small relative content of high energy strontium was found in the rinsed electrode (only 22%). Such low amount of high energy Sr is even more remarkable knowing that the electrode had spent additional 2 weeks at 491°C after rinsing.

Following this line of thought, we can also explain the slower degradation rates observed after the second rinsing. A certain amount of strontium gets permanently removed from the electrode with each treatment in water, which also depletes the total amount of strontium due to small electrode volume. Eventually, this can cause less driving force for Sr segregation. The energy penalty in forming additional A-site vacancies in the bulk of the thin film electrode (as a consequence of the leaching of the Sr), reduces the energy gain by further "Sr-exolution" at the surface. A sketch of the proposed mechanism is shown in Figure 5.15.

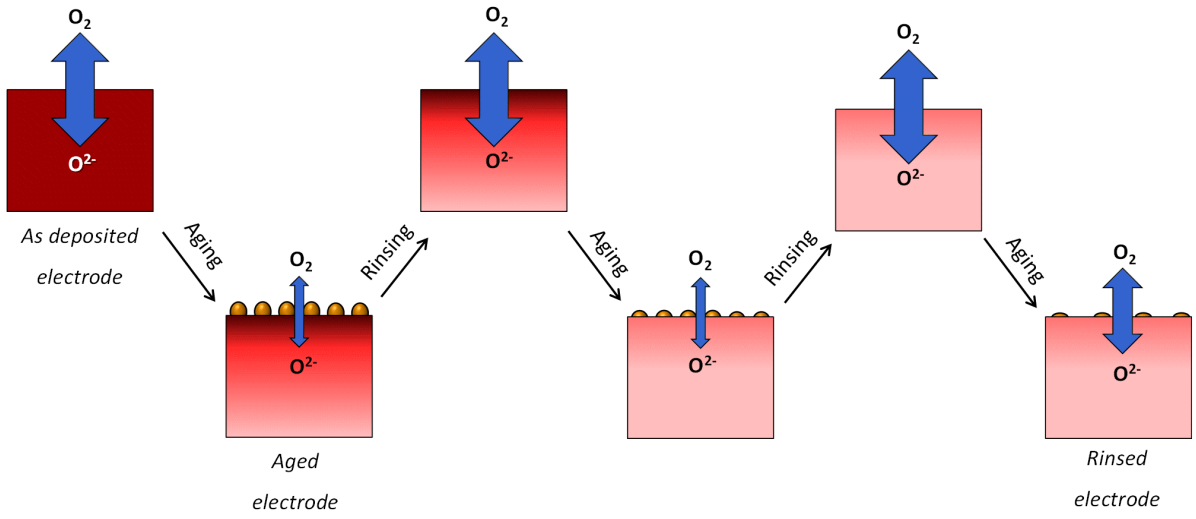

Figure 5.15: An illustration of the proposed degradation and reactivation mechanisms. During aging, strontium segregated to the surface and builds detrimental secondary phases. These phases are removed from the surface by rinsing in water, while the total amount of Sr in electrode gets depleted. After second rinsing, Sr amount in electrode is so much depleted that the driving force for Sr-segregation gets smaller which is then observed as slower degradation rate.

An important implication of these results is that earlier observed 'active' and 'passive' states exist also in thin film electrodes and at temperatures below 600°C. The two states have much different oxygen exchange activities and the transition between them is

reversible and depends on sample processing (thermal treatment, rinsing in water/acids). Since the 'passive' state is characterized by more stable, albeit low oxygen exchange activity, some studies have used the aged electrodes as a the more reliable measure of oxygen exchange activity (e.g. Plonczak *et al.*[148]). On the other hand, in many other studies the reported values refer to 'fresh' electrodes measured shortly after the electrodes are heated to elevated temperatures, corresponding to what we here refer to as 'activated' state. Gradual transition from one state to another further contributes to differences reported by different groups, but also between bulk and thin film electrodes. Therefore, when assessing the performance of perovskite electrode both in thin film and in bulk, special attention should be given to the processing history of the sample.

5.5 Conclusion

The performance of thin LSF electrodes was analyzed between 387° and 594°C and in pO_2 range from 1 to 0.05 bar. Area specific resistance was found to be strongly temperature-dependent with apparent activation energy of ≈140 kJ/mol. Chemical capacitance was only mildly temperature- and pO_2-dependent and in range from 1000 to 1200 F/cm^3. The activation energy for oxygen exchange coefficients k_O and k_{chem} was found to be ≈147 kJ/mol and ≈130 kJ/mol, respectively. Oxygen exchange coefficient values increased with the increasing pO_2 following a power-law relationship $k \sim pO_2^n$. The exponent n was found to be close to ½ suggesting oxygen dissociation as a possible rate determining step. Based on calculated k_{chem} and k_O values, thermodynamic enhancement coefficient is estimated to be in the range from 50 to 100. Oxygen exchange activity varied throughout the experiment. Initially a high oxygen exchange activity ($k_{chem} = 6 \cdot 10^{-6}$ cm/s at 491°C) was found, which gradually decreased over time with a degradation rate of ≈40%/day and eventually reaches $k_{chem} = 1.2 \cdot 10^{-8}$ cm/s at 491°C. Once passivated, the electrode could be reactivated by treatment in water for 5 min at 50°C which, after two rinsing steps, also slows down the degradation rate to ≈5%/day. The effect is ascribed to dissolution of a detrimental Sr-rich secondary phases formed on the sample surface, which was confirmed by XPS analysis (high energy Sr component is much smaller in rinsed electrode). The results suggest that two different states of the perovskite surface;'activated' and 'passive', can be found in also in thin film electrodes. This may explain the observed differences in measured performance of thin films by different groups, and also account for differences between bulk and thin film electrodes.

Supplementary Information

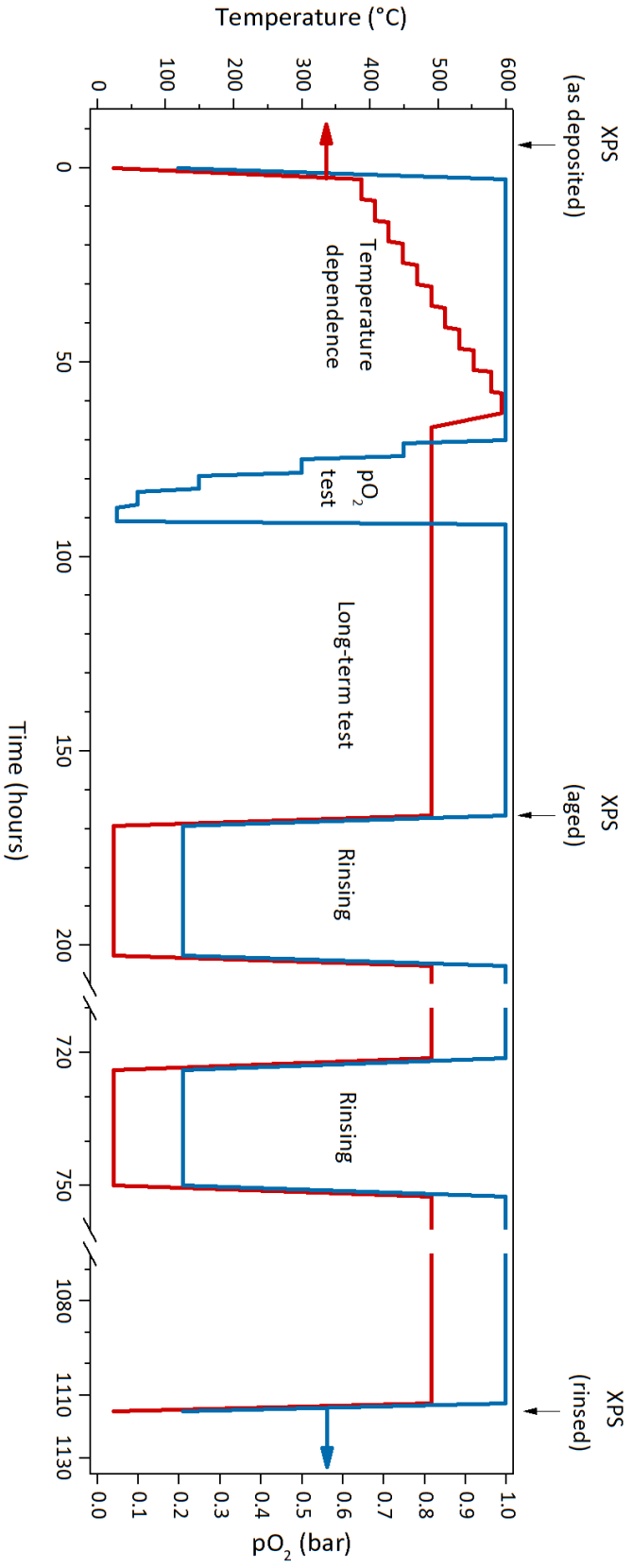

Figure 5.16: Sketch of experimental sequence.

CHAPTER 6

Effects of surface modifications on performance of $La_{0.6}Sr_{0.4}FeO_3$ thin film electrodes

Abstract

The surface of PLD-deposited $La_{0.6}Sr_{0.4}FeO_3$ thin film electrodes was modified by nanoparticulate decoration achieved via addition of nitrate solutions of Sr^{2+}, Fe^{3+}, Ce^{3+}, Gd^{3+}, Ba^{2+}, and Zr^{4+}. The effect on oxygen exchange was assessed by impedance spectroscopy between 387°C and 594°C in the pO_2 range from 0.05 – 1 bar. The stability of the performance of the decorated surfaces was tracked over 60 hours. The electrodes were further investigated by X-ray photoelectron spectroscopy (XPS), scanning electron microscopy (SEM), and profilometry. Promising results are found for Ba-modified electrodes, which demonstrated improved stability and maintained a relatively low ASR of approximately 10 Ωcm^2 at 491°C and pO_2=1 bar.

6.1 Introduction

Solid oxide cells (SOC) are highly efficient, electrochemical devices for conversion of electrical to chemical energy and vice versa. Operation at elevated temperatures (above 750°C) is beneficial for attaining high power density, but poses a challenge for long-term stability and requires the use of more expensive auxilary materials like specialty steels for interconnects. Hence, there is an ongoing effort among the industrial developers and at universities with the aim of decreasing temperatures of operation while maintaining electrochemical performance. This has sparked research interest in the so-called intermediate temperatures region spanning from ≈500 to 750°C.[14] Special cells for operation at even lower temperatures have also been developed.[27,28,162,166] As the operating temperature is lowered, the relatively high activation energy of the oxygen reduction/evolution reaction (ORR/OER) renders the electrochemical activity of the oxygen electrode one

of the major obstacles. Therefore, materials exhibiting better catalytic activity towards ORR at low temperatures, as well as stable performance over time are needed.

The materials best suited to meet these requirements are typically mixed ionic and electronic conductors (MIEC). Promising candidate materials are perovskites such as $(Ba_{0.5}Sr_{0.5})(Co_{0.8}Fe_{0.2})O_{3-\delta}$,[11] double perovskites such as $PrBaCo_2O_{5+\delta}$, and Ruddlesden-Popper type materials such as $LaNiO_{4+\delta}$.[12,13] An alternative approach to obtaining high catalytic activity consists of modifying the surface of typical MIEC materials used as oxygen electrodes at high temperatures, such as $La_{0.6}Sr_{0.4}FeO_{3-\delta}$ (LSF), $La_{0.6}Sr_{0.4}CoO_{3-\delta}$ (LSC), and $La_{0.6}Sr_{0.4}Co_{0.2}Fe_{0.8}O_{3-\delta}$ (LSCF). However, the results obtained by different groups can differ both quantitatively and qualitatively. For example, a well-controlled experiment by Rupp *et al.*[103] where the samples are characterized inside the PLD chamber, shows that the deposition of Sr and Co ions (less than a monolayer) results in significant change in performance of $La_{0.6}Sr_{0.4}CoO_3$ thin film electrodes; Sr-deposition resulted in a decrease, while Co-deposition led to an increase of oxygen exchange activity.[103] Exactly the opposite is found in a study by Mutoro *et al.* on $La_{0.8}Sr_{0.2}CoO_3$ thin film electrodes, deposited and decorated by PLD. There, Sr-decorated were an order of magnitude faster, while Co-decorated an order of magnitude slower than the pristine electrode.[122]

As has been shown in the previous chapters, differences can arise due to multiple reasons including testing setup, fabrication procedure, and thermal history of the samples. Thus, attaining clear guidelines for fabrication of technologically relevant electrodes can be challenging. This study aims to eliminate some of these differences by analyzing a set of electrodes which are fabricated, modified, and tested in the same way. The effect of modifying the surface chemistry by adding small amounts of second phases on the oxygen exchange activity is examined on $La_{0.6}Sr_{0.4}FeO_{3-\delta}$ (LSF) which we have earlier thoroughly investigated in "bulk" (Chapters 3 and 4) and thin film form (Chapter 5). The macroscopic (A≈1 cm^2) thin film electrodes (thickness ≈215 nm) were modified by "drop casting" with Sr(II)-nitrate, Fe(III)-nitrate, a 80:20 mixture of Ce(III)- and Gd(III)-nitrate, Ba(II)-nitrate, or Zr(IV)-nitrate, resembling the procedure used when preparing infiltrated nano-structured technological electrodes.[48,60,62,65,105,167]

The particular cations are selected based on either promising results obtained for other similar MIECs and/or because of the existing controversies in the literature. The latter is the case with the above-mentioned opposing observations by Mutoro *et al.* and Rupp *et al.* which was the reason to analyze the effects of surface modification with Sr and Fe. Besides this, surface modification with Sr has been postulated to improve stability of $La_{0.6}Sr_{0.4}CoO_3$ thin film electrodes by preventing the intrinsic Sr-segregation.[124] Furthermore, Hong *et al.*[31] reported increased oxygen exchange activity of $La_{0.8}Sr_{0.2}FeO_3$ after modifying the electrode surface with Sr-nitrates ascribing the improvement to the formation of second phase RP-type particles and fast transport at Ruddlesden-Popper/perovskite interfaces.

There are also numerous reports on the beneficial effect of mixing MIEC type electrocatalysts with CGO.[16,59,60,162,168–171] Usually, for technological electrodes the materials are brought in contact by mixing powders of the two materials creating composite electrodes,[59,60] by infiltrating CGO in a MIEC backbone,[162,170,171] or by infiltrating a MIEC

in a CGO backbone.[168,169] In few cases adding CGO to the surface of a bulk MIEC has been reported to increase exchange rates, and for bulk composites non-trivial but positive synergistic effects between LSF and CGO have been reported.[16,59]

The beneficial effect of modification with Ba on the oxygen reduction reaction has been reported in literature.[63,139,172,173] Hong *et al.* measured 2-3 times lower ASR between 500 and 800°C for $La_{0.8}Sr_{0.2}FeO_3$, $La_{0.6}Sr_{0.4}Co_{0.2}Fe_{0.8}O_3$, and $La_{0.8}Sr_{0.2}MnO3$ surface decorated with Ba-rich phases after infiltration with barium acetate.[63] The improvement was attributed to formation of $BaCO_3$ nanoparticles which were postulated to facilitate adsorption and dissociation of oxygen.[173]

Finally, from some literature reports modification with Zr could be expected to improve the stability of electrode performance. This effect was shown by Gong *et al.*[174] by depositing atomic layer of ZrO_2 on the surface of $La_{0.6}Sr_{0.4}CoO_3$ electrodes. Furthermore, in a study from Tsvetkov *et al.*[104] on PLD-deposited thin film electrodes at 530°C in air, the authors have shown that surface modification with ions which are less reducible (have higher oxygen vacancy formation enthalpy) than the underlying perovskite leads to an improvement of stability. In case of $La_{0.6}Sr_{0.4}CoO_3$ electrode, the best results were obtained for surface modification with hafnium, but also with zirconium which is chemically very similar to Hf.

In the present study all modified electrodes were subjected to identical thermal treatments throughout the experiment. Special attention was paid to cleanliness of the experimental setup which was the same for all tested electrodes. Furthermore, the testing procedure was the same as in the previous study on non-modified LSF thin film electrode (Chapter 5) which enables direct comparison and expectedly a reliable analysis of effects of surface modification.

6.2 Experimental

The LSF model electrodes were prepared by PLD. Film thickness was 215 nm. One-side polished, (100)-oriented, monocrystalline yttrium-stabilized zirconia (YSZ, 9.5 mol% Y_2O_3, CrysTec GmbH, Germany) with a size of 10 mm x 10 mm x 0.5 mm were used as substrates and served further as electrolytes. Prior to the deposition of the LSF a 35 nm thick CGO ($Ce_{0.8}Gd_{0.2}O_{1.95}$) layer was deposited on the YSZ to serve as a buffer layer. The counter electrode was 15 µm thick porous layer of platinum infiltrated with CPO ($Ce_{0.8}Pr_{0.2}O_{1.9}$). The samples were cooled in the chamber under the same pO_2 with the cooling rate of 5°C/min. In total, 16 cells were produced. A more detailed explanation on the preparation of the cells can be found in Chapter 5.

To test the influence of different surface modifications on electrochemical performance, the thin film electrodes were treated by adding 1, 3 or 10 drops of 5 mmol/l nitrate solutions containing the respective cations (Table 6.1). To ensure uniform coverage of the droplets and avoid inhomogeneous drying ('coffee-stain effect'), 1 vol% of surfactant (Dow Chemicals, Tergitol^{TM} TMN 10) was added to the nitrate solutions. The modification was done on a hot plate at 60°C. Each drop was left to dry at this

temperature in ambient air (≈20 min per drop). The drops were held on the electrode by surface tension enabling the determination of the total amount of cations on the surface. The volume of each drop was approximately 0.125 ml (8 drops per ml of solution). Therefore, the amount of cations in 1, 3, and 10 drops of solution were 0.625, 1.875, and 6.25 µmol, respectively. Dividing these values with the electrode surface area (≈0.66 cm^2) a surface concentration of metal cations can be estimated to be 1, 3, and 10 µmol/cm^2, respectively. A schematic representation of the drop casting procedure is shown in Figure 6.1.

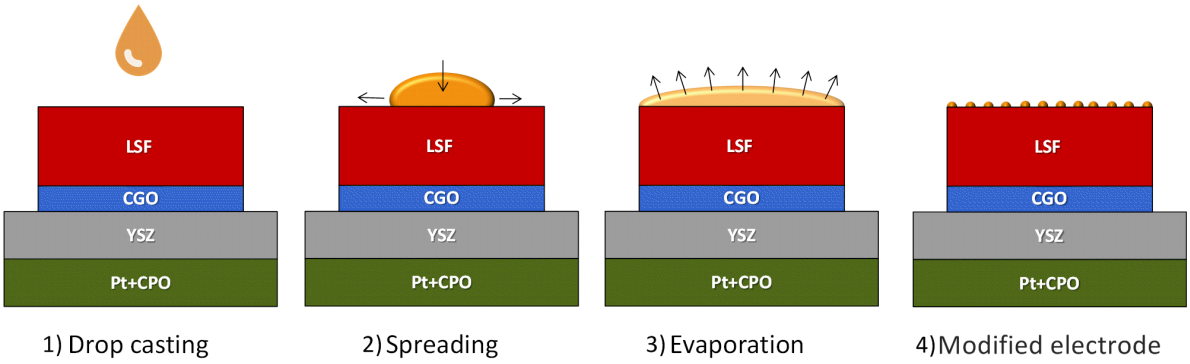

Figure 6.1: Schematic representation of involved in surface modification; 1) A drop is deposited on the surface of the electrode by a micropipette; 2) Drop spreads across the surface; 3) Solvent evaporates; 4) The surface uniformly covered with in particles.

The cells were characterized by electrochemical impedance spectroscopy (EIS). Measurement were carried out in a rig made of alumina. Electrodes were contacted by sandwiching the cells between two current collectors made of woven gold meshes (wire thickness 80 µm, aperture of 250 µm, purity >99.9%) wrapped around CGO pellets. Contact was ensured by applying a mild mechanical force (≈10 kPa). Before the test, all rig elements were cleaned in concentrated HCl and deionized water. The testing environment was a dry O_2/N_2 mixture fed at a flow rate of 5 l/h. By adjusting the flow rates of N_2 and O_2, the pO_2 was varied in range from 1 to 0.05 mbar measured with a

Table 6.1: List of nitrates used for preparation of 5 mmol/L aqueous solutions

Solution	**Powder supplier**	**Purity**
$Sr(NO_3)_2$	Sigma-Aldrich	>99%
$Fe(NO_3)_3{\cdot}9H_2O$	Alfa Aesar	99.998%
$Ce(NO_3)_3{\cdot}6H_2O$	Sigma-Aldrich	99.99%
$Gd(NO_3)_3{\cdot}6H_2O$	Sigma-Aldrich	99.99%
$Ba(NO_3)_2$	Alfa Aesar	99.999%
$ZrO(NO_3)_2{\cdot}xH_2O$	Alfa Aesar	99.9%

zirconia-based oxygen sensor placed in the exhaust pipe. Temperature was measured by a thermocouple placed close to the cell (within 2 mm). Electrochemical impedance was measured with no external current load except the pertubation signal using a Solartron 1260 frequency response analyzer in the frequency range from 10^5 to 10^{-1} Hz with a signal amplitude of 10 mV (the impedance was measured at 48 different frequncies). Logging and parameter fitting was done by an in-house deeloped software "Elchemea". Electrode performance was first tested at 11 different temperatures from 387°C to 594°C. The values reported in the following are averages of three measurements at each temperature. This was followed by a test at different pO_2 from 1 to 0.05 bar at 491°C. Finally, performance stability was tracked over a 60 hour period in pure oxygen (491°C). The results obtained for modified electrodes were compared with a non-modified electrode serving as a reference. In the rest of the text we will refer to values obtained in non-modified electrodes as the 'reference values'. The sketch of the experimental sequence can be found in the supplementary information (Figure 3.7).

The surface composition of thin films was analyzed before and after the electrochemical characterization by XPS using Physical Electronics Versaprobe II X-ray Photoelectron Spectrometer with monochromated Al Kα (1486.65 eV) X-ray radiation source equipped with charge neutralization system under a base pressure of 10^{-9} Torr. The surface and a cross section of the electrodes was also examined by SEM, Zeiss Merlin microscope. Surface roughness was analyzed using a Cyberscan Vantage Profilometer.

6.3 Results and Discussion

The impedance spectra of all electrodes at all experimental conditions had three distinct features similar to our previous study on LSF thin film electrode (Chapter 5). In section 5.3.4.1 we have discussed the interpretation of the low-, medium- and high-frequency part of impedance spectrum in detail. Here, the same approach will be employed for determining the area specific resistance (ASR), the chemical capacitance (C_{chem}) of the working electrode, and the oxygen exchange coefficients (k_O and k_{chem}). As outlined in the experimental section the EIS characterization consisted of three measurement series. First, the electrodes were characterized at different temperatures, which enabled the determination of activation energies. Then, impedance spectra were collected at different pO_2 at a fixed temperature of 491°C in order to deduce possible changes in reaction mechanism, and, finally, the electrode stability was tested over 60 hours.

6.3.1 Electrochemical characterization

6.3.1.1 Modification with Sr (LSF+Sr)

The results of the EIS characterization of the Sr-modified LSF thin film electrodes are shown in Figure 6.2.

The modification lead only to a very moderate effect on the rate of the oxygen reduction reaction as illustrated by the only slightly altered ASR, k_O, and k_{chem} values compared to the reference. Modification with Sr has a mild impeding effect on the oxygen exchange especially at the lower temperatures. The addition of strontium has no effect on C_{chem} and the measured values were in range from 1000 to 1100 F/cm^3, which is the same as observed for the reference values. SEM micrographs of the Sr-modified samples shows uniformly spread nanoparticulate islands across the surface for the sample modified with one drop of nitrate solution. Agglomeration of the nanoparticles is evident for the sample modified with three drops of solution, while the sample modified with ten drops is covered with a porous layer. The fact that the oxygen exchange was not altered significantly even when such porous layer is present on the surface may lead to two different conclusions: (i) either the layer has absolutely no effect on the oxygen exchange performance or (ii) the increase in active surface area compensates for a possible loss of performance due to more Sr on the surface.

Nevertheless, only a relatively small effect on oxygen exchange kinetics (up to 50%) even when the electrode was modified with 10 drops of solution (corresponding to 10 µmol/cm^2) is perhaps somewhat surprising when earlier discussed studies by Rupp *et al.*[103] and Mutoro *et al.*[122] are taken into account. For example, Rupp *et al.* measured a five-fold decrease in oxygen exchange activity after deposition of amounts as small as ≈1 nmol/cm^2 which is 10000 less than in the present study. This may be a consequence of different experimental procedure; Rupp *et al.*[103] and Mutoro *et al.*[122] deposited Sr by PLD deposition from SrO target, while in the present study Sr-particles are formed calcination of Sr-nitrate. Alternatively, this could indicate that LSF performance is less sensitive than LSC to degradation due to external Sr enrichment.

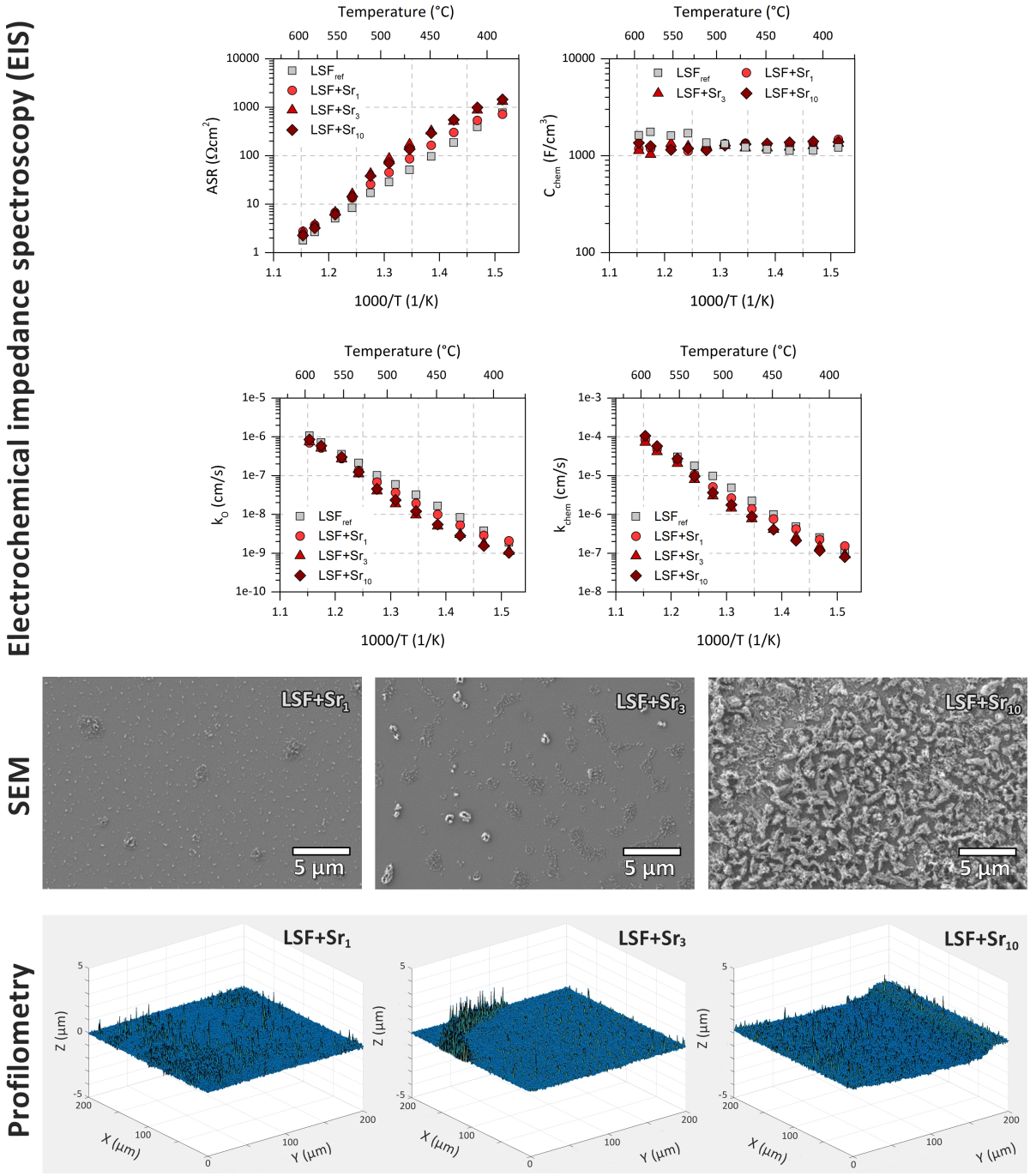

Figure 6.2: Results obtained for Sr-modified electrodes. Top) Electrochemical testing by EIS at different temperatures and in pure oxygen for three different amounts of modification; Middle) SEM images of the electrodes after the test; Bottom) Surface profiles of the electrodes after the test.

6.3.1.2 Modification with Fe (LSF+Fe)

The results of EIS test LSF electrodes modified with iron-nitrate solution are shown in the in Figure 6.3. These electrodes performed differently than the non-modified samples in almost all aspects. There was a significant decrease in ASR, and a corresponding increase in oxygen exchange coefficients, while chemical capacitance of samples modified with 3 and 10 drops of Fe-nitrate solution had more than halved.

Also shown in Figure 6.3 are the profilometry and SEM results. Evidently, the nitrate treatment led to a damage of the electrode through a chemical etching. This is because $Fe(NO_3)_3$ dissolves in water forming hexaaquiron(III) ion ($Fe(H_2O)_6{}^{3+}$) which hydrolyses according to the following reaction:

$$Fe(H_2O)_6^{3+} + H_2O \rightarrow [Fe(H_2O)_5(OH)]^{2+} + H_3O^+ \tag{6.1}$$

rendering the solution acidic. It can be calculated that even in case of a diluted solution (5 mmol/L) the pH will be below 3. Based on SEM and surface profiles (Figure 6.3), it looks like the modification with 3 and 10 drops of solution leads to a severe damage and creation of holes in the volume of the electrodes.

The surface of the electrode modified with one drop of solution is rough, but there are no observable holes. Due to etching-induced changes in the surface area and the electrode volume, some of the assumptions made during the analysis (flat and dense electrode), were not valid after the modification with the $Fe(NO_3)_3$ solution (Figure 6.4). This renders the calculated parameters presented in Figure 6.3 inaccurate. However, they can still provide valuable information about the electrode.

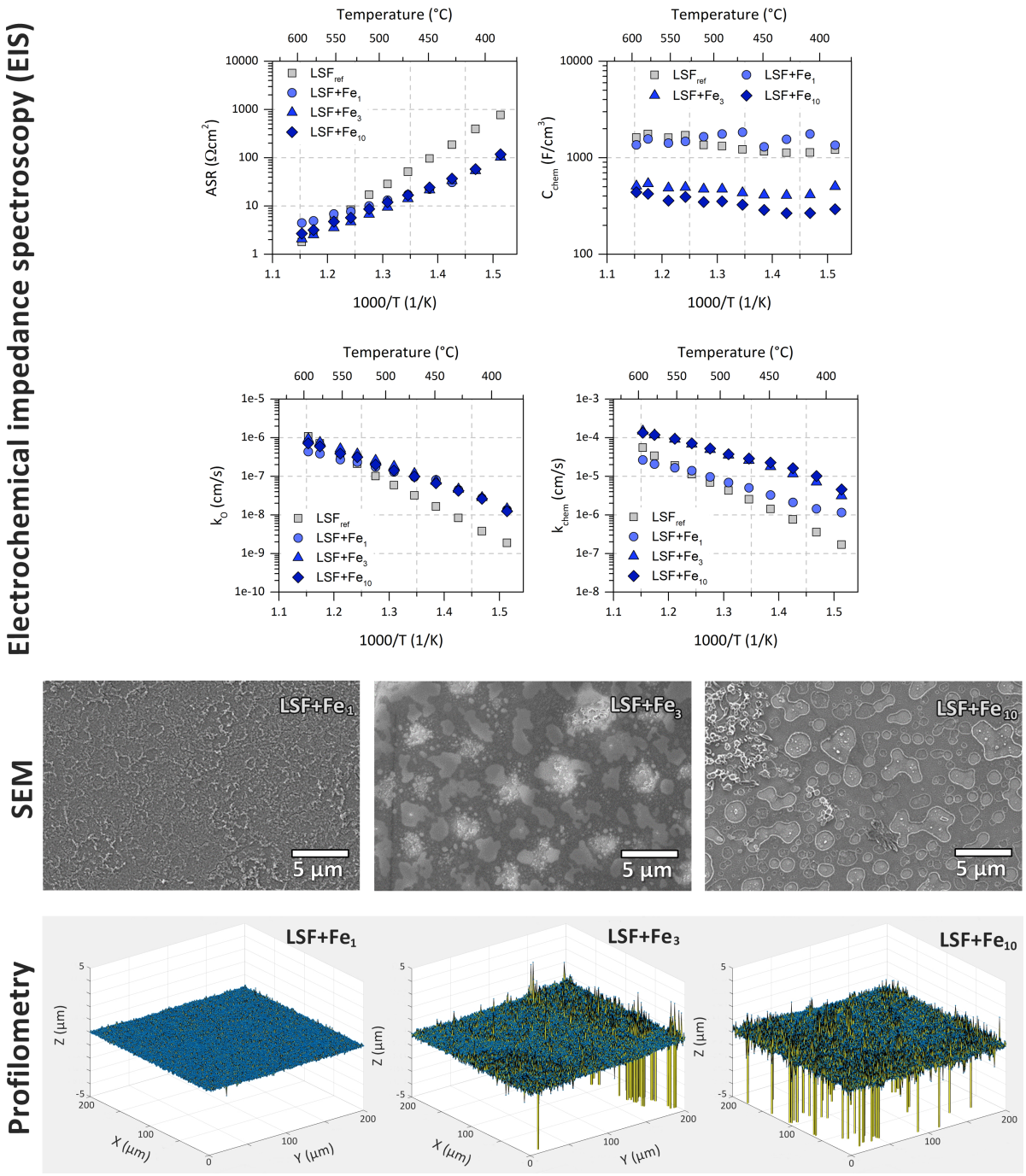

Figure 6.3: Results obtained for Fe-modified electrodes. Top) Electrochemical testing by EIS at different temperatures and in pure oxygen for three different amounts of modification; Middle) SEM images of the electrodes after the test; Bottom) Surface profiles of the electrodes after the test.

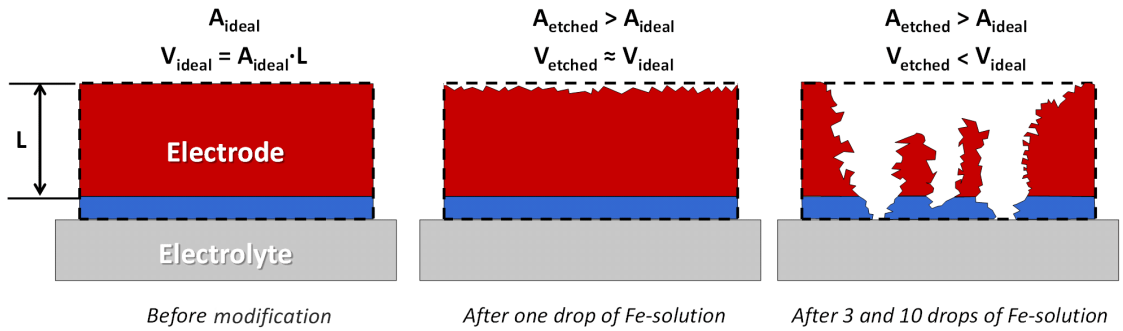

Figure 6.4: Schematic representation of the effect of etching on changes in surface area and electrode volume. Based on SEM and surface profiles (Figure 3), the electrode modified with one drop of solution had only rougher surface, but no holes, while the electrodes modified with 3 and 10 drops of solution were severely damaged with and with visible holes.

For example, the electrode modified with one drop of solution had almost the same C_{chem} as the reference values (1000-1100 F/cm^3), while electrodes modified with 3 and 10 drops of solution had significantly smaller apparent C_{chem} values (300-500 F/cm^3). This a consequence of loss in electrode volume in the latter two cases, since the capacitance was calculated based on the volume before modification (V_{ideal}). This further means that a bit more than 50% of the electrode volume is etched which seems to be in line with the SEM observation (Figure 6.3).

Furthermore, ASR and k_O values were similar for all three electrodes, while k_{chem} values were approximately 10 times higher for the electrodes modified with 3 and 10 drops of solution. Calculation of k_O is based on ASR, which in turn depends on the surface area of the electrode. On the other hand, k_{chem} is inversely proportional to the equilibration time which depends on the volume of electrode. Therefore, loss in electrode volume enables faster equilibration times (summit frequency of the RC semicircle is higher), which then causes an apparent increase in k_{chem} for the electrodes modified with 3 and 10 drops of solution.

However, regardless of the change in volume which renders the absolute values k_{chem} and C_{chem} inaccurate, there seems to be a qualitative change in the nature of oxygen exchange reaction indicated through change in apparent activation energy. The measured activation energies for the Fe-modified/etched samples for k_O and k_{chem} was ≈90 kJ/mol and ≈80 kJ/mol, respectively, which is much smaller than the reference values (≈147 kJ/mol and ≈130 kJ/mol). Notably, a similar activation energy (92±6 kJ/mol) was found earlier in the case of an LSF electrode in 'activated' state of the perovskite surface (see Table 3.2). The 'activated' state is characterized with faster oxygen exchange kinetics and can be found after a high temperature thermal treatment (of an LSF bulk sample, Chapter 3) or after rinsing in water (thin film study, Chapter 5). The measured values thus indicate that the surface of of the Fe-modified electrodes is in the 'activated' state, perhaps not as a consequence of the Fe addition but more due to the chemical etching.

6.3.1.3 Modification with CGO (LSF+CGO)

Modification with mixture of $Ce(NO_3)_3$ and $Gd(NO_3)_3$ results in formation of loosely spread micron-sized particles on the surface (Figure 6.5). Higher amount of modification does not lead to formation of bigger particles, but rather they become more numerous. Cracks in the electrode surface were observed in the places where bigger particles (>2 µm) are present indicating that the particles are in close contact with the electrode and partly immersed in the electrode volume. The surface around the particles appears the same as for the non-modified sample and no chemical etching could be observed on these electrodes. This is further supported by the typical C_{chem} values of approximately 1000 F/cm^3, which suggests that the volume has not changed much despite the observable cracks. Similar to Fe-modified samples (etched samples), the activation energy for the oxygen exchange coefficients and ASR was found to be lower than in non-modified electrode. Less pronounced temperature dependence also means that good performance observed at the low temperatures diminishes at high temperatures and above 500°C it becomes worse than for the non-modified electrode. The performance also gets worse with the further modification. This may suggest that the optimal amount for CGO-modification is below 1 µmol/cm^2. Very similar conclusions were reached in studies by Kiebach *et al.* where $La_{0.75}Sr_{0.25}MnO_3$ electrode was modified with CGO (Ce and Gd nitrate solutions).[168,169] There, the improvement is also found to be most pronounced at the lower temperatures and that the effect diminished when the electrodes were exposed to higher temperatures (800°C).[169] Therefore, CGO modification offers an improvement at low temperature but the amounts of surface decoration should be kept low (possibly below 1 µmol/cm^2).

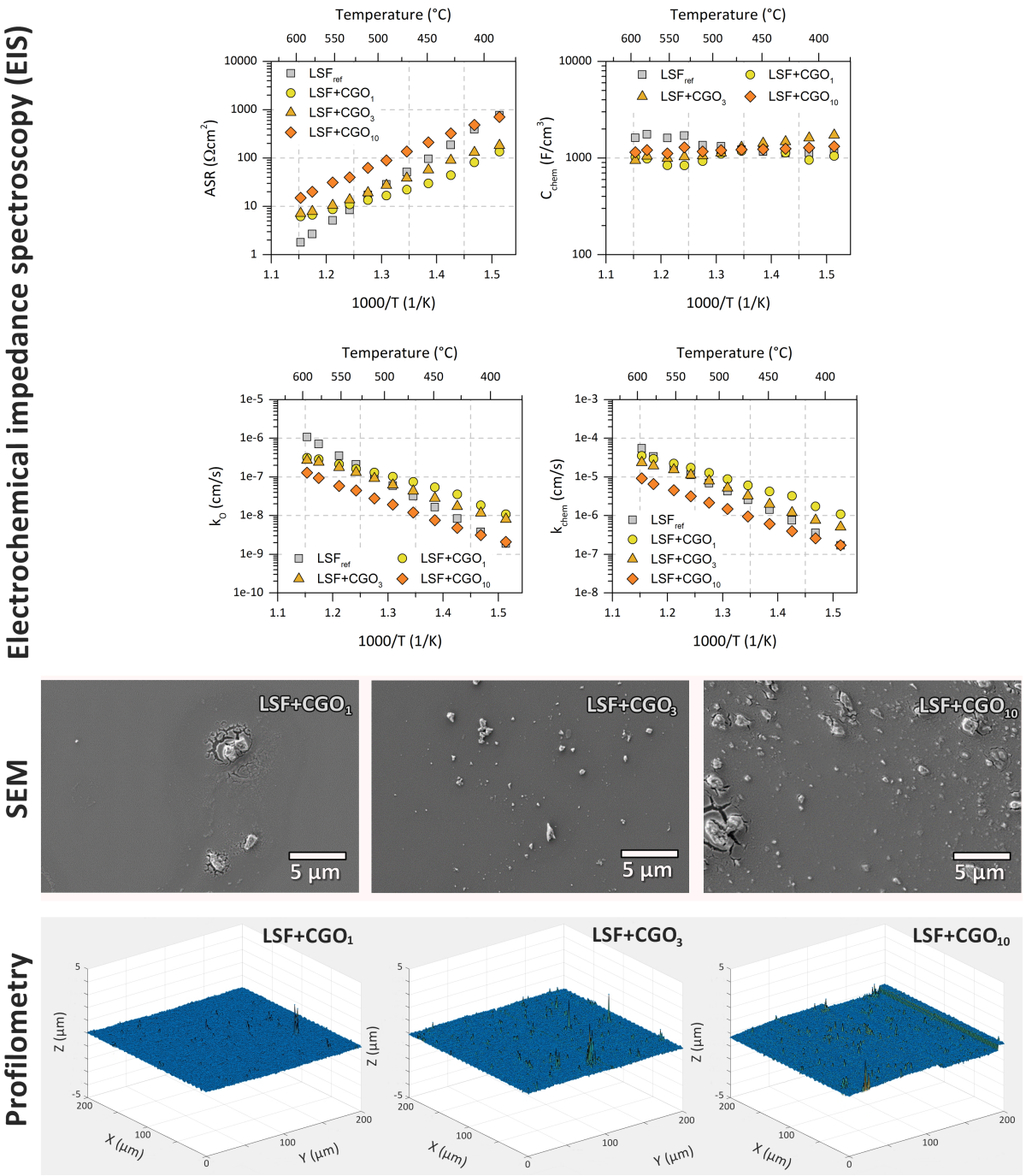

Figure 6.5: Results obtained for CGO-modified electrodes. Top) Electrochemical testing by EIS at different temperatures and in pure oxygen for three different amounts of modification; Middle) SEM images of the electrodes after the test; Bottom) Surface profiles of the electrodes after the test.

6.3.1.4 Modification with Ba (LSF+Ba)

The electrode modified with one drop of $Ba(NO_3)_2$ was uniformly covered with submicron-sized particles and sporadic agglomerates larger than 2 µm (Figure 6.6). There was a certain amount of elongated particles of approximately 5 µm in length and 100-200 nm in diameter. Further modification resulted in formation of larger agglomerates. The agglomerates and elongated particles prevailed almost completely on the electrode modified with ten drops of solution, while there were virtually no submicron particles. The rest of the surface appeared smooth with no signs of chemical etching.

The apparent activation energy of k_{chem} is found to be ≈165 kJ/mol which is slightly higher than for the non-modified electrode (Figure 6.6). The best electrochemical performance was observed in case of electrode modified with one drop of solution. Further modification does not contribute to performance and the electrode modified with 10 drops of solution was very similar to the non-modified one. This finding correlates with the amount of submicron particles on the surface, which may suggest a connection between these particles and the improved performance. One can speculate that the observed change in kinetics can be due to an increase in surface area which will be the higher in case of small particles than when the large agglomerates are formed. This interpretation could be valid only if the particles are actively involved in ORR reaction. However, if this is the case than the electrode modified with 10 drops of solution should perform better that the non-modified one. The results show the opposite trend, so an alternative explanation can be that the triple-phase boundaries between particles/LSF/atmosphere are the places where ORR reaction is fast. In this light, the electrode modified with one drop of solution performs better due to a higher amount of triple phase boundaries when the submicron particles are present. Furthermore, the decline in performance with the increasing amount of modification suggests that the optimal amount is below 0.6 µm (analogous to CGO-modification). Notably, the chemical capacitance of the best performing electrode appears to be temperature dependent, while the further increase in amount of modification decreases the temperature sensitivity of C_{chem}. The C_{chem} of the electrode modified with 10 drops of solution was independent of temperature as observed also for the reference. One can thus speculate a possible connection between submicron-sized particles, faster oxygen exchange reaction, and a change in defect chemistry of the electrode. However, a clear description of this relationship cannot be given at this point.

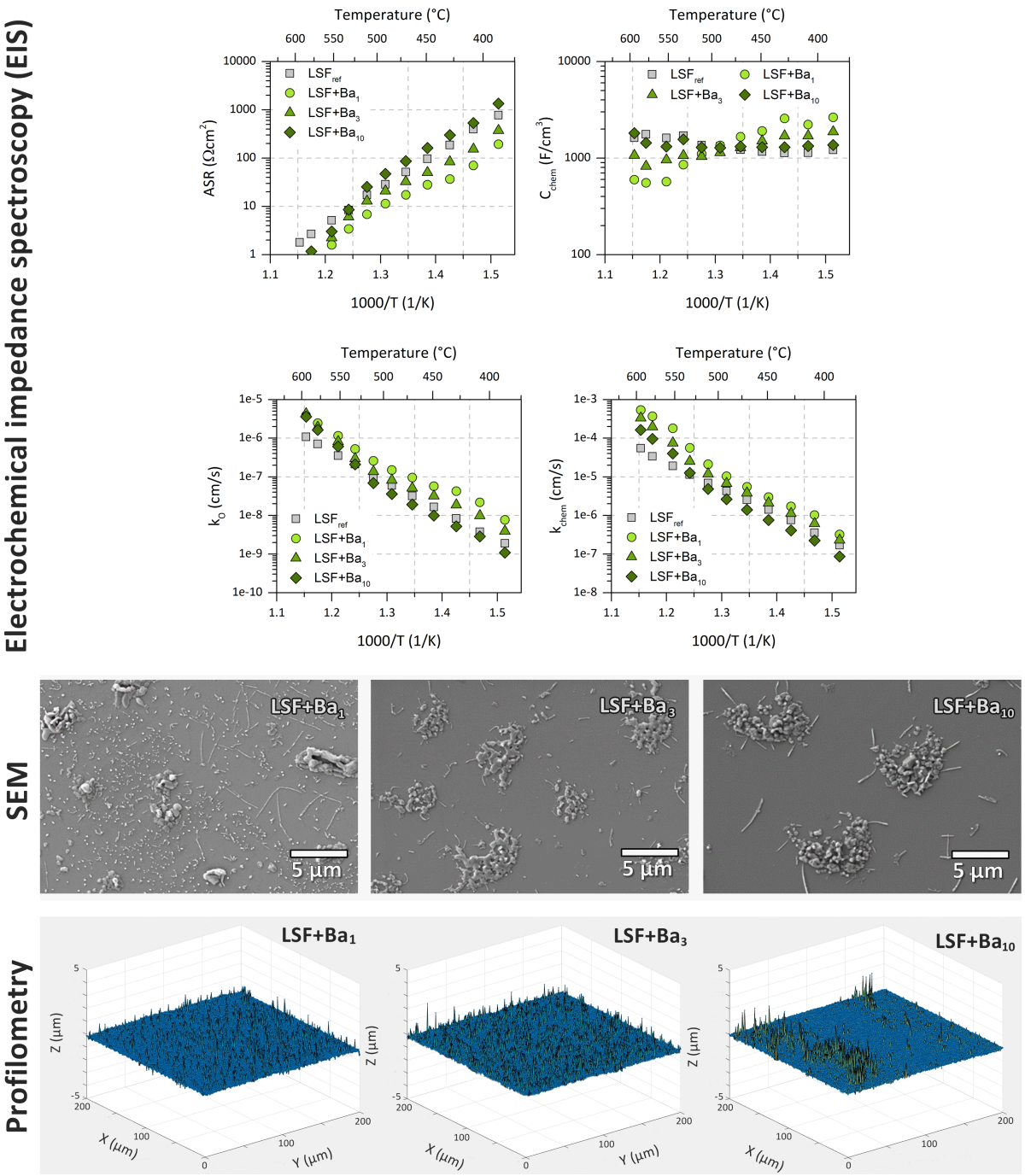

Figure 6.6: Results obtained for Ba-modified electrodes. Top) Electrochemical testing by EIS at different temperatures and in pure oxygen for three different amounts of modification; Middle) SEM images of the electrodes after the test; Bottom) Surface profiles of the electrodes after the test.

6.3.1.5 Modification with Zr (LSF+Zr)

SEM micrographs of electrodes modified with Zr-nitrate solution reveal severe effects of chemical etching similar to the Fe-modified electrodes (Figure 6.7). In the case of the electrode modified with 10 drops of solution, some regions were etched down to the electrolyte. Holes in the electrodes of tens of microns in diameter can be seen in the surface profiles. This is a consequence of acidic behavior of Zr-nitrate in aqueous solutions due to hydrolysis of hydrated Zr^{4+} ion.

$$Fe(H_2O)_x^{4+} + H_2O \rightarrow [Fe(H_2O)_{x-1}(OH)]^{3+} + H_3O^+ \tag{6.2}$$

As in the Fe-modified electrodes, the chemical etching results in significantly smaller values of apparent chemical capacitance. Therefore, the observed 10-fold increase in calculated k_{chem} at lower temperatures should be seen as a consequence of smaller electrode volume. Similar conclusion can be drawn for low ASR/high k_O, where seemingly increased performance can be interpreted as a consequence of increased surface area due to etching.

The apparent activation energy for k_O was ≈90 kJ/mol and ≈75 kJ/mol for k_{chem}. These values are significantly lower than in non-modified electrode, but close to the values obtained for Fe-modified electrode which may indicate that ORR mechanism is different in the etched electrodes.

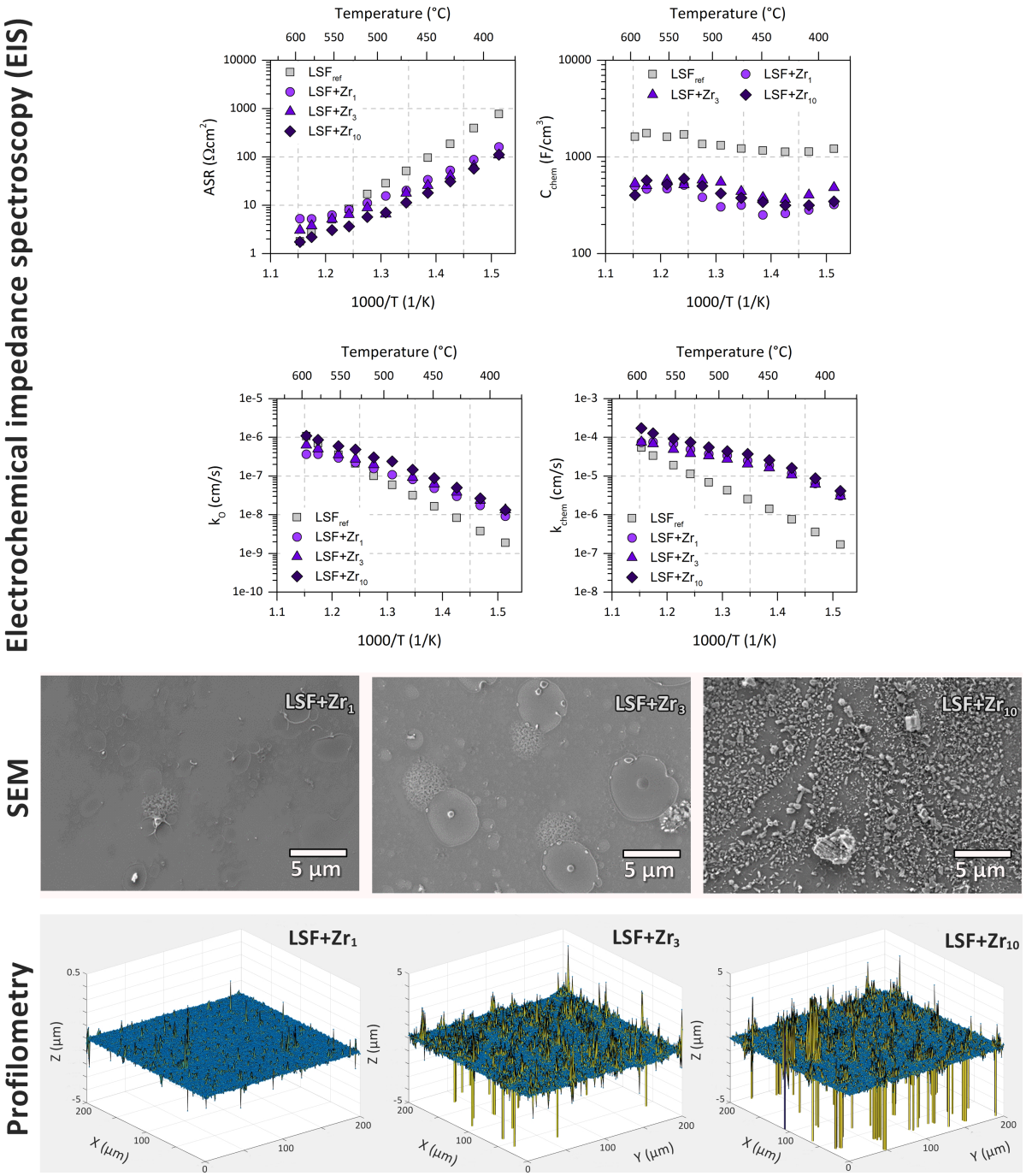

Figure 6.7: Results obtained for Zr-modified electrodes. Top) Electrochemical testing by EIS at different temperatures and in pure oxygen for three different amounts of modification; Middle) SEM images of the electrodes after the test; Bottom) Surface profiles of the electrodes after the test.

6.3.1.6 pO_2-dependence

After the temperature dependence test, the performance of the modified electrodes is measured at six different pO_2 (from 1 to 0.05 bar) and compared with reference values (Figure 6.8). The slope (exponent n in k$\sim$ pO_2^n) for non-modified electrode was found to be $\approx$1/2 suggesting that the rate determining step involves molecular oxygen (O_2).[143] On the other hand, almost all modified electrodes had slope less than ½, which can be a consequence of a change in the ORR mechanism. Values of $n < 0.5$ are expected for mechanisms where rate determining step of ORR reaction involves monoatomic oxygen species (O, O^-, O^{2-}).[142,143]

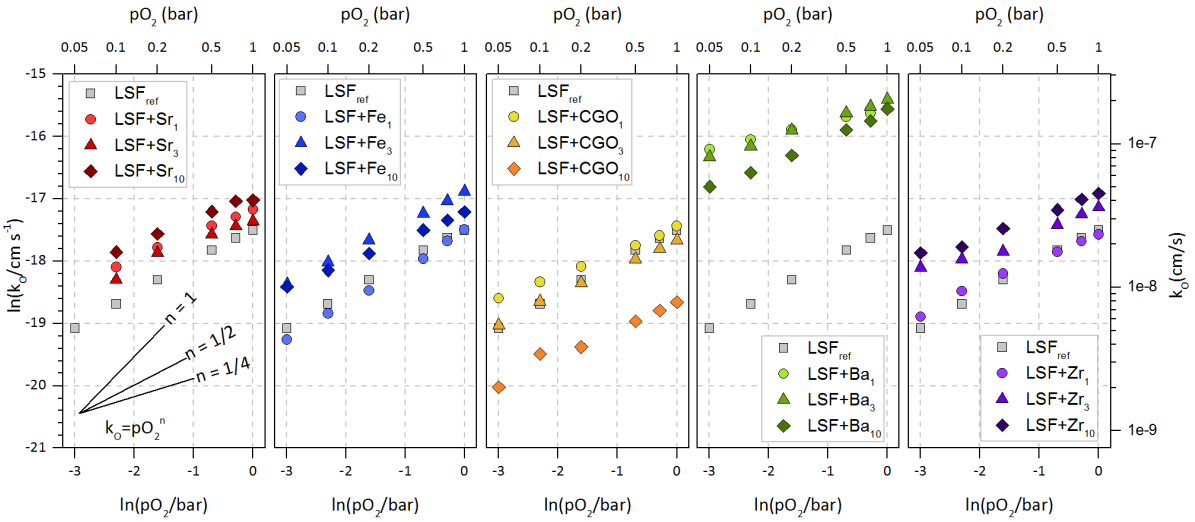

Figure 6.8: pO_2 dependence of k_O in modified electrodes measured at 491°C compared to the reference values.

6.3.1.7 Stability

After the pO_2-dependence test, the stability of the electrode performance was tracked over 60 hours at 491°C in pure oxygen. Figure 6.9 shows the change in area specific resistance and k_O over time for the modified electrodes. In the previous study on LSF thin films, we have observed that the non-modified electrode can have very different oxygen exchange activity and degradation rates before and after rinsing in water (Chapter 5). Namely, rinsing in water was found not only to improve the performance, but also to slow down the degradation. For this reason, both cases are used for comparison with the modified electrodes. Most of the modified electrodes and the non-modified one after rinsing, had ASR values between 30 and 120 Ωcm^2 during the whole test. A clear outlier on one side is the non-modified electrode before rinsing which had higher degradation rate and ASR = 1043.9 Ωcm^2 after 60 days (also shown in Figure 8). On the other side, all Ba-modified electrodes maintained a relatively low ASR ($\approx$10 Ωcm^2) throughout the whole test.

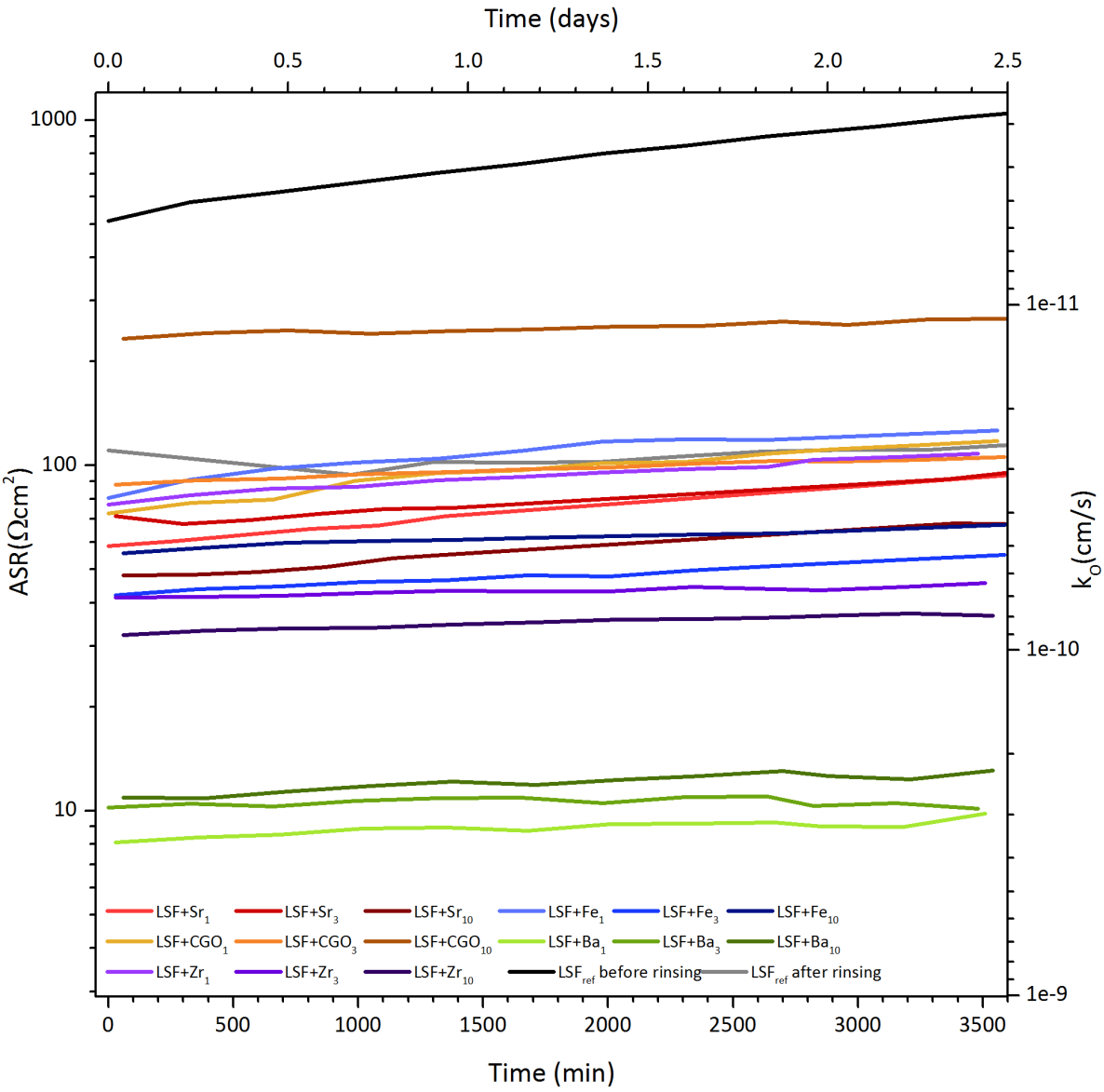

Figure 6.9: Change in ASR/k_O values over 60 hours in oxygen at 491°C.

In order to compare the degradation rates, the relative change in ASR is shown in Figure 6.10. Degradation rates of non-modified electrode before and after rinsing are approximately 40% and 5% per day, respectively. Most of the modified electrodes had degradation rates between these two values. The lowest degradation rates were found for Ba-modified electrodes which degraded less than 10% over 60 hours regardless of the amount of modification.

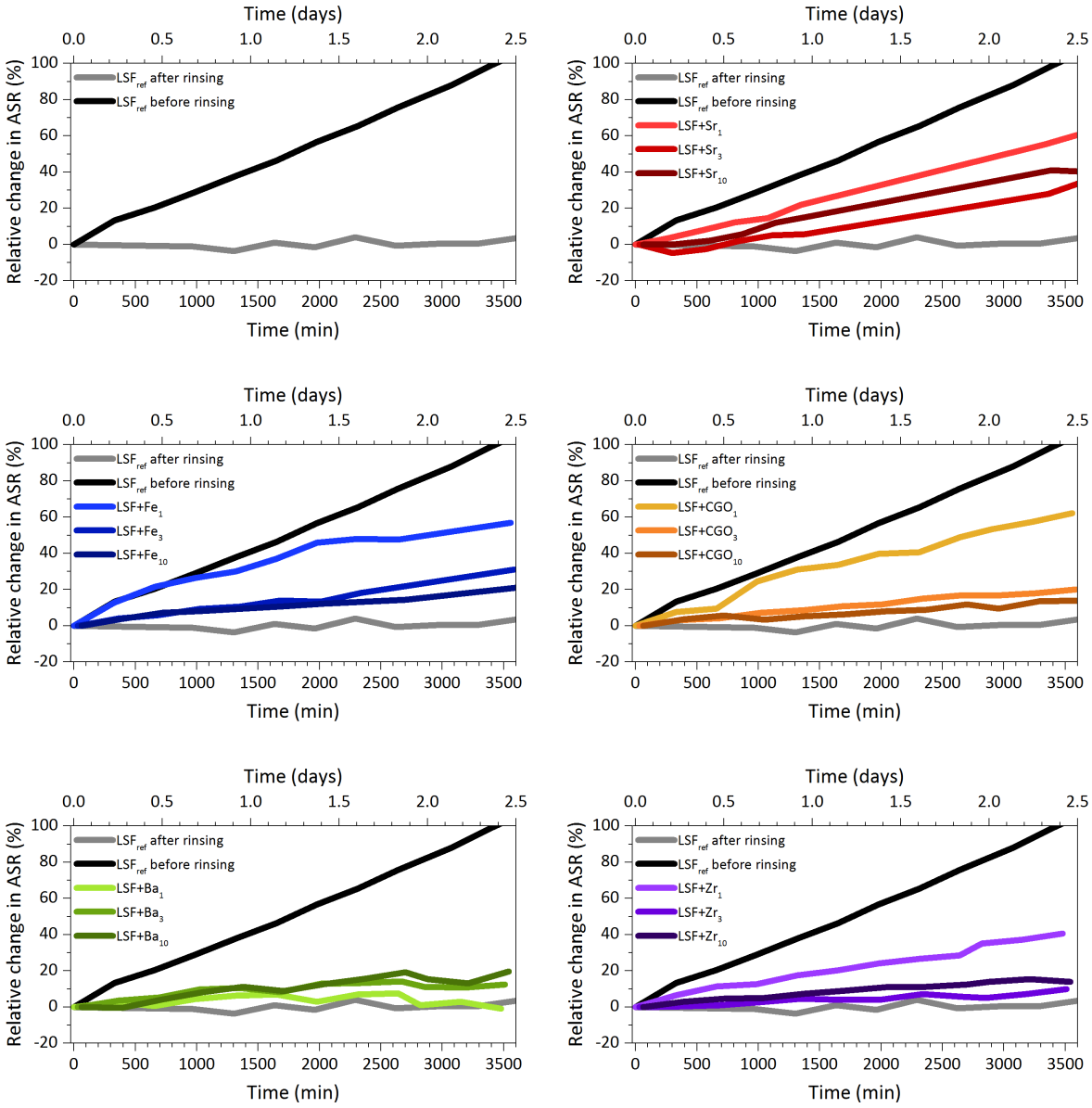

Figure 6.10: Stability of performance expressed as relative change in area specific resistance over 2.5 days in oxygen and at 491°C.

Interestingly, the degradation rates of almost all other electrodes tended to decrease with the increasing amount of modification and to approach degradation rates of rinsed electrodes. Modification with aqueous nitrate solutions of corresponding ions by drop casting seems to exert an effect similar to a rinsing in deionized water. Unlike the approach used in the previous study where blocking and water-soluble secondary phases got flushed away from the surface after being dissolved in water (Chapter 5), here the secondary phases probably get dissolved and redeposited after the droplet had evaporated. This redistribution of detrimental secondary phases probably frees a portion of the electrode surface for fast oxygen exchange reaction. This interpretation could also

be the reason why most of the modified electrodes, and the non-modified electrode after rinsing fell into the group which had ASR between 30 and 120 Ωcm^2.

A way to resolve contributions of individual processes and pinpoint the reasons for degradation is to use analysis of differences in impedance spectra (ADIS).[175] The results of ADIS analysis of modified electrodes are shown in Figure 6.11. Most of the electrodes had peaks below 0.1 Hz. This means that the increase in ASR values arises as the consequence of changes in process at low frequencies (oxygen reduction reaction). Remarkably, the low frequency peak was absent in the Ba-modified electrodes indicating that there was no change in ORR over 60 hours of experiment.

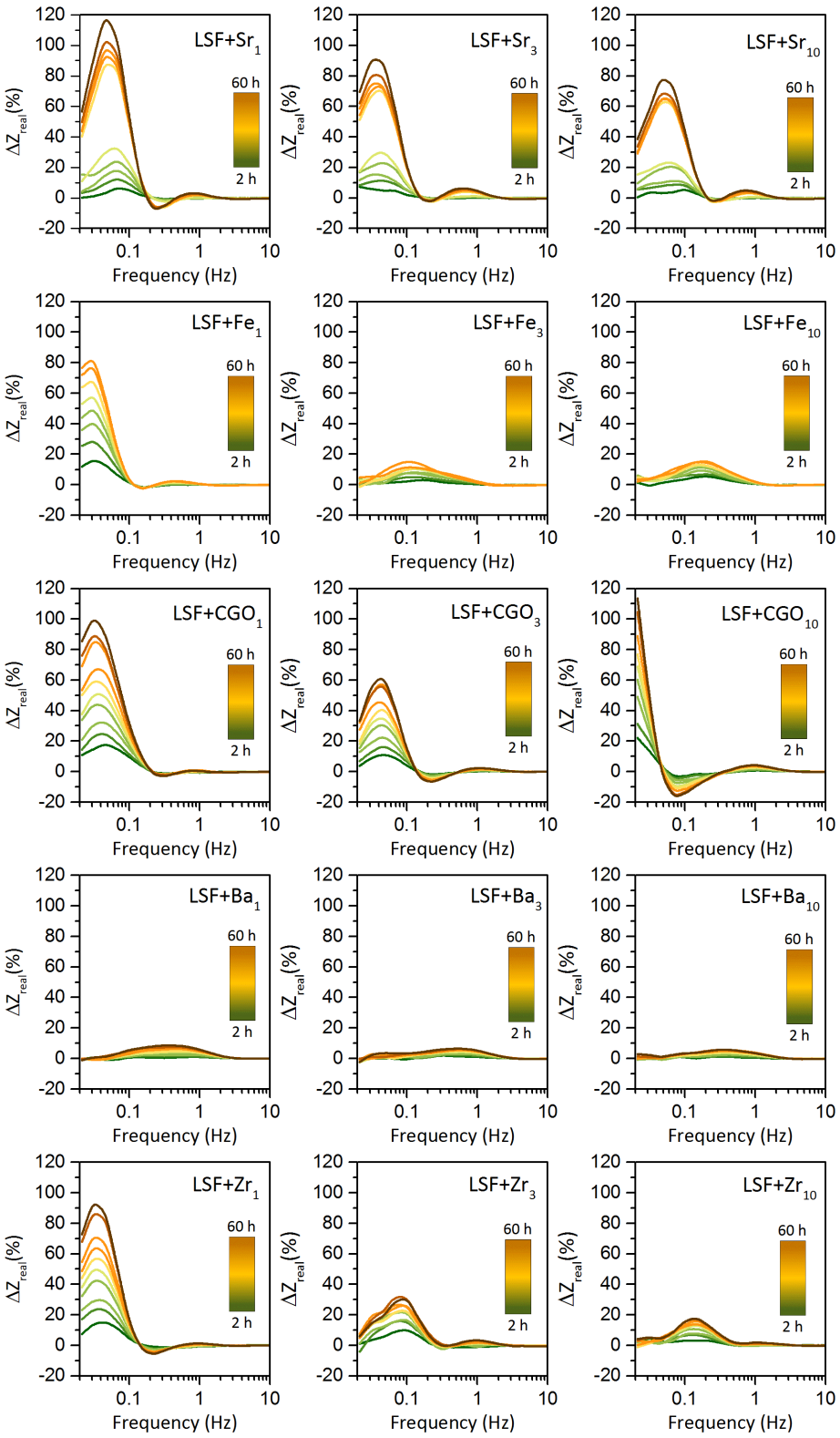

Figure 6.11: ADIS plots of modified electrodes used for identification of processes responsible for the performance degradation over 60 hours at 491°C in oxygen. At frequencies higher than 10 Hz, no differences between impedance spectra could be observed (ΔZreal % = 0), so these frequencies are omitted from plots for better readability.

6.3.1.8 Summary of electrochemical characterization

A summary of the results obtained by electrochemical impedance spectroscopy can be found in Table 6.2. Columns 2, 3 and 4 contain the measured apparent activation energies of area specific resistance (ASR), and oxygen exchange coefficients k_O and k_{chem}, respectively. The results of modified electrodes are compared with the non-modified one and changes are illustrated with the adjacent icons. Dependence of oxygen exchange coefficient k_O on pO_2 is shown in the following column and show that almost all modified electrodes had slopes of pO_2 dependence less than ½. The degradation rate expressed as change in ASR per day is shown in the penultimate column. As a measure of absolute degradation rate, the last column contains the measured ASR values after 2.5 days of testing at 491°C (approximately 7 days of total experiment duration including temperature- and pO_2-dependence tests). Exclamation marks indicate that ASR values of Fe-, and Zr-modified electrodes should be taken with caution due to etching and change in electrode area/volume. Arrows indicate change relative to the reference values. Yellow circles indicate that the change is small. The overall best results are found for group of electrode modified with barium. These electrodes had low degradation rate and maintained low ASR values throughout the experiment.

Table 6.2: Summary of results obtained by impedance spectroscopy for modified electrodes.

Electrode	E_A(ASR) [kJ/mol]	$E_A(k_O)$ [kJ/mol]	$E_A(k_{chem})$ [kJ/mol]	k_O - pO_2 dependence	Degradation rate (ΔASR) [%/day]	ASR at 491°C after 2.5 days [Ωcm²]
LSF_{REF}	139.9	146.6	129.4	0.53	40.8 (5.6)	1043.9 (116.5)
$LSF+Sr_1$	135.7	142.0	149.0	0.40	23.2	93.7
$LSF+Sr_3$	151.8	158.0	158.2	0.39	13.8	95.7
$LSF+Sr_{10}$	157.6	163.9	172.1	0.38	15.9	67.5
$LSF+Fe_1$	70.0	76.0	75.5	0.58	20.6	126.3
LSF+Fe3	88.7	95.0	84.3	0.49	10.4	55.2
$LSF+Fe_{10}$	84.4	90.6	73.2	0.40	5.6	67.5
$LSF+CGO_1$	69.4	75.7	79.9	0.38	24.9	117.8
$LSF+CGO_3$	78.3	84.6	92.5	0.44	8.0	105.8
$LSF+CGO_{10}$	89.8	96.1	92.4	0.42	5.1	266.0
$LSF+Ba_1$	129.5	146.6	169.6	0.22	2.1	10.1
$LSF+Ba_3$	144.4	135.7	162.2	0.31	5.3	9.8
$LSF+Ba_{10}$	174.7	150.7	171.0	0.41	5.9	13.1
$LSF+Zr_1$	80.6	86.9	70.9	0.43	15.9	108.2
$LSF+Zr_3$	82.0	87.6	68.7	0.34	3.5	45.6
$LSF+Zr_{10}$	93.9	100.2	78.4	0.33	6.1	36.8

6.3.2 Surface chemistry (XPS)

6.3.2.1 Survey spectra before and after electrochemical testing

The electrode surface was analyzed by XPS before and after the electrochemical testing. Survey XPS spectra show very few differences before and after the test (Figure 6.12). Nitrogen N 1*s* peak (405 eV) originating from nitrates is present in all modified electrodes and disappears after the impedance test. A small peak at 688 eV associated with F 1*s* can be seen in several modified samples after the test. This is most likely a consequence of contamination in the SEM chamber which has been observed earlier.[176] The results indicate that the degradation is not a consequence of poisoning with some detrimental elements such as chromium, sulfur, or silicon.

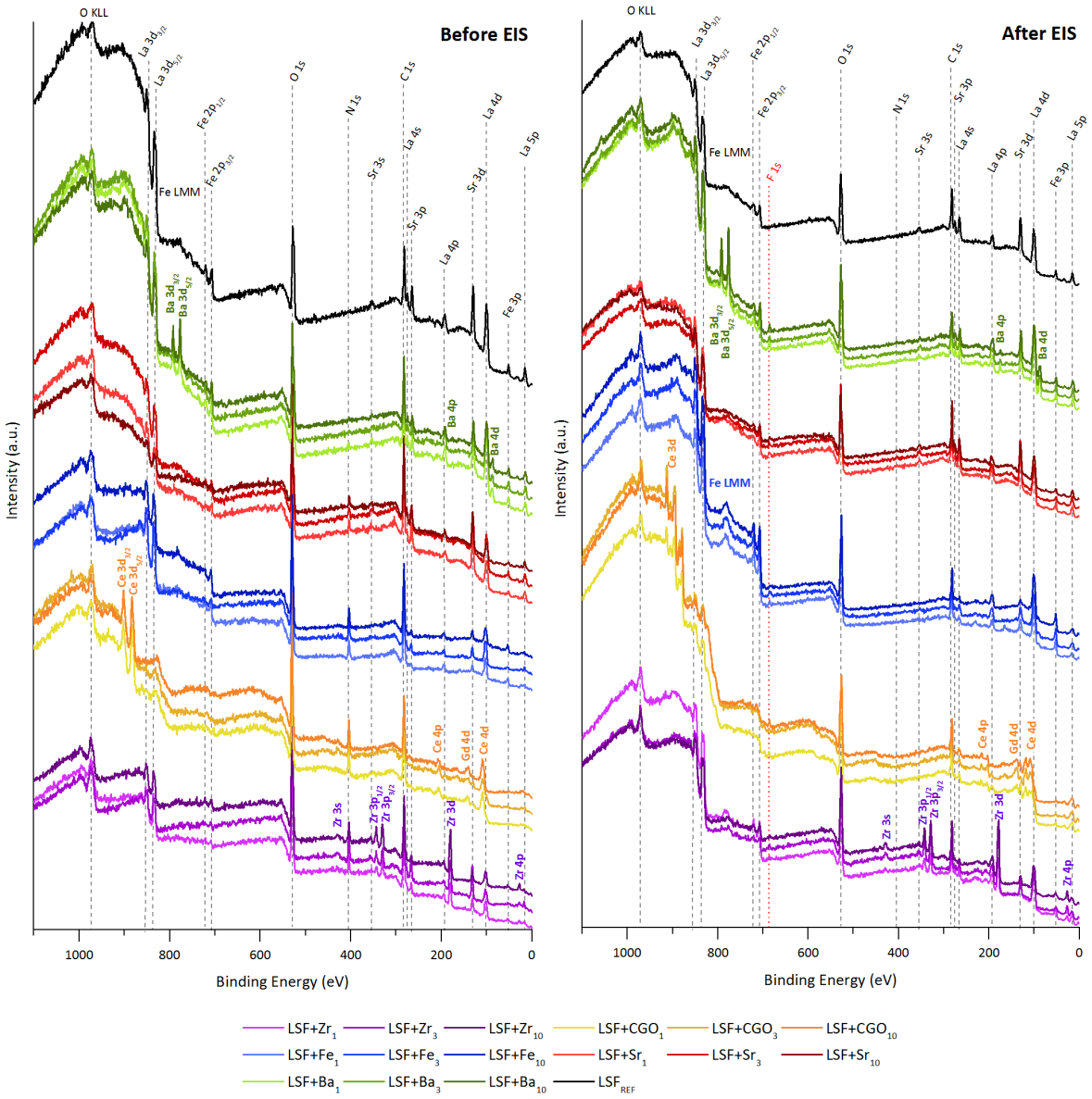

Figure 6.12: XPS survey spectra of the investigated electrodes before (left) and after (rigth) the impedance test.

6.3.2.2 Chemical state of strontium in electrodes

To further investigate the origin of electrode degradation, but also the observed beneficial effect of Ba-modification, the detailed spectra of Sr 3*d* XPS peak are collected before and after the electrochemical characterization. In our previous study we have observed a correlation between electrochemical performance and the chemical state of Sr on the surface (Chapters 4 and 5). To test if the same correlation can be found in electrodes investigated in this study, detailed scans of Sr 3*d* peak were collected before and after the electrochemical testing.

The analysis of the Sr 3*d* XPS peak in modified electrodes is shown in Figure 6.13. The analysis has not been performed on CGO-modified electrode as Sr 3*d* peak is overlapped with Gd 4*d* peak. For clarity, only electrodes decorated with 3 drops of solution are shown since the amount of modification had very mild effect of Sr 3*d* peak shape.

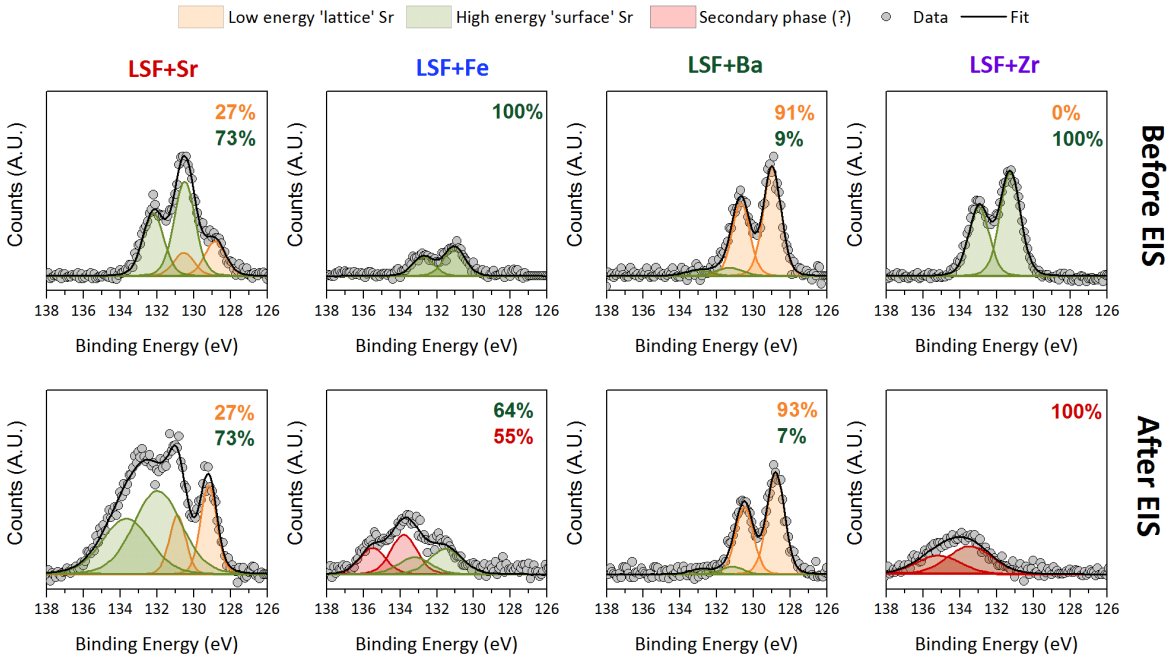

Figure 6.13: Detailed scans of Sr 3*d* XPS peak in modified electrodes. The scans in the top row are collected before the electrochemical impedance spectroscopy (EIS), while the scan after EIS are shown in the bottom row. The percentages in the upper right corner of each plot show the relative amounts the constituting compounds.

Sr-modified electrodes had more high-energy component than the non-modified one. This is understandable if we assume that the low energy component is related to Sr in the perovskite lattice as postulated before (Chapter 4). Thus the increase in high energy component is likely due to visible formation of secondary phase particles on the surface. The ratio between the two compounds does not change after the electrochemical testing, but there seems an increase in the overall Sr amount.

Fe-modified electrodes had only a high energy component (centered at 132 eV) before the test and the intensity of the Sr 3*d* peak (centered at ∼130 eV) was visibly smaller. Both observations are probably a consequence of local disintegration of the LSF lattice. After the electrochemical test a new doublet of peaks emerges at even higher binding energy (unknown secondary phase). This is an indication that some further chemical changes are taking place throughout the electrochemical test. However, more information about this new phase cannot be obtained from the present data. A very similar observation was made in case of Zr-modified electrodes after electrochemical test which further suggests that lack of a low energy Sr component is due to the chemical etching.

The *Ba-modified* electrodes had almost no high-energy component before and after the electrochemical test. The same was the case for other amounts of modification with 1 and 10 drops of solution. It looks as if barium removes the high energy Sr component from the perovskite surface. As discussed earlier, the increase in high energy Sr component is correlated with the decrease in performance and originates from Sr which is not incorporated in the perovskite lattice. How barium 'cleans' the surface from non-lattice strontium cannot be further detailed at present. Based on chemical similarities between Ba and Sr, both belonging to alkaline earth metals in group 2 of the periodic table, one can speculate that Ba competes with Sr in reacting with other elements that are otherwise part of the high energy Sr-phase. In this light, barium would prevent strontium to form secondary phases by depriving it of necessary reagents and reacting with them instead. Determination of the exact mechanism of improvement is however not possible form the data presently at hand.

6.4 Conclusion

Thin film $La_{0.6}Sr_{0.4}FeO_3$ electrodes were investigated by electrochemical impedance spectroscopy at different temperatures (from 387 to 594°C), different pO_2 (0.05 – 1 bar), and the stability was tested over 60 hours at 491°C. The performance of the electrodes modified with Sr-, Fe-, Ce- and Gd-, Ba-, and Zr-nitrate solutions was compared with the non-modified electrode. The electrodes modified with Sr-nitrate performed up to 50% worse than the non-modified electrode, while the activation energies of ASR and oxygen exchange coefficients increased. XPS analysis of these electrodes revealed much higher amount of non-lattice Sr. Unfortunately, modification with Zr- and Fe-nitrate had two effects; i) the intended chemical modification of the surface composition, but also ii) a non-intended damage of the electrode surface due to chemical etching. For this reason, the absolute values of ASR and oxygen exchange coefficients could not be calculated (since the surface area of the electrode is no longer accurately known). However, the activation energies were significantly lower indicating a change in ORR mechanism. CGO-modified electrodes also had much lower activation energies and the oxygen exchange activity increased at low temperature. However , the effect of the modification decreased with the increasing amount of surface addition. Therefore, surface modification with CGO seems a promising way for improving the performance of LSF electrodes at low temperatures for modifications with additions of less than 1 µmol/cm^2. The most interesting results were found for electrodes modified with barium-nitrate. The performance of Ba-modified electrodes was slightly better than the non-modified electrode, while the stability was significantly improved. XPS analysis reveals that the stabilization is likely related to preventing the formation of a detrimental Sr-rich phase. The ASR value found for the Ba-modified electrodes after 7 days of electrochemical testing was around 10 Ωcm^2 at 491°C pO_2=1, while all other modified electrodes had 3-12 times higher ASR.

Supplementary Information

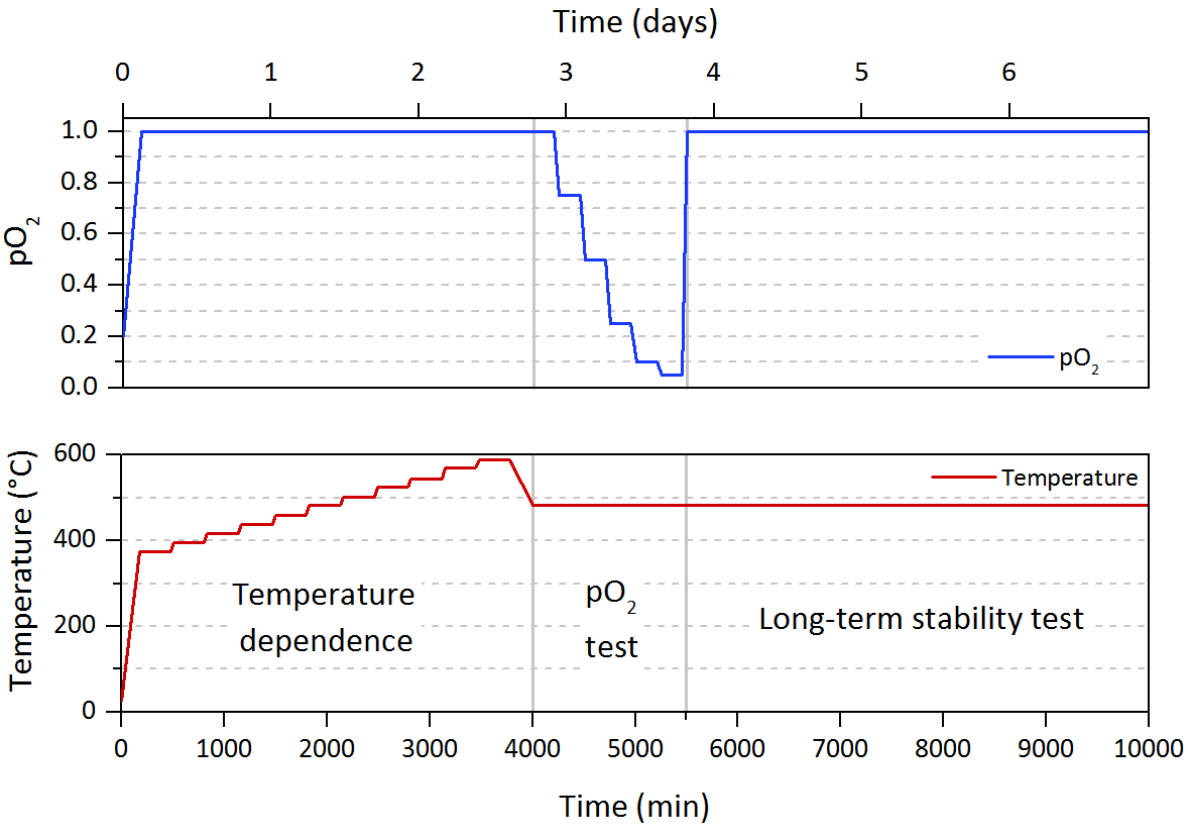

Figure 6.14: Sketch of the experimental procedure.

CHAPTER 7

Summary and Outlook

This thesis aimed towards a better understanding of processes at the gas-solid interface on the oxygen electrode of solid oxide cells, especially with regards to surface chemistry. Throughout the thesis, it was shown that nature the surface of typical MIEC materials is dynamic, significantly different from bulk, and most importantly, a crucial factor in determining the rate of oxygen exchange kinetics.

Chapter 1 showed that the addition of Ruddlesden-Popper phase(s) has a mild effect on oxygen exchange kinetics of $(La_{0.6}Sr_{0.4})_{0.99}FeO_3$. An important distinction was made between the actual and the apparent surface exchange activity which may be higher only because of an increase in active surface area. On the other hand, it was shown that the enhancement in the cobaltite system $(La_{0.6}Sr_{0.4})_{0.99}FeO_3/LaSrCoO_4$ could not be explained in this way. This proved that perovskite/Ruddlesden-Popper interfaces have a beneficial effect on oxygen exchange kinetics in cobaltite systems, albeit not as high as reported in the literature. The study has also revealed a significant scatter in the literature values for the materials of nominally the same composition which was higher than the effect of the surface modification with the Ruddlesden-Popper phase. Based on these conclusions, we can give the following guidelines for future studies:

(i) When modifying the surface of electrode materials with ORR/OER-active phases, one must consider possible effects of the increase in the active surface area.

(ii) Due to inconsistencies in the literature values, very different conclusions of the surface modification can be made depending on the used reference values, i.e., comparing the modified electrode with a poorly performing reference results in high, but erroneous enhancement factors.

Chapter 2 dealt with the problem of inconsistencies in the literature values, showing the importance of the thermal history of the sample for the oxygen exchange activity on $(La_{0.6}Sr_{0.4})_{0.99}FeO_3$ and $(La_{0.6}Sr_{0.4})_{0.99}CoO_3$. The two distinct states of the perovskite surface ('activated' and 'passive') differ almost 60 times in terms of k_{chem} values measured at 650°C on $(La_{0.6}Sr_{0.4})_{0.99}FeO_3$ bar. The transition from one state to another was found to be reversible and to follow Avrami-type behavior characteristic to (re)crystallization phenomena. Proposals for future studies in this direction include:

(i) Similar model electrode studies on the related materials – It would be worthwhile to test the extent of activation/passivation phenomena in other perovskite materials

such as $(La_{1-x}Sr_x)(Co_{1-y}Fe_y)O_{3-\delta}$, $(Ba_{1-x}Sr_x)(Co_{1-y}Fe_y)O_{3-\delta}$ $(La_{1-x}Srx)(Co_{1-y}Ni_y)O_{3-\delta}$, but also perovskite-related materials such as $PrBaCo_2O_{5+\delta}$ and $LaNiO_{4+\delta}$.

(ii) A systematic study of samples with different grain sizes - It was postulated that the amount of grain boundaries has an effect on the susceptibility of the sample to activate/passivate.

(iii) Influence of A/B stoichiometry – Both LSF and LSC samples in this study were A-site substoichiometric. Therefore, it would be useful to test the effect by a systematic variation of A/B ionic ratios.

(iv) Application of the thermal activation in the current technological electrodes. Occasional thermal treatments (every 3-4 days) above 800°C can enable the electrode to reach the 'activated' and perform significantly better at intermediate temperatures (500-700°C).

Chapter 3 revealed the correlation between the activation/passivation phenomena the surface chemistry analyzed by XPS. The chemical state of strontium was found to be particularly important. Passivation of the surface was correlated with an increase in high-energy ('non-lattice') strontium, but also with noticeable changes on the perovskite surface. SEM analysis of the samples quenched at different stages of passivation showed gradual appearance of nanoparticulate precipitates and several hundreds of nanometer-sized plate-like particles identified as $SrSO_4$. Activation was postulated to occur via surface reconstruction, where at high temperatures the strontium from the secondary phases gets dissolved in the perovskite lattice. Some unresolved aspects of this study could be the subject of future studies including:

(i) The composition of the nanoparticulate precipitates – As often the reported in the literature, we assumed that the nanoparticulate precipitates are strontium oxide (SrO_x). However, the exact composition/structure of the precipitates cannot be stated from the data at hand. It should be noted that such information would not fundamentally affect the conclusion given in this study, but it could reveal how to prevent/slow-down the passivation.

(ii) Direct observation of surface reconstruction – XPS quantification strongly indicated that the perovskite surface terminates with the Ruddlesden-Popper phase, which was also speculated in the literature. A high-resolution imaging technique such as high-angle annular dark-field scanning transmission electron microscopy (HAADF-STEM) of the outermost surface layers could be used for this purpose.

(iii) Investigation of surface reconstruction in powders - The surface reconstruction is expected to take place on the surface of individual powder particles as well. By using powdered samples and environmental TEM the surface reconstruction could possibly be observed *in situ*.

Chapter 4 showed the importance of the same activation/passivation phenomena in the thin films and at temperatures below 600°C. The state of low oxygen activity was, similarly to the previous chapters, correlated with the higher amounts of 'non-lattice' strontium. Once passivated, the electrode performance could be reactivated by rinsing the surface in deionized water. The activation was postulated to be a consequence of the dissolution of the impeding Sr-rich phases. After two cycles of rinsing, the passivation was found to slow down. A few points that have not been thoroughly assessed in this study but may contribute to further understanding include:

(i) The effect of thin film thickness – Slower passivation rate after two cycles of rinsing was interpreted as depletion of Sr from the bulk of the thin film electrode. A systematic study of the thin film electrodes with different thicknesses could be used to test this hypothesis; film thicker than 215 nm will probably take more than two cycles to slow-down the degradation.

(ii) A study of Sr-depleted electrodes - Instead of removing excess strontium in several rinsing cycles, one could possibly achieve a similar effect by depositing thin film electrodes from strontium depleted PLD targets.

Chapter 5 examined the effect of adding different metal-nitrates to the surface on thin film LSF electrode on oxygen exchange activity. Modification with Fe(III)- and Zr(IV)-nitrates resulted in severe damage of the electrodes as a consequence of acidity of the solutions. Modification with Sr had only a relatively weak effect by impeding the oxygen exchange activity by approximately 50%. Modification with CGO resulted in lower activation energy, but the improvements in performance could be obtained only below 500°C and at small amount of modification. The most interesting results were obtained on electrodes modified with barium, which improved the electrode stability by preventing the formation of impeding secondary phases of strontium. Possible directions of future studies can be:

(i) Further fundamental studies of the beneficial effect of barium - How exactly barium prevent the formation of impeding secondary phases of strontium cannot be stated at the moment.

(ii) Implementation of Ba in technological electrodes – based on the results obtained in this study, improved activity and stability of the electrodes can be expected. The best results can be obtained by modification with 1 µmol/cm^2 (or possibly lower).

APPENDIX A

ECReX - ECR data fitting tool for experimentalists

ECReX is an MATLAB application based on the work of Ciucci[177] and Otter *et al.*[19] *ECReX* is created in order to address the issues frequently experienced by the experimentalists conducting ECR and features options such as batch fitting, smoothing, flush-time correction, plotting, etc. It can be downloaded for free as a stand-alone application or MATLAB scripts from `https://sites.google.com/view/ecrex`. Figure A.1 shows the main window of *ECReX* application used for analysis and fitting of ECR data.

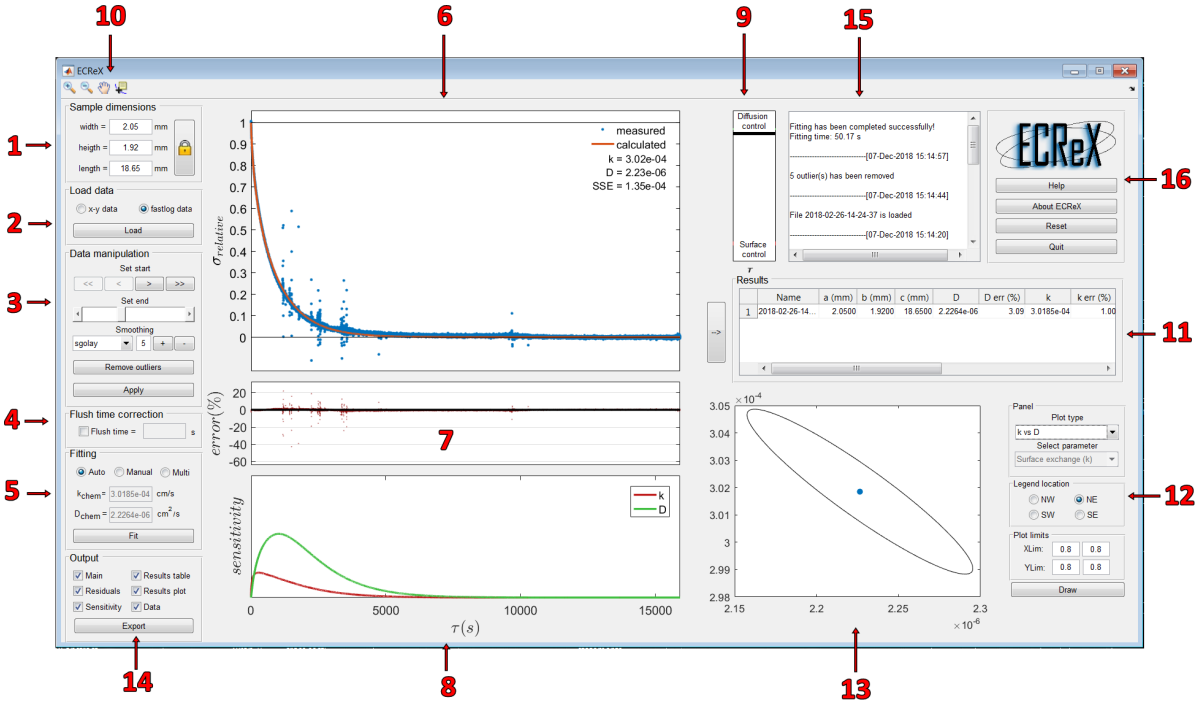

Figure A.1: *ECReX* application main window. The explanations of each numbered part can be found in the text.

1. **Sample dimensions** - this section is used for inserting the dimensions of the analyzed rectangular sample in millimeters. 'Lock' option can be convenient if

the same sample is analyzed at different experimental conditions. This option overrides 'Reset' function;

2. **Load data** – *ECReX* can import two kinds of data files.
   - *X-Y data* option is used for import of *.txt* or *.xy* files with data sorted in two columns. The first column must contain time in seconds and the second column can be any property that changes over time. In ECR this column contains electrical conductivity, but one can also use mass, optical properties, etc. The values can either absolute or relative since, after hitting the button 'Load', data will be re-normalized.
   - *fastlog data* is a DTU-specific format that contains additional experimental parameters such as pO_2, temperature, UNIX time, etc.
3. **Data manipulation** – once imported, the data can be manipulated to remove artifacts from the measurement. NOTE: Data manipulation affects the fitting procedure!
   a) *Set start* option allows the user to assign the start of the relaxation manually. The collection of data may precede the actual start of relaxation (first noticeable changes of the measured property). Failing to correct for this temporal misalignment can lead to wrong estimation of k_{chem} values (usually lower than actual).
   b) *Set end* option has a similar purpose. It can be used to cut the data points collected after the relaxation has taken place (measured values become constant). This can save some computational time, but cutting data points before the constant values are reached will affect the estimation of D_{chem}.
   c) *Smoothing* can be used to improve noisy data. Depending on the quality of data, users can choose the degree and the smoothing function.
   d) *Remove outliers* allows the user to select and remove outliers.
4. **Flush time correction** - this option implements model from Otter et al.[19] and enables fitting of data from a non-ideal experiment where the time constant of pO_2 step change (reactor flushing time) cannot be neglected.
5. **Fitting** - there are three ways of fitting data using ECReX, yet all of them are based on the same equations (Crank's solution).[17]
   - *Auto fit* - the program successively attempts to fit the data by using different values of k_{chem} and D_{chem} and stops once it reaches the minimum sum of standard deviations (SSD). This option usually works fine with high-quality data, yet the user should be aware of the possibility of reaching a local minimum.
   - *Manual fit* - gives the user full control of exploring different parameter values. This can be useful for 'locking' parameters. For example, for the analysis of purely surface phenomenon, the user might want to lock D_{chem} values related to bulk.

- *Multi fit* - this option is useful for fitting large sets of data. All data that has been loaded to the 'Results' table, but not yet analyzed, will be fitted successively in the same way as if the 'Auto' fit option was used.

6. **Main plot** - shows measured and calculated relative conductivity values over time. Current fitting parameters are shown in the upper right corner.

7. **Error plot** - Error plot – graphically shows residuals, i.e. differences between measured data and fitted values in percentages.

8. **Sensitivity plot** - illustrates the sensitivity of k_{chem} and D_{chem} at different points in the experiment. This can be handy for the estimation of the total time needed for the relaxation experiment.

9. **Regime scale** - shows whether the experiment is in surface-, mixed-, or diffusion-controlled regime based on calculated L_α (see Equations 1.5-1.7).

10. **Navigation tools** - to help data manipulation and fitting, the navigation tools can be used to zoom in and out, move the plots and read individual data points.

11. **Results table** - lists all saved measurements. The user can edit the name of the measurement/sample (the default one is inherited from the data file name) and enter the experimental conditions (temperature, pO_2, time). One populates the table by pressing the arrow button (between the table and the main plot).

12. **Plotting panel** - allows the user to plot the selected results from the 'Results' table in one of the four possible ways: k_{chem} vs. D_{chem}, Arrhenius-type plot, pO_2-dependence, long-term stability plot.

13. **Results plot** - shows the selected results. Plot parameters can be changed in the Plotting panel (12).

14. **Export** this option serves to export the data after data manipulation (and fitting). The user can select which plots and data will be saved.

15. **Console** - shares all relevant information with the user while working in $ECReX$.

16. A set of buttons used for resetting, quitting and getting further information about the application.

APPENDIX B

Note on XPS quantification procedure

Quantification of surface composition is based on the comparison of areas of selected XPS peaks. Therefore the first step is correct estimation of peak areas. This can be challenging for some peaks, due to several reasons:

1. peaks may overlap,
2. peak intensity is too small,
3. noisy data,
4. background assignment when the peak sits on a 'shoulder';

For all these reasons, there is an intrinsic uncertainty in XPS quantification due to estimation of peak area. Once the peak areas are determined, the relative atomic content of a component is proportional to the peak area of that component divided with total area of all peaks:

$$\%X_i = \frac{C_i}{\sum_{i=1}^{n} C_i} \sim \frac{Area_i}{\sum_{i=1}^{n} Area_i} \tag{B.1}$$

However, the proper quantification requires several corrections:

1. *Relative sensitivity factors (RSF) based on Scofield cross-sections* – represent the probability for photoemission from a specific electronic state and are based on quantum-mechanical calculations. The probability associated with each peak (RSF) is scaled relatively to carbon C $1s$ peak which has $RSF = 1$;
2. *Angular distribution correction* – a consequence of geometry of the used instrument if the angle between X-ray source and the analyzer is not 54°44' (magic angle);
3. *Transmission function correction* – instrument-related characteristic that accounts for signal attenuation as a function of kinetic energy as it passes through lens system, hemispherical analyzer and the detection system.

4. *Escape depth correction* – photoelectrons are subject to inelastic scattering before escaping the materials. If the peaks used for quantification are of very different binding energies, then the associated photoelectrons can escape from different depths.

Usually, the first three corrections are readily available and implemented by instrument manufacturer. If not, the corrections can be made by calibrating the instrument with a clean and homogenous sample with several well resolved photoelectron peaks (e.g. gold, platinum). The necessity of escape depth correction depends on the selection of peaks for quantification, as well as sample itself. For example, thin carbon layer on samples surface can alter the quantification results due to inelastic scattering of the photoelectrons passing through it. In the ideal case, when no escape depth correction is needed the calculated relative amount of a particular element should be independent of the particular peak used for quantification. For instance, it should not matter whether for quantification of lanthanum in (La,Sr)FeO_3 we use La $3d_{5/2}$ (850 eV), La $3d_{3/2}$ (833 eV), La $4p$ (195 eV) or La $4d$ (104 eV) and divide it with corresponding RSFs, the relative amount of La should be the same. However, in reality the peaks at lower binding energies (higher photoelectron kinetic energies) will be more prevalent since they stem from larger volume (information depth is larger).

A quick way to check if the escape depth correction is needed is to do a quasi-quantification of a single element by comparing contributions from each peak. Using the same example as above, a quasi-quantification of lanthanum should in ideal case give 1/4 (25%) contribution of each peak. If two peaks are used then the ideal result should be 50%:50%, three peaks should give 33%:33%:33% and so on.

Figure B.1 illustrates how escape depth correction can influence the quantification of XPS results in case of LSF sample (day 1). Quasi-quantification is done for La ($3d_{5/2}$, $3d_{3/2}$, $4p$ and $4d$ peaks), Sr ($3s$ and $3d$ peaks) and Fe ($2p$ and $3p$ peaks). It can be seen that when no escape depth correction is applied the peaks at lower BE contributed more than peaks at higher BE. Three different kinds of escape depth corrections available in $CasaXPS$ are compared:

1. *Effective attenuation length correction* - based on equation given by Seah[178] applicable to clean surfaces;

2. *Kinetic energy exponent* – a correction based on assumption that escape depth changes exponentially with kinetic energy[179] ($intensity = K.E.^n$). Parameter n usually takes values between -0.5 and -0.7. However, in this study the closest to ideal case was obtained for the n = -1.6 (shown in the Figure B.1).

3. Carbon layer thickness – this correction is based on the assumption that the inelastic scattering is mainly a consequence of a carbon layer on the surface which is accounted for by using Hill equation.[180] $CasaXPS$ allows the change of parameter CH which corresponds to the layer thickness. The closest to ideal results in this case are obtained for the $CH = 3$. However, in case of 'as polished' sample which had significantly more carbon the ideal conditions were met at $CH = 4$.

The plot on the bottom of Figure B.1 shows how different corrections effect the quantification of LSF based on areas of La $3d$ (850 eV), Fe $2p$ (710 eV) Sr $3d$ (131 eV) peaks. Since Sr peak as much lower binding energy, its photoelectrons will have higher kinetic energy enabling more of them to make through the carbon layer and to the detector. So, if no escape depth correction is applied the amount of Sr will be overestimated, while the amounts of La and Fe will be underestimated.

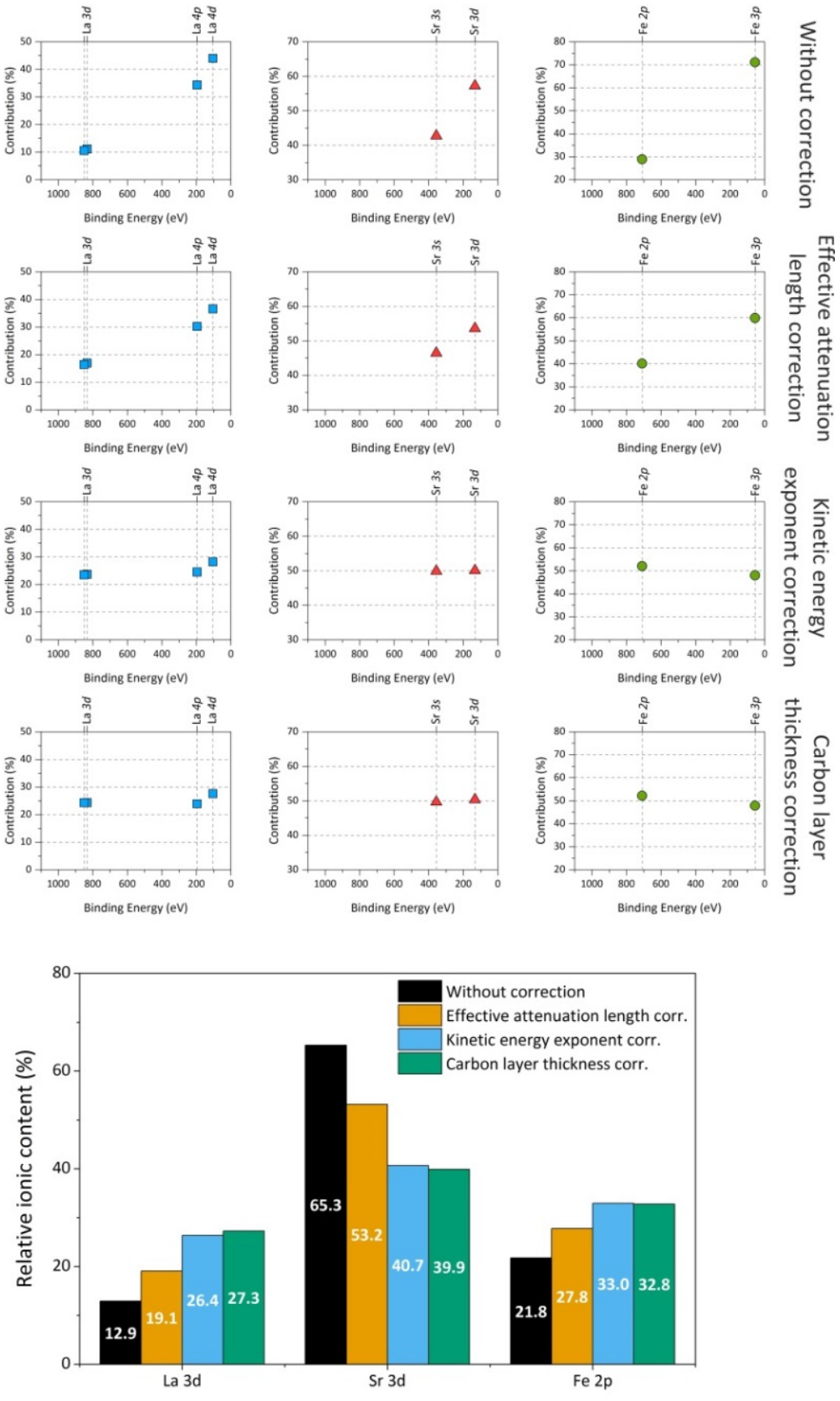

Figure B.1: An illustration of the importance of escape depth correction for quantification of XPS results in the case of LSF (day 1) from Chapter 4.

APPENDIX C

A simple model for the estimation of sheet resistance in thin film model electrodes

Geometry factors can play an important role in thin film model systems characterized by electrochemical impedance spectroscopy (EIS). The effect is expected to become severe for very thin films with low electronic conductivity. This can be prevented, to some extent, by better current collection (CC), i.e. by lowering the distance between CC terminals. There are physical limits to this approach due to limitations of pattering techniques. A simple analytical model has been developed to give guidance on design of thin film model electrodes for EIS studies with the aim of preventing geometry interference. The examined CC setup lies somewhere between discrete contact points (mesh CC) and grid-like CC and as such should give overall sense of impact of particular parameters. For that purpose, a simple 2D model is discussed below.

Figure C.1 shows schematic illustration of thin film model electrode. Current collection (CC) is provided by stripes of a perfect conductor. Thin film is mixed ionic and electronic conductor (MIEC). Electrolyte is ionic conductor and electronic insulator. The symmetry of system allows us neglect y-axis and to focus on a discrete domain indicated by dashed rectangle. Thicknesses of MIEC and electrolyte are t and t_{el}, respectively. Half width of CC stripe is d and distance between them is L.

The approach in estimation of geometry impact will be to compare potential, current and resistance values for thin film of thickness t, electrical conductivity σ, current collector width d, and CC spacing l, versus the ideal case. Figure C.2 shows schematically paths of the species involved in ORR reaction.

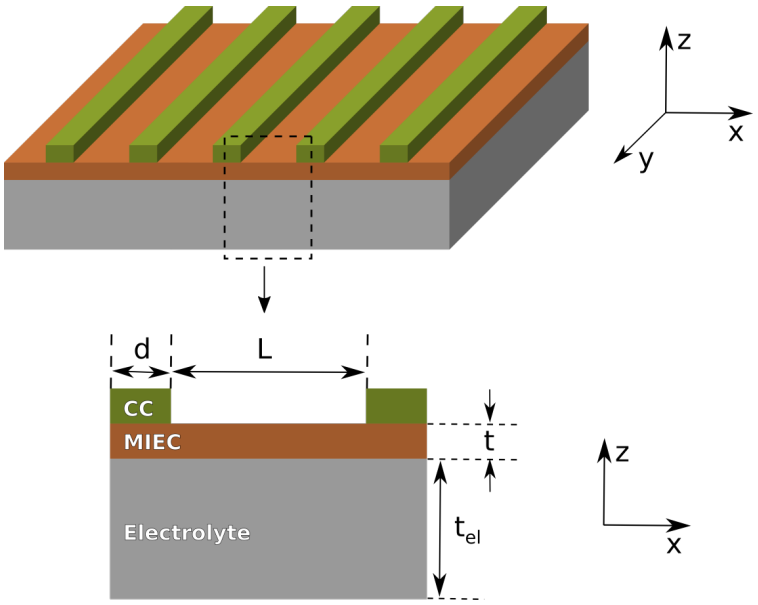

Figure C.1: Schematic illustration of model system geometry.

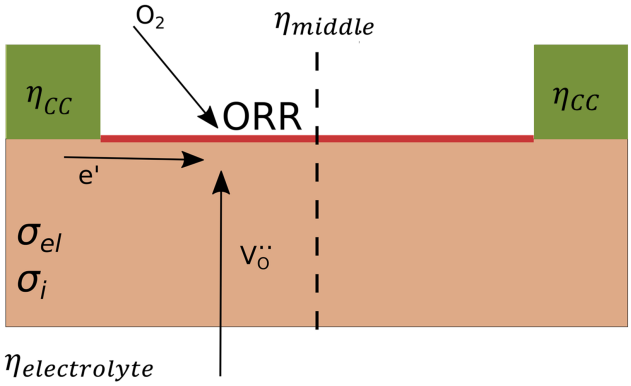

Figure C.2: ORR mechanism on MIEC thin film surface.

Potential distrubution

The first task is to express electric potential as a function of distance from current collector. As already mentioned, there is no change of potential in y direction due to chosen CC geometry, while change in z direction can be neglected since $L \gg t$. Charge conservation law is expressed in equation C.1. Term $\partial q/\partial t$ is the change of the amount of charge in time $[Cs^{-1}m^{-3}]$, J stands for current density $[A/m^2]$ and Q is accumulation/depletion of charge in system $[A/m^3]$.

$$\frac{\partial q}{\partial \tau} + \nabla j = Q \tag{C.1}$$

We consider steady state, DC case ($\omega \to 0$), therefore term $\partial q/\partial t$ equals to zero. Due to chosen geometry, spatial change in current density (∇j) simplifies to dj/dx and is solely a consequence of ORR reaction at the surface which acts as a sink for electrons. Here we assume that source of oxygen vacancies, also needed for ORR reaction, is constant and abundant all over the system. Equation C.1 now becomes:

$$\frac{dj}{dx} = \frac{\text{density of ORR current} \cdot \text{area}}{\text{volume}} = \frac{j_{ORR} \cdot L \cdot y}{t \cdot L \cdot y} = \frac{j_{ORR}}{t} \tag{C.2}$$

In the equation above, j_{ORR} $[A/m^2]$ stands for ORR current density entering the system through the surface, along z-axis. Experimental setup of EIS requires small changes of potential which leads to linear current response. Thus, we can assume j_{ORR} to be directly proportional to the difference between potential at current collector and electrolyte, and inversely proportional to surface resistance R_S $[m^2]$. For simplicity, we will lock potential of electrolyte at 0. We can write the following:

$$\frac{dj}{dx} = \frac{\eta_{CC} - \eta_{electrolyte}}{R_S \cdot t} = \frac{\eta_{CC} - 0}{R_S \cdot t} = \frac{V}{R_S \cdot t} \tag{C.3}$$

Current density on the left-hand side can be expressed through microscopic Ohm's law $J = (\sigma_e + \sigma_i) \cdot E$, where $E = dV/dx$ is electric field. Assuming that $\sigma_{\gg}\sigma_i$ we can write:

$$\frac{d}{dx}(\sigma_e \frac{dV}{dx}) = \frac{V}{R_S \cdot t} \tag{C.4}$$

We can extract constants and rearrange the equation:

$$\frac{d^2V}{dx^2} - \frac{V}{\sigma_e \cdot R_S \cdot t} = 0 \tag{C.5}$$

This is a second-order linear differential equation of form:

$$V'' - \alpha V = 0 \tag{C.6}$$

Where α is a constant and in our case it is:

$$\alpha = \frac{1}{\sigma_e \cdot R_S \cdot t} \tag{C.7}$$

Parameter α lumps together properties which are expected to affect potential distribution and for future analysis we can consider that higher α values mean that obtaining ideal distribution is more challenging. It could be the case when film is very thin, conductivity is small or when surface reaction is fast.

General solution of equation 8 can easily be proven to be:

$$V(x) = C_1 e^{\sqrt{\alpha}x} + C_2 e^{-\sqrt{\alpha}x} \tag{C.8}$$

In order to find constants C_1 and C_2 we apply the following boundary conditions:

$$x = 0 \rightarrow V = V_0 \tag{C.9}$$

$$x = L \rightarrow V = V_0 \tag{C.10}$$

We get system of two equations with two unknowns:

$$(\text{Eq. } C.9) \rightarrow C_1 + C_2 = V_0 \tag{C.11}$$

$$(\text{Eq. } C.10) \rightarrow C_1 e^{\sqrt{\alpha}L} + C_2 e^{-\sqrt{\alpha}L} = V_0 \tag{C.12}$$

Constants C_1 and C_2 can now be expressed:

$$C_1 = V_0 \frac{1}{e^{\sqrt{\alpha}L} + 1} \tag{C.13}$$

$$C_2 = V_0 \frac{e^{\sqrt{\alpha}L}}{e^{\sqrt{\alpha}L} + 1} \tag{C.14}$$

After inserting constants and rearranging equation 10 we get voltage dependence across the gap:

$$V(x) = \frac{V_0}{e^{\sqrt{\alpha}L} + 1}(e^{\sqrt{\alpha}x} + e^{\sqrt{\alpha}(L-x)}) \tag{C.15}$$

The maximal voltage drop (minimum voltage) is at:

$$\frac{dV}{dx} = 0 \tag{C.16}$$

$$\frac{V_0\sqrt{\alpha}}{e^{\sqrt{\alpha}L} + 1}(e^{\sqrt{\alpha}x} + e^{\sqrt{\alpha}(L-x)}) = 0 \tag{C.17}$$

$$x = \frac{L}{2} \tag{C.18}$$

As expected, voltage is at minimum in the middle of gap and its value is:

$$V(L/2) = 2V_0 \frac{e^{\sqrt{\alpha}L/2}}{e^{\sqrt{\alpha}L} + 1} = V_{middle} \tag{C.19}$$

The ratio between V_{middle}/V_0 will serve as an indicator of impact of sheet resistance on voltage distribution:

$$\frac{V_{middle}}{V_0} = 2\frac{e^{\sqrt{\alpha}L/2}}{e^{\sqrt{\alpha}L} + 1} \tag{C.20}$$

As expected, the sheet resistance is more pronounced when thickness and conductivity are reduced, CC spacing is bigger and ORR reaction is faster (R_S is smaller).

Electrical current

We will now examine measured current in the similar manner. Here, the indicator of impact of geometry will be the ratio of current expected for the case when potential is distributed following the equation C.15 versus the case when it is uniformly distributed across the whole film and equal to potential of current collector. In the latter, ideal case, current will be equal to the applied potential divided by surface reaction resistance (R_S).

$$I_{ideal} = j_{ORR}A = \frac{V_0}{R_S} \cdot L \cdot y \tag{C.21}$$

For the case with significant geometry impact, the local electrical potential will influence flow of current. We also assume that small changes in potential will not influence rate of chemical reaction on surface ($R_S = const$).

$$I_{real} = j_{ORR}(x) \cdot A = \int_0^L \frac{V(x)}{R_S} \cdot y \cdot dx = \frac{V_0}{R_S} \cdot y \cdot \frac{2 \cdot tanh(\frac{\sqrt{\alpha}L}{2})}{\sqrt{\alpha}} \tag{C.22}$$

By combining equation C.21 and C.22 we get:

$$I_{real} = \frac{I_{ideal}}{L} \frac{2 \cdot tanh(\frac{\sqrt{\alpha}L}{2})}{\sqrt{\alpha}} \tag{C.23}$$

Therefore:

$$\frac{I_{real}}{I_{ideal}} = 2\frac{tanh(\frac{\sqrt{\alpha}L}{2})}{L\sqrt{\alpha}} \tag{C.24}$$

DC resistance

Let us now examine, perhaps the most important parameter, namely DC resistance of the film. If voltage drop is significant, it leads to lower effective values of electrical current which can be erroneously interpreted as increase in ORR surface resistance. In ideal case we apply voltage V_0 and get current I_{ideal} as a consequence of surface resistance R_s. In real case for applied voltage V_0 we get current I_{real} as a consequence of surface resistance R_S plus a contribution R_α due to geometry.

$$I_{ideal} = \frac{V_0}{R_S} \tag{C.25}$$

$$I_{ideal} = \frac{V_0}{R_S + R_\alpha} \tag{C.26}$$

$R\alpha$ can be expressed as:

$$R_\alpha = \frac{V_0}{I_{real}} - R_S = \frac{V_0}{I_{real}} - \frac{V_0}{I_{ideal}} = V_0(\frac{1}{I_{real}} - \frac{1}{I_{ideal}}) \tag{C.27}$$

By inserting equation C.23 we get:

$$R_\alpha = R_S \frac{\frac{\sqrt{\alpha}L}{2} - tanh(\frac{\sqrt{\alpha}L}{2})}{tanh(\frac{\sqrt{\alpha}L}{2})} \tag{C.28}$$

Finally, we can write an equation which describes the effective increase of DC resistance as a consequence of current collector position, material conductivity, the rate of oxygen exchange, and film thickness.

$$R_{DC} = R_S + R_\alpha = R_S(1 + \frac{\frac{\sqrt{\alpha}L}{2} - tanh(\frac{\sqrt{\alpha}L}{2})}{tanh(\frac{\sqrt{\alpha}L}{2})}) = R_S \frac{\sqrt{\alpha}L}{2} coth(\frac{\sqrt{\alpha}L}{2}) \tag{C.29}$$

$$R_{DC} = L\sqrt{\frac{R_S}{\sigma_e t}} coth(\frac{L}{\sqrt{\sigma_e R_S t}}) \tag{C.30}$$

Parameters investigation

Voltage and current values

Contour plots illustrating voltage drop in the middle of the gap as a function of gap size and dimensionless parameter α are shown in figure C.3. Black lines stand for voltage, blue for current. Shaded area indicates the region where pattering by masking and sputtering becomes challenging. From the graph it is possible to estimate minimum film thickness required to overcome certain threshold in voltage drop, for the given surface reaction resistance and conductivity. For instance, if we decide to put threshold at 99% (we tolerate voltage drop of only 1%), use a material that has electrical conductivity 100 S/cm and surface reaction resistance of 2.5 Ωcm^2, inability of patterning CC features below 100 μm would require film thicker than 50 nm. Putting the same threshold on current, would lead to thickness limit of 35 nm.

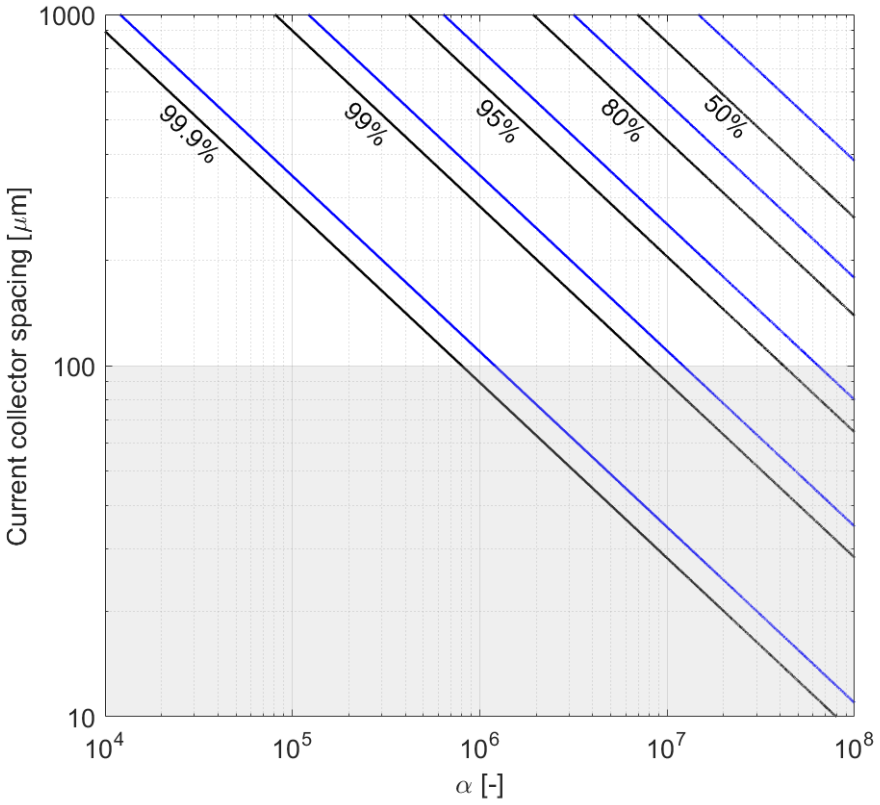

Figure C.3: The effect of current collector spacing and dimensionless parameter α on apparent voltage and current values.

DC resistance

In order to qualitatively illustrate impact of film thickness, conductivity, CC spacing and R_S on apparent DC resistance we make use of the equation C.30. Figure C.4 shows R_{DC} dependence on thickness for different CC spacing. Note that an identical plot can be obtained if we plot R_{DC} as a function of conductivity and keep thickness constant. Similarly, figure C.5 shows R_{DC} dependence on spacing for different thicknesses (or conductivity). Figure C.5 shows that R_{DC} values asymptotically reach RS (experimental aim), with increasing thickness while smaller CC spacing facilitate this trend. Figure C.6 show that R_{DC} departure from R_S is increasing with CC spacing. As expected, this effect is more pronounced for thinner films.

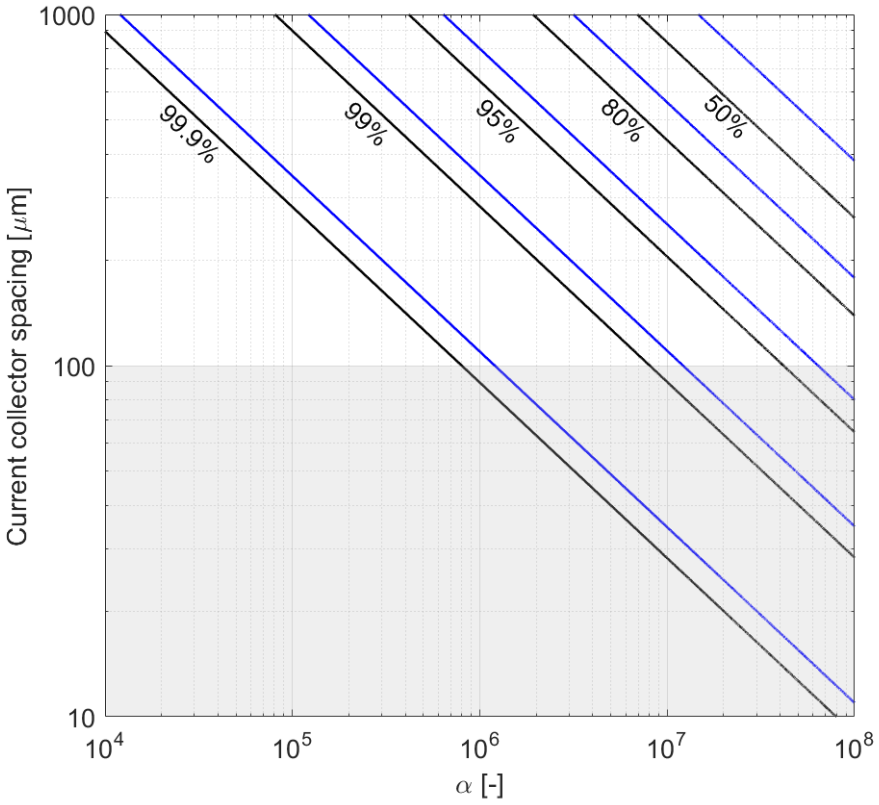

Figure C.4: Qualitative illustration of R_{DC} values as a function of film thickness for different CC spacing.

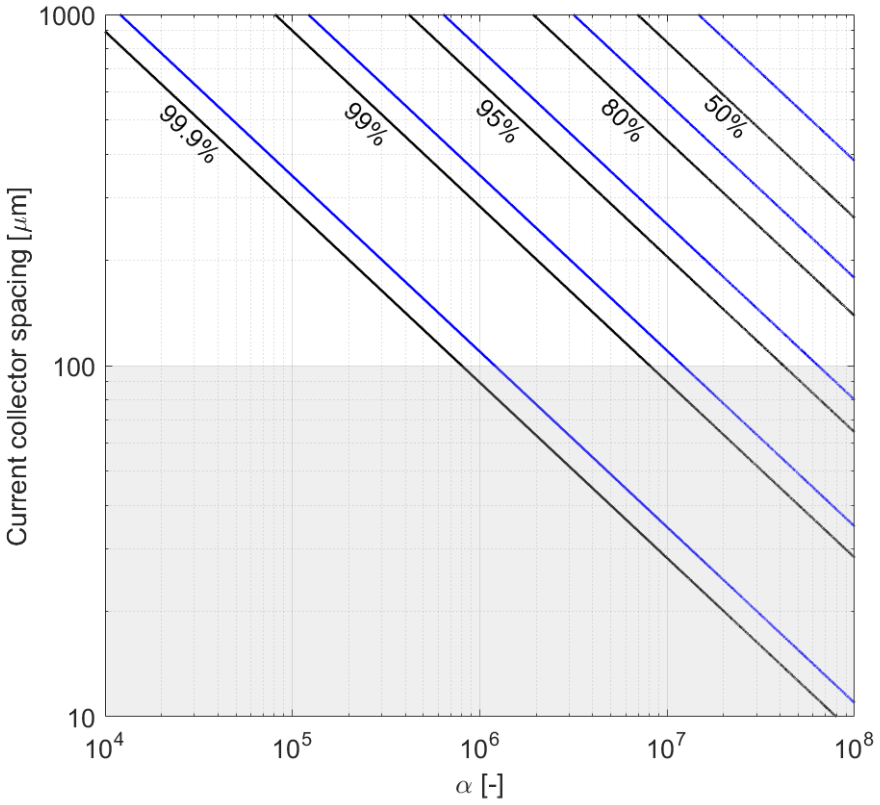

Figure C.5: Qualitative illustration of R_{DC} values as a function of CC spacing for different film thickness.

Quantitative analysis of geometry effect on R_{DC} can be performed in similar way as for current and voltage, by employing contour plot and dimensionless parameter α (Figure C.6). The same information can be extracted from C.3 by using equation C.26. Apparent current values are also plotted for comparison.

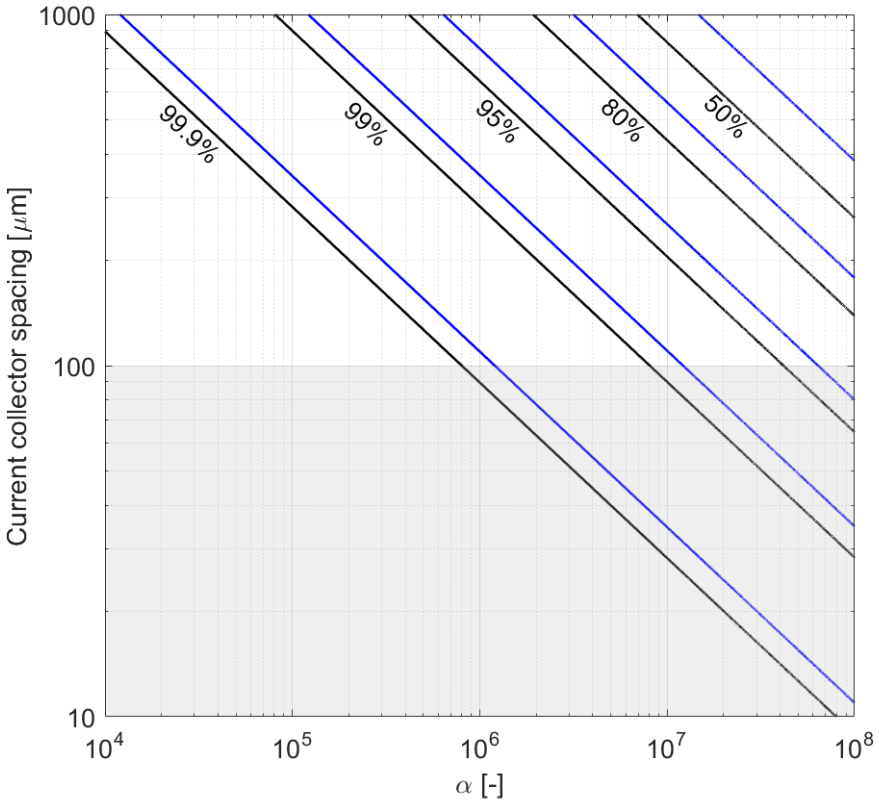

Figure C.6: Contour plot illustrating geometry contribution (R_α) to R_{DC} response. Blue lines represent current values.

Bibliography

(1) The State of the Global Climate in 2018., World Meteorological Organization, 2018.

(2) Convention on Climate Change: Climate Agreement of Paris., United Nations, 2015, pp 1–27.

(3) Technology Roadmap - Energy Storage., International Energy Agency, 2014.

(4) Graves, C.; Ebbesen, S. D.; Mogensen, M.; Lackner, K. S. *Renewable and Sustainable Energy Reviews* **2011**, *15*, 1–23.

(5) Mitterdorfer, A; Gauckler, L. J. *Solid State Ionics* **1998**, *111*, 185–218.

(6) Mogensen, M.; Sammes, N. M.; Tompsett, G. A. *Solid State Ionics* **2000**, *129*, 63–94.

(7) Kharton, V. V.; Marques, F. M.; Atkinson, A. *Solid State Ionics* **2004**, *174*, 135–149.

(8) Mori, M. *Journal of The Electrochemical Society* **1998**, *145*, 1374.

(9) Trini, M.; Jørgensen, P. S.; Hauch, A.; Chen, M.; Hendriksen, P. V. *ECS Transactions* **2017**, *78*, 3049–3064.

(10) Adler, S. B. *Chemical Reviews* **2004**, *104*, 4791–4843.

(11) Shao, Z.; Haile, S. M. *Nature* **2004**, *431*, 170–173.

(12) Sayers, R.; De Souza, R. A.; Kilner, J. A.; Skinner, S. J. *Solid State Ionics* **2010**, *181*, 386–391.

(13) Boehm, E.; Bassat, J. M.; Dordor, P.; Mauvy, F.; Grenier, J. C.; Stevens, P. *Solid State Ionics* **2005**, *176*, 2717–2725.

(14) Brett, D. J. L.; Atkinson, A.; Brandon, N. P.; Skinner, S. J. *Chemical Society Reviews* **2008**, *37*, 1568.

(15) Hagen, A.; Barfod, R.; Hendriksen, P. V.; Liu, Y.-L.; Ramousse, S. *Journal of The Electrochemical Society* **2006**, *153*, A1165.

(16) Druce, J.; Téllez, H.; Ishihara, T.; Kilner, J. a. *Faraday Discuss.* **2015**, *182*, 271–288.

(17) Crank, J. *Oxford University Press* **1975**, 414.

(18) Carslaw, H. S.; Jaeger, J. C.; Feshbach, H. *Physics Today* **1962**, *15*, 74–76.

(19) Den Otter, M. W.; Bouwmeester, H. J. M.; Boukamp, B. A.; Verweij, H *Journal of The Electrochemical Society* **2001**, *148*, J1.

(20) Sase, M; Hermes, F; Yashiro, K; Sato, K; Mizusaki, J; Kawada, T; Sakai, N; Yokokawa, H *J Electrochem Soc* **2008**, *155*, B793–B797.

(21) Crumlin, E. J.; Mutoro, E.; Ahn, S.-J. J.; La O, G. J.; Leonard, D. N.; Borisevich, A.; Biegalski, M. D.; Christen, H. M.; Shao-Horn, Y.; la O', G. J.; Leonard, D. N.; Borisevich, A.; Biegalski, M. D.; Christen, H. M.; Shao-Horn, Y. *The Journal of Physical Chemistry Letters* **2010**, *1*, 3149–3155.

(22) Sase, M.; Yashiro, K.; Sato, K.; Mizusaki, J.; Kawada, T.; Sakai, N.; Yamaji, K.; Horita, T.; Yokokawa, H. *Solid State Ionics* **2008**, *178*, 1843–1852.

(23) Han, J. W.; Yildiz, B. *Energy & Environmental Science* **2012**, *5*, 8598.

(24) Hayd, J.; Yokokawa, H.; Ivers-Tiffee, E. *Journal of the Electrochemical Society* **2013**, *160*, F351–F359.

(25) Chen, Y.; Cai, Z.; Kuru, Y.; Ma, W.; Tuller, H. L.; Yildiz, B. *Advanced Energy Materials* **2013**, *3*, 1221–1229.

(26) Feng, Z.; Yacoby, Y.; Gadre, M. J.; Lee, Y. L.; Hong, W. T.; Zhou, H.; Biegalski, M. D.; Christen, H. M.; Adler, S. B.; Morgan, D.; Shao-Horn, Y. *Journal of Physical Chemistry Letters* **2014**, *5*, 1027–1034.

(27) Tsvetkov, N.; Chen, Y.; Yildiz, B. *Journal of Materials Chemistry A* **2014**, *2*, 14690.

(28) Ma, W.; Kim, J. J.; Tsvetkov, N.; Daio, T.; Kuru, Y.; Cai, Z.; Chen, Y.; Sasaki, K.; Tuller, H. L.; Yildiz, B. *J. Mater. Chem. A* **2015**, *3*, 207–219.

(29) Stämmler, S.; Merkle, R.; Maier, J. *Journal of The Electrochemical Society* **2017**, *164*, F454–F463.

(30) Lee, D.; Lee, Y.-L.; Hong, W. T.; Biegalski, M. D.; Morgan, D.; Shao-Horn, Y. *J. Mater. Chem. A* **2015**, *3*, 2144–2157.

(31) Hong, T.; Zhao, M.; Brinkman, K.; Chen, F.; Xia, C. *ACS Applied Materials & Interfaces* **2017**, 8659—8668.

(32) Søgaard, M; Hendriksen, P.; Mogensen, M.; Poulsen, F; Skou, E *Solid State Ionics* **2006**, *177*, 3285–3296.

(33) Søgaard, M.; Hendriksen, P. V.; Mogensen, M. *Journal of Solid State Chemistry* **2007**, *180*, 1489–1503.

(34) A.J Jennings; Skinner, S.; Helgason, Ö *Journal of Solid State Chemistry* **2003**, *175*, 207–217.

(35) Ten Elshof, J. E.; Lankhorst, M.; Bouwmeester, H. J. M. *Journal of The Electrochemical Society* **1997**, *144*, 1060.

(36) Egger, A.; Bucher, E.; Yang, M.; Sitte, W. *Solid State Ionics* **2012**, *225*, 55–60.

(37) Li, Y.; Gerdes, K.; Liu, X. *Journal of The Electrochemical Society* **2013**, *160*, F554–F559.

(38) Yashiro, K.; Nakamura, T.; Sase, M.; Hermes, F.; Sato, K.; Kawada, T.; Mizusaki, J. *Electrochemical and Solid-State Letters* **2009**, *12*, B135.

(39) Mosleh, M.; Pryds, N.; Hendriksen, P. V. *Materials Science and Engineering: B* **2007**, *144*, 38–42.

(40) Hjalmarsson, P.; Søgaard, M.; Mogensen, M. *Solid State Ionics* **2008**, *179*, 1422–1426.

(41) Carter, S.; Selcuk, A.; Chater, R. J.; Kajda, J.; Kilner, J. A.; Steele, B. C. *Solid State Ionics* **1992**, *53-56*, 597–605.

(42) Hjalmarsson, P. Strontium and nickel substituted lanthanum cobaltite as cathode in Solid Oxide Fuel Cells., Ph.D. Thesis, 2008.

(43) Hjalmarsson, P.; Søgaard, M.; Mogensen, M. *Solid State Ionics* **2009**, *180*, 1395–1405.

(44) Dalslet, B. T.; Søgaard, M.; Hendriksen, P. V. *Solid State Ionics* **2009**, *180*, 1050–1060.

(45) Dalslet, B. T.; Søgaard, M.; Bouwmeester, H. J.; Hendriksen, P. V. *Solid State Ionics* **2009**, *180*, 1173–1182.

(46) Stevenson, J. W.; Armstrong, T. R.; Carneim, R. D.; Pederson, L. R.; Weber, W. J. *Journal of the Electrochemical Society* **1996**, *143*, 2722–2729.

(47) Ten Elshof, J.; Bouwmeester, H; Verweij, H *Solid State Ionics* **1995**, *81*, 97–109.

(48) Ren, Y.; Küngas, R.; Gorte, R. J.; Deng, C. *Solid State Ionics* **2012**, *212*, 47–54.

(49) Lee, W.; Han, J. W.; Chen, Y.; Cai, Z.; Yildiz, B. *Journal of the American Chemical Society* **2013**, *135*, 7909–7925.

(50) Oh, D.; Gostovic, D.; Wachsman, E. D. *Journal of Materials Research* **2012**, *27*, 1992–1999.

(51) Druce, J.; Téllez, H.; Burriel, M.; Sharp, M. D.; Fawcett, L. J.; Cook, S. N.; McPhail, D. S.; Ishihara, T.; Brongersma, H. H.; Kilner, J. A. *Energy and Environmental Science* **2014**, *7*, 3593–3599.

(52) Jung, W.; Tuller, H. L. *Energy and Environmental Science* **2012**, *5*, 5370–5378.

(53) Kubicek, M.; Rupp, G. M.; Huber, S.; Penn, A.; Opitz, A. K.; Bernardi, J.; Stöger-Pollach, M.; Hutter, H.; Fleig, J. *Physical Chemistry Chemical Physics* **2014**, *16*, 2715.

(54) Cai, Z.; Kubicek, M.; Fleig, J.; Yildiz, B. *Chemistry of Materials* **2012**, *24*, 1116–1127.

(55) Wang, S; van der Heide, P. a. W.; Chavez, C; Jacobson, a. J.; Adler, S. B. *Solid State Ionics* **2003**, *156*, 201–208.

(56) Lee, Y.-L.; Kleis, J.; Rossmeisl, J.; Shao-Horn, Y.; Morgan, D. *Energy & Environmental Science* **2011**, *4*, 3966.

(57) Jung, W.; Tuller, H. L. *Advanced Energy Materials* **2011**, *1*, 1184–1191.

(58) Cheng, S.; Huang, H.; Ovtar, S.; Simonsen, S. B.; Chen, M.; Zhang, W.; Søgaard, M.; Kaiser, A.; Hendriksen, P. V.; Chen, C. *ACS Applied Materials and Interfaces* **2016**, *8*, 4548–4560.

(59) Ovtar, S.; Søgaard, M.; Norrman, K.; Hendriksen, P. V. *Journal of The Electrochemical Society* **2018**, *165*, F220–F231.

(60) Hjalmarsson, P.; Mogensen, M. *Journal of Power Sources* **2011**, *196*, 7237–7244.

(61) Hjalmarsson, P.; Hallinder, J.; Mogensen, M. *Journal of Solid State Electrochemistry* **2012**, *16*, 2759–2766.

(62) Ding, D.; Li, X.; Lai, S. Y.; Gerdes, K.; Liu, M. *Energy & Environmental Science* **2014**, *7*, 552.

(63) Hong, T.; Chen, F.; Xia, C. *Electrochemistry Communications* **2015**, *51*, 93–97.

(64) Lee, D.; Lee, Y.-L.; Hong, W. T.; Biegalski, M. D.; Morgan, D.; Shao-Horn, Y. *Journal of Materials Chemistry A* **2015**, *3*, 2144–2157.

(65) Vohs, J. M.; Gorte, R. J. *Advanced Materials* **2009**, *21*, 943–956.

(66) Avrami, M. *The Journal of Chemical Physics* **1939**, *7*, 1103–1112.

(67) Avrami, M. *The Journal of Chemical Physics* **1940**, *8*, 212–224.

(68) Avrami, M. *The Journal of Chemical Physics* **1941**, *9*, 177–184.

(69) Cox-Galhotra, R. A.; McIntosh, S. *Solid State Ionics* **2010**, *181*, 1429–1436.

(70) Striker, T; Ruud, J. A.; Gao, Y; Heward, W. J.; Steinbruchel, C *Solid State Ionics* **2007**, *178*, 1326–1336.

(71) Søgaard, M.; Hendriksen, P. V.; Poulsen, F. W.; Mogensen, M. *Journal of Electroceramics* **2004**, *13*, 811–816.

(72) Saher, S.; Meffert, M.; Störmer, H.; Gerthsen, D.; Bouwmeester, H. J. M. *Journal of Materials Chemistry A* **2017**, *5*, 4982–4990.

(73) Haider, M. A.; McIntosh, S. *Journal of The Electrochemical Society* **2011**, *158*, B1128.

(74) Niania, M.; Podor, R.; Britton, T. B.; Li, C.; Cooper, S. J.; Svetkov, N.; Skinner, S.; Kilner, J. *Journal of Materials Chemistry A* **2018**, *6*, 14120–14135.

(75) Bucher, E.; Sitte, W.; Klauser, F.; Bertel, E. *Solid State Ionics* **2012**, *208*, 43–51.

(76) Bucher, E.; Sitte, W. *Solid State Ionics* **2011**, *192*, 480–482.

(77) Yu, Y.; Luo, H.; Cetin, D.; Lin, X.; Ludwig, K.; Pal, U.; Gopalan, S.; Basu, S. *Applied Surface Science* **2014**, *323*, 71–77.

(78) Dulli, H.; Dowben, P. A.; Liou, S. H.; Plummer, E. W. *Physical Review B - Condensed Matter and Materials Physics* **2000**, *62*, R14629–R14632.

(79) Szot, K; Speier, W *Physical Review B* **1999**, *60*, 5909.

(80) Mutoro, E.; Crumlin, E. J.; Pöpke, H.; Luerssen, B.; Amati, M.; Abyaneh, M. K.; Biegalski, M. D.; Christen, H. M.; Gregoratti, L.; Janek, J.; Shao-Horn, Y. *Journal of Physical Chemistry Letters* **2012**, *3*, 40–44.

(81) Huber, A.-K.; Falk, M.; Rohnke, M.; Luerssen, B.; Amati, M.; Gregoratti, L.; Hesse, D.; Janek, J. *Journal of Catalysis* **2012**, *294*, 79–88.

(82) Wang, W.; Jiang, S. P. *Solid State Ionics* **2006**, *177*, 1361–1369.

(83) La O', G. J.; Shao-Horn, Y. *Journal of The Electrochemical Society* **2009**, *156*, B816.

(84) Jacobson, A. J. *Chemistry of Materials* **2010**, *22*, 660–674.

(85) Adler, S. B.; Lane, J. A.; Steele, B. C. H. *Journal of the Electrochemical Society* **1996**, *143*, 3554–3564.

(86) Ebbesen, S. D.; Jensen, S. H.; Hauch, A.; Mogensen, M. B. *Chemical Reviews* **2014**, *114*, 10697–10734.

(87) Irvine, J. T. S.; Neagu, D.; Verbraeken, M. C.; Chatzichristodoulou, C.; Graves, C.; Mogensen, M. B. *Nature Energy* **2016**, *1*, 15014.

(88) Kleitz, M.; Siebert, E.; Fabry, P.; Fouletier, J., *Solid-state electrochemical gas sensors*; VCH Verlagsgesellschaft mbH: 1991; Vol. 12.

(89) Mogensen, M. B.; Chatzichristodoulou, C.; Graves, C.; Hansen, V.; Hansen, K. K.; Hauch, A.; Jacobsen, T.; Norrman, K. **2016**, *72*, 93–103.

(90) Sunarso, J.; Hashim, S. S.; Zhu, N.; Zhou, W. *Progress in Energy and Combustion Science* **2017**, *61*, 57–77.

(91) Wu, F.; Argyle, M. D.; Dellenback, P. A.; Fan, M. *Progress in Energy and Combustion Science* **2018**, *67*, 188–205.

(92) Cheng, F.; Chen, J. *Chemical Society Reviews* **2012**, *41*, 2172–2192.

(93) Suntivich, J.; Gasteiger, H. a.; Yabuuchi, N.; Nakanishi, H.; Goodenough, J. B.; Shao-Horn, Y. *Nature chemistry* **2011**, *3*, 546–550.

(94) Jiang, S. P. *Journal of Materials Science* **2008**, *43*, 6799–6833.

(95) Jorgensen, M. J.; Primdahl, S; Bagger, C; Mogensen, M. *Solid State Ionics* **2001**, *139*, 1–11.

(96) Hansen, K. V.; Norrman, K.; Jacobsen, T.; Wu, Y.; Mogensen, M. B. *Journal of The Electrochemical Society* **2015**, *162*, F1165–F1174.

(97) Sitte, W.; Bucher, E.; Preis, W. *Solid State Ionics* **2002**, *154-155*, 517–522.

(98) Bucher, E; Sitte, W *Solid State Ionics* **2004**, *173*, 23–28.

(99) Kuhn, M.; Hashimoto, S.; Sato, K.; Yashiro, K.; Mizusaki, J. *Solid State Ionics* **2011**, *195*, 7–15.

(100) Bucher, E.; Sitte, W. *Journal of Electroceramics* **2004**, *13*, 779–784.

(101) Esquirol, A.; Brandon, N. P.; Kilner, J. A.; Mogensen, M. *Journal of The Electrochemical Society* **2004**, *151*, A1847.

(102) Baumann, F. S.; Fleig, J.; Habermeier, H. U.; Maier, J. *Solid State Ionics* **2006**, *177*, 1071–1081.

(103) Rupp, G. M.; Opitz, A. K.; Nenning, A.; Limbeck, A.; Fleig, J. *Nature Materials* **2017**, *16*, 640–645.

(104) Tsvetkov, N.; Lu, Q.; Sun, L.; Crumlin, E. J.; Yildiz, B. *Nature materials* **2016**, *15*, 1010–1016.

(105) Yu, A. S.; Küngas, R.; Vohs, J. M.; Gorte, R. J. *Journal of The Electrochemical Society* **2013**, *160*, F1225–F1231.

(106) Bucher, E.; Gspan, C.; Hofer, F.; Sitte, W. *Solid State Ionics* **2013**, *238*, 15–23.

(107) Schrödl, N.; Bucher, E.; Egger, A.; Kreiml, P.; Teichert, C.; Höschen, T.; Sitte, W. *Solid State Ionics* **2015**, *276*, 62–71.

(108) Hilpert, K. *Journal of The Electrochemical Society* **1996**, *143*, 3642.

(109) Yokokawa, H.; Horita, T.; Sakai, N.; Yamaji, K.; Brito, M. E.; Xiong, Y. P.; Kishimoto, H. *Solid State Ionics* **2006**, *177*, 3193–3198.

(110) Bentzen, J. J.; Høgh, J. V.; Barfod, R.; Hagen, A. *Fuel Cells* **2009**, *9*, 823–832.

(111) Schrödl, N.; Bucher, E.; Egger, A.; Kreiml, P.; Teichert, C.; Höschen, T.; Sitte, W. *Solid State Ionics* **2015**, *276*, 62–71.

(112) Lee, D.; Grimaud, A.; Crumlin, E. J.; Mezghani, K.; Habib, M. A.; Feng, Z.; Hong, W. T.; Biegalski, M. D.; Christen, H. M.; Shao-horn, Y. **2013**.

(113) Chen, Y.; Jung, W.; Cai, Z.; Kim, J. J.; Tuller, H. L.; Yildiz, B. *Energy & Environmental Science* **2012**, *5*, 7979.

(114) Pişkin, F.; Bliem, R.; Yildiz, B. *Journal of Materials Chemistry A* **2018**, *6*, 14136–14145.

(115) Li, Y.; Zhang, W.; Zheng, Y.; Chen, J.; Yu, B.; Chen, Y.; Liu, M. *Chemical Society Reviews* **2017**, *46*, 6345–6378.

(116) Koo, B.; Kim, K.; Kim, J. K.; Kwon, H.; Han, J. W.; Jung, W. *Joule* **2018**, *2*, 1476–1499.

(117) Liu, Y.; Chen, K.; Zhao, L.; Chi, B.; Pu, J.; Jiang, S. P.; Jian, L. *International Journal of Hydrogen Energy* **2014**, *39*, 15868–15876.

(118) Pan, Z.; Liu, Q.; Zhang, L.; Zhang, X.; Chan, S. H. *Journal of The Electrochemical Society* **2015**, *162*, F1316–F1323.

(119) Wang, H.; Yakal-Kremski, K. J.; Yeh, T.; Rupp, G. M.; Limbeck, A.; Fleig, J.; Barnett, S. A. *Journal of The Electrochemical Society* **2016**, *163*, F581–F585.

(120) Qiu, Y.; Pu, J.; Li, J.; Liu, Y.; Hua, B. *Journal of Electrochemical Energy Conversion and Storage* **2017**, *14*, 031002.

(121) Ni, N.; Cooper, S. J.; Williams, R.; Kemen, N.; McComb, D. W.; Skinner, S. J. *ACS Applied Materials & Interfaces* **2016**, *8*, 17360–17370.

(122) Mutoro, E.; Crumlin, E. J.; Biegalski, M. D.; Christen, H. M.; Shao-Horn, Y. *Energy & Environmental Science* **2011**, *4*, 3689.

(123) Crumlin, E. J.; Ahn, S.-J.; Lee, D.; Mutoro, E.; Biegalski, M. D.; Christen, H. M.; Shao-Horn, Y. *Journal of the Electrochemical Society* **2012**, *159*, F219–F225.

(124) Li, Y.; Zhang, W.; Wu, T.; Zheng, Y.; Chen, J.; Yu, B.; Zhu, J.; Liu, M. *Advanced Energy Materials* **2018**, *1801893*, 1801893.

(125) Szot, K.; Speier, W.; Herion, J.; Freiburg, C. *Applied Physics A: Materials Science & Processing* **1997**, *64*, 55–59.

(126) Meyer, R.; Szot, K.; Waser, R. *Ferroelectrics* **1999**, *224*, 323–329.

(127) Molak, A.; Paweczyk, M.; Kubacki, J.; Szot, K. *Phase Transitions* **2009**, *82*, 662–682.

(128) Rupp, G. M.; Limbeck, A.; Kubicek, M.; Penn, A.; Stöger-Pollach, M.; Friedbacher, G.; Fleig, J. *Journal of Materials Chemistry A* **2014**, *2*, 7099–7108.

(129) Rupp, G. M.; Téllez, H.; Druce, J.; Limbeck, A.; Ishihara, T.; Kilner, J.; Fleig, J. *J. Mater. Chem. A* **2015**, *3*, 22759–22769.

(130) Huber, A.-K.; Falk, M.; Rohnke, M.; Luerßen, B.; Gregoratti, L.; Amati, M.; Janek, J. *Phys. Chem. Chem. Phys.* **2012**, *14*, 751–758.

(131) Abernathy, H.; Finklea, H. O.; Mebane, D. S.; Song, X.; Chen, Y.; Gerdes, K. *Solid State Ionics* **2015**, *272*, 144–154.

(132) Ranganathan, S.; Von Heimendahl, M. *Journal of Materials Science* **1981**, *16*, 2401–2404.

(133) Liu, F.; Sommer, F.; Bos, C.; Mittemeijer, E. J. *International Materials Reviews* **2007**, *52*, 193–212.

(134) Nenning, A.; Opitz, A. K.; Rameshan, C.; Blume, R.; Knop-gericke, A.; Rupprechter, G.; Klo, B.; Fleig, J. *The Journal of Physical Chemistry C* **2016**, 1461–1471.

(135) Chen, Y.; Téllez, H.; Burriel, M.; Yang, F.; Tsvetkov, N.; Cai, Z.; McComb, D. W.; Kilner, J. A.; Yildiz, B. *Chemistry of Materials* **2015**, 5436–5450.

(136) Cai, Z.; Kubicek, M.; Fleig, J.; Yildiz, B. *Chemistry of Materials* **2012**, *24*, 1116–1127.

(137) Pitscheider, S. In-operando spatially resolved probing of solid oxide electrolysis/-fuel cells., Ph.D. Thesis, 2018.

(138) Crumlin, E. J.; Mutoro, E.; Hong, W. T.; Biegalski, M. D.; Christen, H. M.; Liu, Z.; Bluhm, H.; Shao-Horn, Y. *Journal of Physical Chemistry C* **2013**, *117*, 16087–16094.

(139) Hong, T.; Brinkman, K. S.; Xia, C. *ChemElectroChem* **2016**, 1–10.

(140) Cheng, X.; Fabbri, E.; Nachtegaal, M.; Castelli, I. E.; El Kazzi, M.; Haumont, R.; Marzari, N.; Schmidt, T. J. *Chemistry of Materials* **2015**, *27*, 7662–7672.

(141) Wu, J.; Pramana, S. S.; Skinner, S. J.; Kilner, J. a.; Horsfield, A. *J. Mater. Chem. A* **2015**, 23760–23767.

(142) Chueh, W. C.; Haile, S. M. *Annual Review of Chemical and Biomolecular Engineering* **2012**, *3*, 313–341.

(143) Mosleh, M.; Sogaard, M.; Hendriksen, P. V. *Journal of The Electrochemical Society* **2009**, *156*, B441.

(144) Nielsen, J.; Jacobsen, T.; Wandel, M. *Electrochimica Acta* **2011**, *56*, 7963–7974.

(145) Nielsen, J.; Hjelm, J. *Electrochimica Acta* **2014**, *115*, 31–45.

(146) Bouwmeester, H; Kruidhof, H; Burggraaf, A *Solid State Ionics* **1994**, *72*, 185–194.

(147) Baumann, F. S.; Fleig, J.; Cristiani, G.; Stuhlhofer, B.; Habermeier, H.-U.; Maier, J. *Journal of The Electrochemical Society* **2007**, *154*, B931.

(148) Plonczak, P.; Sogaard, M.; Bieberle-Hütter, A.; Hendriksen, P. V.; Gauckler, L. J. *Journal of The Electrochemical Society* **2012**, *159*, B471.

(149) Lynch, M. E.; Liu, M. *Journal of Power Sources* **2010**, *195*, 5155–5166.

(150) Wedig, A.; Lynch, M. E.; Merkle, R.; Maier, J.; Liu, M. *ECS Transactions* **2012**, *45*, 213–224.

(151) Boukamp, B. A.; Hildenbrand, N.; Nammensma, P.; Blank, D. H. A. *Solid State Ionics* **2011**, *192*, 404–408.

(152) Boukamp, B. A.; Hildenbrand, N.; Bouwmeester, H. J.; Blank, D. H. *Solid State Ionics* **2015**, *283*, 81–90.

(153) La O', G. J.; Ahn, S.-J.; Crumlin, E.; Orikasa, Y.; Biegalski, M. D.; Christen, H. M.; Shao-Horn, Y. *Angewandte Chemie International Edition* **2010**, *49*, 5344–5347.

(154) Kogler, S; Nenning, A; Rupp, G. M.; Opitz, A. K.; Fleig, J *Journal of The Electrochemical Society* **2015**, *162*, F317–F326.

(155) Orsini, A.; Medaglia, P. G.; Sanna, S.; Traversa, E.; Licoccia, S.; Tebano, A.; Balestrino, G. *Superlattices and Microstructures* **2009**, *46*, 223–226.

(156) Jamnik, J.; Maier, J. *Physical Chemistry Chemical Physics* **2001**, *3*, 1668–1678.

(157) Baumann, F. S.; Maier, J.; Fleig, J. *Solid State Ionics* **2008**, *179*, 1198–1204.

(158) Chung, B. W.; Pham, A.-q.; Haslam, J. J.; Glass, R. S. **2002**, 325–330.

(159) Adler, S. B. *Solid State Ionics* **1998**, *111*, 125–134.

(160) Januschewsky, J.; Stöger-Pollach, M.; Kubel, F.; Friedbacher, G.; Fleig, J. *Zeitschrift für Physikalische Chemie* **2012**, *226*, 889–899.

(161) Darbandi, A. J.; Hahn, H. *Solid State Ionics* **2009**, *180*, 1379–1387.

(162) Samson, A. J.; Hjalmarsson, P.; Sogaard, M.; Hjelm, J.; Bonanos, N. *Journal of Power Sources* **2012**, *216*, 124–130.

(163) Kawada, T.; Suzuki, J.; Sase, M.; Kaimai, A.; Yashiro, K.; Nigara, Y.; Mizusaki, J.; Kawamura, K.; Yugami, H. *Journal of The Electrochemical Society* **2002**, *149*, E252.

(164) Rupp, G. M.; Téllez, H.; Druce, J.; Limbeck, A.; Ishihara, T.; Kilner, J.; Fleig, J. *J. Mater. Chem. A* **2015**, *3*, 22759–22769.

(165) Huber, T. M.; Kubicek, M.; Opitz, a. K.; Fleig, J. *Journal of the Electrochemical Society* **2014**, *162*, F229–F242.

(166) Gao, Z.; Mogni, L. V.; Miller, E. C.; Railsback, J. G.; Barnett, S. A. *Energy Environ. Sci.* **2016**, *9*, 1602–1644.

(167) Samson, A; Sogaard, M.; Knibbe, R; Bonanos, N *Journal of The Electrochemical Society* **2011**, *158*, B650.

(168) Kiebach, R.; Knöfel, C.; Bozza, F.; Klemensø, T.; Chatzichristodoulou, C. *Journal of Power Sources* **2013**, *228*, 170–177.

(169) Kiebach, R.; Zielke, P.; Høgh, J. V.; Thydén, K.; Wang, H. J.; Barford, R.; Hendriksen, P. V. *Fuel Cells* **2016**, *16*, 80–88.

(170) Chrzan, A.; Karczewski, J.; Gazda, M.; Szymczewska, D.; Jasinski, P. *Journal of the European Ceramic Society* **2017**, *37*, 3559–3564.

(171) Shah, M.; Barnett, S. A. *Solid State Ionics* **2008**, *179*, 2059–2064.

(172) Hong, T.; Chen, F.; Xia, C. *Journal of Power Sources* **2015**, *278*, 741–750.

(173) Cao, X.; Hong, T.; Yang, R.; Tian, J.-H.; Xia, C.; Dong, J.-C.; Li, J.-F. *The Journal of Physical Chemistry C* **2016**, 22895−22902.

(174) Gong, Y.; Palacio, D.; Song, X.; Patel, R. L.; Liang, X.; Zhao, X.; Goodenough, J. B.; Huang, K. *Nano Letters* **2013**, *13*, 4340–4345.

(175) Jensen, S. H.; Hauch, A.; Hendriksen, P. V.; Mogensen, M.; Bonanos, N.; Jacobsen, T. *Journal of The Electrochemical Society* **2007**, *154*, B1325.

(176) Tripkovic, D. *Laboratory Notes, Unpublished work*.

(177) Ciucci, F. *Solid State Ionics* **2013**, *239*, 28–40.

(178) Seah, M. P. *Surface and Interface Analysis* **2012**, *44*, 1353–1359.

(179) Lindau, I.; Spicer, W. *Journal of Electron Spectroscopy and Related Phenomena* **1974**, *3*, 409–413.

(180) Hill, J.; Royce, D.; Fadley, C.; Wagner, L.; Grunthaner, F. *Chemical Physics Letters* **1976**, *44*, 225–231.

{2.7182818284}ϑωερτυθιοπσδφγηξκλ